

**IMPROVING MEASUREMENTS BASED ON THE CAT'S EYE RETRO-
REFLECTION**

by

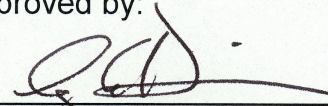
Katherine Mary Medicus

A dissertation submitted to the faculty of
The University of North Carolina at Charlotte
in partial fulfillment of the requirements
for the degree of Doctor of Philosophy
in Mechanical Engineering

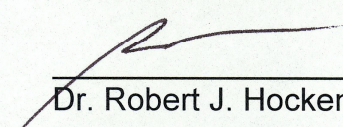
Charlotte

2006

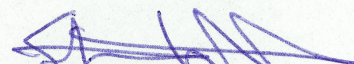
Approved by:



Dr. Angela D. Davies




Dr. Robert J. Hocken



Dr. Stuart Smith



Dr. Farmarz Farahi



Dr. Wanda Nabors

© 2006
Katherine Mary Medicus
ALL RIGHTS RESERVED

ABSTRACT

KATHERINE MARY MEDICUS. Improving Measurements Based on the Cat's Eye Retro-Reflection. (Under the direction of DR. ANGELA D. DAVIES)

The interferometric radius measurement of refractive optical components is used to identify the effect of uncertainties in the cat's eye position. This measurement is typically modeled using a geometric ray model and is found by first placing the part at the confocal position and then the cat's eye position and measuring the distance the part moves between the two. I demonstrate that using the simple geometric ray model instead of a more complex Gaussian or a physical optics model causes biases in the radius measurement. These biases depend on the model, the interferometer configuration (numerical aperture, etc.), the nominal radius of the test part, and the amount of interferometer aberration. Biases on the order of parts in 10^4 exist for 1 mm radius parts and larger for smaller parts. The biases are calculated using a Gaussian model and software package to approximate a physical optics model for both micro- (< 1 mm) and macro-scaled parts. Both models test the effect of the numerical aperture, the radius of the test part, the distances in the interferometer, and the effect of aberrations on the radius measurements. The models have large uncertainties, many of which due to experimental details that cannot be modeled. Thus, a direct correction of the bias is not possible. Rather, the models serve to indicate the order of magnitude of the effects. Experiments on a micro-interferometer are used to test for these biases and show an effect on the measured radius when the aberration (in the interferometer) is increased.

ACKNOWLEDGMENTS

I would like to thank the University of North Carolina at Charlotte and the Mechanical Engineering and Engineering Science Department for the opportunity to pursue my doctoral studies. The Center for Precision Metrology Affiliates program provided the funding for this project and deserves much gratitude. My advisor, Dr. Angela Davies has been a source of inspiration and knowledge. Thank you so much for all your help and support. Also, I would like to thank all the faculty and staff of the CPM and my fellow students who have always helped me when I need it. Final thanks go to my family. Mom and Dad, thanks for all the love and support. Jon, you were there for me when I needed it, thanks so much. I'm looking forward to the all the years ahead.

TABLE OF CONTENTS

CHAPTER 1: INTRODUCTION	1
1.1 Overview of this Work	1
1.2 Using this Research	2
1.3 The Cat's Eye Reflection	3
1.3.1 Application of the Cat's Eye Reflection	4
1.3.2 Intensity at Focus	5
1.4 Measurement of the Radius	6
1.4.1 Other Methods for Measuring the Radius	7
1.4.2 Setup of an Interferometric Radius Measurement	7
1.4.3 Previous Research in Radius	8
1.4.4 Previous Work on Measuring Radius on Micro-Optics	10
1.5 Uncertainties Affected by the Cat's Eye Position	12
1.5.1 Null Position Location	13
1.5.2 Modeling the Cat's Eye and Confocal Positions	15
1.5.3 Aberrations in the Phase Measuring Interferometer	19
1.5.4 Input Variations	20
1.5.5 Offset of the Cat's Eye Position Due to Phase Change	20
1.6 Summary	21
CHAPTER 2: THE GAUSSIAN MODEL OF A RADIUS MEASUREMENT	23
2.1 Introduction	23
2.2 The Radius Measurement in a Gaussian Model	24
2.3 The Gaussian Beam Model	25
2.3.1 The Matrices of the Gaussian Model	29
2.3.2 Finding the Confocal and Cat's Eye Positions	31
2.3.3 The Perfect Cat's Eye and Confocal	31
2.4 Determining the Inputs	36
2.4.1 Calculating q_{in} , Case 1	36
2.4.2 Calculating q_{in} , Case 2	37

2.4.3 Calculating q_{in} , Case 3, and focal length	38
2.4.4 Summary of q_{in}	42
2.4.5 The Remaining Input Parameters	42
2.5 Obtaining Radius from the Model	43
2.6 Results of the Code for Micro-Scale Parts	46
2.6.1 Testing Varying Radius for the Different q_{in} Cases	46
2.6.2 Testing the Effect of Varying NA	50
2.6.3 Varying the Propagation Distances, d_t and d_r	51
2.7 Curvature at the Test Part	54
2.8 Results for Macro-Scale Parts	56
2.9 Checking Assumptions	57
2.10 Conclusions about the Model	63
CHAPTER 3: A PHYSICAL OPTICS MODEL OF THE RADIUS MEASUREMENT USING FRED	66
3.1 Introduction to FRED	66
3.2 Sources	67
3.2.1 Circular Aperture Input Beam	67
3.2.2 A Gaussian Beam Input	68
3.3 The Focusing Lens	69
3.3.1 Using a Spherical Lens	70
3.3.2 Using a Spherical Lens with a Conic Surface	71
3.3.3 Using a Parabola	73
3.4 The Detector and Analysis	75
3.5 Reading the Phase Data in Matlab	76
3.5.1 Unwrapping	76
3.5.2 The Zernike Coefficients	77
3.6 Setup of the Simulated Radius Measurements in FRED	78
3.7 Summary of Radius Procedure	80
3.8 Measurements using the Single Gaussian Beam.	81
3.8.1 Varying Radius	81

3.8.2 Varying NA	83
3.8.3 Varying the Propagation Distances, d_t and d_r	85
3.9 Measurements using the Circular Input	86
3.9.1 Varying Radius	86
3.9.2 Varying NA	87
3.9.3 Varying Propagation Distances	88
3.10 Adding Spherical Aberration	89
3.10.1 Spherical Aberration with the Top Hat Beam	90
3.11 Masking	95
3.12 Macro Scale Radius	98
3.13 Summary of Results	98
3.13.1 Circular Aperture Input Beam	98
3.13.2 Gaussian Input Beam	100
3.14 Uncertainty	100
CHAPTER 4: EXPERIMENTAL VERIFICATION ON MORTI	104
4.1 Introduction	104
4.2 Setup of MORTI for Reflection Measurements	106
4.2.1 Design of Imaging Leg	107
4.3 Alignment of the Scale	112
4.4 Alignment of MORTI and Calibration of the Scale	113
4.4.1 Mechanical Alignment	114
4.4.2 Alignment of DMI	115
4.4.3 Calibration of Scale	119
4.5 Alignment of Twyman-Green Interferometer	120
4.5.1 Input Beam and Beamsplitter	120
4.5.2 Reference Mirror	123
4.5.3 Objective Lens	124
4.5.4 Imaging Optics	124
4.6 The Focusing Effect	125
4.6.1 Demonstration of the Focusing Issue	126

4.6.2 Simulation of the Focusing Issue, Without the Imaging Leg	131
4.6.3 Effect on Radius Measurement	135
4.6.4 Considering Spherical Aberration	137
4.6.5 Focusing Effect with Imaging Leg	139
4.6.6 Focusing Effect on the Macro-Scale	143
4.6.7 Comparison to Theoretical, Without Imaging Leg	144
4.6.8 Comparison to Theoretical, With Imaging Leg	146
4.6.9 Conclusion of the Focusing Effect	150
4.7 Operation of MORTI	151
4.8 Measurement of Spheres	152
4.8.1 The Spheres	152
4.8.2 Uncertainty due to Fitting	156
4.8.3 Repeatability	157
4.8.4 Varying L_{23}	158
4.8.5 Changing the Mask Size	158
4.8.6 Vary the Objective Lens NA	160
4.8.7 Adding Spherical Aberration	162
4.9 Measurement of the Microscope Objective	167
4.10 Uncertainty	168
4.11 Conclusions	170
 CHAPTER 5: THE EFFECT OF PHASE CHANGE ON REFLECTION ON THE CAT'S EYE POSITION	 172
5.1 Introduction and Background	172
5.1.1 Connection to Radius and Cat's Eye	175
5.2 Theoretical Calculations of the Phase Change	176
5.2.1 Non-Normal Angle of Incidence	177
5.2.2 Normal Angle of Incidence	180
5.2.3 Determining the Values of the Index of Refraction	180
5.2.4 Phase Change Values at Normal Incidence	181
5.2.5 Phase Change Values at Non-Normal Incidence	182

5.3 Impact on the Cat's Eye Position	183
5.3.1 Added Defocus Due to the Phase Change	183
5.3.2 The Offset Due to Phase Change	186
5.3.3 Offset as a Function of Uncertainty in the Refractive Index	188
5.3.4 Offset due to the TM mode	189
5.4 Experimental Plan	190
5.4.1 Sample Preparation	190
5.4.2 Measurement Plan, Normal Incidence	191
5.4.3 Determining the Phase Change at a Air/Metal Interface	192
5.4.4 Measurement Plan, Non-Normal Incidence	194
5.5 Analysis and Results	195
5.5.1 Analysis, Normal Angle of Incidence	196
5.5.2 Analysis, Varying Angle of Incidence	197
5.5.3 Uncertainty	197
5.5.4 Results, Normal Angle of Incidence	199
5.5.5 Results, Varying Angle of Incidence	200
5.6 Conclusions and Continuing Work	201
CHAPTER 6: DISCUSSION OF RESULTS AND COMPARISON	203
6.1 Introduction	203
6.2 Numerical Aperture and Part Size	204
6.3 Spherical Aberration	206
6.3.1 Ray Trace Model	207
6.3.2 Retrace in the FRED Model and in Experiment	210
6.3.3 Spherical Aberration	212
6.3.4 The Focal Shift	215
6.3.5 Comparing FRED and Experiment with Spherical Aberration	216
6.4 Masking	220
6.5 Macro-Scale Parts	221
6.6 Uncertainty	222
CHAPTER 7: FUTURE WORK AND CONCLUSIONS	224

7.1 Future Work	224
7.1.1 Retrace Errors	224
7.1.2 Phase Change	225
7.1.3 MORTI	226
7.1.4 Model of Focal Region	227
7.1.5 FRED	228
7.2 Conclusions	228
REFERENCES	231
APPENDIX A: ZERNIKES	235
APPENDIX B: MATLAB PROGRAMS	236
Program 1: guassian.m	236
Program 2: der_test.m	240
Program 3: get_20_40_from_fred.m	242
Program 4: read_fred.m	243
Program 5: mask_cricle.m	244
Program 6: zern_radius_angle.m	246
Program 7: zern_estim.m	247
Program 8: foc_effect_no_image.m	255
Program 9: foc_effect_w_image.m	256
APPENDIX C: CALIBRATION DATA	258

CHAPTER 1: INTRODUCTION

1.1 Overview of this Work

This work uses the interferometric radius measurement to investigate the cat's eye retro-reflection. The overall goal of this research is to identify and reduce the uncertainty in the radius measurement (and other types of measurements) caused by the cat's eye retro-reflection.

This work is comprised of simulation and experiment. The radius measurement and the cat's eye retro-reflection is simulated analytically with a Gaussian model of light and computationally with the computer software package FRED which attempts to simulate a full physical optics model of light. In simulation, I studied different aspects of the measurement to determine the effect of each on the uncertainty and bias in the radius measurement. These aspects include the size of the test part, the configuration of the interferometer, imperfections (aberrations) in the interferometer, and the phase change on reflection. In experiment, I measured the radius on an interferometer and the effect of the above aspects is investigated.

Each of the above aspects contributes to the final uncertainty of the radius measurement. The goal is to determine how much this contribution is for each aspect and then determine if that aspect is limiting the final uncertainty in any given measurement.

The uncertainty and bias in the radius measurement tends to increase with decreasing part size. Because of this, this investigation will focus on micro-scale parts with the hope that the errors in the measurement will be observable. Some errors may be too small to observe on macro-scale parts. But, depending on the required uncertainty goal, these errors may still need to be accounted for with macro-scale parts and would be important to consider in ultra-precision measurements. It was a series of ultra-precision radius measurements of a 25 mm radius part carried out at NIST several years ago that motivated this study [27]. This work is described Section 1.4.3.

1.2 Using this Research

This work can be used to determine which aspects of the measurement limit the uncertainty of a specific part. The uncertainty goal must first be identified, though. This will vary from application to application and part to part. With the radius measurement, the uncertainty is commonly identified as “a part in 10^x ” where x is commonly 4 or 5 for precision measurements and a higher number indicates a lower required uncertainty. For example, a part in 10^4 for a 25 mm radius test part is 2.5 μm and for a 0.2 mm radius test, five parts in 10^4 is 500 nm. Described this way, the difficulty of measuring micro-scale parts with high precision is not surprising.

After the measurement uncertainty goal is clearly defined, this work can be used to identify which aspect(s) of the measurement limit the uncertainty. Throughout this work, each aspect will have an associated measurement

uncertainty (using the 10^x term). This will identify when the aspect has become the limiting factor in the final uncertainty.

1.3 The Cat's Eye Reflection

The cat's eye reflection is a retro-reflection, that is, the incoming beam and outgoing beams are always parallel, even if the incoming beam is not perpendicular to the reflector. This is different from a standard mirror and is akin to a corner cube reflector. A cat's eye reflection is named due to the bright spot that you see in the eye of a cat when you shine a light toward it at night [1].

The cat's eye reflection is used in measurements because it can be used to define a point in space. If a test part is placed at the cat's eye position, that position is uniquely defined for the test part in the optical axis. It is this property that forms the basis for optical measurements such as radius.

A typical cat's eye retro-reflection is realized using a focusing lens and a reflecting surface, Figure 1-1. Because the reflecting surface is placed at the focus of the lens, a cat's eye retro-reflection occurs. The configuration of the cat's eye reflector can take different forms: the focusing lens could be a mirror, the reflecting surface can have curvature, or the lens and mirror could all be the same spherical component (specific material and geometric properties are required).

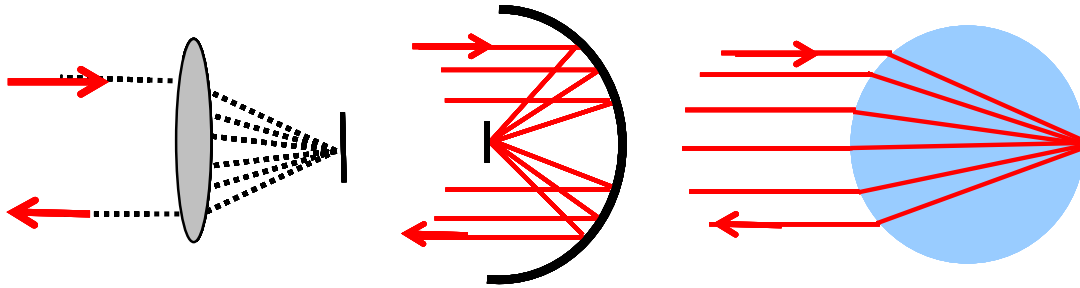


Figure 1-1: Schematic of various configurations of the cat's eye reflection.

1.3.1 Application of the Cat's Eye Reflection

Percy Shaw appears to have developed the first cat's eye retro-reflectors for road safety in Great Britain in 1935 after the reflection from the eye of a cat prevented him from running off the road [2]. Sheets of cat's eye retro-reflectors are used on signs and in other traffic applications to improve visibility [3].

Cat's eye retro-reflectors are used in laser tracking systems [4,5] instead of corner cubes because the cat's eye has a larger acceptance angle. A cat's eye reflector replaces the corner cube reflectors in open-path Fourier transform infrared spectrometry to reduce cost, mass and fragility [6]. The stability of a He-Ne laser is improved by using a cat's eye reflector in the cavity [7].

Several authors have investigated the best parameters for the cat's eye retro-reflector for different applications [8, 9, 10]. Parameters such as mirror curvature, spacing tolerances, focal length, aperture, and alignment errors must be considered to design a cat's eye retro-reflector with minimized aberrations. The lens and mirror of the cat's eye retro-reflectors are considered a single component. After assembly, the lens and mirror do not move relative to one another. A different application is to move the mirror relative to the lens to determine the position of the mirror when the cat's eye retro-reflection takes

place. The interferometric radius measurement [26] uses this approach. This is the measurement that I will use to investigate the affect of the cat's eye retro-reflection.

1.3.2 Intensity at Focus

The physical optics model of the intensity at focus has been studied extensively [11]. This understanding is import to consider in the contest of the cat's eye reflection. It was found, under certain conditions, the point of maximum intensity does not coincide with the focal length of the system [12]. There is an axial shift along the Z axis (axial and optical axis) which can lead to a bias in determining the cat's eye position. This focus shift is not a factor in systems with a Fresnel Number, N , much much greater than one. The Fresnel Number is defined as

$$N = \frac{(a/2)^2}{\lambda f}$$

Equation 1-1

where a is the aperture diameter, λ the wavelength of the light, and f the focal length of the lens. A small Fresnel number means that the diffraction of the beam is significant as compared to the focal length, almost as if the beam is spreading by diffraction faster than it is focusing. A large Fresnel number means that the diffraction spread is small compared to the focusing. For the current measurement system, the Fresnel number, N , ranges from 260 to 1,500 for varying focal lengths. Therefore, the shift in the maximum intensity does not effect the current measurement of the cat's eye position.

1.4 Measurement of the Radius

The radius (sometimes misnamed in literature as the radius of curvature) of spherical components is a key parameter in determining the geometry and performance of an optical test part, for example, spherical refractive lenses with a continuous relief structure or spherical mirrors. For spherical components, the radius is defined as the radius of the best fit sphere (by a least squares method) over the aperture of interest. The interferometric radius measurement is well suited to conduct investigations on the cat's eye position because a cat's eye retro-reflection is required for the interferometric radius measurement. Further, the interferometric radius measurement of micro-lenses allows for more rigorous study of the cat's eye position because the effect of surface curvature will be emphasized and therefore more easily observed than for macro-scale optics.

Phase shifting interferometry is well suited to measure the radius of optical components due to its low uncertainty values, the non-contact nature of the measurement, and its ability to adapt to parts of varying sizes [13]. With careful implementation, the radius of spherical parts can be measured to 0.001% (parts in 10^5) [25] for macro-scaled parts. This measurement is typically performed on a radius bench with either a Fizeau or Twyman-Green Interferometer. The interferometric radius measurement uses the interferometer to determine the location of the two critical null positions (called the confocal and cat's eye), Figure 1-2. A scale of some type is used to measure the distance the component moves between the two null positions. This distance is the radius of the component.

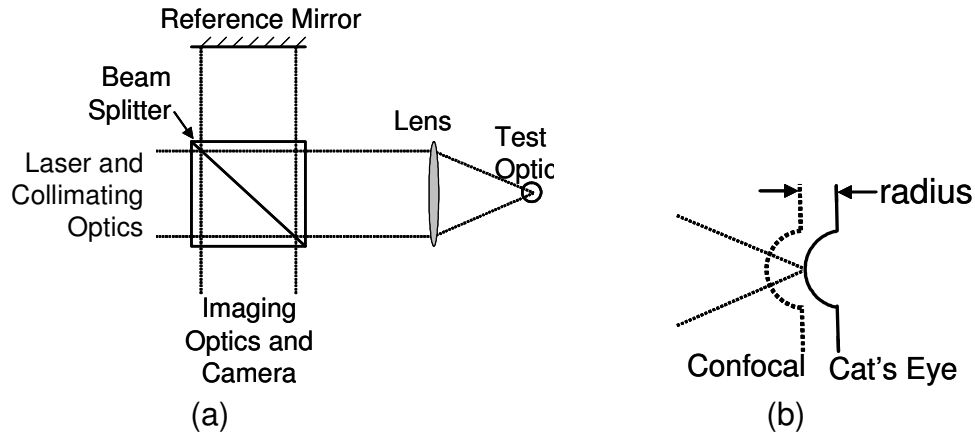


Figure 1-2: (a) Schematic of a Twyman-Green interferometer. (b) The confocal and cat's eye positions.

1.4.1 Other Methods for Measuring the Radius

Mechanical methods to measure the radius of a test part include templates, spherometers [14], and mechanical surface profilers [15]. A disadvantage of all of these methods is they are contact measurements, have limited ranges, and may have uncertainty too high for precision applications. Optical methods include scanning white light interferometry (SWLI) [16], the Foucault (knife edge) test, an autocollimator, and a traveling microscope [14]. All of the tests are limited by the high uncertainty, speed, and/or by the size of test part. The interferometric radius measurement is preferred for precision applications.

1.4.2 Setup of an Interferometric Radius Measurement

This work focuses on a micro-scale Twyman-Green interferometer, as shown in the schematic in Figure 1-2(a). The laser and collimating optics produce a collimated beam of He-Ne 632.8 nm light. A beam splitter then divides the light into the reference arm and test arm. In the reference arm, the reference mirror reflects the light back to the beam splitter. In the test arm, a lens (e.g., a

microscope objective) is used to focus the light to the test part. The test part is placed at a null position of either the confocal or cat's eye reflections as shown in Figure 1-2(b). After the reflection from the test part, the light is collimated by the lens and returns to the beam splitter. Imaging optics and a camera are then used to focus and capture the interferometer pattern.

The confocal reflection occurs when the optic is placed in the test beam of the interferometer such that the wavefront curvature of the incoming beam and the curvature of the test optic match. A confocal reflection acts as a mirror. In the geometric model, the cat's eye reflection occurs when the surface of the optic is coincident with the focus of the test beam. The cat's eye reflection acts as a retro-reflector. Further discussion of the cat's eye position in a non-geometric model can be found later in this work in Chapter 2 and Chapter 3.

1.4.3 Previous Research in Radius

Previous work in precision radius measurements using phase measuring interferometry include Selberg [25] and Schmitz, et al. [27] who investigated Fizeau interferometers on the macro-scale (150 mm and 300 mm apertures) with test parts near 25 mm radius. Both of these investigators focused on calculating and reducing the biases and uncertainties in the measurement. The sources of uncertainty can be divided into two categories: mechanical and optical. The mechanical sources include the motion of the radius slide, the alignment of the axes, the displacement measuring interferometer (used to measure the distance traveled), Abbe errors, cosine errors, the deadpath, the environment, turbulence, and the laser system. The optical uncertainties include the phase measuring

interferometer (an imperfect wavefront), surface figure of the test part, and variation in the aperture. Schmitz, et al. [27] also considered the uncertainty in the radius due to using a geometric ray model instead of a physical optics model.

The final combined standard uncertainty and the bias in the measurement of a Zerodur 24.446 mm radius sphere as calculated by Schmitz, et al. [27] depends on the transmission sphere used. The uncertainties and the measurement divergence as compared to mechanical measurement are summarized in Table 1-1. The largest contributors to uncertainty are deadpath uncertainty (an uncertainty from the displacement measuring interferometer) and the null position calculation (determining where confocal and cat's eye are). The smaller NA transmission spheres (larger f/#) have a higher uncertainty. Even with accounting for the all the known sources of uncertainties and biases in the measurements, the investigators found an unexplained discrepancy between the interferometric radius measurement and the mechanical CMM measurement. This discrepancy ranges fro different measurements, but is as large as 250 nm in some cases.

Table 1-1: Uncertainty and bias results from radius measurement of Zerodur sphere [27].

Transmission Sphere	Combined Standard Uncertainty (nm)	Fractional Error	Measurement Bias(nm)
f/1.1 (0.45 NA)	57	2 Parts in 10 ⁶	0
f/3.2 (0.16 NA)	158	6 Parts in 10 ⁶	-183
f/4 (0.13 NA)	298	1 Part in 10 ⁵	-275

Selberg did not perform a full uncertainty analysis, but did investigate many sources of error but concluded that measurements at the level of 0.001% (parts in 10^5) are possible for parts with radius greater than 100 mm and for parts smaller than 100 mm measurement accuracy is typically limited to the micrometer range. The Abbe errors can dominate the error budget in the radius measurement and are in the range of 10 to 100 μm .

Griesmann, et. al., performed the precision radius measurements on a silicon sphere with a radius of 46.8 mm [17]. The uncertainty in one measurement was found to be 20 nm with the deadpath errors being the largest contributor. In addition, the radius was measured on different locations of the sphere. The authors found a high standard deviation in the radius measurement of 88 nm even though the sphere had low form errors of approximately 70 nm peak to valley.

Recent research by Davies and Schmitz has introduced a new technique for reducing uncertainty in the radius measurement caused by error motions in the slideway [18]. This work used a homogenous transformation matrix (HTM) to describe the motion of the test part from the confocal to cat's eye positions. Using this method, the authors calculated an uncertainty in radius of 7 μm for a 408 μm radius part, 2 parts in 10^2 , due to the mechanical error motions of the slideway.

1.4.4 Previous Work on Measuring Radius on Micro-Optics

Both commercial and research interferometers have been built for testing micro-lenses. The size of the test lenses is not easily defined. Some definitions

for micro-lenses include, focal length of 500 μm [22], volume of 1 mm^3 and features of 10 μm [16], smaller than 2 mm radius [21], focal length of 0.5 to 1 mm [19], and “a lens which can not be handled by the hand” [20].

In many cases, the nominal radius of measurable parts is not specified. At times, the micro-interferometers are specified only with input beam diameter and resolution and range of the radius scale. It would be easy, but wrong, to suppose that the resolution of the scale defines the smallest measurable radius (taking into account the desired uncertainty). Another factor is imaging, where a long imaging arm is required for micro-optics in a standard interferometer set-up. This was demonstrated by Schwider and Falkenstörfer [21] where a major limitation in building their micro-interferometer was the physical constraints due to the imaging of the test part. The researchers did measure the radius, but did not investigate the uncertainty of the measurement.

Mersereau, et al. [22] presented an early review paper on various methods for measuring and testing micro-lenses. The authors suggest measuring the radius of small parts on an interferometer, but do not discuss the details of the measurement tool or uncertainty.

Commercial instruments to measure the radius of micro-lenses by interferometry are limited in their availability and uncertainty. Zygo Corporation's MicroLUPI, produced in 2001, was a tool used to measure the figure error and radius of micro-lenses [23]. The MicroLUPI is currently not in production. The uncertainty of the radius measurement on this tool is not known. Zygo's current tool for measuring radius of micro-lenses is the PTI 250 Interferometer [24] with 1

μm resolution in radius and a 25 mm test beam diameter. It appears that this tool would not be able to measure parts smaller than 1 mm radius due to the main limitation of the radius resolution and likely the imaging of the optic. The Mini-Fiz from Fisba Optik has many of the same limitations.

This work includes a description of the micro-interferometer at UNC Charlotte. This instrument has an aperture of 8 mm and is capable of measuring the radius of parts ranging from 200 μm to 1 mm in radius. A more detailed description of the interferometer is in Chapter 4. This tool will be used to investigate the cat's eye retro-reflection in the interferometric radius measurement.

1.5 Uncertainties Affected by the Cat's Eye Position

The following sections briefly describe the uncertainties in the radius measurement that are affected by the cat's eye position. These include locating the cat's eye position, determining the radius using a Gaussian or a physical optics model, offset of the cat's eye due to phase change on reflection, aberrations in the phase measuring interferometer (PMI), and variations in the input beam aperture, part size, and objective numerical aperture (NA). These uncertainties are briefly explained here and are discussed in further detail in subsequent chapters.

There are, of course, other sources of uncertainty that are not directly related to the cat's eye position. These include slide motion uncertainties, uncertainty in measuring the length, Abbe offset, cosine error, environmental effects, and additional uncertainties due to the PMI (for example, uncertainty in

the laser wavelength, unwrapping errors, and phase stepping errors). As mentioned, discussion of these uncertainties can be found in the literature and the work presented here adds to this body of knowledge.

1.5.1 Null Position Location

In practice, determining when the test optic is at either the cat's eye or confocal positions can be difficult. Visually, these positions occur when the interference pattern is nulled, i.e. the minimal number of fringes is seen. For the radius measurement, this occurs when the defocus term (a_2^0) of the Zernike polynomial series (see Appendix A for description of the Zernike series) is zero. This is because the definition of radius is a best fit sphere. When the a_2^0 (a spherical polynomial) goes to zero, the wavefront at confocal is equal to the best fit sphere over the aperture of the measurement. However, it is not mechanically possible to position the test part where the interference pattern is exactly nulled. This positioning error is known as a null cavity error that leads to a non-zero a_2^0 term. One method for correcting this was shown by Selberg [25] and others [13,26]. This method determines the distance the part is offset from the null position. The calculation is based on the a_2^0 term and the numerical aperture of the system (NA is the sine of the half angle of the cone of light) of the system. The NA is often not known to low uncertainty which leads to significant uncertainty in the correction and therefore the radius estimate.

A lower uncertainty method, and the one used for this dissertation, is to correct for the null cavity error as described by Schmitz, et al. [27]. Multiple

measurements are taken through confocal and through cat's eye and a plot of a_2^0 (defocus) vs. position along the optical axis (Z) is then constructed for each position. Each data point is one interferometric measurement. A linear fit is performed on the data and the intercept (where $a_2^0 = 0$) is the best estimate of the null position. The difference between the two intercepts is the radius. An example is shown in Figure 1-3 where the both the cat's eye and confocal measurements are shown.

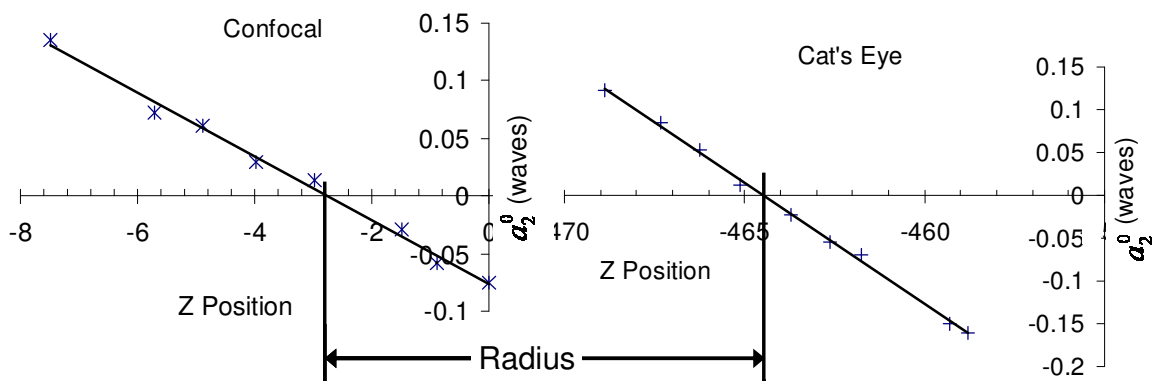


Figure 1-3: Example of the null cavity correction for the radius measurement. The units on the Z position axis are inconsequential here.

An uncertainty in the fit leads to an uncertainty in the radius. The standard deviation, S , of the fit is

$$S = \sqrt{\frac{\sum_{i=1}^m E_i^2}{m-2}},$$

Equation 1-2 [27]

where E_i is the difference at each data point between the model and the measured data and m is the total number of data points. The equation of the linear fit is

$$a_2^0 = m Z_{pos} + b ,$$

Equation 1-3

where m is the slope and b the y-axis intercept. Considering a standard deviation of the fit, the maximum and minimum possible values of the null position, Z_{null} are found using

$$Z_{null} = \frac{-b \pm S}{m} .$$

Equation 1-4.

The error in radius due to the fit is then

$$R_{Error,Fit} = \sqrt{(Z_{CF,max} - Z_{CF,min})^2 + (Z_{CE,max} - Z_{CE,min})^2} ,$$

Equation 1-5

where CF indicates the confocal position and CE the cat's eye position. This calculation of the error in the fit only accounts for scatter in the Z position and the a_2^0 term due to random errors. This uncertainty in radius due to the fit does not include potential biases in the identification of the null position (such as a phase change on reflection bias). I show the amount of the uncertainty in radius due to the fit in Chapter 4.

1.5.2 Modeling the Cat's Eye and Confocal Positions

Possible models of the cat's eye position are shown in Figure 1-4. Radius measurements have typically used the perfect geometric model [26] to indicate

the cat's eye position. In this model, the light is focused to a point and is coincident with the apex of the test part. Investigations indicate that using this model can create significant errors in the radius in two ways, when the incoming wavefront is aberrated and when the nominal part radius is small (1 mm or less) [27,28]. This is demonstrated in Chapter 2 and 3 and is explained briefly here.

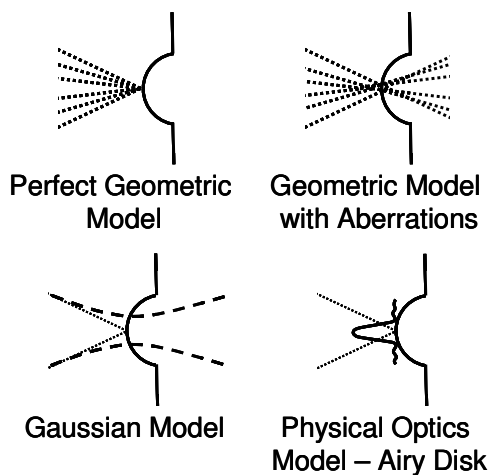


Figure 1-4: A schematic of the various methods for modeling the cat's eye reflection.

To reduce these errors, other models should be used. An imperfect system can be modeled by adding aberrations to the incoming light. The cat's eye can also be modeled using a Gaussian model or a real physical optics model as shown in Figure 1-4. If a geometric model is used instead of a Gaussian model, initial investigations show that errors are as shown in Table 1-2.

Table 1-2: Error from using a geometric model instead of a Gaussian model.

Nominal Part Radius	Fractional Error (Error/Radius)
250 μm	6 parts in 10^5
1 mm	3 parts in 10^6
25 mm	2 parts in 10^7

In comparing the larger (25 mm) part to the smaller (250 μm), the part error is different by a factor of 10^2 . This shows that the Gaussian (instead of the geometric) model must be considered for smaller parts when the measurement goal is parts in 10^5 . For the larger part, though, the Gaussian model need only be considered when the measurement goal is parts in 10^7 . This is a preliminary example only and more detail on the calculation of these errors is found in Chapter 2.

Part of using these models is defining the part location where the cat's eye reflection occurs. Using the Gaussian model as an example, does the cat's eye occur at the waist or somewhere else? This question and these additional models are investigated in this work.

Other work exists in the literature on using a Gaussian model of the cat's eye for a radius measurement [27]. The authors investigated a Gaussian beam model with aberrations in this experiment on a 25 mm radius part with the software program Zemax to propagate the Gaussian beam. They first assumed that the cat's eye reflection occurred at the beam waist. Then the offset of the beam waist from the geometric focus was calculated. This offset occurs due to the input beam parameters and aberrations in the system. The offset was then

assumed to be the bias in the radius, 6 nm (in a negative sense) for a 25 mm radius part. Therefore the true radius is predicated to be smaller than the measured value.

Part of this dissertation research has been developing a more detailed model of the radius measurement by propagating a Gaussian beam. The method is briefly described here and in more detail in Chapter 2 [28]. The model considers a non-aberrated system and uses Matlab for the analysis (optical propagation software is not required). The model is an improvement over the published work by considering both the reference and test beams and including propagation distances. Even in a non-aberrated system, the model shows a bias error in the radius measurement when a “perfect geometric” model is used instead of a Gaussian model. The error is significant for smaller radius parts (< 1 mm). The model only considers a perfect Gaussian beam and therefore does not include added aberrations.

An approximation of the full physical optics model of the cat's eye position can be generated using an optical modeling software package such as FRED. This software was used to model the radius measurement. This work is briefly described here and in more detail in Chapter 3. FRED is a three dimensional package where optical elements are assembled to simulate an experiment. For the radius measurement the interferometer was set up using a source, beam splitter, a mirror, a lens, a test part, and a detector. For the measurement the simulated light was sent through the system, and the resultant output intensity and phase was read by the detector. The test part was moved through confocal

and cat's eye and the resultant phase was read at each point. By analyzing this phase, the simulated radius can be determined. Also, aberrations can be modeled in a simulation package such as FRED.

1.5.3 Aberrations in the Phase Measuring Interferometer

As described above and shown in Figure 1-2(a), the phase measuring interferometer (PMI) is used to identify the confocal and cat's eye positions. The models of radius described above use a perfect wavefront for the PMI; that the beam has no aberrations. In practice, no system is perfect and the PMI has aberrations that affect the radius measurement. Retrace errors are a subset of errors that are caused by aberrations in the PMI and do affect the radius measurement. A retrace error occurs when the rays reflected from the part do not follow the same path back through the interferometer.

The most promising method to test the effect of aberrations is with a physical optics simulation package like FRED and in experiment. The current Gaussian model does not incorporate added aberrations. In the FRED model and in experiments it is easy to add spherical aberration to the system using a glass plate in the converging beam. The primary effect of the glass plate is to add an offset in the focus point away from the objective and, because of the breakdown of the approximation of $\sin \theta \cong \theta$ in Snell's law, the secondary effect is to add spherical aberration to the wavefront. A thicker plate leads a larger focus shift and aberration. Spherical aberration, a_4^0 , is a common aberration in optical components and will have the largest effect on cat's eye and the radius

measurement. These experiments with adding aberration to a system are found in Chapter 4.

Preliminary results with the FRED model show that for a 0.25 mm radius test part, 0.16 waves of a_4^0 (spherical aberration) will produce errors of 8 parts in 10^4 . For 6 waves of spherical aberration and a 0.5 mm radius part, the errors are 3 parts in 10^3 . These errors occur when the perfect geometric model is used instead of an aberrated physical optics model.

1.5.4 Input Variations

Both the Gaussian model and the FRED model were used to test the affect of various input parameters on the cat's eye position and the radius measurement. Parameters varied include the input beam aperture, part size, objective numerical aperture (NA), and propagation distances in the interferometer.

1.5.5 Offset of the Cat's Eye Position Due to Phase Change

Light reflected from a part will undergo a phase change which will affect the radius measurement and can be appreciated using a simple geometric ray model.

The phase change on reflection only impacts the radius measurement through the identification of the cat's eye and confocal null positions. The null position will change if there is a change in the reflected wavefront curvature. The phase change on reflection is constant over the aperture at confocal because the incident angle does not vary, therefore the confocal position is not affected by the

phase change. It is not a concern what the phase change is, just that it is constant. At cat's eye, though, the incident angle varies across the beam aperture in a geometric optics model. This variation changes the wavefront curvature. This curvature will present itself as an offset of the cat's eye position as shown in Chapter 5. The geometric model represents the worse case scenario. This leads directly to a bias in the measured radius on the order of 4 parts in 10^6 for a 0.25 mm radius part, or 1 nm bias.

1.6 Summary

This chapter provides a basic description of the cat's eye position and the interferometric radius measurement. The radius measurement in the micro-range is used to investigate the biases introduced in cat's eye position.

The sources of uncertainty in the radius measurement that are affected by the cat's eye position include: the null position location, model approximations (Gaussian or physical optics with FRED), wavefront aberrations, system parameters, and the phase change on reflection. The upcoming sections describe these sources of uncertainty in more detail and provide a comparison between the experimental radius measurements and the simulated radius measurement, using the Gaussian Model or the FRED model. The initial expectation was that the majority of the bias in a radius measurement would be a result of the cat's eye position shifting, but simulations show that the confocal and cat's eye position shifts are on the same order of magnitude.

A summary of the results of this dissertation research along with other published findings are shown in Figure 1-5. The expected bias in the radius

measurement when the geometric non-aberrated model is used instead of a more detailed model is shown versus the radius of the test part. This chart is explained in more detail later in this work, but is shown here to demonstrate the magnitude of the error. The spread in the data (the rectangular boxes) incorporates different numerical apertures and added spherical aberration.

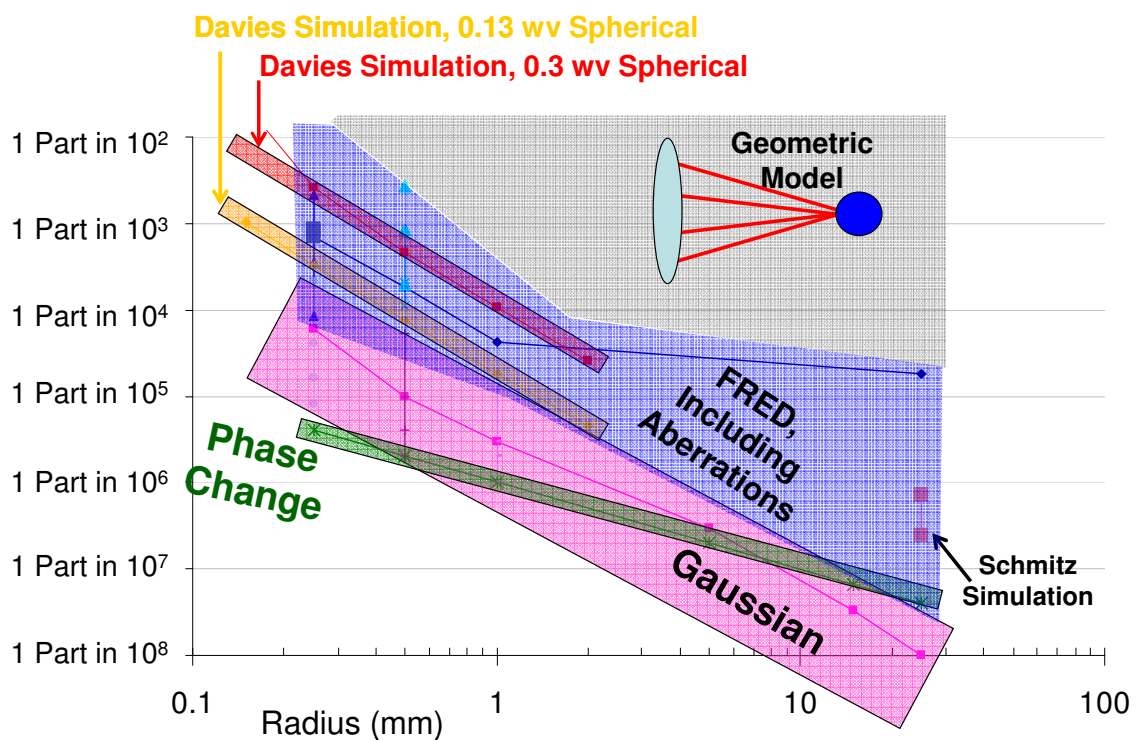


Figure 1-5: The error in the radius measurement when the geometric model is used instead of a more detailed model. The Davies simulation is from [41, 54] and the Schmitz simulation is in [27]

CHAPTER 2: THE GAUSSIAN MODEL OF A RADIUS MEASUREMENT

2.1 Introduction

The radius measurement model and the cat's eye reflection is typically represented by a simple geometric model, that is, rays from an objective (or transmission sphere) form a cone and are focused to a point [26]. This simple geometric model breaks down as the test optic becomes smaller and/or higher precision is required. Ultimately a full physical optics model is required, which includes diffraction effects and aberrations. This chapter looks at a Gaussian model of the cat's eye reflection and the radius model to explore the approximate impact of diffraction effects alone. The model assumes an aberration free wavefront, but captures basic diffraction with the spread of the wavefront with propagation and a finite beam footprint at focus.

Laser light is typically modeled using a Gaussian beam [29]. Here, only the fundamental mode (the TEM_{00}) is used. To be modeled as a Gaussian beam, the amplitude of the electric field must vary slowly as the beam propagates. This assumption is examined later in this chapter. An example of a Gaussian intensity profile is shown in Figure 2-1, but it is the phase, not intensity of the wavefront that is used for the radius measurement. The phase of a Gaussian beam is constant along this intensity profile. Of course, with masking, the intensity profile will look like a cropped Gaussian. This method of propagating a Gaussian beam

has been investigated for the cat's eye retro-reflector to determine the best parameters for the system [10].

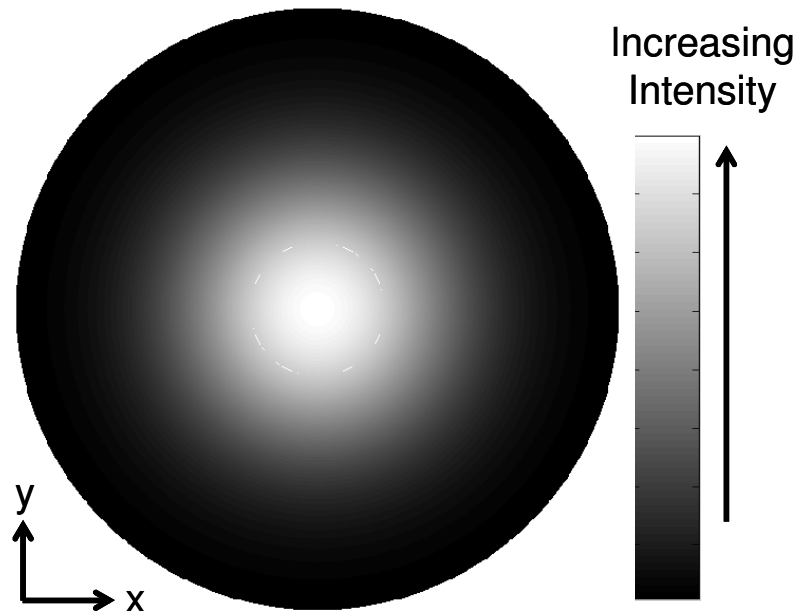


Figure 2-1: Example of Gaussian intensity profile. The X and Y directions indicate the axes of the intensity. The Z axis is the direction of light propagation (in/out of the page)

2.2 The Radius Measurement in a Gaussian Model

A schematic of the radius measurement is shown in Figure 2-2 with Gaussian parameters. Here, the input beam has a Gaussian intensity profile instead of the uniform intensity profile and perfect collimation, as assumed in the geometric model. The radius measurement is defined in terms of Gaussian model parameters that describe the light propagation. In the reference arm, the beam propagates a distance d_r , reflects off the reference mirror (labeled Ref. mirror in Figure 2-2) and again propagates a distance of d_r . In the test arm, the beam propagates a distance d_t , is focused by a lens with focal length, f ,

propagates a distance s , reflects from the test optic with radius r , propagates a distance s , is collimated by a lens with focal length f , and propagates a distance d_t to return to the beam splitter. Note that in Figure 2-2, the paraxial rays are shown to demonstrate the operation of the interferometer and do not indicate the Gaussian profile.

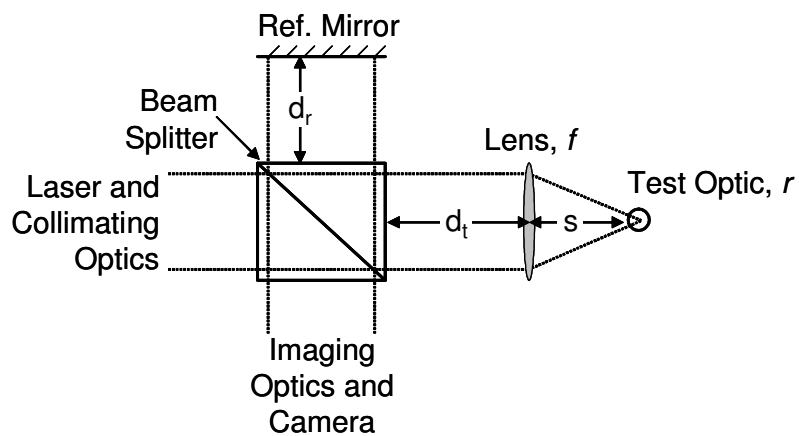


Figure 2-2: A schematic of the radius measurement.

2.3 The Gaussian Beam Model

To derive the characteristics of the Gaussian profile, I start with the wave equation,

$$\nabla^2 \mathbf{E} + k^2(\mathbf{g})\mathbf{E} = 0$$

Equation 2-1

where \mathbf{E} is the electric field vector, and \mathbf{g} is the position vector (normally identified using \mathbf{r}). This equation is valid when the fraction change of ϵ (the dielectric constant or permittivity) in one wavelength is much much less than one.

This is true here where the propagation is in air. This derivation is described by Yariv [30]. The term $k^2(\mathbf{g})$ is given by

$$k^2(g, \phi, z) = k^2 - k k_2 g^2$$

$$g = \sqrt{x^2 + y^2}$$

Equation 2-2

where x and y are the directions shown in Figure 2-1, and k the wave number, $2\pi n/\lambda$ (n = index of the material and λ = wavelength of the light). Because the transverse (t) dependence is on \mathbf{g} only (the propagation is in the z direction), the Laplacian operator, ∇^2 , goes to

$$\nabla^2 = \nabla_t^2 + \frac{\partial^2}{\partial z^2} = \frac{\partial^2}{\partial r^2} + \frac{1}{g} \frac{\partial}{\partial g} + \frac{\partial^2}{\partial z^2}.$$

Equation 2-3

I assume a solution of Equation 2-1 of the form

$$\mathbf{E} = \psi(x, y, z)e^{-ikz}.$$

Equation 2-4

After substituting Equation 2-4 into Equation 2-3 and Equation 2-2 into Equation 2-1, Equation 2-1 now takes the form

$$e^{-ikz} \left[\nabla_t^2(\psi) + \frac{\partial^2 \psi}{\partial z^2} + (k^2 - k k_2 g^2) \psi \right] = 0.$$

Equation 2-5

The first and second derivatives with of Equation 2-4 with respect to z are

$$\frac{\partial \mathbf{E}}{\partial z} = \psi e^{-ikz} - ik\psi e^{-ikz}$$

$$\frac{\partial^2 \mathbf{E}}{\partial z^2} = e^{-ikz} (-2ik\psi' - k^2\psi + \psi'')$$

Equation 2-6

where the prime indicates the derivative with respect to z . The second derivative is substituted into Equation 2-5 to form

$$e^{-ikz} [\nabla_i^2(\psi) + -2ik\psi' - k^2\psi + \psi'' + k^2\psi - k k_2 g^2 \psi] = 0.$$

Equation 2-7

The ψ'' term goes to zero based on the assumption that the variation of the electric field is slow enough that $k\psi' \gg \psi'' \ll k^2\psi$. This assumption is considered later in this chapter. Equation 2-7 then becomes

$$\nabla_i^2(\psi) + -2ik\psi' - k k_2 g^2 \psi = 0.$$

Equation 2-8

Using Equation 2-3, Equation 2-8 can be rewritten as

$$\frac{\partial^2 \psi}{\partial r^2} + \frac{1}{g} \frac{\partial \psi}{\partial g} + -2ik \frac{\partial \psi}{\partial z} - k k_2 g^2 \psi = 0.$$

Equation 2-9

A solution for ψ , using a Gaussian equation, is assumed of the form

$$\psi = \exp \left[-iP(z) - \frac{ik}{2q(z)} g^2 \right]$$

Equation 2-10

where P and q are functions of z . The first and second derivatives with respect to g and the first derivative with respect to z of Equation 2-10 are required to solve Equation 2-9. These derivatives are

$$\begin{aligned}\frac{\partial \psi}{\partial g} &= \exp\left[-iP - \frac{ikg^2}{2q}\right] \left(\frac{-ikg}{q}\right), \\ \frac{\partial^2 \psi}{\partial g^2} &= \exp\left[-iP - \frac{ikg^2}{2q}\right] \left(\frac{-ik}{q} - \frac{k^2 g^2}{q^2}\right), \text{ and} \\ \frac{\partial \psi}{\partial z} &= \exp\left[-iP - \frac{ikg^2}{2q}\right] \left(-iP' - \frac{k^2 g^2}{2} \left(\frac{1}{q}\right)'\right).\end{aligned}$$

Equation 2-11

Substituting the derivatives (Equation 2-11) into Equation 2-9 results in

$$\exp\left[-iP - \frac{ikg^2}{2q}\right] \left[\frac{-2ik}{q} - \frac{k^2 g^2}{q^2} - 2kP' - k^2 g^2 \left(\frac{1}{q}\right)' - kk_2 g^2\right] = 0,$$

Equation 2-12

where a prime indicates the derivative with respect to z . If Equation 2-12 is to hold true for all values of g , the coefficients of each g term must sum to zero, resulting in

$$\begin{aligned}g^0: \quad \frac{-2ik}{q} - 2kP' &= 0 & P' &= \frac{-i}{q} \\ g^2: \quad -\frac{k^2}{q^2} - k^2 \left(\frac{1}{q}\right)' - kk_2 &= 0 & \frac{1}{q^2} + \left(\frac{1}{q}\right)' + \frac{k_2}{k} &= 0\end{aligned}$$

Equation 2-13

The real and imaginary parts of q , the complex radius can be expressed as

$$\frac{1}{q} = \frac{1}{R} - i \frac{\lambda}{\pi n w^2}$$

Equation 2-14 [30]

where R is the radius of the wavefront, w the beam half width, and n the index of the propagation medium (air with $n = 1$). The radius of the wavefront, R , and the beam half width, w , and consequently the complex radius are functions of position along the optical axis. That is, as the beam propagates in space (or through an optical system), the beam curvature and size change. The complex radius and propagation through the optical system are used to model the radius measurement.

I am considering an optical system where the input is the complex radius, q_{in} . As the beam passes through each element in this system, the complex radius will vary for each position along the optical axis. Each element in the system can be represented by a 2x2 matrix, M , [29, 31]

$$M = \begin{bmatrix} A & B \\ C & D \end{bmatrix}.$$

Equation 2-15

Where the output beam complex radius, q_{out} [30], can then be calculated using

$$q_{out} = \frac{Aq_{in} + B}{Cq_{in} + D}.$$

Equation 2-16

2.3.1 The Matrices of the Gaussian Model

The reference and test beams are considered separately for the Gaussian analysis of the radius measurement. Each element in the test and references

arms can be modeled using the matrix method of analysis. These elements are propagation, mirrors, and lenses.

The following are equations representing propagation through a distance d , a thin lens with focal length f , and a mirror with radius r (the test optic) [29]:

$$M_{\text{Prop}} = \begin{bmatrix} 1 & d \\ 0 & 1 \end{bmatrix} \quad M_{\text{Lens}} = \begin{bmatrix} 1 & 0 \\ -1/f & 1 \end{bmatrix} \quad M_{\text{Optic}} = \begin{bmatrix} 1 & 0 \\ 2/r & 1 \end{bmatrix},$$

Equation 2-17

Because the radius of the reference mirror is infinite, the reflection matrix for the reference mirror is

$$M_{\text{Mref}} = \begin{bmatrix} 1 & 0 \\ 0 & 1 \end{bmatrix}.$$

Equation 2-18

Each arm of the interferometer is then represented by the multiplication of the matrices of each element in the arm. The reference arm matrix, M_{ref} , after the beam splitter, is propagation, reflection, and propagation as shown by

$$M_{\text{ref}} = \begin{bmatrix} 1 & d_r \\ 0 & 1 \end{bmatrix} \begin{bmatrix} 1 & 0 \\ 0 & 1 \end{bmatrix} \begin{bmatrix} 1 & d_r \\ 0 & 1 \end{bmatrix} = \begin{bmatrix} 1 & 2d_r \\ 0 & 1 \end{bmatrix}.$$

Equation 2-19

The matrix for the test arm (after the beam splitter), M_{test} is more complex with propagation by d_t , focusing, propagation by s , reflection at r , propagation by s , collimation, and propagation by d_t in

$$M_{\text{test}} = \begin{bmatrix} 1 & d_t \\ 0 & 1 \end{bmatrix} \begin{bmatrix} 1 & 0 \\ -1/f & 1 \end{bmatrix} \begin{bmatrix} 1 & s \\ 0 & 1 \end{bmatrix} \begin{bmatrix} 1 & 0 \\ 2/r & 1 \end{bmatrix} \begin{bmatrix} 1 & s \\ 0 & 1 \end{bmatrix} \begin{bmatrix} 1 & 0 \\ -1/f & 1 \end{bmatrix} \begin{bmatrix} 1 & d_t \\ 0 & 1 \end{bmatrix}.$$

Equation 2-20

The M_{ref} and M_{test} matrices are simplified and used in Equation 2-16 to calculate the output beam complex radius of curvature of the reference and test beams respectively, qr_{out} and qt_{out} . The parameter qt_{out} is a function of the position s (the propagation distance after the lens) while qr_{out} is constant and depends on the interferometer configuration.

2.3.2 Finding the Confocal and Cat's Eye Positions

The confocal and cat's eye positions both occur when qr_{out} equals qt_{out} meaning the curvatures match and the interference pattern is constant. The reference arm qr_{out} is first calculated using Equation 2-19 and Equation 2-16 and the test arm qt_{out} is calculated using Equation 2-20 and Equation 2-16. Since qt_{out} is a function of the position of the test part (s) and qr_{out} is a constant there will be two positions where qr_{out} equals qt_{out} , each corresponding to a different value of s . One value defines the cat's eye position and the other, the confocal position. The radius is then calculated as the difference between these s values. It should be noted that this method requires a q_{in} , focal length of the lens, and the propagation distances, d_t and d_r . The nominal values for these parameters are based on the experimental setup. They are varied in simulation to study their affect on radius.

2.3.3 The Perfect Cat's Eye and Confocal

The analysis in this chapter will show that compared to a perfect geometric model where rays come to a perfect focus, a shift in the cat's eye position, confocal position, and the radius value occur when the Gaussian model is

considered. Consequently, assuming a perfect geometric model will lead to an error. The errors are dependent on the size of the test part and the interferometer conditions. An error in the cat's eye position means that it does not occur at one focal length. An error in the confocal position means that it does not occur at one focal length minus the input radius. An error in the radius means that the output radius (cat's eye position minus confocal position) is not equal to the input radius. However, the model could be adjusted to achieve an output radius equal to the input radius (termed the "perfect" cat's eye (f) and confocal ($f-r$) positions). I model this condition to explore changes that could be made to the experiment to eliminate or minimize errors. This condition is described in the following paragraphs.

The propagation distances, d_t and d_r , are set to provide a cat's eye at one focal length and a confocal at one focal length minus the input radius. However, the propagation distances for the perfect cat's eye are not the same as for a perfect confocal.

The matrix that describes the output at the beam splitter can be written as

$$M_{BS} = \begin{bmatrix} 1 & d_t - d_r \\ 0 & 1 \end{bmatrix} \begin{bmatrix} 1 & 0 \\ -1/f & 1 \end{bmatrix} \begin{bmatrix} 1 & s \\ 0 & 1 \end{bmatrix} \begin{bmatrix} 1 & 0 \\ 2/r & 1 \end{bmatrix} \begin{bmatrix} 1 & s \\ 0 & 1 \end{bmatrix} \begin{bmatrix} 1 & 0 \\ -1/f & 1 \end{bmatrix} \begin{bmatrix} 1 & d_t - d_r \\ 0 & 1 \end{bmatrix}.$$

Equation 2-21

This equation is a combination of Equation 2-19 and Equation 2-20.

A perfect confocal occurs at s equal to f minus r if the output at the beamsplitter is a mirror image of the input. This mirror image means that M_{BS} ,

Equation 2-21 must equal the matrix of reflection from a mirror with infinite radius as shown by

$$M_{CF} = \begin{bmatrix} 1 & 0 \\ 0 & 1 \end{bmatrix}.$$

Equation 2-22

For a perfect cat's eye reflection, s is equal to f . The matrix M_{BS} is not equal to a matrix for a mirror reflection, rather, it must represent a retro-reflection in this case. The matrix for the retro-reflection is

$$M_{CE} = \begin{bmatrix} -1 & 0 \\ 0 & -1 \end{bmatrix}.$$

Equation 2-23

Using the required values for s , and then setting Equation 2-21 equal to Equation 2-22 and Equation 2-23, the parameter $d_t - d_r$ for each position can be determined. This is shown in

CE:

$$\begin{aligned} & \begin{bmatrix} 1 & d_t - d_r \\ 0 & 1 \end{bmatrix} \begin{bmatrix} 1 & 0 \\ -1/f & 1 \end{bmatrix} \begin{bmatrix} 1 & f \\ 0 & 1 \end{bmatrix} \begin{bmatrix} 1 & 0 \\ 2/r & 1 \end{bmatrix} \begin{bmatrix} 1 & f \\ 0 & 1 \end{bmatrix} \begin{bmatrix} 1 & 0 \\ -1/f & 1 \end{bmatrix} \begin{bmatrix} 1 & d_t - d_r \\ 0 & 1 \end{bmatrix} = \begin{bmatrix} -1 & 0 \\ 0 & -1 \end{bmatrix} \\ & \begin{bmatrix} -1 & \frac{2}{r} [f^2 + f * r - r * (d_t - d_r)] \\ 0 & -1 \end{bmatrix} = \begin{bmatrix} -1 & 0 \\ 0 & -1 \end{bmatrix} \\ & \frac{2}{r} [f^2 + f * r - r * (d_t - d_r)] = 0 \\ & (d_t - d_r)_{CE} = f + \frac{f^2}{r} \end{aligned}$$

Equation 2-24

and

CF :

$$\begin{bmatrix} 1 & d_t - d_r \\ 0 & 1 \end{bmatrix} \begin{bmatrix} 1 & 0 \\ -1/f & 1 \end{bmatrix} \begin{bmatrix} 1 & f - r \\ 0 & 1 \end{bmatrix} \begin{bmatrix} 1 & 0 \\ 2/r & 1 \end{bmatrix} \begin{bmatrix} 1 & f - r \\ 0 & 1 \end{bmatrix} \begin{bmatrix} 1 & 0 \\ -1/f & 1 \end{bmatrix} \begin{bmatrix} 1 & d_t - d_r \\ 0 & 1 \end{bmatrix} = \begin{bmatrix} 1 & 0 \\ 0 & 1 \end{bmatrix}$$

$$\begin{bmatrix} 1 & \frac{2}{r}[f^2 - f*r - r*(d_t - d_r)] \\ 0 & 1 \end{bmatrix} = \begin{bmatrix} 1 & 0 \\ 0 & 1 \end{bmatrix}$$

$$\frac{2}{r}[f^2 - f*r - r*(d_t - d_r)] = 0$$

$$(d_t - d_r)_{CF} = f - \frac{f^2}{r}$$

Equation 2-25

These positions are not equal. The calculated values for $d_t - d_r$ for typical values of f and r are shown in Figure 2-3 and Figure 2-4.

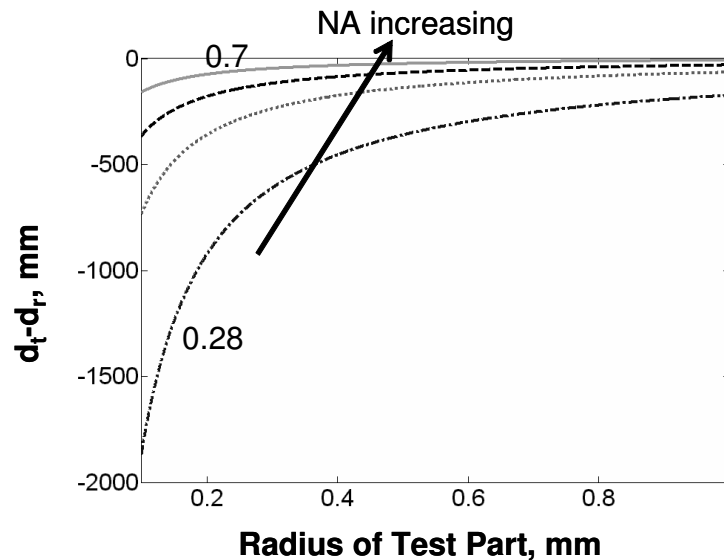


Figure 2-3: Results of Equation 2-25, a perfect confocal, with varying NA (NA related to focal length with a 4 mm input beam radius)

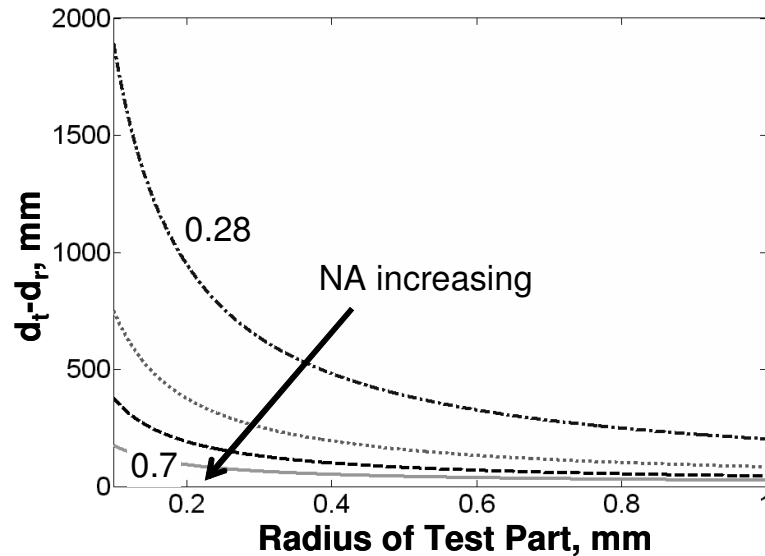


Figure 2-4: Results of Equation 2-24, a perfect cat's eye, with varying NA (NA related to focal length with a 4 mm input beam radius)

The negative values for $d_t - d_r$ for the confocal position indicate that for a perfect confocal, d_r , reference arm propagation distance must be greater than d_t , (test arm propagation distance).

Obviously, moving either the reference mirror or the objective lens during the measurement is not feasible. In addition, many of the required configurations are not practical on the interferometer (e.g. greater than 1 meter for a 100 μm part). Also, a precise measurement of the physical distance of the reference mirror and/or the lens is prohibitively costly in both time and money. Therefore, we will set the reference mirror and lens locations in the model using approximate values from the physical interferometer. We will study the effect of the position of these parts on the radius.

Because the lens and reference mirror can not be placed at the position required, the cat's eye and confocal reflections will not occur at $s = f$ and $s = f - r$,

respectively. The model described above is used to determine the new positions.

2.4 Determining the Inputs

The goal of this algorithm is to determine the error in the measured radius which changes with varying inputs like objective lens (focal length and NA), input beam radius, q_{in} , and part radius. In the sections below, we describe three cases to calculate q_{in} and then the calculation of each of the remaining inputs. The matrices for the reference and test propagation described above require that the q_{in} be defined after the beamsplitter. But, the actual q_{in} I describe below is defined before the beamsplitter due to the physical location of apertures. To make the analysis simpler, I did not consider the propagation through the beam splitter. This is valid because both beams will propagate through the same conditions in the beamsplitter. It will be shown that if the two beams propagate in the same manner, the calculated radius from the model does not vary. This is shown in the second case for calculating q_{in} .

2.4.1 Calculating q_{in} , Case 1

There are multiple methods to calculate the input beam complex radius, q_{in} . I first consider the case (known as case 1) of a standard interferometer with an aperture stop immediately before the beam splitter. The aperture stop is overfilled such that the real part of the complex curvature goes to zero, that is, the beam intensity and phase are constant along the stop. The complex q_{in} for this case is then

$$q_{in} = -i \frac{\pi w^2 n}{\lambda} .$$

Equation 2-26

where w is the radius of the aperture stop, n the index of the medium (here assumed to be 1) and λ is the wavelength of the incident light (632.8 nm in most cases). For the case of a 4.5 mm radius aperture stop (approximately equivalent to the micro-interferometer used in this research), q_{in} is $0 - i*100532.95$ mm.

2.4.2 Calculating q_{in} , Case 2

We next consider case 2, where the aperture stop is not immediately before the beam splitter, Figure 2-5. The beam will propagate over the distance d_A to the beam splitter. This is shown in matrix form as

$$M = \begin{bmatrix} 1 & d_A \\ 0 & 1 \end{bmatrix} .$$

Equation 2-27

The q at the aperture is found using Equation 2-26 and then q_{in} is found using Equation 2-16 with the matrix from Equation 2-27,

$$q_{in} = d_A - i \frac{\pi w^2 n}{\lambda} .$$

Equation 2-28

The complex part of the curvature does not change; therefore q_{in} is $d_A - i*100532.95$ mm, for the nominal case. Later, we will investigate the effect of d_A on the q_{out} .

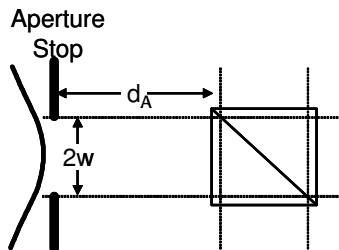


Figure 2-5: Schematic of case 2, the aperture stop is some distance, d_A from the beam splitter.

2.4.3 Calculating q_{in} , Case 3, and focal length

Case 3 describes a system without an aperture. This is the only case that does not crop the Gaussian beam. The input beam curvature at the beamsplitter is determined by working backwards from the focus point. The inputs are the numerical aperture, NA, and the focal length. The waist of a Gaussian beam at focus, w_0 is defined as

$$w_0 = \frac{\lambda}{\pi NA}$$

Equation 2-29

The complex curvature at this point, q_0 is then

$$q_0 = i \frac{\pi w_0^2}{\lambda} = i \frac{\lambda}{\pi NA^2}$$

Equation 2-30

I then use another matrix to travel from the focus point to the input of the beam splitter as shown in Figure 2-6. The beam starts with a complex curvature q_0 at f , propagates a distance f , passes through the lens, f , and propagates a distance, d_t , as in

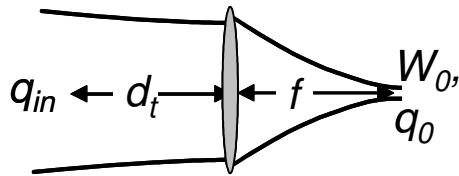
$$M = \begin{bmatrix} 1 & d_t \\ 0 & 1 \end{bmatrix} \begin{bmatrix} 1 & 0 \\ -1/f & 1 \end{bmatrix} \begin{bmatrix} 1 & f \\ 0 & 1 \end{bmatrix} = \begin{bmatrix} 1 - d/f & f \\ -1/f & 0 \end{bmatrix}.$$

Equation 2-31

Using Equation 2-16 and q_0 , the q_{in} can be calculated for varying focal lengths and numerical apertures shown by

$$q_{in} = d_t - f - i \frac{\pi NA^2 f^2}{\lambda}.$$

Equation 2-32

Figure 2-6: Schematic of case 3, determining q_{in} .

The focal length, f , and the NA of the focusing lenses are found from the information supplied by the manufacturer [32]. The focal lengths and NAs for the focusing lenses are shown in Table 2-1. These numbers correspond to those of the microscope objectives used in the micro-interferometer MORTI. The resultant q_{in} for case 3 (rounded to the mm) as calculated using Equation 2-32 also shown in Table 2-1 where 632.8 nm was used for the wavelength. The d_t parameter is adjusted based on the physical attributes of the micro-interferometer.

Table 2-1: The calculated q_{in} from the NA and f for micro-scale parts.

NA	f (mm)	Aperture Diameter, a (mm)	q_{in} (mm), Case 3
0.28	20	13	$d_t - 20 + i*155690$
0.42	10	9	$d_t - 10 + i*87575$
0.55	4	6	$d_t - 4 + i*24029$
0.7	2	4	$d_t - 2 + i*1556$

This set of NA and focal lengths are from the microscope objectives used to measure micro-parts. The measurement of a macro-part is typically performed using transmission spheres with a different set of NAs and focal lengths. The transmission sphere information is normally reported using the F-number ($f/\#$). The NA of the transmission sphere is then found using

$$NA = 0.5 / f / \#$$

Equation 2-33

Then, the focal length must be found from the geometrical relationships that define the NA, shown in Figure 2-7. Using the aperture diameter, a , and the NA of the transmission sphere, the focal length of can be found using

$$NA = \sin(\theta)$$

$$\tan(\theta) = \frac{a/2}{f}$$

$$f = \frac{a/2}{\tan(\arcsin(NA))}$$

Equation 2-34

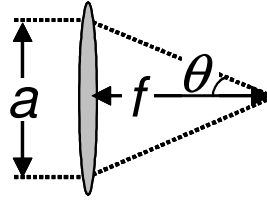


Figure 2-7: Schematic demonstrating the calculation of the focal length from the NA.

Using F-numbers from typical transmission spheres, the focal length and q_{in} from case 3 were calculated for two typical aperture sizes: 102 mm (4 in) and 300 mm shown in Table 2-2 and Table 2-3. The propagation distance d_t for these cases was zero, because the beam splitter is the transmission sphere, therefore the distance between is zero. These show considerably larger focal lengths for the macro-scale parts than for the micro-parts.

Table 2-2: The calculated q_{in} and f from the NA for macro-scale parts for the Veeco Interferometer, $a = 101.6$ mm (4 in).

F-Number	NA	f (mm)	q_{in} (mm), Case 3
0.75	0.67	56.8	$-56.8 + i*7190013$
1.5	0.33	143.7	$-143.7 + i*11164128$
3.5	0.14	352.0	$-352.0 + i*12056598$

Table 2-3: The calculated q_{in} and f from the NA for macro-scale parts for macro-scale interferometer.

F-number	NA	f (mm)	q_{in} (mm), Case 3
1.1	0.45	293.9	$-293.9 + i*86837557$
3.2	0.16	948.2	$-948.2 + i*114267643$
4	0.13	1190.6	$-1190.6 + i*118932860$

2.4.4 Summary of q_{in}

We have shown three methods for determining the parameter q_{in} and shown the various NA and focal length parameters. Case 2 for determining q_{in} matches the experiment best, but case 3 is the most valid for the Gaussian model because the other cases consider cropped Gaussian beams. The propagation model requires a full Gaussian beam, but general knowledge states the propagation model is valid when the beam is cropped at or greater than the $1/e$ point of the curve. Case 1 and 2 are then valid under the assumption that the cropping occurs at or beyond the $1/e$ point.

2.4.5 The Remaining Input Parameters

The other relevant input parameters to be determined are d_t , d_r , and r . For micro-scaled parts, the distances in the test arm (d_t) and in the reference arm (d_r) are based on values for the micro-interferometer, 50 mm to 100 mm and 150 mm to 300 mm, respectively. Finally r is defined by the test optics, and I am examining micro optics with radii ranging from 20 μm to 1 mm.

For macro-scaled parts, the distances d_t and d_r will typically be zero. This is because the measurement on the larger parts is performed on a Fizeau interferometer where the transmission flat is the beamsplitter, the reference mirror, and the focusing element. The r range of interest from the macro-scaled parts is from 10 mm to 50 mm.

2.5 Obtaining Radius from the Model

Our goal is to determine the output radius of the test part and resultant error based on the input parameters described above. First, q_{in} and the focal length are calculated based on one of the methods described above. Next, q_{out} of the reference and test arms are calculated using Equation 2-16, Equation 2-19, and Equation 2-20. A range of values are calculated for $q_{t_{out}}$ by varying s , taking care to encompass the both the cat's eye and confocal positions ($f-2r < s < f+r$). The curvature, $curv$, for both the reference and test arms is defined as the real part of the inverse of q_{out} and are given by

$$\begin{aligned} curv_{test} &= \text{real}\left(\frac{1}{q_{test\ out}}\right) \\ curv_{ref} &= \text{real}\left(\frac{1}{q_{ref\ out}}\right) \end{aligned}$$

Equation 2-35

Note that $curv_{ref}$ has a single value for all positions and $curv_{test}$ is a function of s , the distance between the lens and the test part.

The cat's eye and confocal positions occur when the $curv_{test}$ and $curv_{ref}$ match. To do this, we define $curv_{out}$ as

$$curv_{out} = \text{real}\left(\frac{1}{q_{test\ out}}\right) - \text{real}\left(\frac{1}{q_{ref\ out}}\right) = 0$$

Equation 2-36

The cat's eye and confocal positions occur at the s position where $curv_{out}$ is zero. An example graph of the $curv_{out}$ function is shown in Figure 2-8 with the confocal and cat's eye shown. The intermediate curvature match near 9.47 mm

is the result of a focusing issue discussed in Chapter 4 and is easily discarded as a solution.

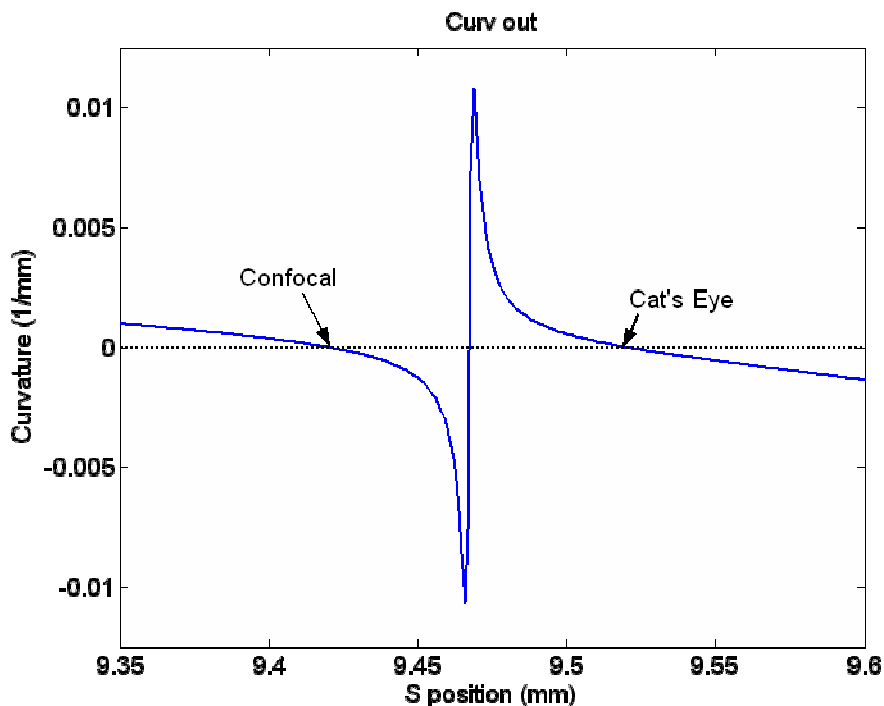


Figure 2-8: Example of a $curv_{out}$ function, inputs are $NA = 0.42$, $\lambda = 632.8$ nm, $d_t = 100$ mm, $d_r = 150$ mm, $r = 100$ μ m, and $q_{in} = 90.48 + 71991i$ (case 3). The objective is located to the left at 0 mm.

The cat's eye and confocal positions were found by determining the s value where the function crossed the x-axis (in 0.1 nm sized steps) such that the position is certain to ± 0.1 nm. The radius is then found by subtracting the confocal position, s_{CF} , from the cat's eye position, s_{CE} , and the radius error is computed:

$$Radius_{out} = s_{CE} - s_{CF}$$

$$Radius_{error} = Radius_{out} - r$$

Equation 2-37

The error is positive when $Radius_{out} > r$ input radius, indicating that the measured sphere is larger than actual, and negative if the $Radius_{out} < r$, indicating that the measured radius is smaller than actual. I will also examine the error in radius in terms of “number of parts in 10^x ”, which is the $Radius_{error}$ divided by the nominal radius. Values of this are shown on the results graphs that follow.

The offset of the cat’s eye position is the s_{CE} position minus the nominal position (the focal length) and the confocal offset is the s_{CF} position minus the nominal position (the focal length minus the input radius) as shown by

$$\begin{aligned} CE_{offset} &= S_{CE} - f \\ CF_{offset} &= S_{CF} - (f - r) \end{aligned}$$

Equation 2-38

By this convention, an offset toward the lens is positive and away is negative.

To summarize, the radius is found using the following steps:

- Calculate q_{in} and f
- Calculate qt_{out} (function of s) and qr_{out}
- Calculate $curv_{out}$ as a function of s
- Determine the two s positions where $curv_{out}$ is zero
- Radius is the difference between the two positions

The Matlab code for the Gaussian Model can be found in Appendix B, Program 1, gaussian.m.

2.6 Results of the Code for Micro-Scale Parts

I am interested in testing the error in the radius of the test part as it depends on several parameters. The nominal values for these parameters are based on the experimental setup. They are varied in simulation to study their effect on radius. The results of the simulations are given in the sections below. The conclusions based on these results are discussed later.

2.6.1 Testing Varying Radius for the Different q_{in} Cases

We first tested parts with varying radius using the difference cases to determine q_{in} . For all these cases: $d_t = 50$ mm and $d_r = 150$ mm, $\lambda = 632.8$ nm, the index of the air is 1, the NA is 0.42, the half aperture size is 4.5 mm diameter, and the focal length is 10 mm). We are testing radius ranging from 0.02 mm to 1 mm. The radius error shown in Figure 2-9 was calculated using q_{in} from case 1 where the aperture is well defined at the beam splitter.

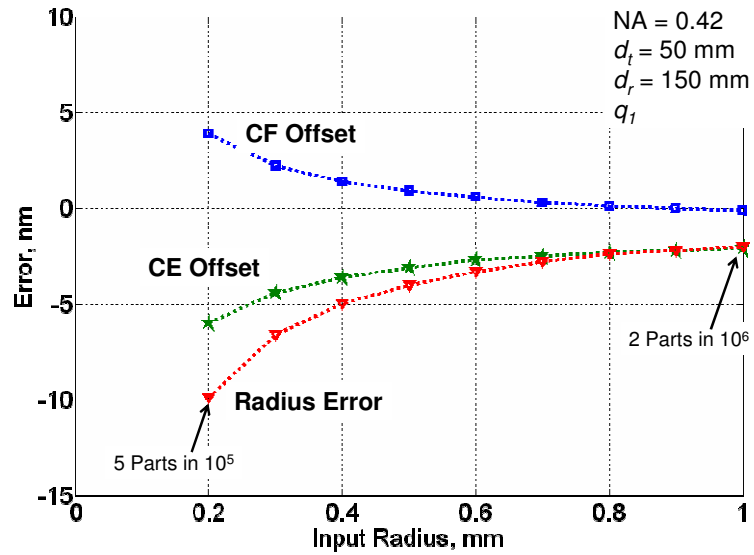


Figure 2-9: Radius Error for varying input radius using q_{in} from case 1 ($q_{in} = 0 - i * 100532$ mm).

The radius error shown in Figure 2-10 and Figure 2-11 were calculated using q_{in} from case 2 where the aperture is well defined a distance d_A before the beam splitter. The distance d_A was tested at 20 mm (Figure 2-10) and 50 mm (Figure 2-11). From these results, there is no effect from the propagation distance d_A .

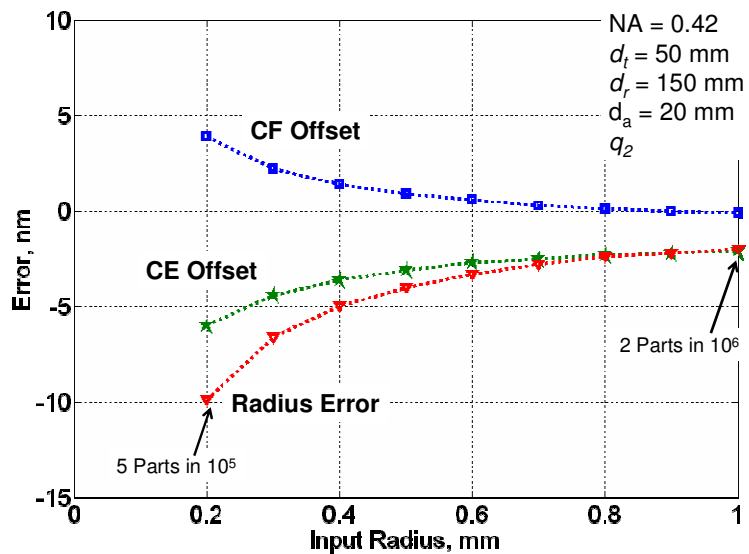


Figure 2-10: Radius Error for varying input radius using q_{in} from case 2 ($q_{in} = 20 + i \cdot 100532$ mm, $d_A = 20$ mm).

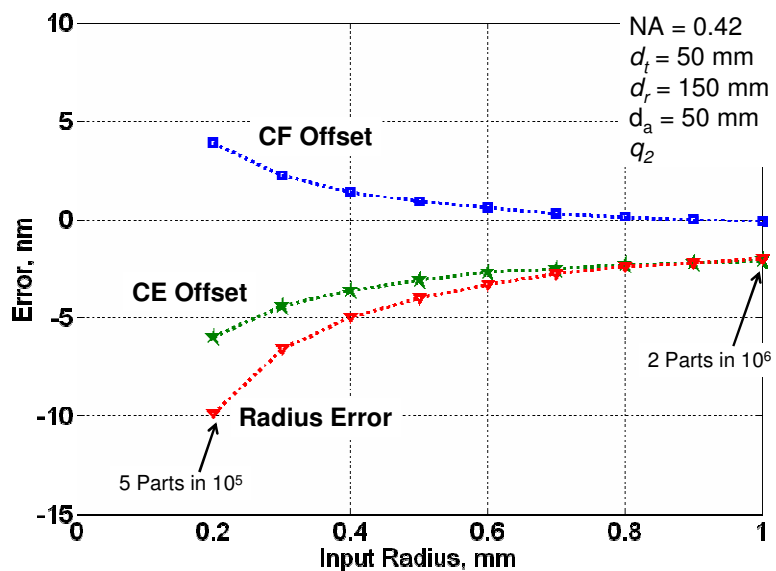


Figure 2-11: Radius Error for varying input radius using q_{in} from Case 2 ($q_{in} = 50 + i \cdot 100532$ mm, $d_A = 50$ mm).

The radius error shown in Figure 2-12 was calculated using q_{in} from Case 3, where q_{in} is based on the a diffraction limited spot at the focal point.

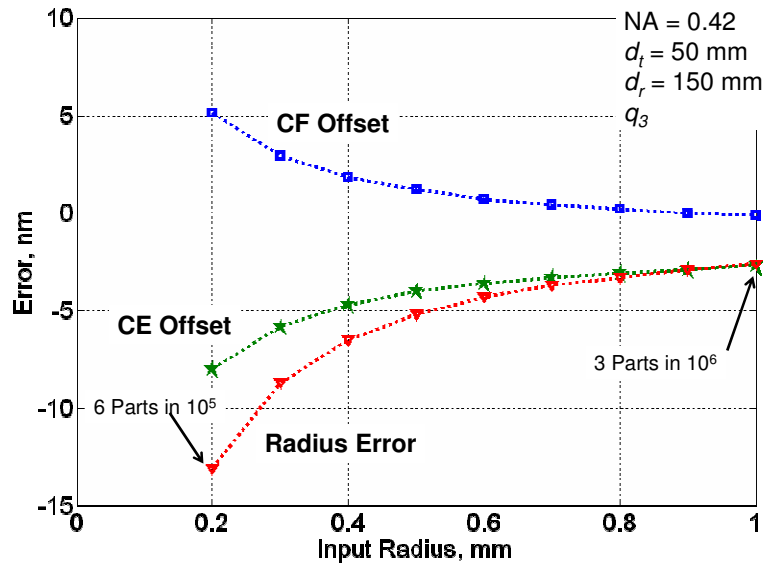


Figure 2-12: Radius Error for varying input radius using q_{in} from Case 3 ($q_{in} = 40 - 87575i$ mm).

From these results (Figure 2-9, Figure 2-10, Figure 2-11, and Figure 2-12) the following observations can be made. The real part of the q_{in} does not have an effect on the result, and the complex part of q_{in} does have an effect on the results.

The real part of q_{in} has no bearing on the results shown, therefore the distinction between case 1 (aperture at the beam splitter) and case 2 (aperture before the beam splitter) is not necessary. This is because the test and reference beams both travel the path between the aperture and the beam splitter.

The complex part of q_{in} does have an affect on the magnitude, but not the trend of the radius error. While case 1 (rather than case 3) more closely models the actual interferometer, there is an assumption that the q_{in} from case 1 (flat curvature) is accurately propagated using the Gaussian matrix model. The more

accurate method is to use case 3 for the input of the system. The comparison to the actual system will be done in a subsequent section.

2.6.2 Testing the Effect of Varying NA

I only consider case 3 for varying the microscope objective. Case 3 is the aperture less system. Cases 1 and 2 were not considered because varying the NA in these cases is not possible in experiment.

The objective is varied, which affects the NA, focal length, and aperture diameter of the lens. The propagation distances are set to $d_t = 50$ mm, $d_r = 150$ mm, and $\lambda = 632.8$ nm. The error in radius for a $500 \mu\text{m}$ part when using q_{in} from case 3 is shown in Figure 2-13 and for a $250 \mu\text{m}$ part is shown in Figure 2-14.

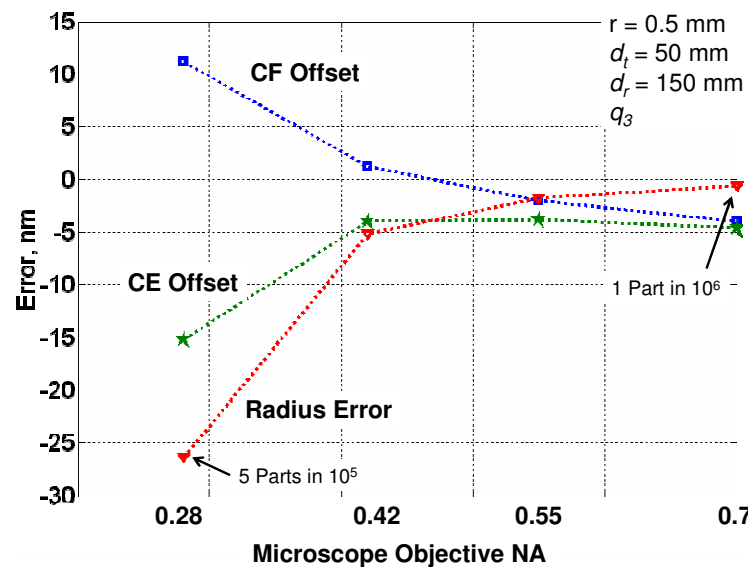


Figure 2-13: Error in a $500 \mu\text{m}$ part, varying NA, q_{in} from case 3.

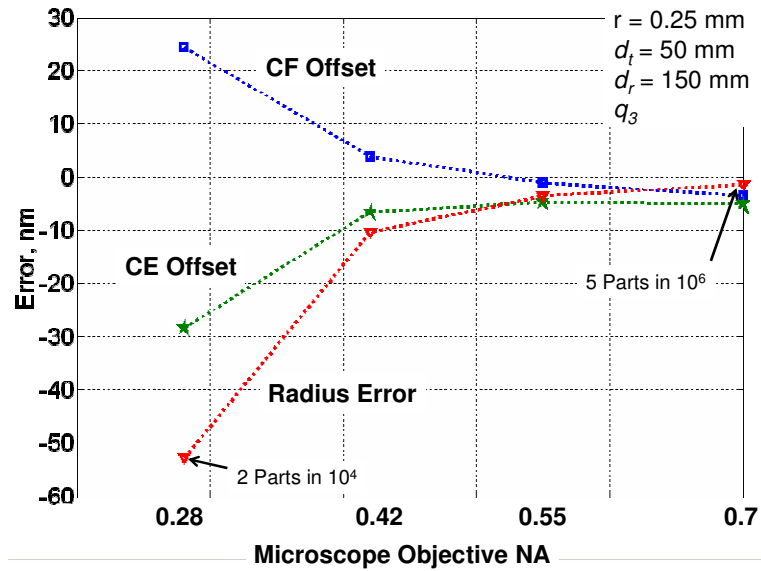


Figure 2-14: Error in a 250 μm part, varying NA, q_{in} from case 3.

The radius error increases as NA of the objective decreases even as the focal length increases.

2.6.3 Varying the Propagation Distances, d_t and d_r

The propagation distances, d_t and d_r , were varied and the resultant errors examined. The aperture diameter is set to 9 mm, NA = 0.42, $\lambda = 632.8$ nm and an input part radius of 250 μm . First d_r was set at 150 mm and q_{in} from case 1 was used. The radius error was tested for varying d_t as shown in Figure 2-15. The results from case 2 are identical and are not shown here.

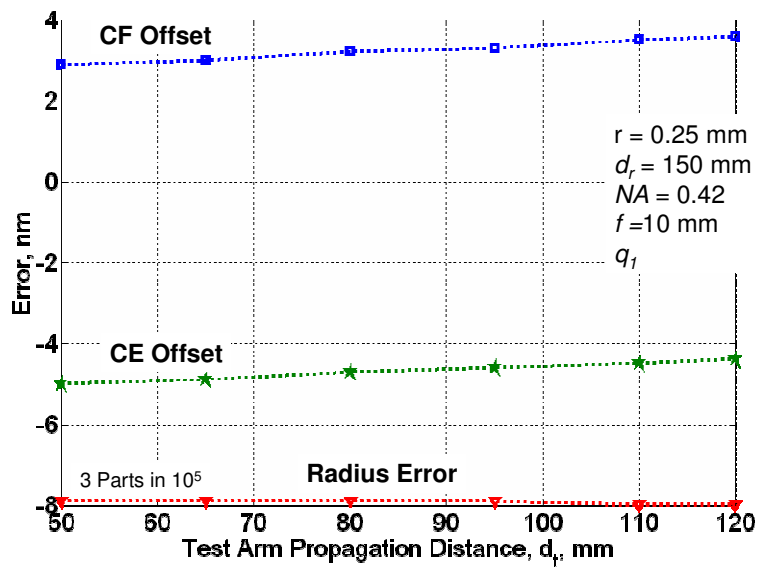


Figure 2-15: Radius Error for varying d_t using q_{in} from case 1, $r = 250$ μm .

I also tested varying d_t using q_{in} from case 3. The radius errors for this case are shown in Figure 2-16.

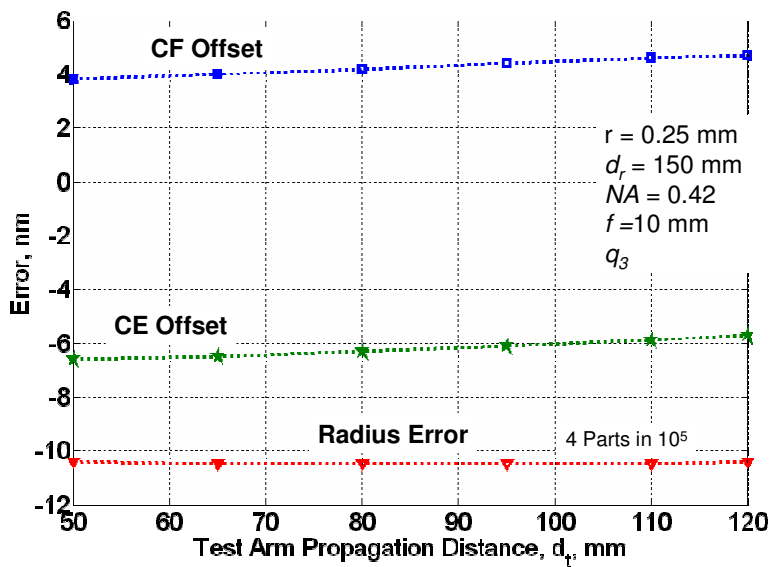


Figure 2-16: Radius Error for varying d_t using q_{in} from case 3, $r = 250$ μm .

Next, d_t was held at 50 mm and d_r was varied. The results when using q_{in} from case 1 and case 3 are shown in Figure 2-17 and Figure 2-18. As before, the results from case 2 are the same as for case 1.

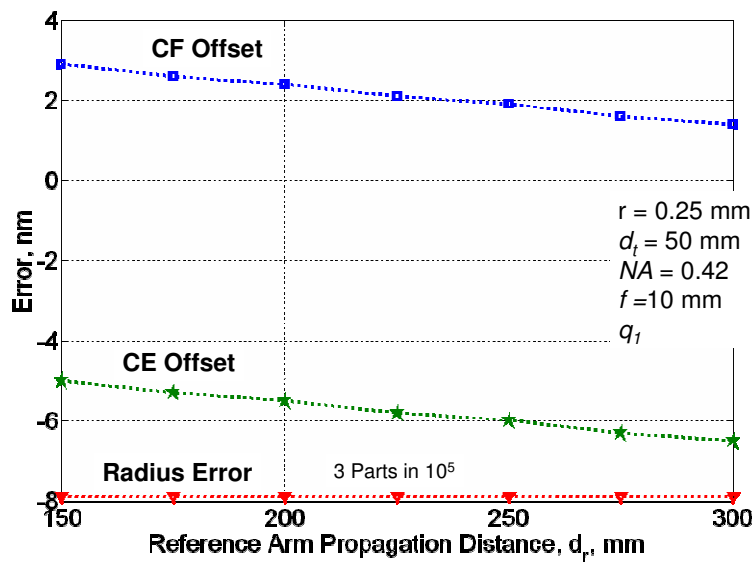


Figure 2-17: Radius Error for varying d_r using q_{in} from case 1, $r = 250 \mu\text{m}$.

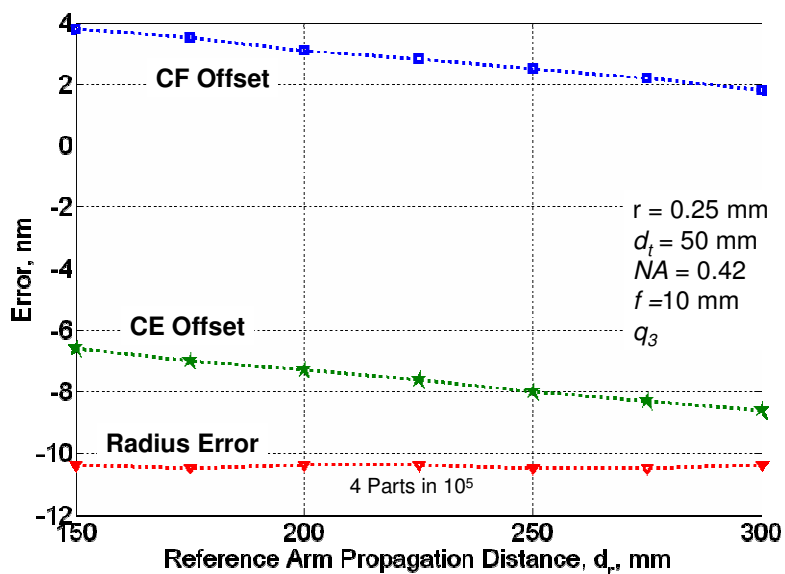


Figure 2-18: Radius Error for varying d_r using q_{in} from case 3, $r = 250 \mu\text{m}$.

The above results (Figure 2-15, Figure 2-16, Figure 2-17, and Figure 2-18) indicate that the magnitude of the radius error is similar to previous results, but does not vary with changing d_t or d_r . However, the cat's eye and confocal positions do vary, but, the difference between the two is always the same. This is true regardless of the method to calculate q_{in} . Therefore, the propagation distance is not a factor in the radius measurement, but may be a factor in other types of interferometric measurements. For example, propagation distance would matter if the measurement is absolute and not differential.

2.7 Curvature at the Test Part

The test beam has a real curvature at the part surface cat's eye retro-reflection because this position is offset from the minimum waist of the beam (where the curvature is zero). This is counter to previous work that assumed that the cat's eye retro-reflection occurred at the beam waist [27]. Therefore the test beam has curvature at the test optic surface for the cat's eye position. This was calculated using another matrix that propagated the test beam from the input through the focus lens to the cat's eye position. This is shown in Appendix B, Program 1. Table 2-4 shows the results from this program. In this test, $d_t = 50$ mm and $d_r = 150$ mm, $\lambda = 632.8$ nm, the index of the air is 1, the NA is 0.42, the aperture size is 9 mm diameter, and q_{in} from case 3 was used as the input. In addition, the curvature of the wavefront at the test optic surface for the confocal position was also calculated to compare. Also, the waist radius of the beam (1/e point) at the test optic surface was calculated using Equation 2-14.

Table 2-4: Table of the Curvatures and Waists at the test optic surface for the cat's eye and confocal positions.

	Input Radius (mm)	Input Beam Curvature (1/mm)	Beam Curvature at CE (1/mm)	Beam Curvature at CF (1/mm)	Beam Waist at CE (μm)	Beam Waist at CF (mm)
0.28	0.25	4	-4.5	-4.0	0.72	0.07
	0.5	2	-2.5	-2.0	0.72	0.14
	1	1	-1.5	-1.0	0.72	0.28
0.42	0.25	4	-5.9	-4.0	0.48	0.10
	0.5	2	-3.9	-2.0	0.48	0.21
	1	1	-2.9	-1.0	0.48	0.42
0.55	0.25	4	-16.3	-4.0	0.37	0.14
	0.5	2	-14.3	-2.0	0.37	0.28
	1	1	-13.2	-1.0	0.37	0.55

I am comparing the input part curvature to the beam curvature at the confocal and cat's eye positions. The input part curvature is positive, while the beam curvatures are negative. This is due to how the positions are defined and is not a concern. As expected, at confocal the curvature of the beam is equal to the curvature of the test part. This is similar to a geometric model, where the curvature of the beam matches exactly with the curvature of the test part at confocal. With more significant figures, the beam curvature at confocal does vary slightly as compared to the part curvature. This is because there is a small offset in the confocal position when the Gaussian model is considered.

In the geometric picture, the beam curvature at the focal point is undefined. In the Gaussian model, the beam curvature at the focal point is zero (the beam radius goes to infinity). Because the cat's eye position does not occur at the

Gaussian focal point, the beam curvature has value as shown. The beam curvature is larger and the beam waist is smaller at cat's eye for the larger NA measurements.

2.8 Results for Macro-Scale Parts

I also performed this Gaussian analysis for macro-scale parts, nominal radius from 5 to 45 mm to compare to studies to a larger interferometer with apertures in the range of 6 inches. Varying the radius on the macro-scale interferometer using a f/1.1 transmission sphere is shown in Figure 2-19 and varying the transmission sphere for a 25 mm radius part is shown in Figure 2-20.

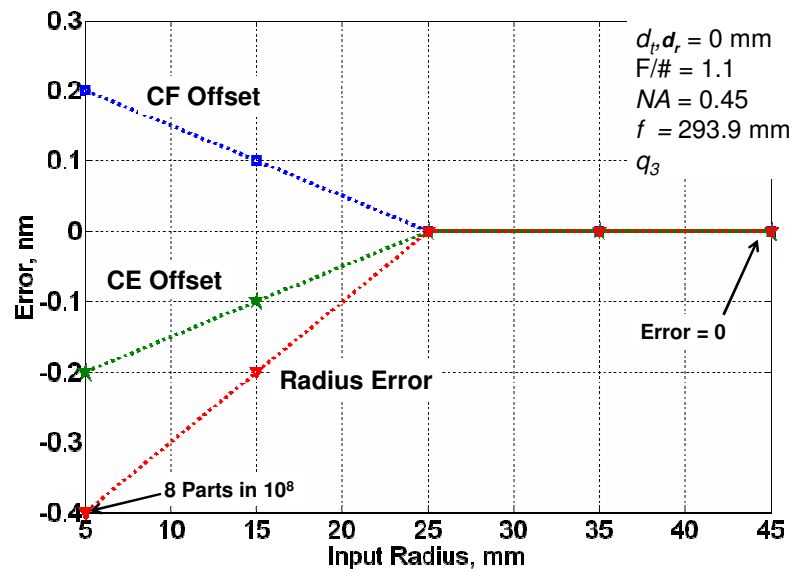


Figure 2-19: The error on the macro-scale interferometer for the 0.45 NA transmission sphere for varying radius.

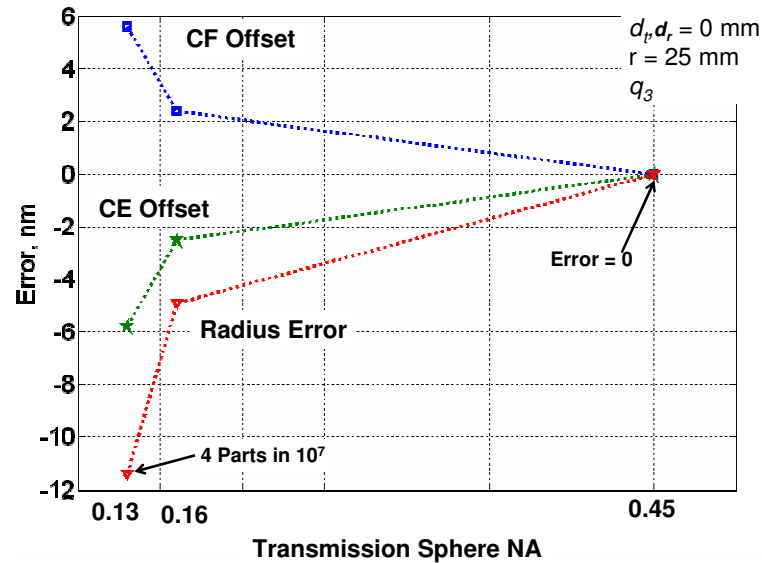


Figure 2-20: The error on the macro-scale interferometer for a 25 mm radius part with varying transmission sphere NA.

As expected, the errors for these larger interferometers are much smaller than for the micro-interferometer and follow similar trends. Schmitz, et al. [27] performed a Gaussian propagation model of the radius measurement on the XCALIBIR interferometer, a large scale interferometer, which found a 6 nm bias error in radius for a 25 mm radius test optic using the f/4 transmission sphere (NA = 0.13). Using the model presented here, the bias in radius is -11 nm, 4 parts in 10^7 , shown in Figure 2-19. The small difference between the two models is because the model used by Schmitz, et al. considered a wavefront with aberrations and the cat's eye reflection occurring at the minimum waist (where the curvature is zero).

2.9 Checking Assumptions

Section 2.3 is based on the assumption that the amplitude of the electric field varies slowly enough that $k\psi' \gg \psi'' \ll k^2\psi$, where prime indicates the

derivative with respect to z . This assumption was required to derive the Gaussian propagation model and is verified here. The area of interest is in the focal region, when the beam is converging, as shown in Figure 2-21. The z direction is shown and as is the g direction (the square root of $x^2 + y^2$). Only the part of ψ that depends on g is required to check this assumption. From Equation 2-10,

$$\psi \propto \exp\left[-\frac{ik}{2q_3(z)}g^2\right]$$

Equation 2-39

where q_3 is the complex curvature after the lens.

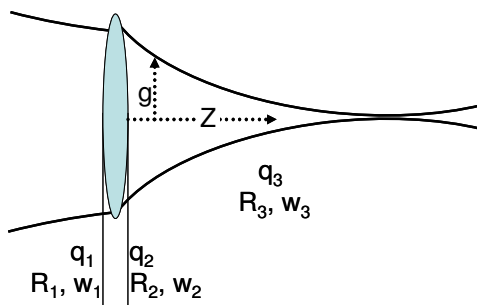


Figure 2-21: Schematic for checking the assumptions.

The complex curvature before the lens, q_1 , is

$$\frac{1}{q_1} = \frac{1}{R_1} - \frac{i\lambda}{\pi w_1^2}.$$

Equation 2-40

The complex curvature after the beam passes through the lens, q_2 , is found through matrix method and is

$$\frac{1}{q_2} = \frac{1}{q_1} - \frac{1}{f}$$

Equation 2-41

where f is the focal length of the lens. The complex curvature as the beam propagates after the lens, q_3 , is

$$\begin{aligned} q_3 &= q_2 + z \\ \frac{1}{q_3 - z} &= \frac{1}{q_1} - \frac{1}{f} \\ \frac{1}{q_3 - z} &= \frac{1}{R_1} - \frac{i\lambda}{\pi w_1^2} - \frac{1}{f} \\ q_3 - z &= \frac{1}{\frac{1}{R_1} - \frac{i\lambda}{\pi w_1^2} - \frac{1}{f}} \\ q_3 - z &= A \end{aligned}$$

Equation 2-42

after substituting Equation 2-40 and Equation 2-41. Now q_3 is a function of the physical inputs to the system, R_1 , w_1 , and f . The A is used for simplification purposes. Returning to Equation 2-39, ψ is now

$$\begin{aligned} \psi &\propto \exp\left[-\frac{ikg^2/2}{A+z}\right] \\ \psi &\propto \exp\left[-\frac{iB}{A+z}\right], \\ B &= \frac{kg^2}{2}, \quad k = \frac{2\pi}{\lambda} \end{aligned}$$

Equation 2-43

where B is used to simplify the mathematics. The first and second derivatives of ψ with respect to z are

$$\psi' \propto \exp\left[-\frac{iB}{A+z}\right] \left[\frac{iB}{(A+z)^2}\right] \quad \text{and}$$

$$\psi'' \propto \exp\left[-\frac{iB}{A+z}\right] \left[\frac{iB}{(A+z)^2}\right]^2 + \exp\left[-\frac{iB}{A+z}\right] \left[\frac{-2iB}{(A+z)^3}\right].$$

Equation 2-44

The assumption $k\psi' \gg \psi'' \ll k^2\psi$ can now be checked with the knowledge of the following inputs: R_1 , w_1 , f , λ , and g . The radius of the wavefront, R_1 , is large, 1000 mm was used here. The waist at the lens, w_1 , and the focal length, f , depend on the objective used, here tested at 4.5 mm and 10 mm for a 0.42 NA objective. The area of interest for g (the distance perpendicular to the z axis) varies with position after the lens because the beam waist changes. I must consider when g is at the waist or larger. Where g is two times w_3 is a good starting point. Figure 2-22 shows a plot of the radius (R_3) and waist (w_3) of the wavefront after the lens for a 10 mm focal length lens, 4.5 mm input waist (w_1), and 1000 mm input radius (R_1). The g for this case is then two times the waist and varies with the z position.

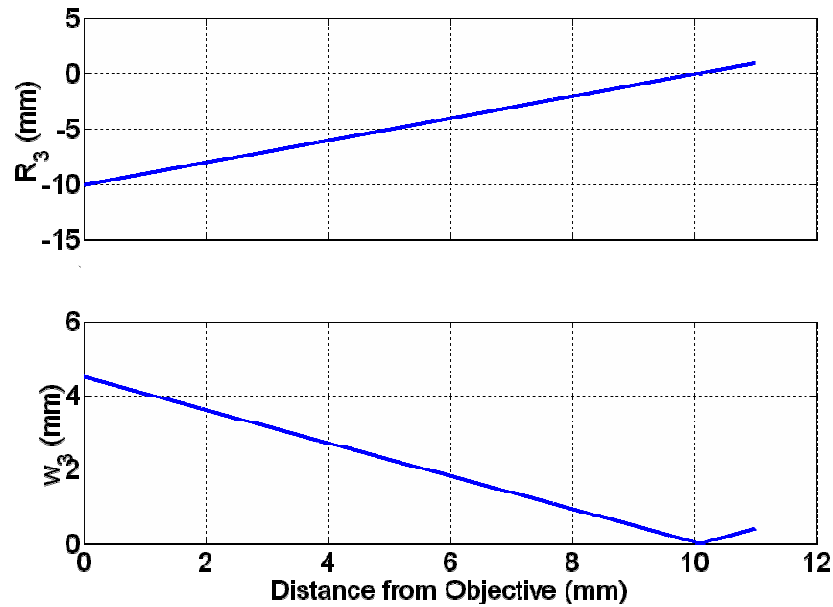


Figure 2-22: The radius and waist of the wavefront after the lens, where $f = 10$ mm and the objective is located at 0.

The comparison between $k\psi'$, ψ'' , and $k^2\psi$ is done using the amplitude of ψ , ψ' , and ψ'' , where amplitude is the square root of the real component squared plus the imaginary component squared. I used the Matlab computer program `der_test.m` in Appendix B, Program 2 for the calculation. The results of $k\psi'$, ψ'' , and $k^2\psi$ as calculated using Equation 2-43 and Equation 2-44 are shown in Figure 2-23. The values of $k\psi'$, ψ'' , and $k^2\psi$ do not change with the propagation distance, this is because the value of g does vary. For this case, $k\psi' \gg \psi'' \ll k^2\psi$ holds true. Table 2-5 shows the comparison for all the objective lenses used in this experiment. The statement $k\psi' \gg \psi''$ does not hold true for the 0.55 and 0.7 NA objective lenses. The $k\psi'$ is larger than ψ'' , but not much larger as required for the Gaussian propagation model. It then appears that the Gaussian propagation model begins to break down in systems with numerical aperture of

0.55 and larger. I must therefore be careful about the conclusions drawn from the simulation of the 0.55 and 0.7 NA objectives. A full physical optics model is required to carefully investigate this limit, however it is likely that the Gaussian model captured the correct order of magnitude of the effect. A more detailed physical optics model is discussed in the next chapter.

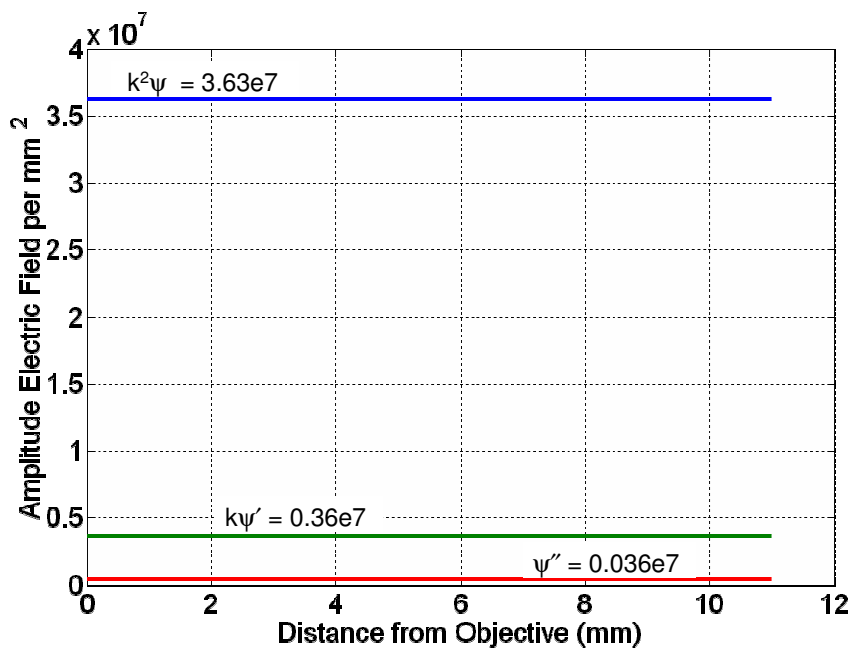


Figure 2-23: Comparison between $k\psi'$, ψ'' , and $k^2\psi$ for $f = 10$ mm, $w_1 = 4.5$ mm, and $R_1 = 1000$ mm.

Table 2-5: The values of $k^2\psi$, $k\psi'$, and ψ'' in units of electric field per μm^2 .

NA	$k^2\psi$	$k\psi'$	ψ''
0.28	36.27	1.84	0.09
0.42	36.27	3.60	0.36
0.55	36.27	10.12	2.82
0.7	36.27	18.06	8.99

For comparison, I also tested a macro-scale case where $f = 100$ mm and $w_1 = 25$ mm. For this case $k^2\psi = 36.27$ electric field per μm^2 , $k\psi' = 1.11$ electric field per μm^2 , and $\psi'' = 0.03$ electric field per μm^2 . The assumption $k\psi' \gg \psi'' \ll k^2\psi$ holds true for this macro-scale case.

2.10 Conclusions about the Model

From the results above the following observations are made:

- The measured part is smaller than the input radius.
- The error in the cat's eye position is normally slightly larger in magnitude than the error in the confocal position.
- The cat's eye position is shifted towards the objective lens, shown in Figure 2-24.
- The confocal position is shifted away from the objective lens, shown in Figure 2-24.
- Radius error increases (apparently exponentially) as the radius decreases.
- Radius error increases (apparently exponentially) as NA decreases.
- Propagation distances d_t and d_r do not affect the radius measurement.
- There is beam curvature at the test optics surface for the cat's eye position that varies with NA.

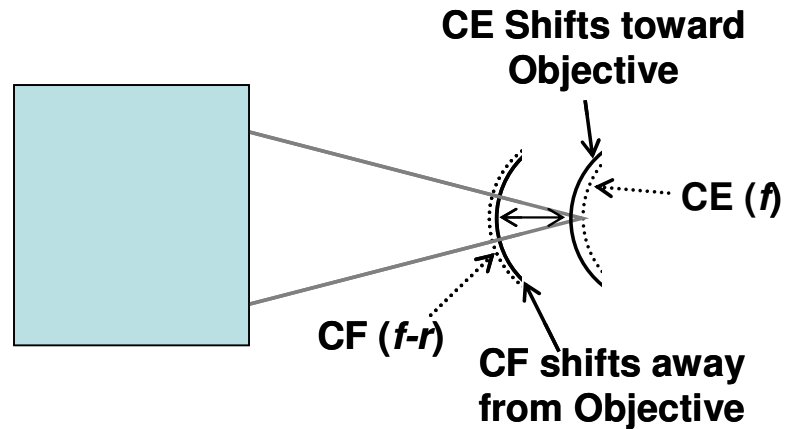


Figure 2-24: Schematic showing the shift of the confocal and cat's eye position. The solid lines are the positions determined from the model.

It is interesting to note that decreasing the NA (equivalent to stopping the beam down) will increase the errors in the radius. Yet, often a beam is stopped down to reduce spherical aberration and therefore reduce a bias in the measurement due to the aberration.

The model begins to break down for the 0.55 and 0.7 NA objective lenses. These objectives have a much smaller beam waist at the focus point. A detailed physical optics model is required to more understand the measurements at these NAs. In any case, the Gaussian model shows that an approximate treatment of diffraction effects and beam propagation introduces small errors, much smaller than errors caused by wavefront aberrations. The following chapter describes a method for modeling the radius measurement with a physical optics sense using the software package FRED, where effects of diffraction and wavefront aberration are both included in principle.

It must be noted that aberrations cannot be added to this model. The intensity of the beam is set to a Gaussian profile and cannot be changed. The radius model in FRED can be used to add aberrations to the system.

CHAPTER 3: A PHYSICAL OPTICS MODEL OF THE RADIUS MEASUREMENT USING FRED

3.1 Introduction to FRED

The FRED software package, by Photon Engineering [33], is a physical optics modeling software package. FRED approximates a physical optics model by approximating a source beam as a grid of points with each point sending out a Gaussian profile. Each Gaussian beamlet is sent through the optical system in the same manner as the ABCD matrices used in Chapter 2 [34, 35]. After each beamlet passes through the system, wavefront of the beams on the “detector” are summed to approximate a physical optics model.

FRED is a visual software package where the lens, mirrors, and sources are all displayed in their relative positions. The “rays” of the source are then traced and read by a detector. The term ray is used here to indicate the Gaussian beamlet of each point. The detector is where the beamlets are all summed.

First, each component (source, focusing lens, and detector) used to simulate the radius measurement is described. Then the procedure for performing the simulated radius measurement is described. Finally, the results from the various simulated radius measurements are shown.

3.2 Sources

Two sources were tested: a constant intensity beam with a circular aperture and a beam with a Gaussian intensity profile (used to compare to Chapter 2). Both sources were set with a 632.8 nm, Helium-Neon wavelength and they were designated as coherent and unpolarized (random polarization).

3.2.1 Circular Aperture Input Beam

The circular input beam has a constant intensity over the entire aperture. That is, the beam has a top hat intensity profile and is collimated. This beam is constructed by the FRED program from the sum of small Gaussian beamlets, called rays by the FRED program. The term ray is used here to indicate the small Gaussian beamlet, not the geometric model ray.

The key input to the circular source is the number of rays. With more rays the top hat profile is more true to absolute. But, the program is slower with more rays. A source of 31 rays by 31 rays over the circular aperture was used. This was decided upon after testing the 11x11, 31x31, 51x51, 81x81, and 101x101 configurations. The detail of this testing is not shown in full here but the results are summarized as follows. The number of input rays was varied at different positions along the optical axis and the resultant phase output was examined for changes. Varying the number of input rays caused an uncertainty of up to ± 0.027 waves in the defocus term of the output phase map. This directly leads to an uncertainty of up to ± 31 nm in both the cat's eye and confocal positions. This uncertainty is constant for a setup. Therefore if the setup is not changed during

the simulated experiments, the uncertainty becomes a possible bias that must be considered.

The energy density (proportional to intensity) of the circular aperture top hat beam (31x31) is shown in Figure 3-1. The input beam aperture diameter is 8 mm.

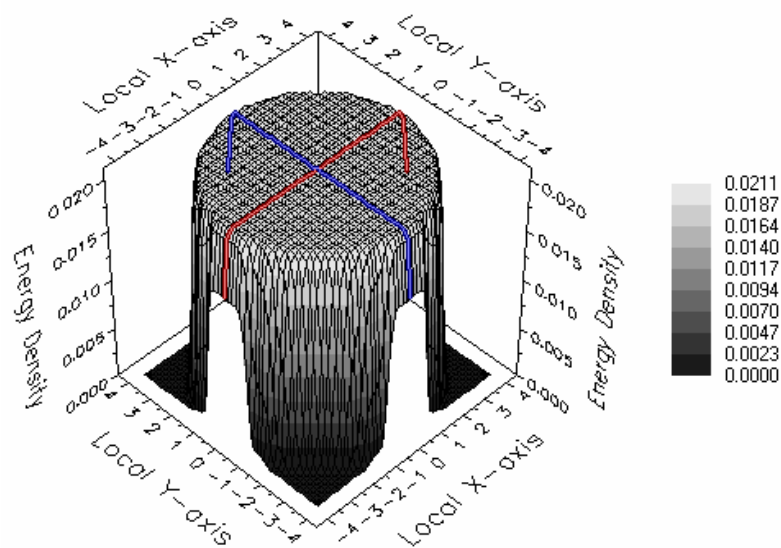


Figure 3-1: The energy density (proportional to intensity) of the circular beam. The units on the z-axis are inconsequential and are mm on the x- and y-axes.

3.2.2 A Gaussian Beam Input

For comparison to the Gaussian Model shown in Chapter 2, a Gaussian beam must be used as the input beam. A special source was required for this. A normal source uses the sum of many Gaussian beamlets to form a top hat intensity function. For this special source, one Gaussian beamlet was used. The parameters of that single beam were varied such that it would be the proper size. This is accomplished by changing the coherent beam parameters: “Adjacent

Beams Overlap Factor” = 0.886226925, “Secondary Ray Scale Factor” = 0.1, and the beam semi aperture is 4 mm in X and Y. Normal parameters are 1.5 for Adjacent Beams and 1 for Secondary Ray. Figure 3-2 shows the energy density (proportional to intensity) of the single Gaussian beam. Note how this compares to Figure 3-1 where the energy density is a top hat. For the following simulated radius measurements in FRED, both the single Gaussian source and the top hat source will be used.

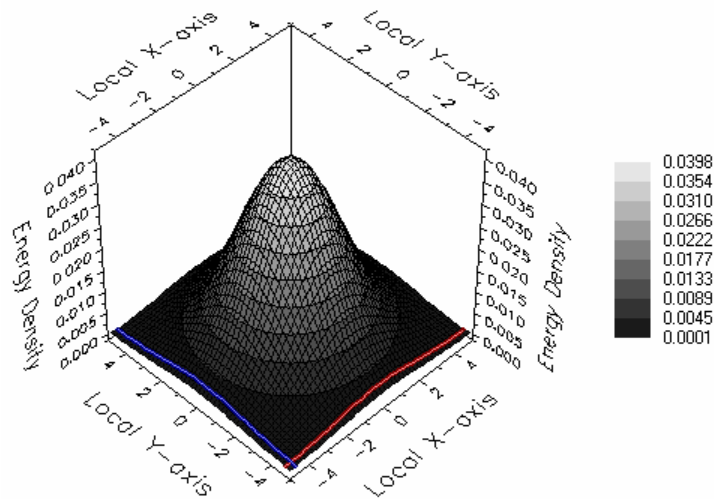


Figure 3-2: The energy density of the single Gaussian beam. The units on the z-axis are inconsequential and are mm on the x- and y-axes.

3.3 The Focusing Lens

The next component in the measurement is the focusing lens. In experiment this is a microscope objective with multiple lenses. This objective can not be simulated in FRED due its proprietary nature. In simulation, we are seeking a component that will produce a diffraction limited focal point. This will

allow testing a perfect system (no aberrations) and then aberrations can be added to determine the effect on the radius measurement.

3.3.1 Using a Spherical Lens

A complicated part of building the FRED model is that the program does not allow the use of a perfect lens, i.e. a perfect “thin lens”. The program uses lenses that could be manufactured. In most cases, this creates spherical aberration in the beam. I initially want to simulate the radius measurement using a perfect (non-aberrated) beam. This non-perfect lens is demonstrated in the following example.

The circular aperture 8 mm diameter beam was set at the origin. A lens with focal length 10 mm, bending parameter of 1, diameter of 10 mm, and thickness of 4 mm is placed 1 mm from the source. The bending parameter indicates the shape of each surface of the lens; here the parameter of 1 is a convex-plano lens. Figure 3-3 shows this model with the rays traced.

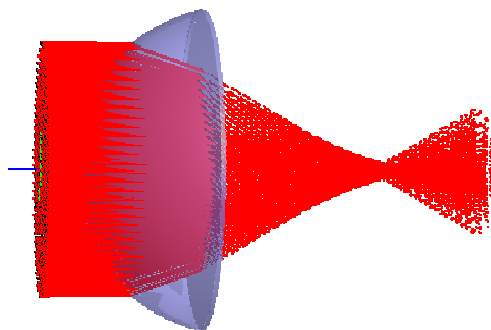


Figure 3-3: The FRED model with a Spherical Lens.

Even by looking at the figure, it is obvious that rays are very spread out at the focus point of the lens indicating spherical aberration. We can perform a “Best Geometric Focus” analysis to determine the size of the spot. The Best Geometric Focus as defined by FRED is the RMS smallest point of the ray package. Figure 3-4 shows the output of this analysis. The numbers of interest are boxed in a dotted line. The Z position (the z direction is along the optical axis) is located at 11.06768 mm, not the 11 mm as expected. The RMS of the ray bundle is 0.159 mm, quite large. This analysis also reports the NA of the system, here 0.51.

```

BEST FOCUS: (new)
749 rays
Coordinate system: global
A ray filter has been applied.

Best Focus:
RMS:
Principal Directions:
Avg Ray Direction:
(unit length):
Max Angular Spread:
Numerical Aperture:
Equivalent F/#:

Min/Max Positions Along the Principal Directions:
Min:
Max:

```

	X	Y	Z	RMS
Best Focus:	-6.66e-16	6.19e-16	11.06768	0.159402
RMS:	0.105071	0.105071	0.057697	0.105071
Principal Directions:	-1	0	0	0.105071
	0	1.04e-16	1	0.057697
	0	-1	-6.93e-18	0.105071
Avg Ray Direction:	3.32e-17	2.91e-17	0.942931	
(unit length):	3.52e-17	3.08e-17	1	
Max Angular Spread:	39.4282 degrees			
Numerical Aperture:	0.506482			
Equivalent F/#:	0.851213			
Min/Max Positions Along the Principal Directions:				
	1	2	3	
Min:	-0.280867	-0.168247	-0.280867	
Max:	0.280867	0.047007	0.280867	

Figure 3-4: The Best Focus Analysis for the example shown in Figure 3-3.

3.3.2 Using a Spherical Lens with a Conic Surface

A common solution to try and reduce the spherical aberration caused by lenses is to use conic surfaces on the lens. Using a simple guess and test, I attempted to reduce the RMS number by using different conic numbers on the convex surface of the lens. The FRED package does not have an optimization

option that would solve for the best conic number like other software packages. Therefore, the guess and test method was used. A conic number of -0.6 appears to have the best results and is shown in Figure 3-5 and Best Geometric Focus Analysis is shown in Figure 3-6.

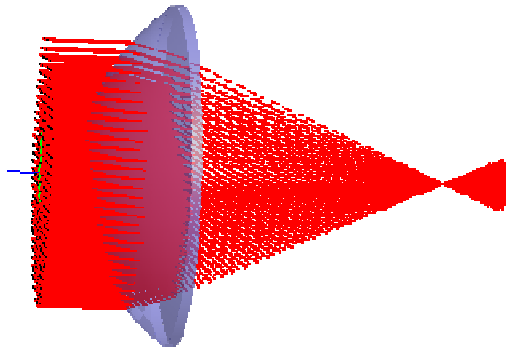


Figure 3-5: The FRED model with a spherical lens with a conic surface on the front face.

```

BEST FOCUS: (new)
749 rays
Coordinate system: global
A ray filter has been applied.

Best Focus:
RMS:
Principal Directions:
Avg Ray Direction:
(unit length):
Max Angular Spread: 23.70322 degrees
Numerical Aperture: 0.401999
Equivalent F/#: 1.138857

Min/Max Positions Along the Principal Directions:
Min:
Max:

```

	X	Y	Z	RMS
Best Focus:	-5.64e-17	-7.43e-16	12.10935	
RMS:	0.002543	0.002543	0.000920	0.003712
Principal Directions:	-1	0	0	0.002543
	0	4.16e-17	-1	0.000920
	0	1	-1.80e-16	0.002543
Avg Ray Direction:	2.16e-17	2.54e-17	0.958286	
(unit length):	2.26e-17	2.65e-17	1	
Min/Max Positions Along the Principal Directions:				
Min:	-0.005748	-0.001542	-0.005748	
Max:	0.005748	0.001069	0.005748	

Figure 3-6: The Best Focus Analysis for the example shown in Figure 3-5.

The spread of the rays in Figure 3-5 is much smaller than in Figure 3-3 and the RMS of the spot has been reduced to 0.0037 mm from 0.1594 mm. But, this spot is again too large. The conic lens does not reduce the aberration enough.

3.3.3 Using a Parabola

The next obvious step was to use a parabola. Parabolas are used in experiments and simulation to create a diffraction limited spot or a non-aberrated beam. Initially an off-axis parabola was tested for the radius model, but positioning the off-axis parabola was time prohibitive to do in FRED. Aligning an off axis parabola in experiment is less difficult.

The radius of the parabola is chosen to provide the desired NA. The NA is found using the “Best Geometric Focus”. The conic constant of the parabola is always -1.

A full parabola was used to perform the radius measurement simulations in FRED, shown in Figure 3-7. The parabola is placed at the origin and the source 15 mm away. The parabola has a 7 mm focal length and a diameter of 10 mm. The source is again He-Ne and is 6 mm in diameter. Only every tenth ray was traced in Figure 3-7 for visualization purposes only. The “Best Geometric Focus” information is shown in Figure 3-8. The z position of the best focus is at 7 mm as expected and the RMS of the spot is very small at 9.45×10^{-15} mm (considered here to be zero).

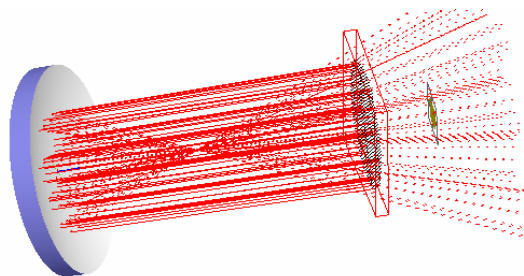


Figure 3-7: The parabolic model with rays traced.

```

BEST FOCUS: (para_radius_NA4048)
749 rays
Coordinate system: global
A ray filter has been applied.

Best Focus:
RMS:
Principal Directions:
Avg Ray Direction:
(unit length):

Max Angular Spread: 23.88194 degrees
Numerical Aperture: 0.404853
Equivalent F/#: 1.129274

Min/Max Positions Along the Principal Directions:
1 2 3
Min: -9.77e-15 -7.10e-15 -1.15e-14
Max: 1.37e-14 2.66e-15 1.24e-14

```

Figure 3-8: The Best Focus Analysis for the example shown in Figure 3-7.

To use the full parabola for the radius measurement, a special step was required in the ray tracing. When the part is placed at the focus, the rays from the source will be blocked by the test part. Therefore the ray tracing must be done in these steps 1) source, 2) parabola, 3) test part, 4) parabola, and 5) detector. This type of ray tracing (skipping components) is called a “User Defined Ray Path” in FRED. The traced rays with the order of tracing are shown in Figure 3-9 (again only some of the rays are shown for visualization purposes). Figure 3-10 shows the FRED window where the user defined ray path is entered.

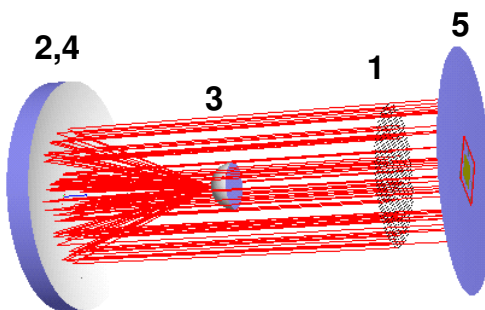


Figure 3-9: The rays traced in the user defined ray path for the parabolic model shown in Figure 3-7.

	Surface (or entity)	Ray Control
2	.para.Reflecting Surfa	Reflect
3	.test.Reflecting Surfac	Reflect
4	.para.Reflecting Surfa	Reflect
5	.camara.Surf 1 ()	Pause/transmit
		Transmit

Figure 3-10: The user defined ray path: Parabola, test part, Parabola, Camera.

3.4 The Detector and Analysis

The detector simulates the camera. In the program, it is a plane where all the rays are summed. The detector has a certain number of pixels over which the rays are averaged. As with the source, more pixels are more accurate, but more time is required. After testing the detector in a similar manor to testing the source, an 81 by 81 pixel array was decided upon.

To determine the uncertainty due to the number of detector pixels, I performed an analysis similar to the one in Section 3.2.1 that showed an uncertainty of ± 31 nm based on the number of input rays. Varying the number of camera pixels resulted in an uncertainty in the Zernike defocus term of 0.0546 waves, leading to a possible offset uncertainty of ± 64 nm for the 0.42 NA objective.

For the radius measurement, the phase at the detector is required. First the rays are traced using the advanced ray trace described above. Then a “coherent scalar ray analysis” (an option in the Analyses menu) was performed. With this, the energy density was calculated and then the wrapped phase is found. This phase data is then saved in a test file and then read into Matlab where the

Zernike Defocus term is calculated. The phase map is reported in waves (where one wave is 632.8 nm).

3.5 Reading the Phase Data in Matlab

The Zernike coefficients (Appendix A) of the phase map are required for the radius measurement. This analysis cannot be done in FRED; it must be done in Matlab.

The data from FRED is a text file and the Matlab program `read_fred.m` (Appendix B, Program 4) is used to read this file. Next the program `mask_circle.m` (Appendix B, Program 4) masks the data to a circle. The phase map is unwrapped using the built in Matlab function `unwrap.m`. The Zernike coefficients are then found using `zern_radius_angle.m` (Appendix B, Program 5) and `zern_estim.m` (Appendix B, Program 6). Programs 4, 5, and 6 were developed at the National Institute of Standards and Technology and are used here with permission. The main program `get_20_40_fred.m` (Appendix B, Program 3) is used as a main program that calls Programs 7, 8, and 9 and plots the resultant phase map.

3.5.1 Unwrapping

The internal Matlab function `unwrap.m` is next used to unwrap the data. This is because the calculation of the phase requires the use of an arctangent function which only goes from $-\pi$ to $+\pi$. These discontinuities in the data need to be fixed in computation.

The Matlab function `unwrap.m` is not without errors. There are rare times, even if the `unwrap` function is performed in both the X and Y directions, that the resultant dataset still has unwrapping errors. There are more involved unwrapping functions than the simple Matlab function, but many of these are propriety. The easiest solution is to discard the phase maps that have an unwrapping error. This is valid because there are multiple data points when solving for the cat's eye and confocal positions, but will increase the fitting error as described in Chapter 1. After unwrapping, the phase data must be converted to height [26] data using

$$\frac{height}{\lambda} = \frac{Phase}{4\pi} .$$

Equation 3-1

The extra factor of two in this conversion is because a Tywman-Green interferometer is double pass in height.

3.5.2 The Zernike Coefficients

After the data has been unwrapped, the Zernike polynomial coefficients (Appendix A) of the height map are solved for using Programs 5 and 6. Generally, the program is set to solve for the first 36 Zernikes. Program 6 returns the variable `vpar` which includes all 36 Zernike coefficients. The Zernike defocus term, a_2^0 (used to find cat's eye and confocal, Section 1.3.1) is the fifth term in this array and the spherical aberration, a_4^0 is the thirteenth term.

3.6 Setup of the Simulated Radius Measurements in FRED

A radius measurement was set up in FRED using a source (circular aperture or Gaussian), a parabola (with the desired NA), a reference mirror, a test part, and a detector. The test part is a reflecting spherical component with the desired radius. The reference mirror is a flat reflecting surface.

For comparison to the Gaussian model both the test and reference arms need to be traced. This is done by placing the parabola at the d_t propagation distance and a reference mirror is placed at the d_r propagation distance from the source. This is shown in Figure 3-11. For the experiment, each arm of the interferometer is traced separately as shown in Figure 3-12. The reference arm is only traced once. The test arm is traced as follows.

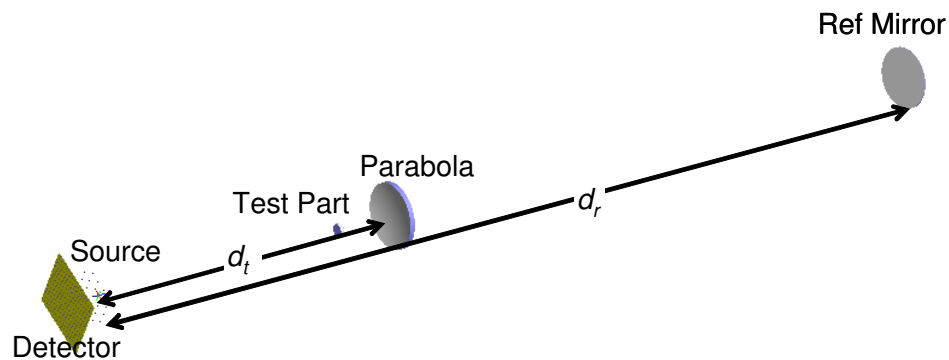


Figure 3-11: Schematic of radius measurement in FRED showing the propagation distances.

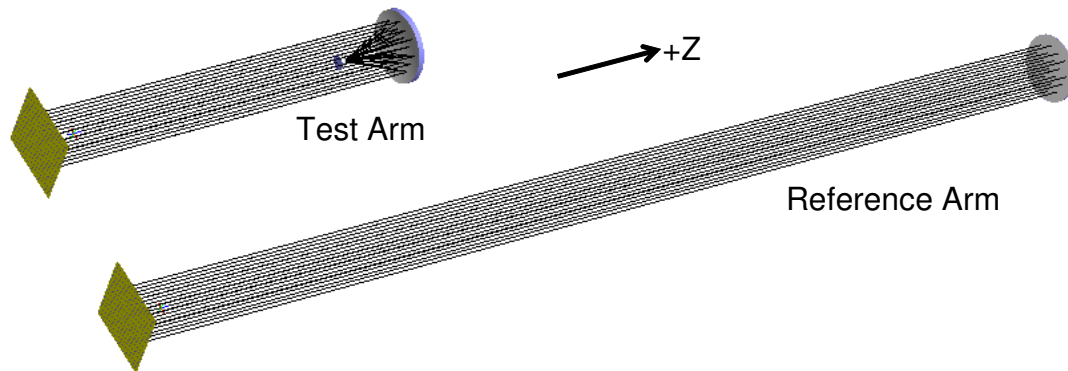


Figure 3-12: The test arm and reference arm with rays traced. Note that the test arm requires the use of the “user defined ray path.”

The test part is placed at a Z position slightly ($5\ \mu\text{m}$) less than the best focus position. The rays are traced using the required user defined ray path. The “Coherent Scalar Wave Field” is computed by FRED at the camera. The phase at that point is saved as a text file. The test part is then stepped through the cat’s eye position in steps of $1\ \mu\text{m}$ with the rays traced and the phase calculated and saved at every step. The same is done around the confocal position. The approximate confocal position is one radius more than the approximate cat’s eye positions.

All of the phase map files (reference and test) are then read into Matlab and the Zernike coefficients are calculated. First the reference defocus term is subtracted from the each of the test defocus terms. Then two plots are formed: corrected defocus versus Z position for cat’s eye and confocal. A line is fit to the data in each plot and the intercepts are the cat’s eye and confocal positions. The difference between the two is the simulated measured radius.

The cat's eye and confocal offset terms are also calculated in this step. The cone of light points to the left in the FRED model, but the cone of light points to the right in the Gaussian model in Chapter 2. Because of this, the calculation of the bias in cat's eye and confocal is different, but the convention remains the same. A positive bias indicates a shift away from the parabola, while a negative bias indicates a shift toward the parabola. A positive error in radius indicates that the measured sphere is larger than the input and a negative error in radius indicates that the measured sphere is smaller than the input.

3.7 Summary of Radius Procedure

The procedure for the simulated radius measurement is summarized in following list.

1. In FRED, the test beam is turned off and the reference beam is traced. The reference phase map is calculated and saved.
2. In FRED, the reference beam is turned off and the test beam is traced (using the advanced ray trace). The test phase map is calculated and saved. This is done multiple times for ten phase maps near the cat's eye positions and ten near the confocal position.
3. Matlab is used to import the phase map, unwrap the data, convert the phase to height, mask the data to a circle, and calculate the Zernike Defocus term for each phase map. It is in this step that any data with phase unwrapping error is discarded.
4. In Matlab, the reference defocus value is subtracted from each test defocus value.

5. In Matlab, the corrected defocus value is plotted versus Z position for both cat's eye and confocal and the intercepts are calculated.
6. In Matlab, the radius is the difference between the two intercepts.
7. In Matlab, the cat's eye and confocal offset terms are calculated.

3.8 Measurements using the Single Gaussian Beam.

The single Gaussian beam was used as the input for the following simulated radius measurements. The single Gaussian source described in Section 3.2.2 was used as the input. These results can be compared to the Chapter 2 simulations. The simulated measurements were performed as described in Section 3.6.

3.8.1 Varying Radius

I first tested varying the radius of the test part. Only three radii (0.25 mm, 0.5 mm, and 1 mm) were tested due to the amount of time one test takes. The propagation distances d_r and d_t are 150 mm and 50 mm from the source. The focal length of the parabola is 10 mm. To achieve the desired 0.42 NA objective, I varied the input beam diameter and then check the NA of the parabola using the "Best Focus" function. A beam diameter of 8.92 mm resulted in a NA of 0.4185.

Figure 3-13 shows the results from the 0.5 mm part. The phase maps at each data point are shown. The missing phase maps had unwrapping errors and were discarded. The calculated radius of this part is 0.500022 mm, indicating an

error of 22 nm. Figure 3-14 shows the radius error and position bias terms for various radii parts. The radius error increases with the decreasing radius.

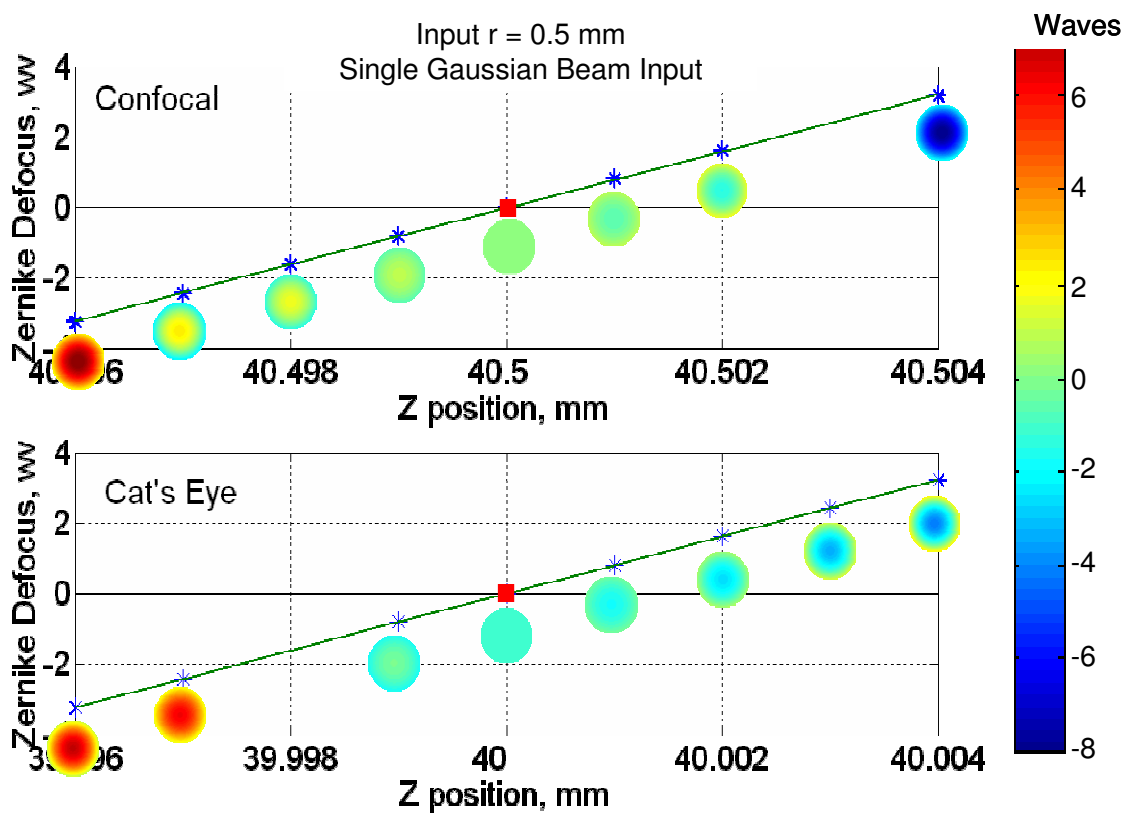


Figure 3-13: The results from the FRED test of a 0.5 mm radius part single Gaussian beam input. The parabola is to the right at 50 mm.

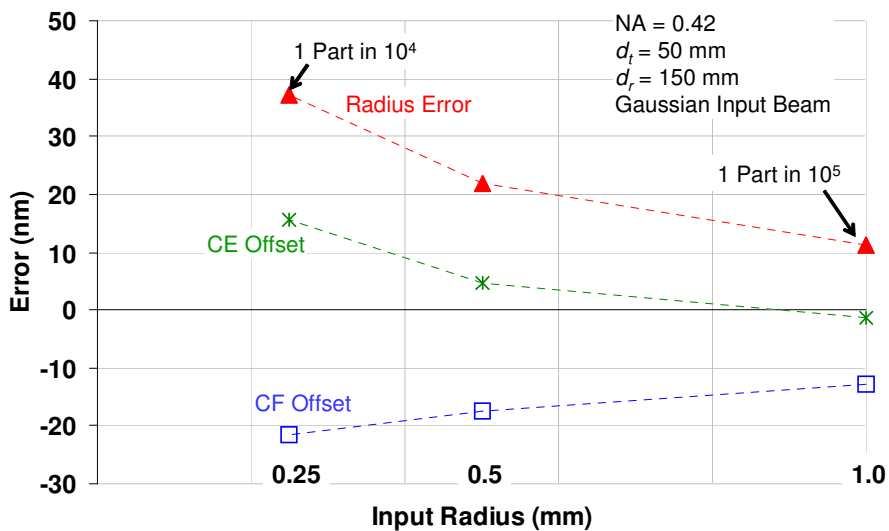


Figure 3-14: Results from FRED, varying radius, single Gaussian beam input.

3.8.2 Varying NA

Next, I varied the numerical aperture of the parabola by setting the proper focal length and then adjusting the input beam diameter as required to achieve the desired NA. The propagation distance are the same as before, $d_r = 150$ and $d_t = 50$. The results for a part of 0.5 mm radius are shown in Figure 3-15 and for a 0.25 mm radius part in Figure 3-16.

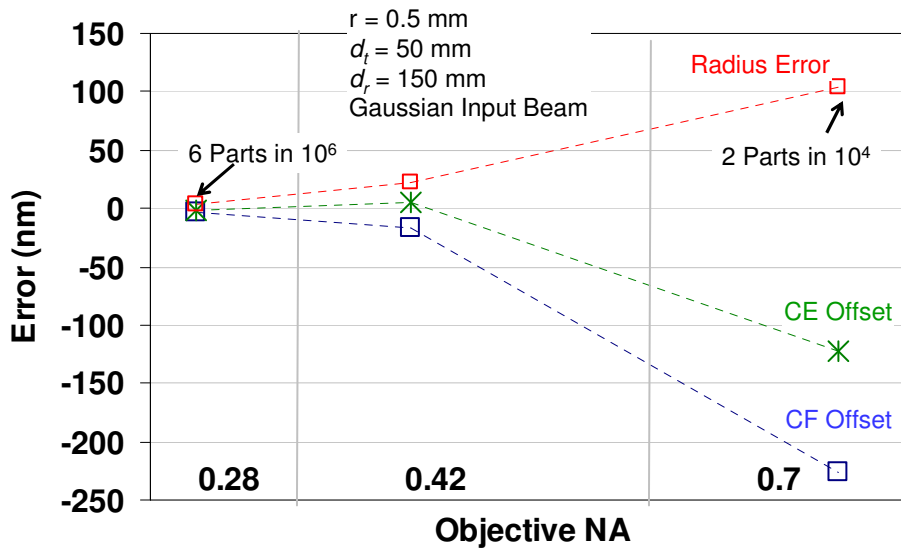


Figure 3-15: Results from FRED, varying NA, single Gaussian beam input, input radius = 0.5 mm.

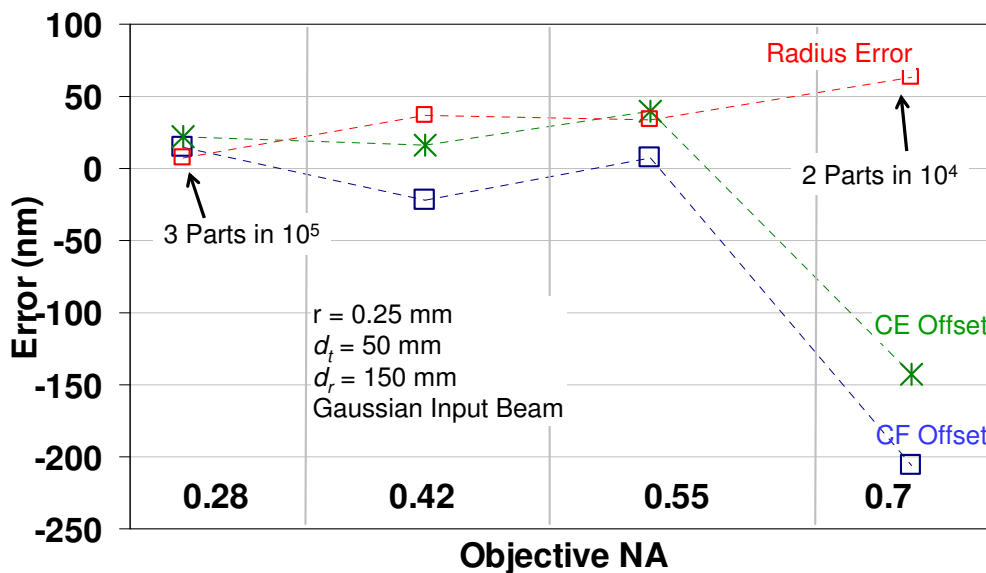


Figure 3-16: Results from FRED, varying NA, single Gaussian beam input, input radius = 0.25 mm.

The error for the 0.7 objective for both the 0.25 mm and 0.5 mm input radius cases is quite large. This does not compare well to the Gaussian simulation in Chapter 1 which showed an increasing error with decreasing NA.

This is due to the model beginning to break down. The FRED model is under the same constraint as the Gaussian model, that the field can not vary quickly. The analysis in Chapter 2 showed that the 0.55 NA and the 0.7 NA objectives may not meet this constraint. This model break down is especially relevant in the Gaussian Beam input to FRED rather than the circular beam input because only one Gaussian beam is used. The model break down leads to a large uncertainty in the fit of the defocus vs. position graph, Figure 3-13. For most cases, the uncertainty in the radius due to the fit (as calculated as described in Chapter 1) is ± 40 nm to ± 70 nm. The uncertainty in the 0.7 NA objective fit for both the 0.25 mm and 0.5 mm input radius part was near ± 500 nm. Because of this, the data for the 0.7 NA objective is invalid.

3.8.3 Varying the Propagation Distances, d_t and d_r

I next tested varying the reference arm propagation distance. Only the reference arm propagation distance is shown here, varying the test arm propagation distance showed similar results. The results from varying the reference propagation distance, d_r , from 150 mm to 300 mm are shown in Figure 3-17. This model shows a very small effect in the position of the cat's eye and confocal reflections. But, the shift in each position is in the same direction, so there is no effect on the radius error.

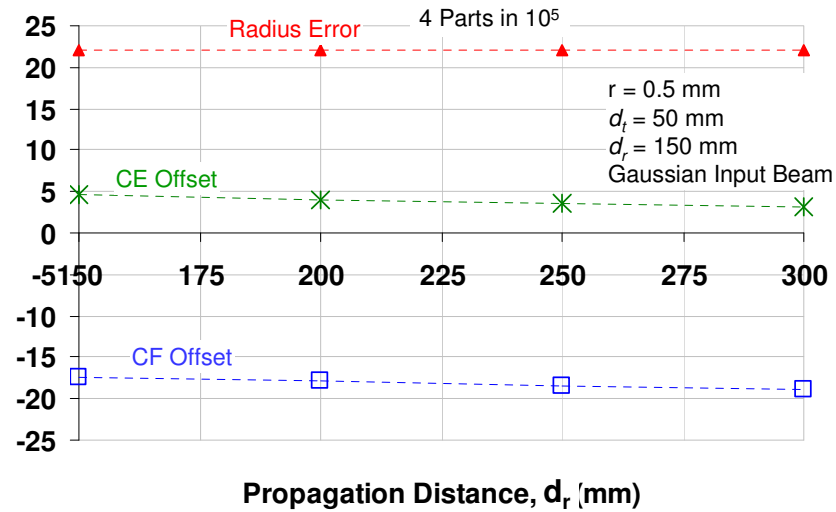


Figure 3-17: Results from FRED, varying the reference propagation distance, d_r , single Gaussian beam input, input radius = 0.5 mm.

3.9 Measurements using the Circular Input

I then changed the input source to a beam with a circular aperture top hat profile beam as described in Section 3.2.1 and the radius was measured as described in Section 3.7. The circular aperture beam is closer to experiment but the actual wavefront is likely somewhere between the two.

3.9.1 Varying Radius

The results from varying the radius of the test part are shown in Figure 3-18. Only three radii (0.25 mm, 0.5 mm, and 1 mm) were tested due to the amount of time one test takes. The propagation distances d_r and d_t are at 150 mm and 50 mm from the source, the beam diameter is 8.92 mm, and the NA is 0.4185 as before. The radius error is larger than for the Gaussian single beam input but on the same order of magnitude. The trend is similar, that the error increases with decreasing radius.

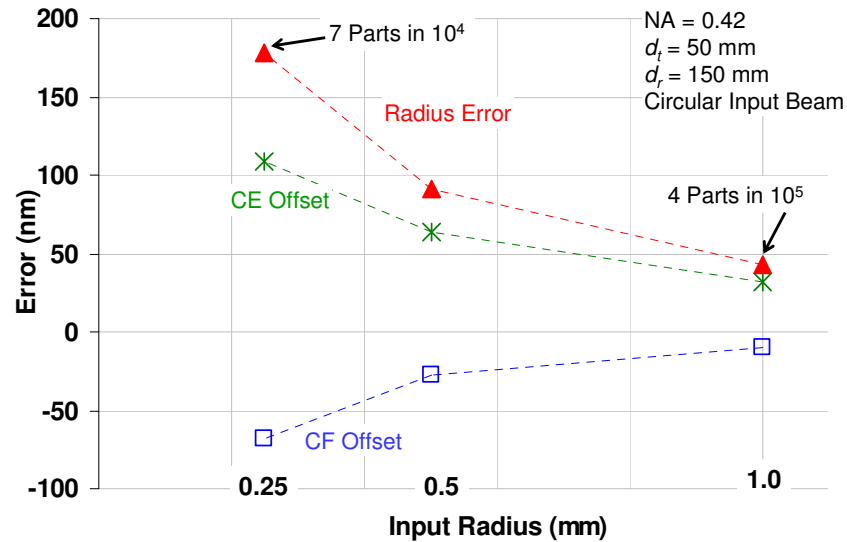


Figure 3-18: Results from FRED, varying radius, circular aperture beam input.

3.9.2 Varying NA

The results for varying the NA of the parabola are for 0.5 mm radius part are shown in Figure 3-19 and for a 0.25 mm radius part in Figure 3-20. The propagation distance are the same as before, $d_r = 150$ and $d_t = 50$. The radius error increases with the decreasing NA (increasing spot size). The radius error is much larger for the smaller radius parts, Figure 3-20 and is 2 parts in 10^3 , which is significant when precision measurements are desired.

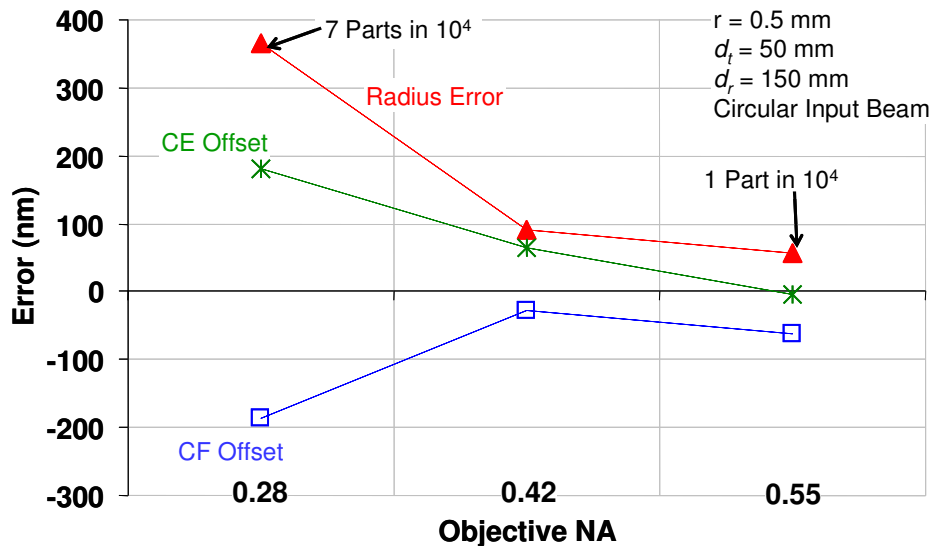


Figure 3-19: Results from FRED, varying NA, circular aperture beam input, input radius = 0.5 mm.

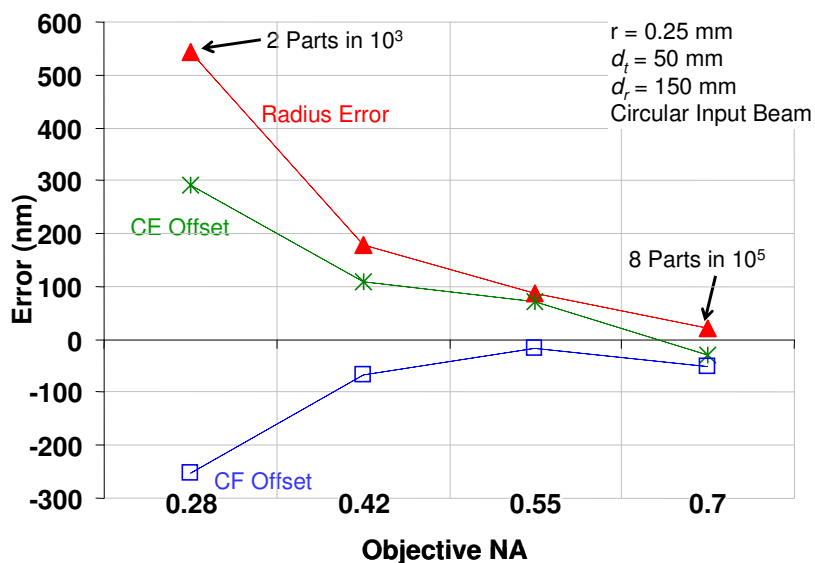


Figure 3-20: Results from FRED, varying NA, circular aperture beam input, input radius = 0.25 mm.

3.9.3 Varying Propagation Distances

The results for varying the propagation distance, d_r , are shown in Figure 3-21. The propagation distances tested are comparable to the micro-

interferometer. As with the Gaussian model in Chapter 2, the varying the propagation distance shifts the confocal and cat's eye positions slightly, but has no effect on the radius measurement. Similar errors are shown when varying the test propagation distance, d_t .

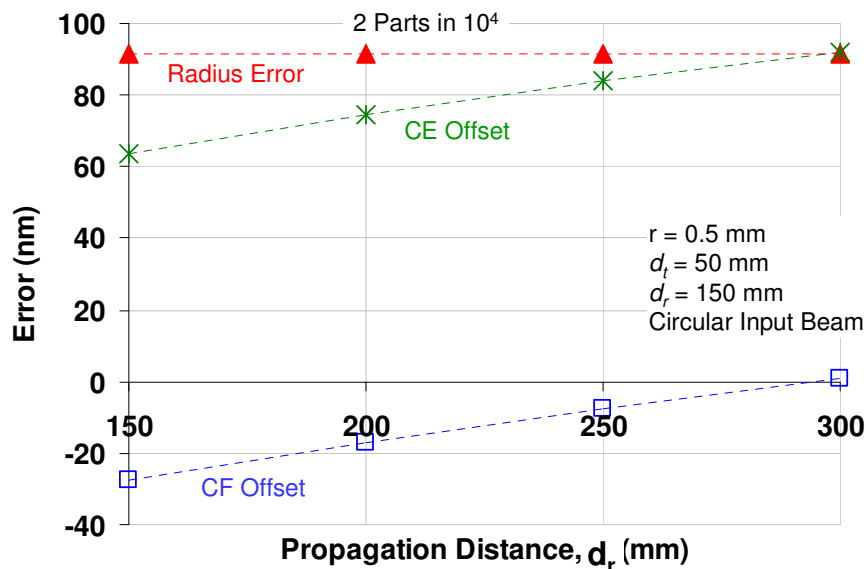


Figure 3-21: Results from FRED, varying d_r , circular aperture beam input, input radius = 0.5 mm.

3.10 Adding Spherical Aberration

The above results only consider a non-aberrated system, i.e. the light is focused to a diffraction limited focal spot. Experimentally, all systems will have aberration. Spherical aberration will have the largest impact on the radius measurement (from a symmetry consideration) and it is a common aberration in optical systems. Spherical aberration is easily added to a system by inserting a parallel window in a converging beam, as shown in Figure 3-22. The thickness of the window corresponds to the glass window used in experiments.

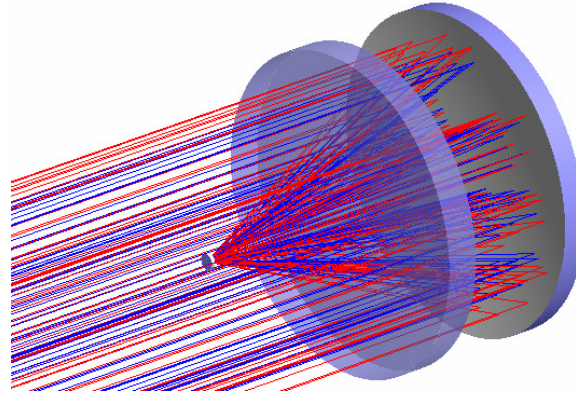


Figure 3-22: Picture from FRED with the additional spherical aberration.

Because the single Gaussian beam input can not have aberrations, adding spherical aberration would not affect the radius results. The window would cause the cat's eye and confocal positions to shift, but the difference between the two remains the same. This is the same reason why aberration could not be added to the Gaussian model in Chapter 2. I confirmed this by adding windows to the 0.42 NA interferometer with a single Gaussian beam input. For a 0.5 mm input radius the radius error remained 22 nm as shown in Figure 3-14 no matter the window thickness.

3.10.1 Spherical Aberration with the Top Hat Beam

Figure 3-23 shows the simulated radius measurement of a 0.5 mm radius sphere in a 0.42 NA interferometer with a 0.254 mm thick glass plate. The output is 0.500176, an error of 176 nm. The measured part is larger than the input. The cat's eye and confocal positions shifted away from the interferometer as expected by -1347 nm (cat's eye) and -1523 nm (confocal). Figure 3-24 and Figure 3-25 show the simulated measurement results for varying the thickness of the glass plate. The large shift in the cat's eye and confocal positions are due to

the primary effect of adding a glass plate, the focus shifts away from the objective. The amount of spherical aberration (a_4^0) at cat's eye is also shown.

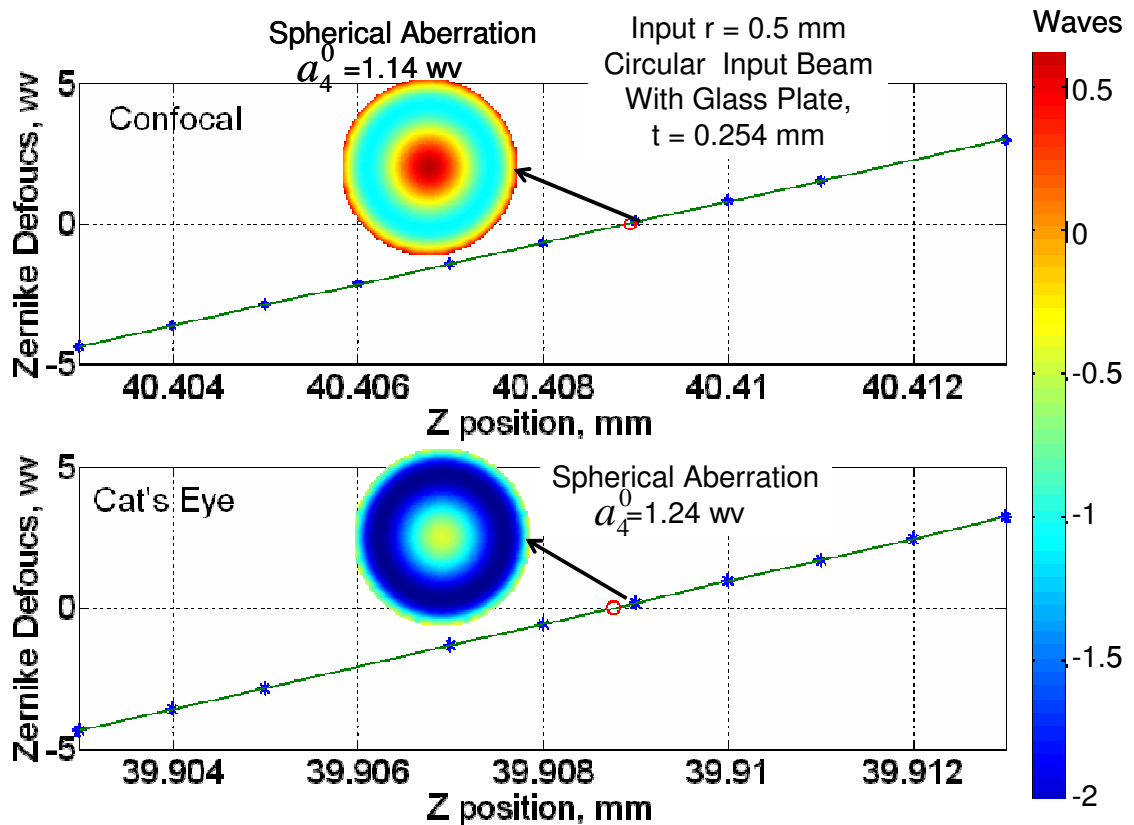


Figure 3-23: Results from a 0.5 mm input radius sphere with circular input beam with a 0.254 mm glass plate. The parabola is located to the right at 50 mm.

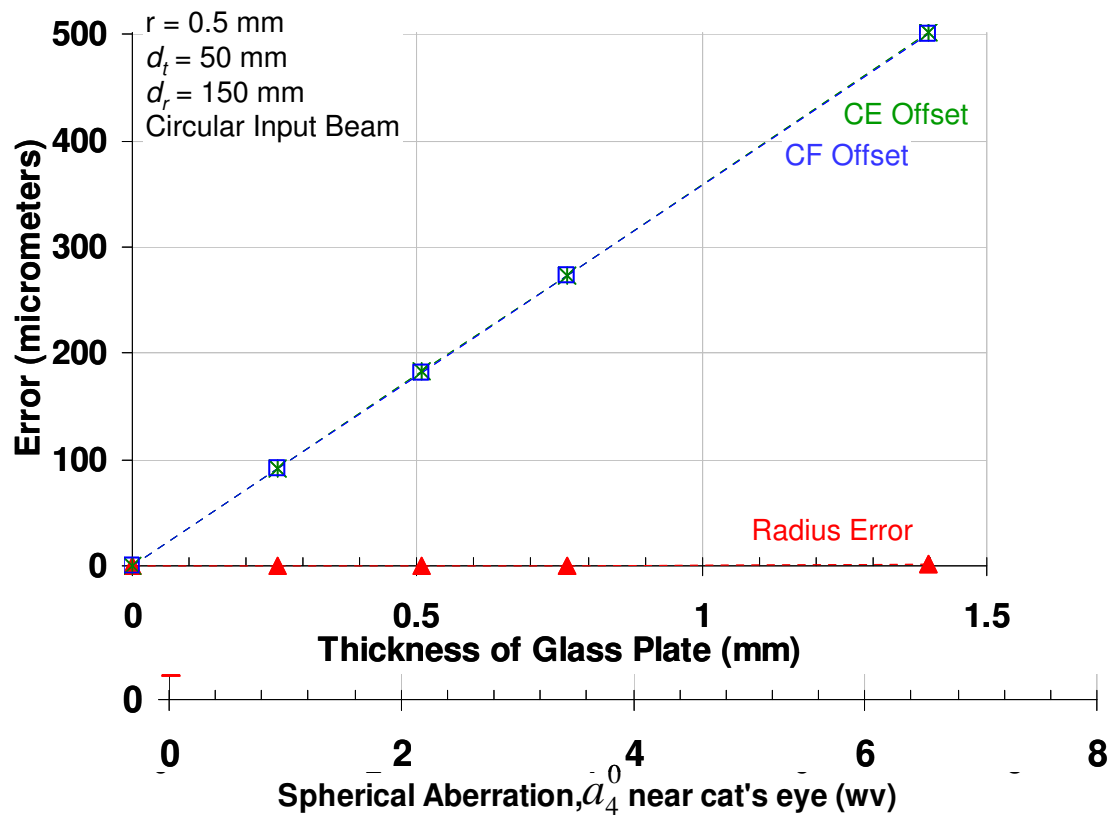


Figure 3-24: The bias in the radius measurement for varying spherical aberration for a 0.42 parabolic objective. Note that the error is now in micrometers.

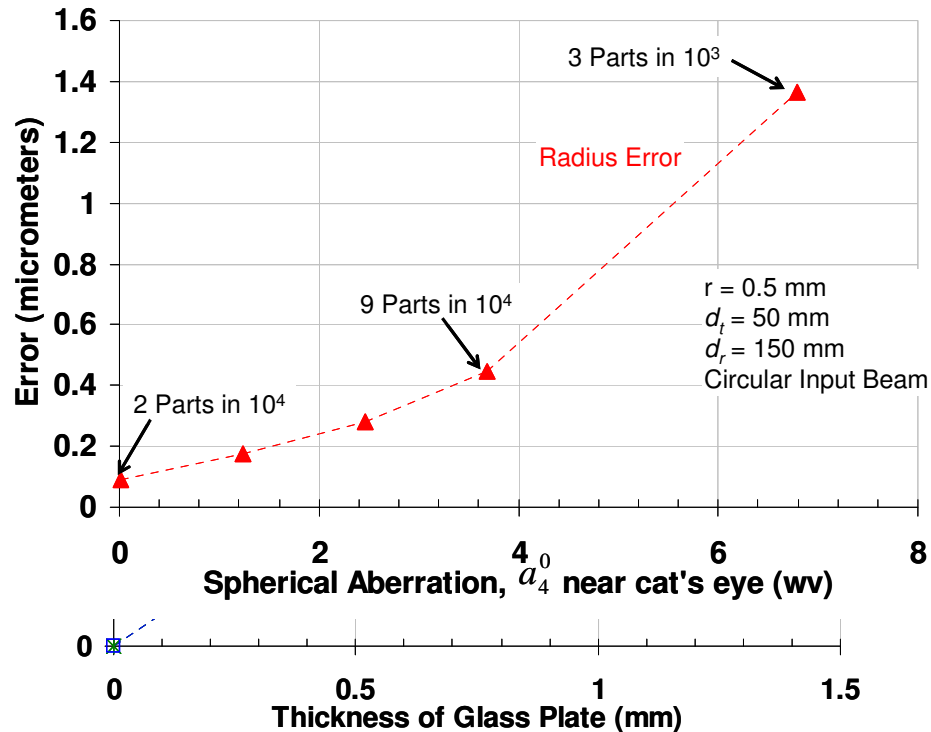


Figure 3-25: The error in radius when spherical aberration is introduced, an expanded view of Figure 3-24. Note that the error is now in micrometers.

The amount of spherical aberration per mm of glass plate is high as compared to the initial measurements shown in Chapter 4. One glass plate in experiment results in about 0.3 waves of spherical aberration for a 1 mm radius part. In FRED, one glass plate of the same thickness results in about 1.4 waves of spherical aberration (shown in Figure 3-23). The difference between the 1.4 waves and 0.3 waves can not be explained just by the different radius parts.

Two additional factors can explain this difference. The parabola in the FRED model focuses the “rays” of light in a different manner than the microscope objective will, explained in further detail in Chapter 6. In addition, the experimental data is normally masked, which will reduce the amount of spherical

aberration. I discuss the masking in Section 3.11 and Chapter 6 and the effect of the parabola in Chapter 6.

Therefore, to better compare to the experimental results, I reduced the thickness of the glass plate in the simulation for the lower spherical aberration. This is shown in Figure 3-26 and Figure 3-27. The amount of resultant aberration is much smaller for the thinner plates, as expected, and the shift is away from the objective and smaller for the thinner plates. The radius error changes very little as the thickness of the glass plate is increased over this range, from 7 parts in 10^4 to 9 parts in 10^4 . This may demonstrate that the relationship between plate thickness and amount of spherical aberration in the wavefront is not linear.

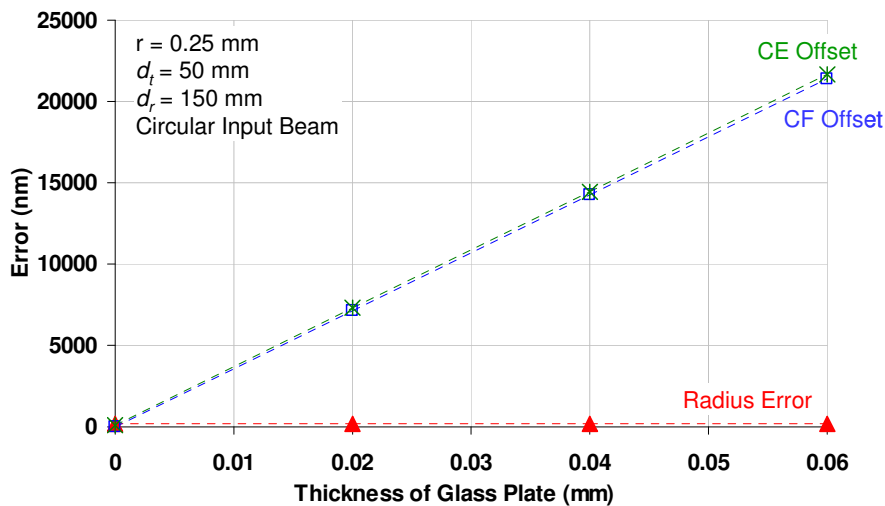


Figure 3-26: The bias in the radius measurement for varying spherical aberration for a 0.42 parabolic objective for an input radius of 0.25 mm.

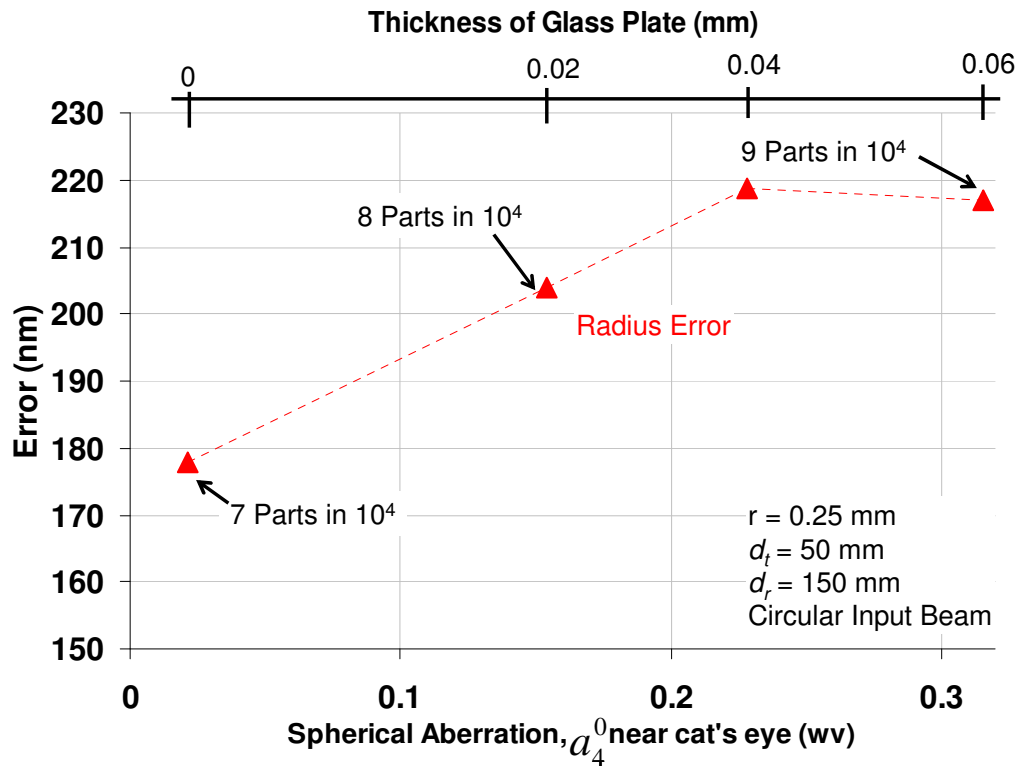


Figure 3-27: The bias in the radius measurement for varying spherical aberration for a 0.42 parabolic objective for a input radius of 0.25 mm, expansion of Figure 3-26.

3.11 Masking

The masking of the data in the experiments causes the amount of spherical aberration to drop quickly with reduced mask size. At the same time, masking causes the amount of defocus to rise. This defocus will affect the data of the defocus vs. position graph and therefore the radius. This effect is demonstrated in the Figure 3-28 and Figure 3-29. A simulated wavefront with 1 wave of spherical aberration is shown in Figure 3-29, along with the masked data and the resultant defocus term. This defocus term will cause the data to shift and therefore masking data can lead to an erroneous result. As expected, smaller amounts of aberration cause smaller effects on the defocus term. A calculation

of the amount of shift in the cat's eye and confocal positions (and therefore the radius) due to the masking is shown in Chapter 6.

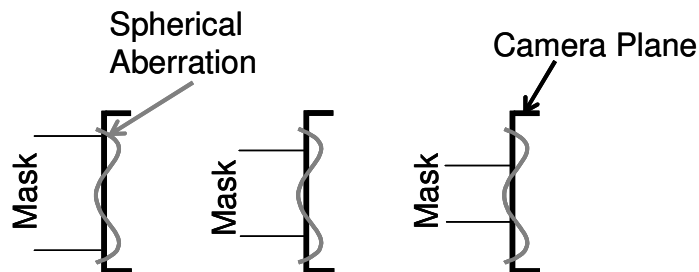


Figure 3-28: Schematic showing how mask size affects the defocus term.

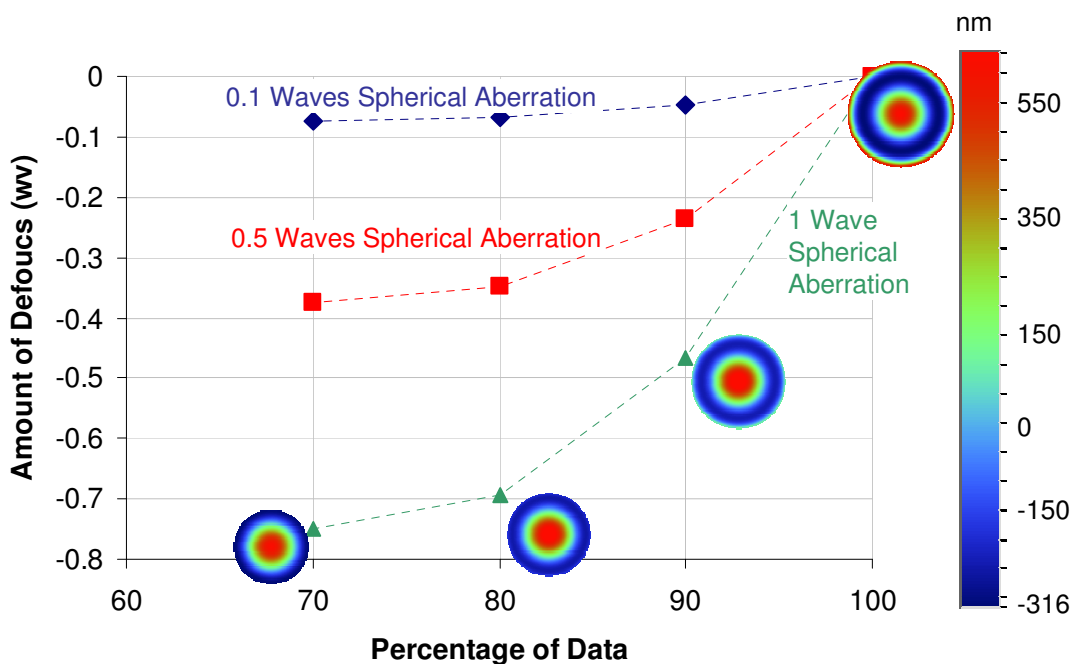


Figure 3-29: Demonstration of mask size effect of the defocus term.

In the FRED model, all of the data is captured at the detector and no masking is normally required. If the mask size is reduced, though, the error in the radius and the amount of spherical aberration is reduced as shown in Figure

3-30. This mask size reduction was done in the Matlab step of the analysis, after I imported the data and before unwrapping and fitting to Zernikes. For comparison, the amount of spherical aberration when the part is near cat's eye for the glass plate of the same thickness, 0.254 mm, is 0.0148 wv for a nominally 1 mm radius sphere. The smaller spheres have higher aberration.

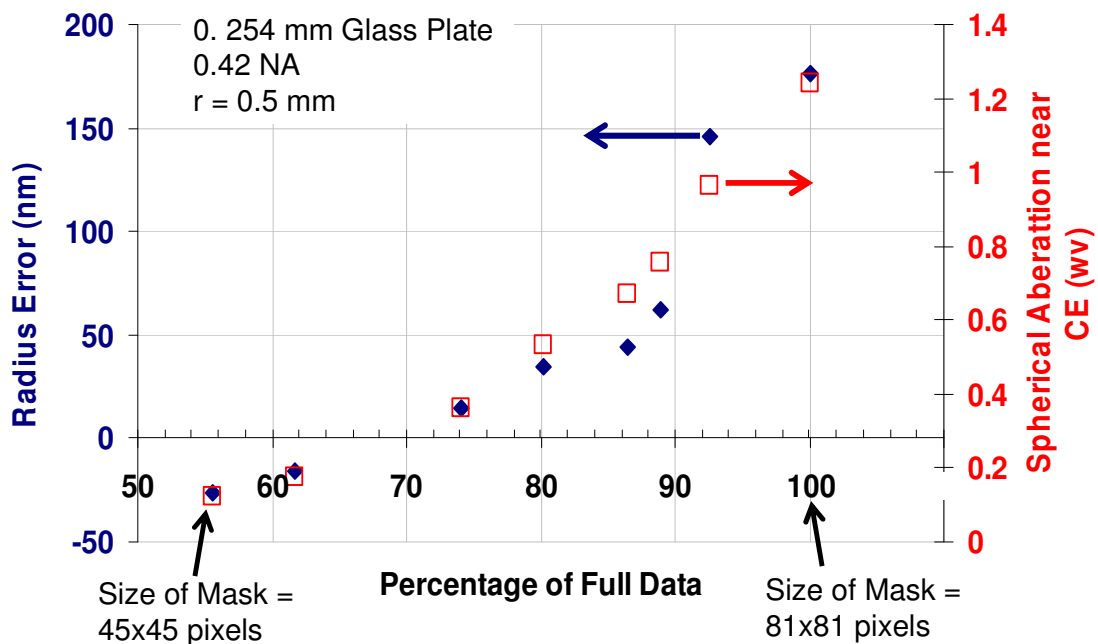


Figure 3-30: The radius error (blue diamond, left axis) and amount of spherical aberration (red square, right axis) as the mask size changes for a 0.5 mm radius sphere with a 0.254 mm thick glass plate.

But, of course I can not just reduce the mask size in the FRED data to compare to the experimental data. The number of pixels is not enough to accurately define the wavefront. The best method for comparing to simulation is to reduce the thickness of the glass plate until the desired spherical aberration is obtained.

Reducing the mask size as described here is different than the analysis described in Section 3.2.1 and Section 3.4 where varying the number of input rays and the number of pixels in the camera showed an uncertainty of ± 31 nm and ± 64 nm, respectively. In that analysis, the full wavefront on the detector was considered. Here, only a portion of the wavefront is considered.

3.12 Macro Scale Radius

I also tested a model of a macro-scale interferometer with a f/4 transmission sphere. The NA of the parabola used in the model was 0.128, the focal length 1190 mm, and the source beam diameter is 306 mm. The results for both the circular aperture input beam and the Gaussian input beam for a 25 mm input radius test part are shown in Table 3-1.

Table 3-1: Results of FRED model for a 25 mm input radius sphere.

	CF Offset (nm)	CE Offset (nm)	Radius Error (nm)	Fractional Error
Circular	-231	230	461	2 parts in 10^5
Gaussian	6	-6	-11	5 parts in 10^7

3.13 Summary of Results

3.13.1 Circular Aperture Input Beam

The results from the circular aperture input beam, without aberration, show a measured sphere larger than the input, a shift in the cat's eye position away from the objective, and a shift in the confocal position toward the objective as shown in Figure 3-31. This error increases with smaller numerical aperture and

with smaller input radius. The propagation distance has no effect on the radius and a small effect on the cat's eye and confocal positions. In general, the errors in the results from the circular aperture input beam are larger than for the Gaussian input beam.

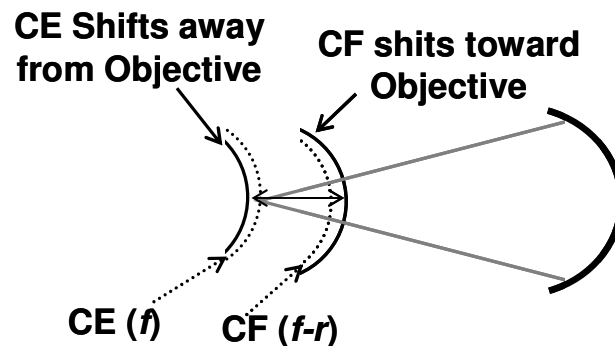


Figure 3-31: Schematic of the results from the circular aperture input beam without aberration.

When the spherical aberration is added the cat's eye and confocal positions both shift away from the objective as shown in Figure 3-32. But, because the cat's eye position shifts more than the confocal position, there is an error in the radius, leading to a measured sphere larger than the input radius. This error is quite large for the larger amount of aberration. When the spherical aberration is 0.3 waves and less, it is difficult to say divisively that the radius error changes with small increases in aberration.

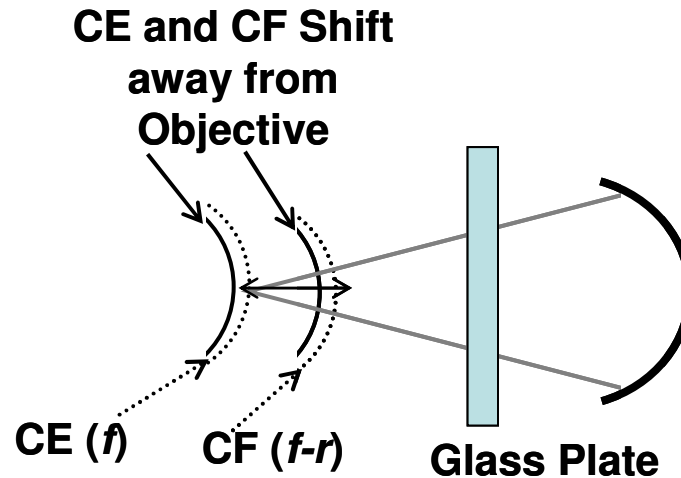


Figure 3-32: Schematic of the results from the circular aperture input beam when spherical aberration is added.

3.13.2 Gaussian Input Beam

The results from the Gaussian input beam, without aberration, show few divisive results. The results from the 0.7 NA objective have a large uncertainty due to fitting and can not be used to look for trends. The remaining errors are small, but, in general, the measured sphere is larger than the input, the shift in the cat's eye position is away from the objective, and the shift in the confocal position is toward the objective as shown in Figure 3-31. Varying the propagation distance has virtually no effect on the error.

3.14 Uncertainty

Although the author of FRED enthusiastically supported the ability of FRED to simulate the cat's eye reflection in early conversation [33, 36], I certainly expect the model assumptions to be challenged near the focal region, sometimes called the caustic. Near the caustic the rays are not normal to the wavefront and the "phase go[es] astray" [37]. This is even the case for the non-aberrated

wavefront. The analysis of the wave field has errors. A recent publication summarized the situation well; “For example, the analysis of a wave field that has a caustic at a curved interface between different media remains a significant challenge...We are unaware of any existing ray-based models that can analyze such cases” [37]. The curved interface described here is the test part in a radius measurement. In an attempt to fix this problem, Forbes and Alonso [37] propose modifying the Gaussian beamlets source in the optical modeling software (such as FRED) as follows.

The wave field in the caustic region in FRED varies with the number of input rays as shown by an error in radius (Section 3.2.1). In FRED, the parameters of the each ray, or beamlet, are fixed for all the rays in a single source. These parameters describe the size of the beamlet, how fast it spreads, and the overlap between beamlets. The new method [37, 38] determines the optimum beamlet parameters across the source so that the wave field at the caustic becomes insensitive to the parameter values. In other words, the simulation will not be realistic if the results depend on simulation parameters to like beamlet size and density. This approach reduces the uncertainty in the wave field in the caustic region, but does not yet completely solve the curved surface problem. This method for optical modeling is obviously outside the scope of this work, but is introduced here to demonstrate the errors in FRED and as a direction for future study.

The model break down is also demonstrated as described in Section 3.8.2. The FRED model must meet the same constraint as the Gaussian model, that is,

the field can not vary too fast. In the Gaussian model, the constraint applied to the whole beam diameter. In the FRED model, with the circular input beam, the constraint applies to each Gaussian beamlet. The beamlets do not vary as fast as the whole beam diameter, and therefore the FRED model meets this criterion for beams with larger NAs (other errors persist, though). Future work could include a detailed calculation to check where the beamlets vary too fast and therefore, where the FRED model breaks down based on the slowly varying criterion.

The model break down is partially demonstrated by the uncertainty fitting of the defocus vs. position graph. This uncertainty is also caused by other errors, like errors in the unwrapping algorithm, the pixel nature of the camera (the Zernike analysis would prefer a continuous function), errors in the Zernike fitting algorithm. The uncertainty in the radius due to the fit for the circular aperture input beam varied in the range of ± 20 nm to ± 40 nm for most cases, but increased to ± 190 nm for the 0.7 NA objective. The uncertainty in the radius due to the fit for single Gaussian input beam varied in the range of ± 40 nm to ± 70 nm for most cases, but increased to ± 500 nm for the 0.7 NA objective. The high uncertainty at 0.7 NA demonstrates the model break down. The uncertainty in the fit for the 25 mm part is ± 1 nm or less, suggesting a correlation between small radii and a greater chance of the model breaking down, as expected. For the small radii parts, the size of the caustic region is large compared to the size of the test part.

A source of uncertainty in the FRED model is choosing the number of input ray beamlets and the number of pixels in the camera. These choices lead to an uncertainty of ± 31 nm (source) and ± 64 nm (detector) in the output radius.

I used a simple root sum square method to combine these three sources of uncertainty, ± 40 nm from fitting, ± 31 from the source, and ± 63 nm from the detector. The uncertainty in the radius from the FRED model is estimated as ± 81 nm. The uncertainty of ± 81 is 8 parts in 10^5 for a 1 mm radius part, 2 parts in 10^4 for a 0.5 mm radius part, and 3 parts in 10^4 for a 0.25 mm radius part. Because this uncertainty is large, it is unlikely that FRED can be used to correct for biases not considered in the geometric model with high precision. FRED can still be used to look for trends.

The comparison between the results of the FRED model, the Gaussian model from Chapter 2, and the experimental results is in Chapter 6.

CHAPTER 4: EXPERIMENTAL VERIFICATION ON MORTI

4.1 Introduction

The Micro-Optic Reflection and Transmission Interferometer, MORTI, is located in a temperature controlled metrology lab in the Cameron Applied Research Center at the University of North Carolina at Charlotte. The operating wavelength of the interferometer is helium-neon, 632.8 nm. MORTI operates in either reflection mode (as a Twyman-Green interferometer) or transmission mode (as a Mach-Zehner interferometer). In reflection mode, the user can measure the radius and figure error of micro-optic continuous relief refractive surfaces. In transmission mode, the user can measure the back focal length and transmitted wavefront measurements of micro-optic refractive surfaces. This work focuses on the radius measurement of spheres in the reflection mode.

Throughout this description of MORTI, the z axis is the axis that the light travels and x-y is the plane perpendicular to this axis. These axes change (with respect to gravity) as the light travels through the system.

MORTI is built on the Mitutoyo microscope base with the following modifications, shown in Figure 4-1. Replacing the top of the microscope is a large metal spacer and a breadboard. This breadboard holds the collimating optics, the reference mirror, and the imaging optics of the reflection mode. A 25 mm diameter hole is located in the breadboard to allow light to travel down to the

microscope objectives. On top of the breadboard is the trinocular head from the original microscope affixed with bases to elevate it over the hole in the breadboard. This trinocular head is used to view the test part by eye.

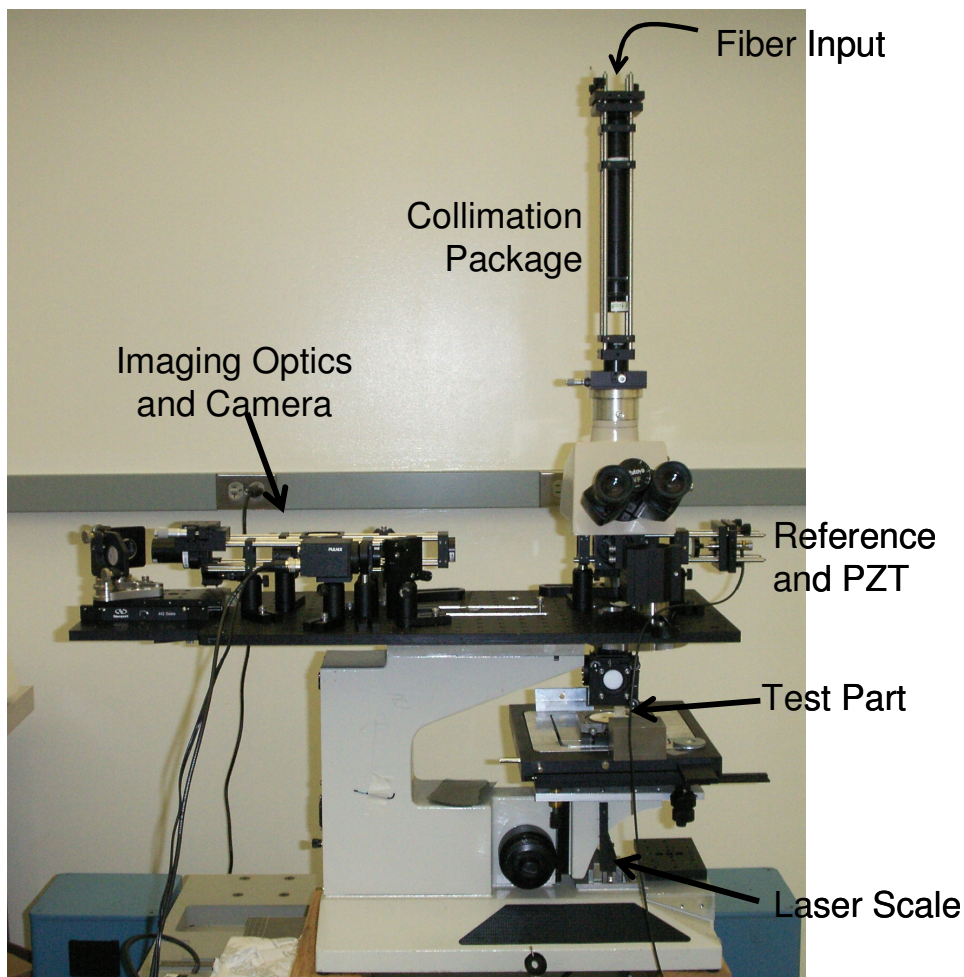


Figure 4-1: The Micro-Optic Reflection and Transmission Interferometer.

The fixture holding the microscope objectives is attached to the bottom of the breadboard and is shown Figure 4-1. This fixture was original to the microscope has space for four objectives and rotates to change objectives. Below the objectives, there is a tip/tilt adjustment to the existing x-y translation

measurement stage. At the base of the measurement stage, there are two fixtures to hold the displacement scale, a Sony laser scale.

4.2 Setup of MORTI for Reflection Measurements

Light from the 5 mW He-Ne laser is coupled into a single mode fiber where it passes to the collimating leg. A fixture to hold the fiber end, a microscope objective to collimate the light, and two lenses to expand the beam to 8 mm diameter are located in this collimating lens tube. This collimating leg is attached to a tip/tilt stage which is fixed on four metal rods. The tube passes through the middle of the rods. The rods are fixed on to an x-y translation stage which is attached to the body of the microscope through the trinocular head.

After the light passes through the collimating lens tube and through the hole in the x-y translation stage, it passes through a beamsplitter. This beam splitter is held in a tip/tilt stage in a cube. Also attached on this cube is the reference mirror (affixed to a PZT transducer) through four rods. The cube is attached to the breadboard using two bases. The light is split by the beamsplitter where half travels to the reference mirror and half travels below the breadboard through the microscope objective to measurement stage where the test optic is placed.

After reflection from the test optic and the reference mirror, the light is added at the beamsplitter and is redirected to the imaging leg. The imaging leg has two afocal systems designed to relay the image of the test optic to the camera. The afocal systems used here are two lenses spaced at a distance equal to the sum of the two focal lengths. The design of this system follows. A z-translation stage is located between afocal system one and afocal system two.

This translation stage allows for focusing on parts of different sizes. After the light passes through afocal system two, it is reflected from two plane mirrors. These mirrors are used to direct the light to the Pulnix CCD camera through a wavelength (632.8 nm) banded filter. The schematic in Figure 4-2 shows the imaging leg of the MORTI.

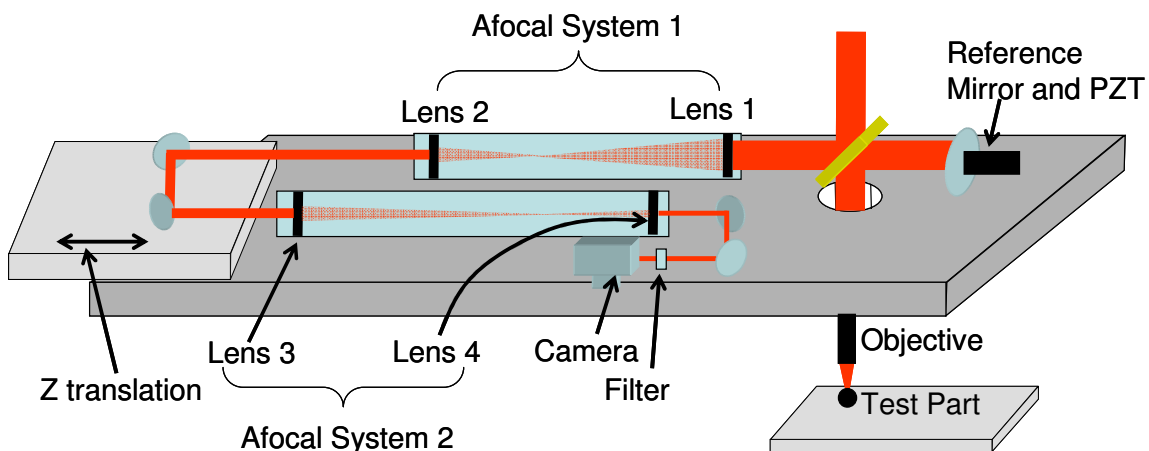


Figure 4-2: Schematic of MORTI in reflection mode. Note that the trinocular head and collimating lens tube are not shown here but are mounted about the hole in the breadboard.

4.2.1 Design of Imaging Leg

The imaging optics must meet the following requirements; at confocal, the image of the test part surface must be located at the camera plane and the size of that image must fill (but not overflow) the camera array. The parameters that are adjusted to achieve these requirements are the focal lengths of the lenses, the distance between the objective and Lens 1, the distance between lens 2 and lens 3, and the distance between lens 4 and the camera. The parameters that can not be varied are the distance between lens 1 and lens 2 and the distance

between lens 3 and lens 4 as these are the afocal systems and must be spaced at the sum of the focal lengths.

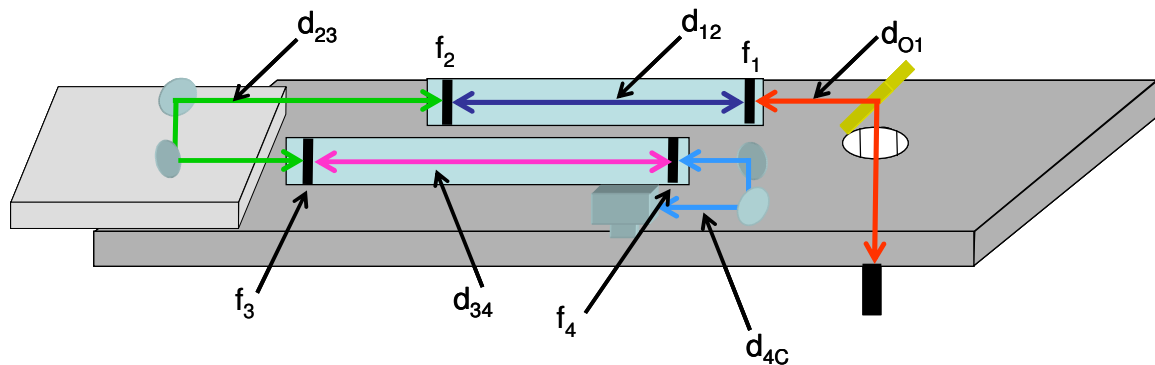


Figure 4-3: The imaging leg of MORTI showing the distances involved. Figure 4-2 shows the label of the components.

I will not describe the complete methodology for designing the imaging leg here, as it was a long iterative process among many people. The process did involve testing various lenses and distances while trying to fit the system within the physical constraints defined by the breadboard. A perfect system was not possible for all the microscope objectives for the full range of radii. The current system is optimal for the 0.42 NA objective, but measurements are still possible for the other objectives. The next iteration of MORTI will include a redesign of the imaging system to improve this.

The lenses in the imaging system are achromatic lenses and are anti-reflection coated. The distances and focal lengths of the system are:

- $d_{O1} = 310$ mm, distance from the objective to lens 1,
- $d_{12} = 350$ mm, distance from lens 1 to lens 2,
- d_{23} , distance from lens 2 to lens 3 (ranges from 150 mm to 400 mm),

- $d_{34} = 205.6$ mm, distance from lens 3 to lens 4,
- $d_{4C} = 130$ mm, distance from lens 4 to the camera,
- f_O , focal length of the objective (10 mm for the 0.42 NA objective),
- $f_1 = 250$ mm, focal length of lens 1,
- $f_2 = 100$ mm, focal length of lens 2,
- $f_3 = 75.6$ mm, focal length of lens 3, and
- $f_4 = 130$ mm, focal length of lens 4.

The next step is to determine what d_{23} should be for the various nominal test part radii. This is done using the imaging equations, where s_o indicates the location of the test part relative to the objective lens. The part is located at the confocal position,

$$s_o = f_o - r,$$

Equation 4-1

where f_o is the focal length of the objective and r is the nominal part radius. The location of the image of the test object through the objective is s_o' and is found from

$$\frac{1}{s_o} + \frac{1}{s_o'} = \frac{1}{f_o}.$$

Equation 4-2

This image is then relayed through lens 1 and lens 2 using

$$\begin{aligned}
 s_1 &= d_{01} - s_o' \\
 \frac{1}{s_1} + \frac{1}{s_1'} &= \frac{1}{f_1} \\
 s_2 &= d_{12} - s_1' \\
 \frac{1}{s_2} + \frac{1}{s_2'} &= \frac{1}{f_2}
 \end{aligned}$$

Equation 4-3

The image is next relayed through lens 3 and lens 4, but the distance d_{23} is unknown. To solve for d_{23} , I worked backwards, starting by setting d_{4C} equal to s_4' . This states that the final image is located on the camera plane. From here s_3' is solved for using

$$\begin{aligned}
 d_{4C} &= s_4' \\
 \frac{1}{s_4} + \frac{1}{s_4'} &= \frac{1}{f_4} \\
 s_4 &= d_{34} - s_3'
 \end{aligned}$$

Equation 4-4

Then, s_3 is found and d_{23} easily calculated using

$$\begin{aligned}
 \frac{1}{s_3} + \frac{1}{s_3'} &= \frac{1}{f_3} \\
 d_{23} &= s_3 + s_2'
 \end{aligned}$$

Equation 4-5

The distance d_{23} for a range of radii of test part and for a range of objective lenses is shown in Figure 4-4. I will use this chart when taking measurements on MORTI to help with focusing. Figure 4-4 which will give a starting point for the distance d_{23} .

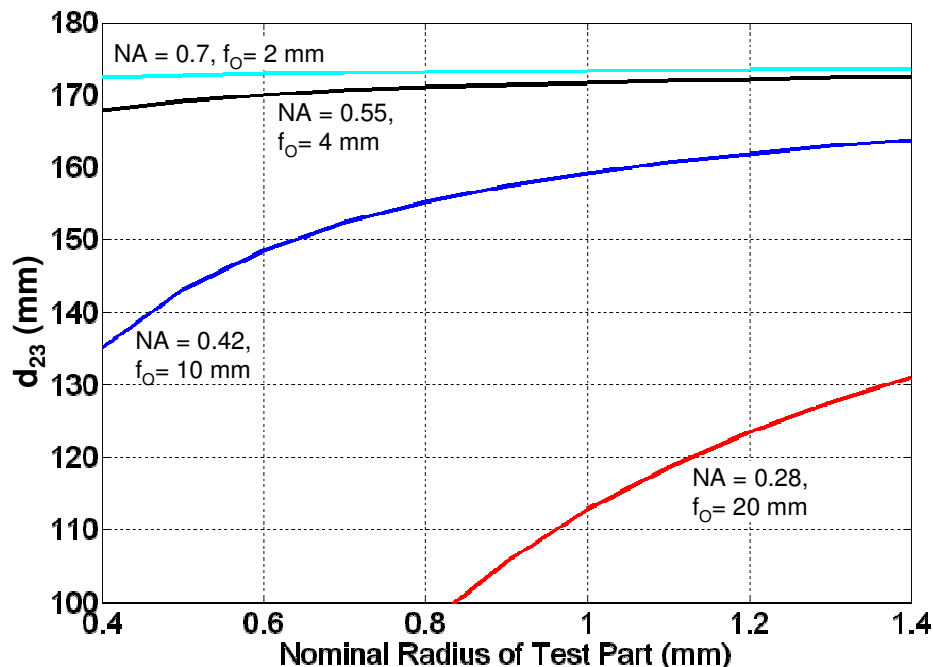


Figure 4-4: The distance between lens 2 and lens 3 for various part radii and objectives.

Figure 4-4 is only a starting point for focusing on the part surface when at confocal. Because this graph is not exact, fine tuning of d_{23} by eye is required. This is because the interferometer does not exactly correspond to the equations and numbers used to calculate d_{23} . There are multiple reasons for this deviation. I measured the distances on the interferometer base using a simple ruler, likely to within 5 mm. I did not measure the focal lengths of the lenses; I used the values from the manufacturer. Equation 4-1 through Equation 4-5 approximates all the lenses as thin lenses, which is not the case, especially for the microscope objective. Because Figure 4-4 is used a starting point only and the focusing is done by eye, these approximations are acceptable.

The afocal systems were set up on the Veeco Interferometer by checking the retro-reflection from an optical flat to determine when the lenses two focal are lengths apart.

4.3 Alignment of the Scale

A Sony Laser Scale model BS77 is used to measure the distance the stage moves in the vertical z-axis. The scale consists of two parts, a reader, and the glass scale, and works on the principle of a diffraction grating scan. An electronics board processes the signal from the reader to in an A/B quadrature manner.

The scale was attached so the glass scale is coincident with the optical axis to reduce the Abbe error. The glass scale is attached to the bottom of the stage by steel rods and the reader is attached to the microscope base by an aluminum fixture as shown in Figure 4-5.

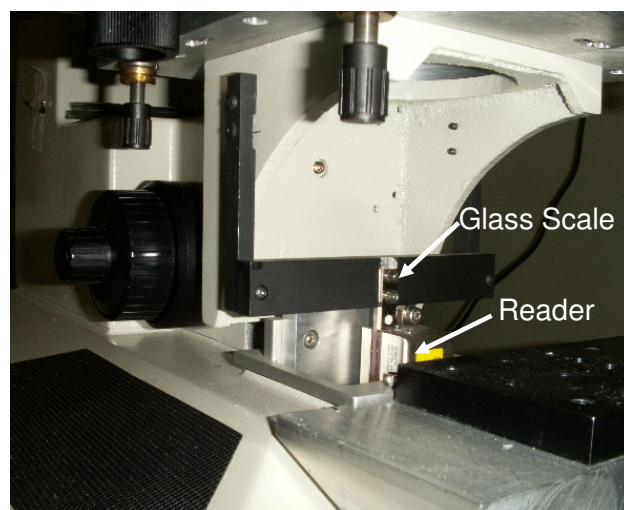


Figure 4-5: Picture of Sony Laser scale.

The alignment of the scale and the reader relative to each other is critical in spacing and angle. To make this alignment easier, small springs were placed over the screws that attach the glass scale to the steel rod and also the reader to the aluminum fixture. By rotating these screws either together or separately the spacing and the angle between the glass scale and reader can be adjusted with fine precision. First, through, the initial alignment is done by eye. The reader is attached to the aluminum fixture and then the glass scale is fixed to the steel rods such that the glass scale is centered in the reader and appears to be parallel to the reader. The use of additional springs does not observably compromise the alignment stability.

For the final alignment, the sine, cosine, and ground signals are picked off from the electronics box and feed into an oscilloscope. On the oscilloscope, the sine and cosine signals are plotted versus one another, a Lissajous plot, which is a circular plot. The diameter of this circle indicates the alignment of the glass scale to the reader. For optimal alignment, the diameter must be near 0.5 V in diameter. The screws on the glass scale and reader are adjusted until the circle grows in size and stays large for the entire range of the scale, approximately 8 mm. This alignment can easily be checked on the oscilloscope during measurements.

4.4 Alignment of MORTI and Calibration of the Scale

The following section describes the alignment of the interferometer and the calibration of the scale. MORTI is unusual in that the calibration of the scale

does not rely on a calibration artifact, but instead uses a displacement measuring interferometer (DMI) for the length calibration.

4.4.1 Mechanical Alignment

The first step is to define the absolute reference axes (X_{abs} , Y_{abs} , and Z_{abs}). A beamsplitter is glued on to a reference optical flat which will be used to define the axes. The alignment between the beamsplitter face and optical flat was checked on a CMM for a 90° angle. The optical flat is located in a fixture shown in Figure 4-6 that allows for course and fine rotation of the beamsplitter in the x-y plane. The fixture is first coarsely rotated to align the edge of the beam splitter to the x-y axes by eye. Then an indicator is placed on the x-face of the beamsplitter. The stage is moved in the y-direction and the motion of the indicator needle is recorded. The fixture is then finely rotated to reduce the amount the indicator needle moves as the stage is moved in the y-direction. The process is repeated with the indicator on the y-face and the motion in the x-direction. The final alignment shows an approximate $5 \mu\text{m}$ error over the 10 mm length of the beamsplitter, an error of 0.5 millirad (1.7 arcmin). The X_{abs} and Y_{abs} are now defined by the edge of the beamsplitter.

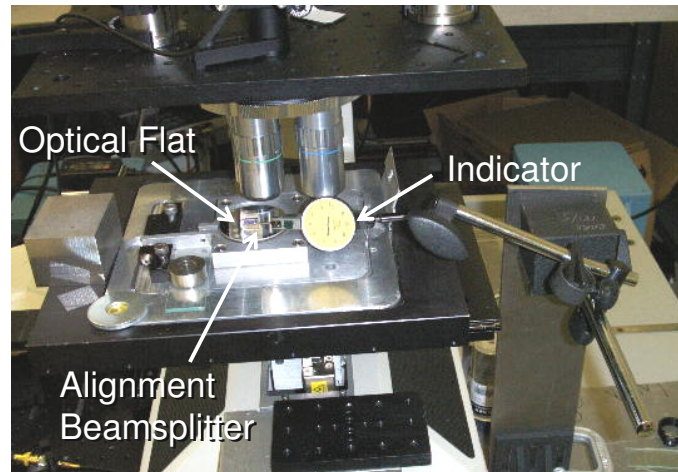


Figure 4-6: Picture of the optical flat, beamsplitter, and indicator used for alignment purposes.

Next, the indicator is placed on the x-face and the stage is moved in the z-direction and the indicator needle was observed. The stage tip/tilt is adjusted to reduce the indicator needle motion. The process is then repeated with the indicator on the y-face and the motion in the z-direction. The Z_{abs} is now defined as perpendicular to the reference optical flat.

4.4.2 Alignment of DMI

Next, the HP 5528 Displacement Measuring Interferometer (DMI) is set up. The DMI and an imaging interferometer are on a breadboard located above MORTI on a tripod as shown in Figure 4-7 and Figure 4-8. The HP laserhead is set in the “straightness” mode because the beam is not offset as with typical DMI measurements. The imaging interferometer (II) on the breadboard consists of a beamsplitter that allows 96% of the DMI light through and 4% is reflected to the II reference mirror. The test arm of this imaging interferometer is redirected down by the fold mirror. The fold mirror has tip/tilt adjustments and is on a stage for

motion in the direction shown in Figure 4-7. After the beam travels through the hole in MORTI's breadboard, it passes through the DMI polarizing beamsplitter where the two modes of the DMI beam are split to the DMI reference mirror and the optical flat. The DMI polarizing beamsplitter and reference mirror are in a fixture that is held in the microscope objective holder. This fixture allows for tip/tilt of the reference mirror and tip/tilt and rotation of the beamsplitter and is shown in Figure 4-9.

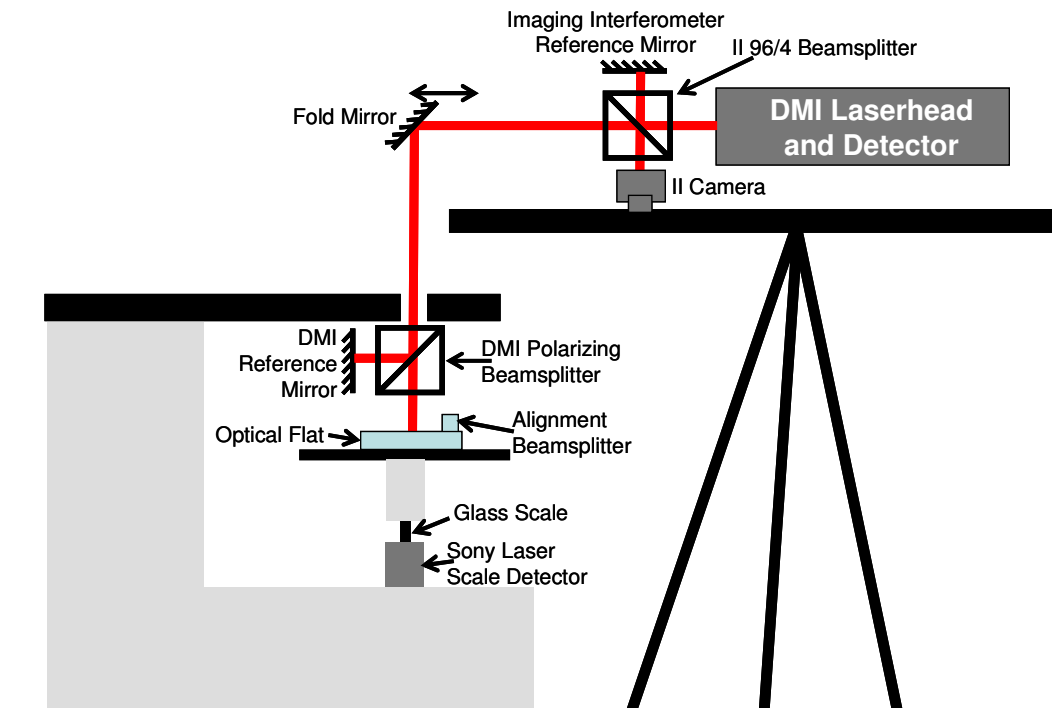


Figure 4-7: Schematic of the DMI alignment.

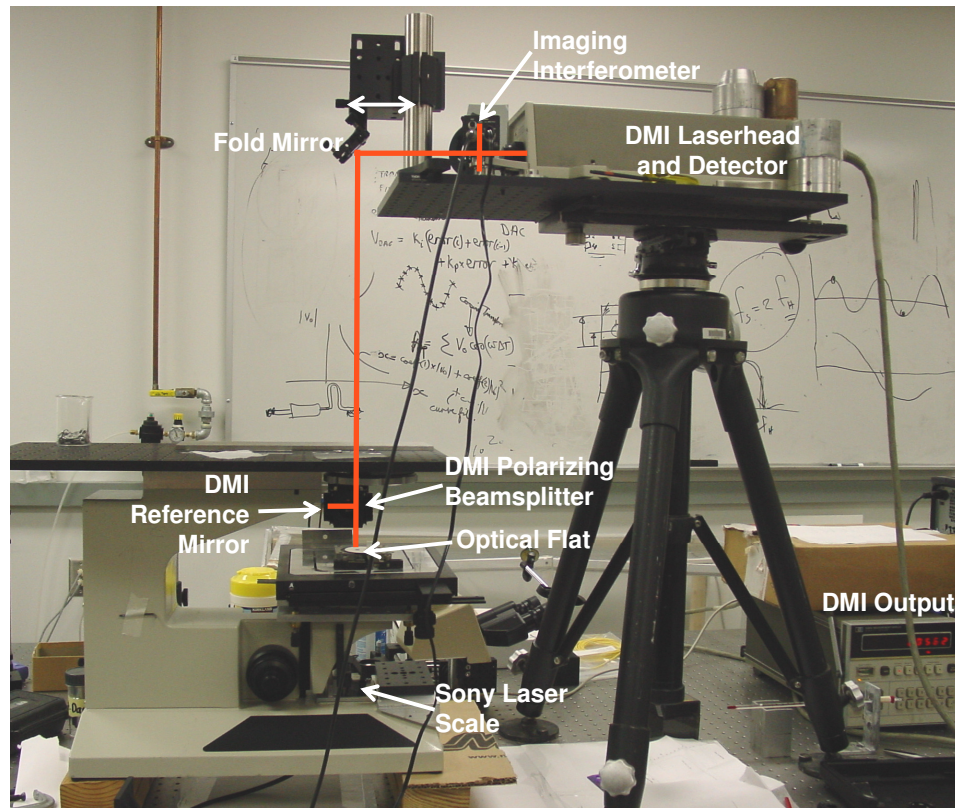


Figure 4-8: Picture of the DMI.

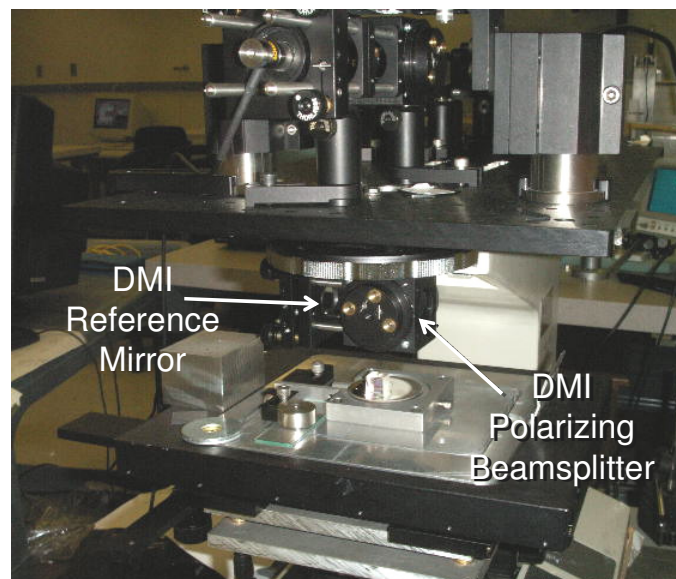


Figure 4-9: Picture of DMI Interferometer showing polarizing beamsplitter and DMI reference mirror.

The DMI must be aligned such that it is parallel with the motion axis. Because the optical flat is aligned perpendicular to the motion axis, the DMI can be aligned perpendicular to the optical flat and will therefore be parallel to the motion axis. The imaging interferometer is used to perform this alignment. The beam is coarsely aligned by moving the tripod and DMI laserhead such that the beam passes to the imaging interferometer beamsplitter. Four percent of the light passes to the imaging interferometer reference mirror, reflects, and then passes through the beamsplitter to the camera. The remaining 96% of the light passes through the beamsplitter, reflects from the fold mirror, passes through the hole in the breadboard, and through the DMI polarizing beamsplitter. A corner cube retroreflector is placed over the optical flat to align the imaging interferometer reference mirror. The beam then reflects from this retroreflector and travels back to the imaging interferometer camera. The tip and tilt of the imaging interferometer reference mirror is adjusted to remove the fringes between the two beams.

The next step is to align the DMI beam perpendicular to the optical flat. The retroreflector (which was sitting on the optical flat) is removed and the DMI reference mirror is blocked using a piece of paper. An interference pattern between two beams is formed at the imaging interferometer camera: 1) the 96% intensity beam that reflects from the optical flat and 2) the 4% intensity beam that reflects from the imaging interferometer reference mirror. The fringe pattern is nulled by adjusting the tip/tilt of the fold mirror which simulates adjusting the tip/tilt of the entire DMI breadboard. The beam that returns from the

optical flat must also return into the DMI laserhead. This is done by adjusting translation on the fold mirror and the DMI tripod. This translation is alternating with the tip/tilt adjustment until the fringe pattern is nulled and the beam returns into the DMI laserhead. Now the DMI beam is perpendicular to the optical flat.

4.4.3 Calibration of Scale

Next, the Sony Laser scale model is calibrated using the DMI. The imaging interferometer reference mirror is blocked during this step. The DMI polarizing beamsplitter must be adjusted to provide the optimum splitting of the beam. First one mode of the laser is blocked using a polarizer and the beam splitter is rotated in the turret until the beam to the optical flat is bright and the beam to the DMI reference mirror is dark. Then the other mode of the laser is blocked by rotating the polarizer 90° and the beam to the optical flat should be dark and the beam to the DMI reference mirror should be bright. When the rotation of the polarizing beamsplitter is adjusted as best as possible, the beam to the optical flat is blocked using paper, and the DMI reference mirror is adjusted using tip/tilt so the return beam returns into the DMI laserhead. The beam to the optical flat is unblocked. At this point, DMI should register a reading as the stage (holding the optical flat) moves in the z-direction. However, it is likely that fine tuning of the DMI polarizing beamsplitter is required. This is done by rotating and adjusting the tip/tilt of the beamsplitter. When this adjustment is correct, the DMI will register a reading throughout the travel range (approximately 6 mm).

Now that the DMI and the Sony laser scale are both aligned, the scale can be calibrated. This was done by moving the stage in the z-direction and

recording the reading from the DMI output and the edisplay software (laser scale). This was repeated multiple times traveling up and down in varying step sizes. The data for this calibration is shown in Appendix C. The calibration factor is 0.8621535 in mm/edisplay unit.

The laser scale is now calibrated and the DMI breadboard and the DMI interferometer are removed so the interferometer can be set up.

4.5 Alignment of Twyman-Green Interferometer

4.5.1 Input Beam and Beamsplitter

The input beam is first collimated using a shear plate and the Veeco Interferometer. The collimation package includes a fixture to hold the fiber, a 10x microscope objective to collimate the light, and two lenses to expand the beam to 8 mm diameter. The spacing of these components is critical. The fiber tip is spaced at the microscope objective's focal length. For expansion, the two lenses are placed at a distance equal to the sum of the two focal lengths. The spacing between the two lenses is done using the Veeco Interferometer with a return flat. The microscope objective is then added. The fiber is then attached to the tube. With the laser on and light traveling through the fiber, a shear plate is placed on the other end of the tube (on the opposite side of lenses). The fiber holder is then moved relative to the microscope objective until the pattern on the shear plate is nulled. The components are then fixed with superglue.

Before the collimation package can be placed on the interferometer, the trinocular head must be placed on the breadboard as shown in Figure 4-10. The head was modified with legs so that it sits above the bread board and has x-y

stage and fixture to hold the collimation package. The hole in the trinocular head was placed above the hole on the breadboard. The collimation package is then attached to the trinocular head. With the laser on, the position of the trinocular head is adjusted such that the light travels through the center of the hole in the breadboard.

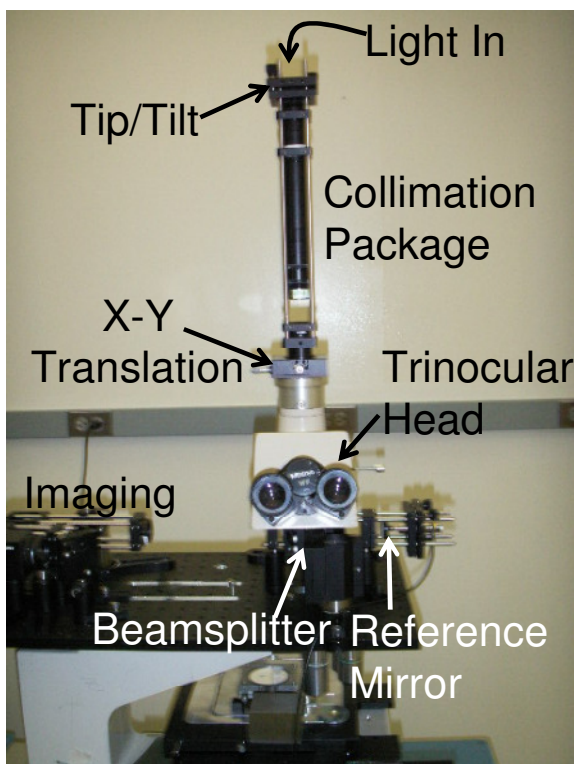


Figure 4-10: Picture of trinocular head and collimation package.

Between the trinocular head and the breadboard is the beamsplitter and reference mirror. For this part of the alignment, the reference mirror is replaced with a cornercube retro-reflector. The beamsplitter is aligned so that the test beam passes through the beamsplitter to the optical flat. The reference beam reflects from a retroreflector. The interference pattern between the two beams

travels to the fold mirror assembly (located on a z-translation stage) and then to the camera. At this point, the imaging lenses are not in the system. The fold mirror assembly was aligned on the Veeco interferometer such that the two mirrors are 45° to the axis of motion of the z-translation stage. The camera is also placed on the breadboard.

The input beam (from the collimation package) is next aligned such that it is perpendicular to the optical flat. This alignment is done by adjusting the tip/tilt and the x-y translation of the collimation package. This is an iterative process and may require moving the trinocular head if the translation stage goes out of range. This alignment is easier with a smaller input, accomplished by closing the aperture at the base of the collimation package.

The two spots that must be aligned are from the corner cube and from the optical flat. First the two spots are aligned coincident immediately after the beamsplitter (as viewed on paper) using the x-y translation. Then the tip/tilt is adjusted so the spots are coincident on the camera, approximately 1000 mm from the beamsplitter. Then the spots are again checked close to the beamsplitter, with an x-y translation if required. And then, the tip/tilt is adjusted if required to null the fringe pattern between the two spots on the camera.

After this alignment is complete, the rotation of the beamsplitter and the rotation of the z-translation stage (fold mirrors) needs to be checked. The beam that travels from the beamsplitter to the camera should not change height. This can be checked using a ruler and changing the rotation of the beamsplitter if required, while making sure the reference beam still hits the retroreflector. The

rotation of the z-translation stage is checked by moving the stage and observing the fringe pattern on the screen. A very small spot is best here. If the spot moves left/right on the screen as the stage translates, the rotation must be changed using the screws that attach the stage to the breadboard. When the spot doesn't move on the screen as the stage translates, the alignment is correct.

After the beamsplitter and translation stage alignment, the alignment of the collimation package should be checked again using the same method as before, the two spots overlap close to the beamsplitter and form a null fringe pattern at the camera.

4.5.2 Reference Mirror

The next step is to align the reference mirror. The retro-reflector is removed, and the reference mirror with attached PZT is placed on the rods as shown in Figure 4-11. The reference mirror is mounted on a tip/tilt stage. This tip/tilt is adjusted to align the reference mirror to the optical flat by nulling the fringe pattern on the camera.

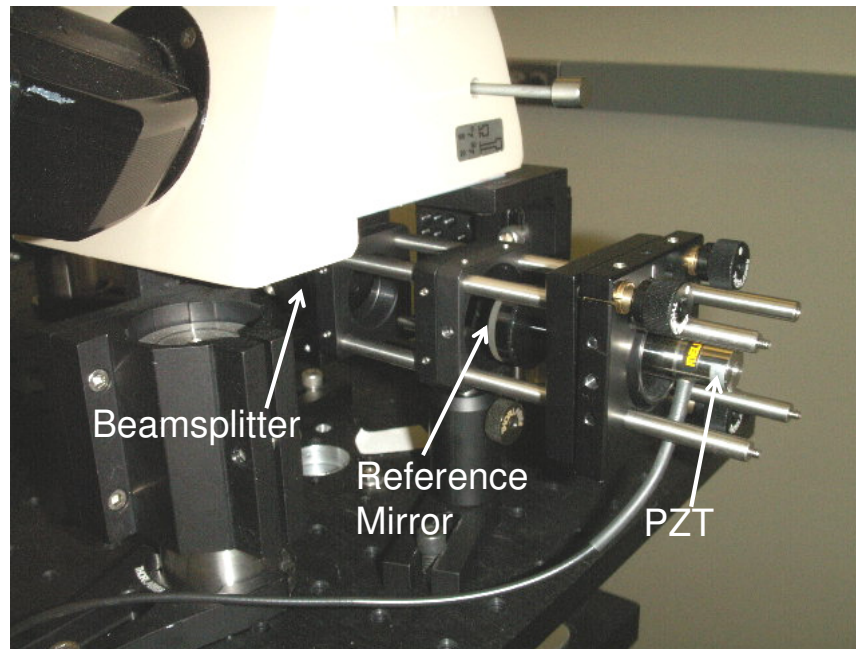


Figure 4-11: Picture of the reference mirror with attached PZT.

4.5.3 Objective Lens

After the reference mirror is aligned, the objective is rotated into place and a cat's eye reflection is obtained from the optical flat. The objective lenses are shown in Figure 4-6. The output of the objective lens is checked to be certain that the input aperture of the objective is overfilled. If not, the fixture that holds the objective lenses can be moved slightly. The reference mirror might need adjustment because the objective is not perfectly aligned to the microscope body. This adjustment is required to remove any tilt fringes at the cat's eye position.

4.5.4 Imaging Optics

The final step in assembling MORTI is the imaging optics. The optics are first setup using the Veeco Interferometer using two afocal systems as described in Section 4.2.1. The z-spacing of the lenses in the afocal systems are fixed.

The two afocal systems are placed on the breadboard in their required positions (as measured with a ruler) as shown in Figure 4-12. The x-y position of the two afocal systems must be adjusted to achieve the proper height off the breadboard and to center the beam in the lenses. An alignment tool (shown in Figure 4-12), which is sized for the cage system used, makes the alignment easier.

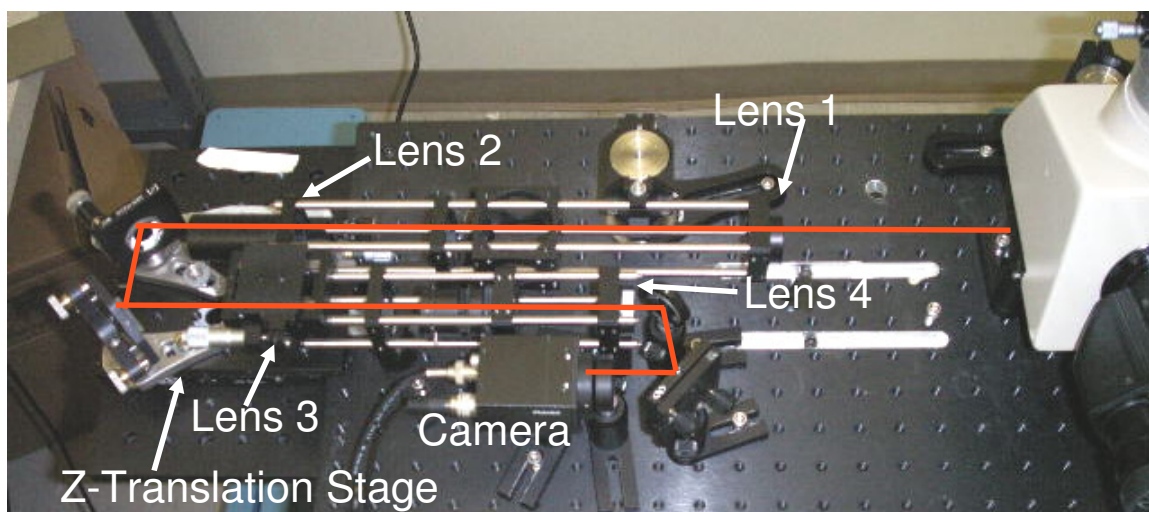


Figure 4-12: Picture of imaging optics.

4.6 The Focusing Effect

There was an interesting effect observed while setting up the interferometer. As the optical flat moved through cat's eye, a circular fringe interference pattern and a bright spot appeared on the camera unexpectedly. I will show that this effect is inherent in all interferometers, but is very prominent in micro-interferometers. It will not affect the measurement to first order with careful planning.

4.6.1 Demonstration of the Focusing Issue

I aligned the interferometer as described in Section 4.5 above, without the imaging leg in. The light from the beamsplitter traveled directly to the focusing fold mirror assembly to the fold mirrors that directed the beam onto the camera. Using the 0.42 NA objective, I positioned the optical flat at cat's eye. The schematic of this is shown in Figure 4-13 where f is the focal length of the objective and d_{OC} indicates the distance that the light travels from the objective, through the beam splitter to the camera. Note that this schematic has omitted the focusing fold mirror assembly and the other fold mirrors that occur between the beamsplitter and the camera.

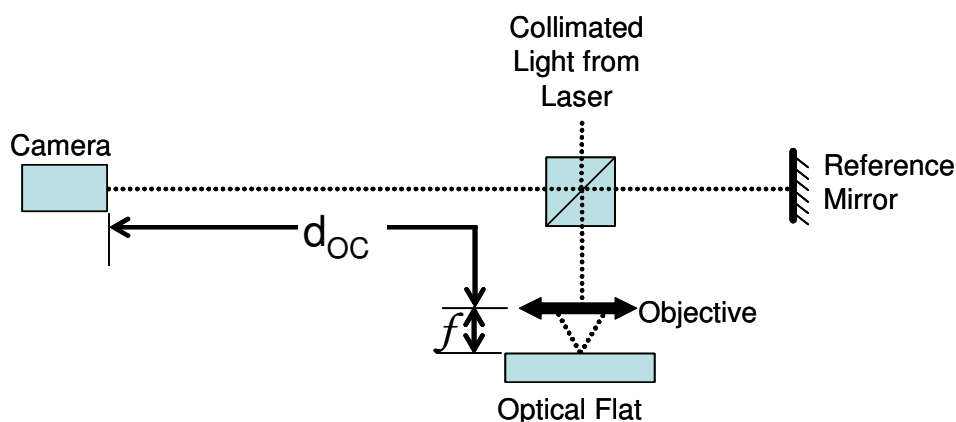


Figure 4-13: Schematic of simplified interferometer.

I observed an unexpected interference pattern as the optical flat moved through cat's eye. The optical flat was above cat's eye where circular fringes resulted with a positive defocus value (region A in Figure 4-14) as expected. As the flat moved through cat's eye, the circular fringe pattern fluffed out to form

large tilt fringes at the cat's eye (point B in Figure 4-14). As the flat moved further down, circular fringes with a negative defocus value formed as expected (region C in Figure 4-14). But, as the flat moved even further, the fringes got very dense and a small bright spot formed on the camera (Point D in Figure 4-14). A measurement was not possible at this point. Then, as the part moved even further down, a circular fringe pattern formed with positive defocus value (region E on Figure 4-14). This was most unexpected. All previous research in radius measurements shows the trend line from region C continuing in a negative direction.

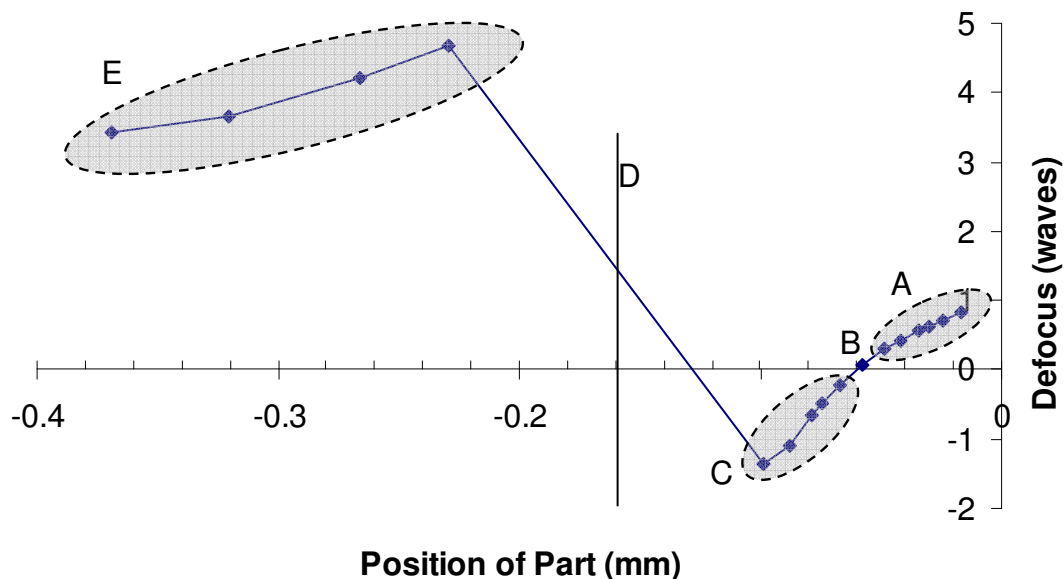


Figure 4-14: Measurement of Optical Flat on simplified MORTI using the 042 NA objective ($f = 10$ mm) and $d_{OC} = 540$ mm.

Initial observations pointed to stray light causing the odd interference pattern in region E. This led to me testing each component in the system for a

stray light effect. In this analysis, I removed a window in the camera, improved the collimation package, and tested different objective lenses, but still the pattern persisted.

This pattern is not a stray light effect, but rather a continuation of the standard interference pattern and is inherent in micro-interferometers due to the short focal length of the objective. This is explained as follows and is demonstrated in Figure 4-16. It is necessary to examine the wavefront for each region at the camera. Only the wavefront from the test arm is considered in the analysis, the reference arm wavefront is assumed to be flat. The curvature of the wavefront at the camera is calculated from the location of the image of the optical flat. The optical flat is located at a distance d_{PART} from the objective lens. It is the location of the focus point (cat's eye position) that is of interest, though. The distance from the objective, s_O , to the apparent location of the focus point is

$$s_O = 2(d_{PART} - f_O) + f_O$$

Equation 4-6

as shown in Figure 4-15.

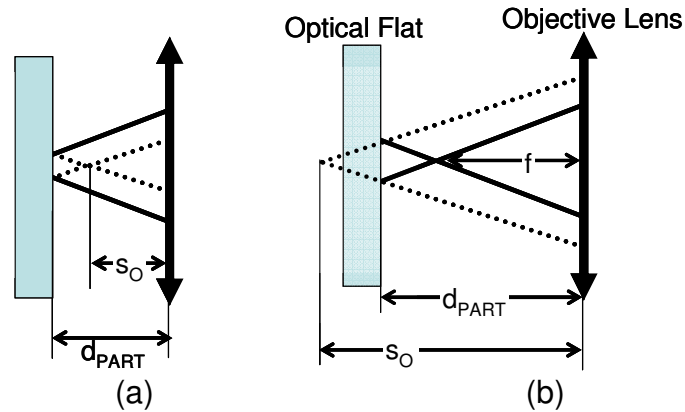


Figure 4-15: Schematic showing the relationship between d_{PART} and s with the optical flat (a) before cat's eye and (b) beyond cat's eye.

The distance d_{PART} is set to range around the focus point. Then the location of the image of the part can then be calculated using the simple ray tracing formula

$$\frac{1}{s_o} + \frac{1}{s'} = \frac{1}{f},$$

Equation 4-7

where s_o is the distance from the lens to the part and s' is the distance from the lens to the image. I confirmed the results from this equation, and the schematic based on it (Figure 4-14), by drawing the rays by hand. The schematic is explained as follows.

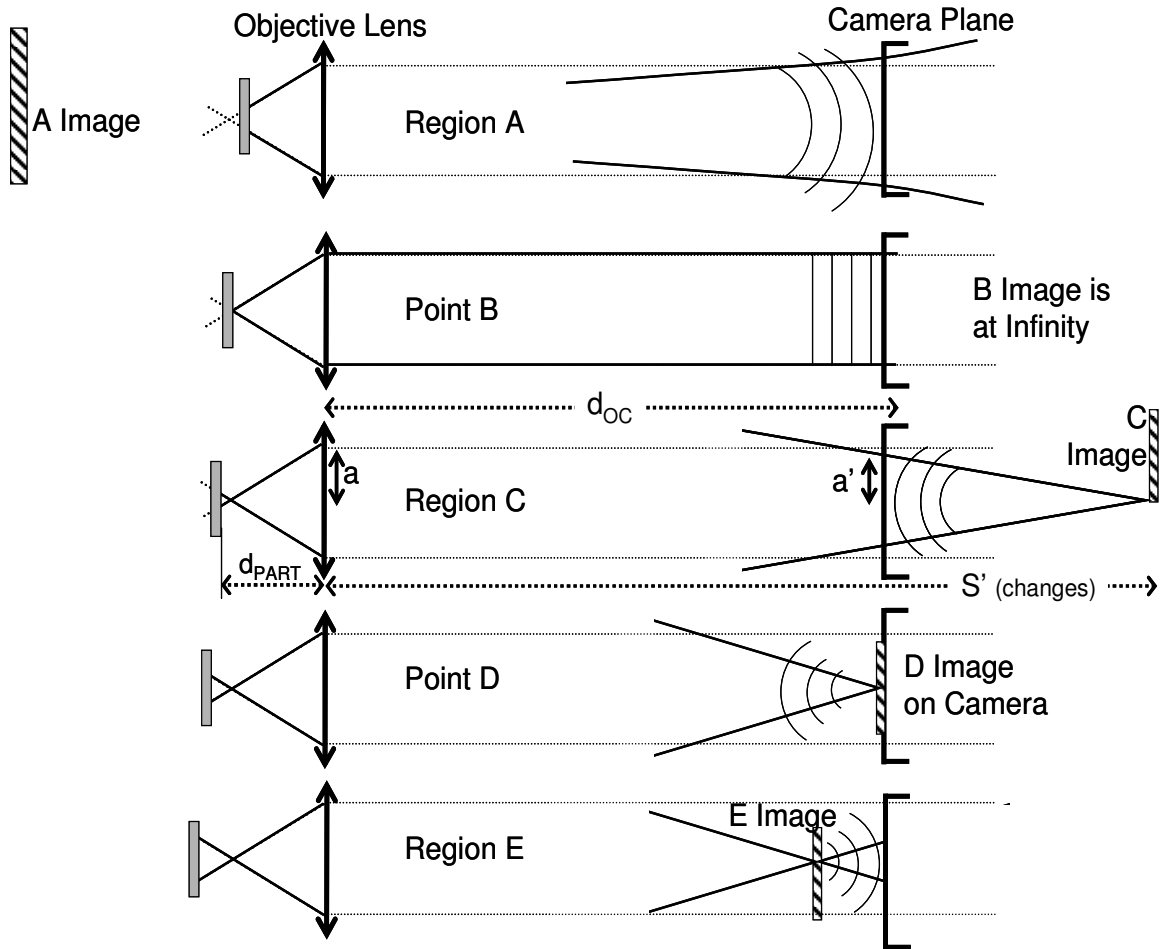


Figure 4-16: Schematic of the wavefront at the camera as the optical flat is moved through cat's eye. The heights of the images are arbitrary.

In region A, the flat is inside of the optical ($d_{PART} < f$); the image of the object is virtual and is located to the left of the objective lens. This results in a diverging beam at the camera and the expected positive defocus value from the interference between this wavefront and the flat wavefront from the reference mirror.

As the optical flat moves from region A to point B, the image moves more to the left until the optical flat is at cat's eye ($d_{PART} = f$). Here, the image of the flat is

at infinity and the test arm wavefront is flat resulting in a zero defocus value of the interference pattern.

The optical flat then moves from point B to region C, where the optical flat is located past the focus point ($d_{PART} > f$). The image formed is real and far to the right, beyond the camera plane. This results in a converging beam at the camera and a negative defocus value of the interference pattern.

Between region C and point D, the image is moving from the far right to the left until the optical flat reaches point D. At this point, the image is coincident with the camera plane. I observed this experimentally with the small bright spot on the camera.

Beyond point D and in region E, the image is formed between the lens and the camera plane. This results in a diverging beam at the camera plane and a positive defocus value of the interference pattern. Experimentally, this was the interference pattern that was so unexpected.

The following analysis calculates the location of each of these regions and demonstrates why this is a factor in micro-scale radius measurements and not macro-scale.

4.6.2 Simulation of the Focusing Issue, Without the Imaging Leg

I wrote a Matlab program (Appendix B, Program 8, `foc_effect_no_image.m`) to perform this simple analysis. The program uses the following logic. The optical flat moves through the cat's eye position and for each position of d_{PART} , the following are calculated: the location of the focus point (s_O), the location of the image (s'), the radius of the wavefront (R) at the camera, the half aperture

size of the wavefront (a') at the camera, and the sag of the wavefront at the camera (h). The location of the image, s' is calculated using Equation 4-7 with $f = 10$ mm (the 0.42 objective). The radius of the wavefront, R , is s' minus d_{OC} (distance from the objective to the camera), with the sign convention of a diverging beam has a positive radius and a converging beam has a negative radius. The half aperture size of the wavefront at the camera (a') is calculated from the simple ratio

$$\frac{a'}{a} = \frac{R}{s'}$$

Equation 4-8

using similar triangles. The sag of the wavefront at the camera is then calculated using

$$h = abs(R) - \sqrt{R^2 + a'^2}$$

Equation 4-9.

The absolute value of R in the sag equation is mainly for visualization purposes. Therefore the sag reported here is related to the defocus value. The slope of the sag vs. position graph is not equal to the slope of the defocus vs. position graph, but the zero crossing values will correspond to the same position value. The graph of sag vs. part position for varying values of distance d_{OC} is shown in Figure 4-17. Points B (part is at cat's eye) and D (image is on camera) are shown with d_{OC} having different values for the varying camera distances. Region A (part is inside the focal length), is to the left of point B, region C (part is outside focal length) is between points B and D, and region E (part is outside focal length and the image is between the objective and camera) is to the right of point D.

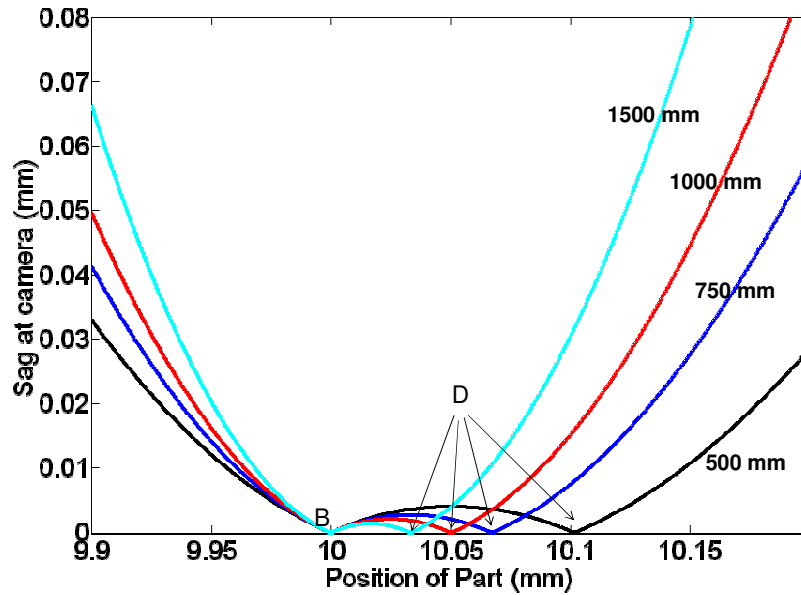


Figure 4-17: Sag at the camera in simplified micro-interferometer. Each line is a different d_{OC} value, the focal length of the objective is 10 mm, and the half aperture, a , is 4 mm. The objective is located to the left, at 0 on the x-axis.

In addition, varying the objective is shown in Figure 4-18. The aperture and focal length change for each objective. The values for the given focal lengths and aperture size correspond to the actual objective lenses used in experiments. This graph demonstrates why this focus effect is not seen in macro-scale experiments where the focal length is on the order of 150 mm.

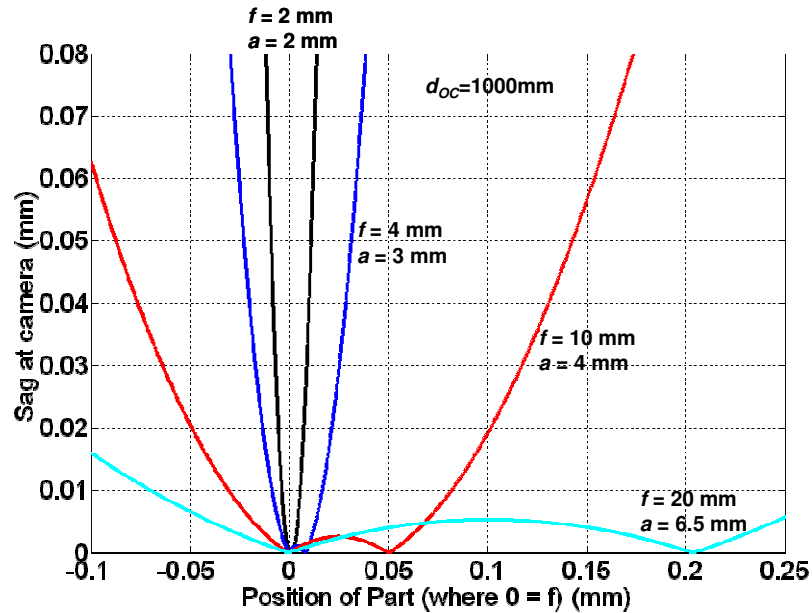


Figure 4-18: Sag at the camera in simplified micro-interferometer. Each line is a different focal length and aperture (corresponding to the different objective lenses) value and the distance d_{OC} is 1000 mm. The objective is located to the left, on focal length away from zero.

The radius of the wavefront at the camera (R) results are as expected as shown for $d_{OC} = 1000$ mm in Figure 4-19. When the optical flat is located inside cat's eye the radius is positive and moves to positive infinity. Outside the cat's eye position, the radius moves from negative infinity through zero (this is point D) to positive.

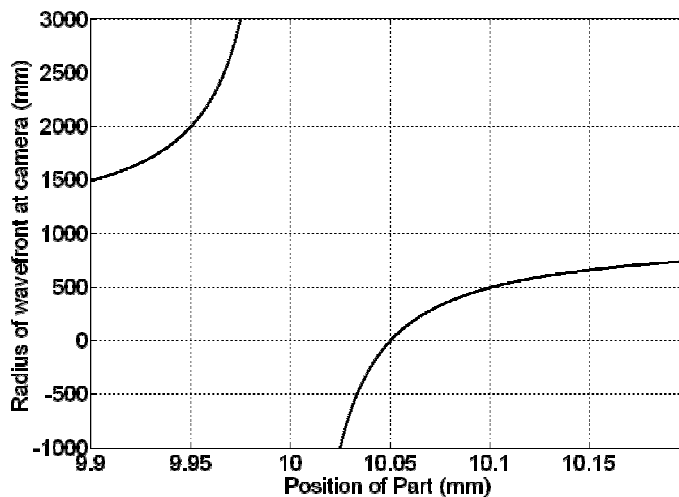


Figure 4-19: Radius of wavefront for $f = 10$ mm, $a = 4$ mm and $d_{OC} = 1000$ mm. The objective is located to the left, at 0 on the x-axis.

The above is summarized as follows. The cat's eye position does not move with varying the input parameters. The distance between the cat's eye position and the image focus point does vary with changing focal length and the distance from the objective to the camera.

4.6.3 Effect on Radius Measurement

Now that we understand why this focusing issue occurs, we must determine how it affects the radius measurement. The goal is to determine how far in region C (from Figure 4-16) are valid measurements obtainable. The two effects that will determine this are the linearity of the sag vs. position curve (and therefore the defocus vs. position curve) and the half width of the beam at the camera. These two effects are related and it may be that they give the same answer to the permitted length.

To demonstrate the linearity effect, see Figure 4-20. Region A (above cat's eye) appears linear for $30 \mu\text{m}$, and possibly longer, for all focal lengths. The

length that region C remains linear varies with the focal length of the objective. The 4 mm focal length objective has an approximate length of only $2\ \mu\text{m}$ whereas the 20 mm objective is clearly linear up to $30\ \mu\text{m}$ and possibly longer. Remember that the distance from the objective to the camera will also affect this linearity distance. This again demonstrates why this effect is not a concern with macro-scale measurements which have much longer focal lengths.

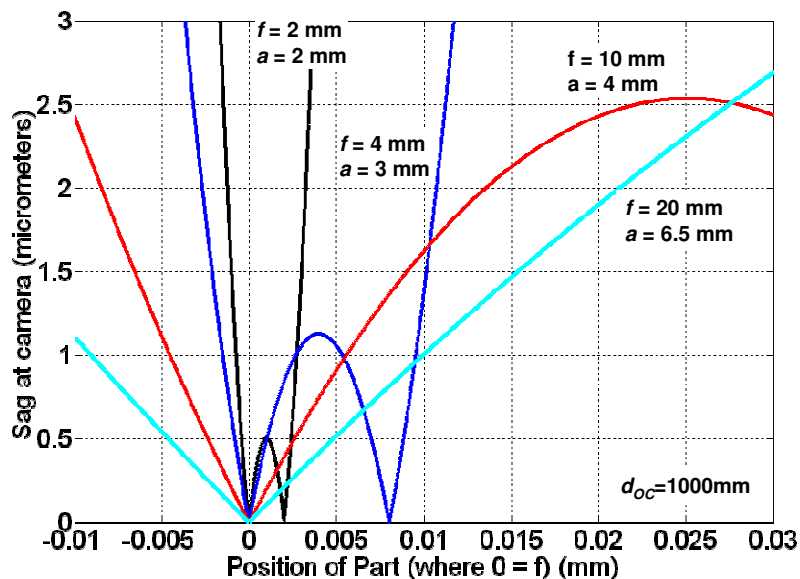


Figure 4-20: Sag at camera from micro-interferometer for varying focal lengths. Close up view of Figure 4-18. Note that the sag is now in μm . The objective is located to the left, one focal length from zero.

The second effect is the size of the beam at the camera (a'). When the part is in region A, a' is always larger than a (the beam diameter at the objective). As soon as the part enters region C, a' becomes smaller than a . This leads to a masking issue and can be shown by examining Figure 4-21, a graph of a' vs. position of the optical flat. Note that a' here is negative before region D because

the image is inverted, an inconsequential effect. At point B a' is equal to a and at point D a' is zero, both as expected. Now, to determine how the mask should be set. From Figure 4-20 we can say that the 10 mm focal length curve is linear up to $20\ \mu\text{m}$. Using the data from Figure 4-21, a' is 2.4 mm at 10.02 mm. This shows that the mask size of the data must be set at 2.4 mm or smaller for all measurements through the cat's eye position. If the mask is set at 4 mm (the size of a' at cat's eye), the measurements in region C will be erroneous because of bad data on the edge of the measurement.

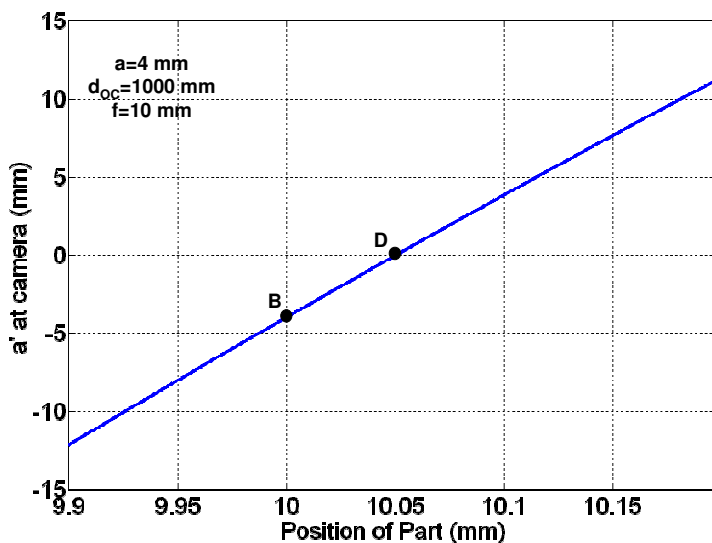


Figure 4-21: The size of the beam at the camera, a' . The objective is located to the left, at 0 on the x-axis.

4.6.4 Considering Spherical Aberration

The analysis thus far has considered a perfect wavefront and has shown that the mask size and the length of region C are critical issues when measuring the radius of micro-optics. We next consider if the test arm wavefront has

spherical aberration, a common error in interferometers. This analysis is not complete, but is presented here to demonstrate the possible bias that would arise from a spherical aberration error.

Figure 4-22 shows a schematic of the measurement with spherical aberration. The mask size is chosen from the size of the wavefront in region C. The same size mask is used (and shown) for point B and region A. In each region the spherical aberration (shown in gray) spreads from edge to edge on the wavefront. The measurement in region C will show a spherical aberration. But in region A and at point B, the spherical aberration is clipped and therefore will present itself as a defocus error. This defocus error will lead directly to a bias in the measurement of position.

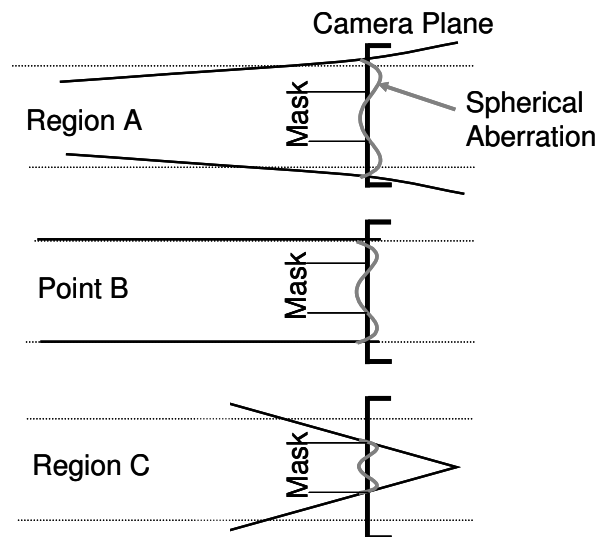


Figure 4-22: Schematic of measurement with spherical aberration.

4.6.5 Focusing Effect with Imaging Leg

The results above are for an interferometer without imaging optics. Radius measurements are, of course, taken with imaging optics, so that the part can be in focus when at the confocal position. The interferometer is set so that the part is in focus at confocal (for the figure measurement). The required configuration of the micro-interferometer for focusing on the part was discussed in Section 4.2.1. The distances and focal lengths are the same for this analysis.

An analysis similar to the one in Section 4.6.2 was performed to determine if a similar focusing effect occurred and if it affected the radius measurement. The analysis was similar, but more complicated because the image of the object passes through the objective plus the four lenses instead of just the lenses. The goal is to determine the sag of the wavefront at the camera. To do this, the radius of the wavefront at the camera (R) and the height of the wavefront at the camera (a_c) are required.

To find the radius of the wavefront at the camera, the location of the image (of the part) relative to the camera must be found. This is done by determining the location of the image through objective and then each of the subsequent lenses. These distances are s_0' , s_1' , s_2' , s_3' , and s_4' and are defined relative to their respective lenses. First, the distance from the test part to the objective, s_0 is set. From this point, s_0' is calculated. Then, s_1 (the distance from this image to lens 1) is found from d_{O1} minus s_0' . This process is repeated until the radius of the wavefront at the camera is known. This process is shown in

$$\begin{aligned} \frac{1}{s_o} + \frac{1}{s_o'} &= \frac{1}{f_o} & s_1 &= d_{o1} - s_o' \\ \frac{1}{s_1} + \frac{1}{s_1'} &= \frac{1}{f_1} & s_2 &= d_{12} - s_1' \\ \frac{1}{s_2} + \frac{1}{s_2'} &= \frac{1}{f_2} & s_3 &= d_{23} - s_2' \\ \frac{1}{s_3} + \frac{1}{s_3'} &= \frac{1}{f_3} & s_4 &= d_{34} - s_3' \\ \frac{1}{s_4} + \frac{1}{s_4'} &= \frac{1}{f_4} & R &= d_{4C} - s_4' \end{aligned}$$

Equation 4-10.

Next, the height of the wavefront at the camera, a_C is determined. First, the magnification of the two focal systems, M_{AF} , is calculated from

$$M_{AF} = \frac{f_2}{f_1} \frac{f_4}{f_3}$$

Equation 4-11.

Then the a_C is found from similar triangles as in Equation 4-8 and is

$$a_C = \frac{a R M_{AF}}{s_4'}$$

Equation 4-12,

where a is the half aperture width of the objective and R the radius of the wavefront at the camera. Finally the sag equation is the same as Equation 4-9.

The Matlab program in Appendix B, Program 9, `foc_effect_w_image.m`) shows the focusing effect when imaging is considered.

The sag at the camera for the MORTI (with the imaging leg) is shown in Figure 4-23. The distance d_{23} was set as if a 0.5 mm radius part was being measured, as shown in Figure 4-4. The cat's eye position, point B, is as expected, at the focal value. Point D, on the other hand, changes for the different objective lenses, even so far as to be above cat's eye for the 0.28 NA and 0.42 NA objectives and below for the 0.55 NA and 0.7 NA objectives. The radius of the wavefront at the camera plane for the same conditions is shown in Figure 4-24. This is as expected, that the radius goes to infinity at the cat's eye (point B) and goes to zero at point D. Varying the distance between lens 2 and lens 3, d_{23} , was tested as shown in Figure 4-25. The position of point D is sensitive to the value of d_{23} , much more so than in Section 4.6.2 where a small change in d_{OC} had a much smaller change in the location of point D.

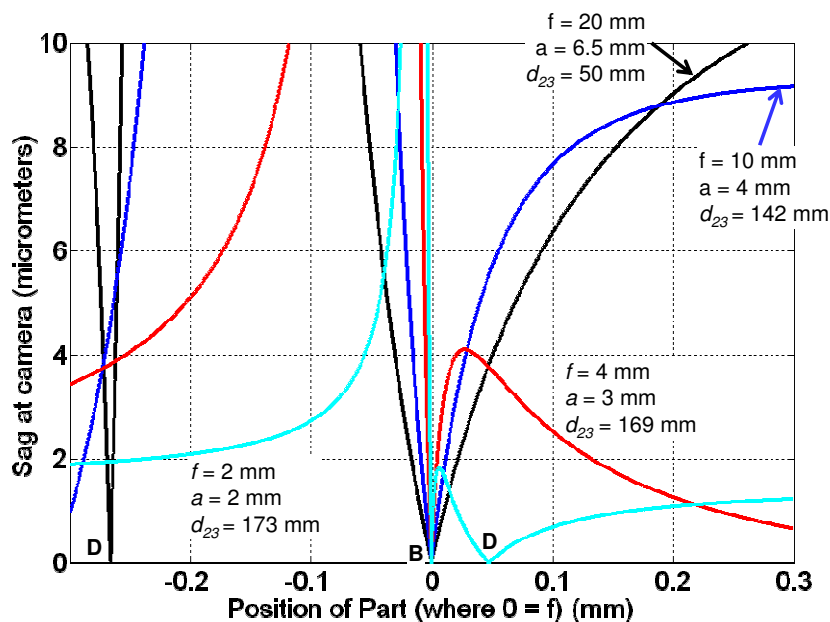


Figure 4-23: Sag at the camera for MORTI for the objective lenses. The objective is located to the left, one focal length from zero.

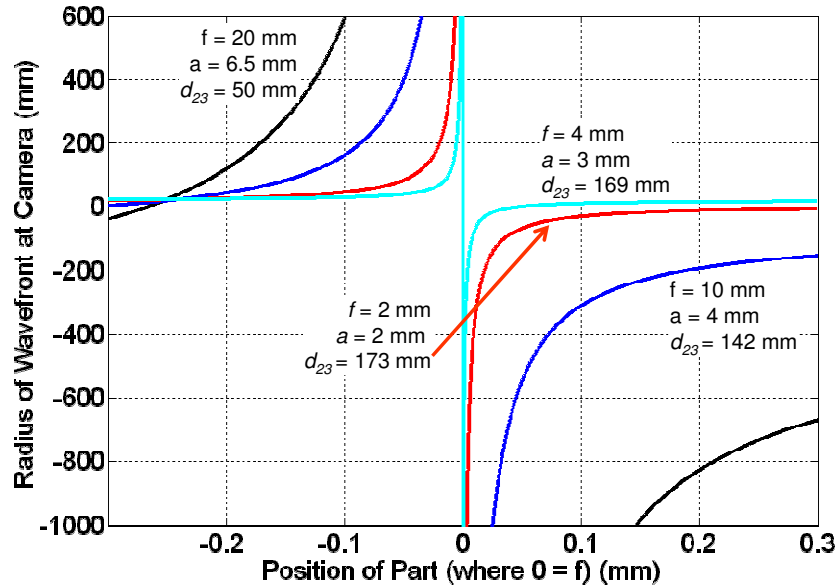


Figure 4-24: Radius of wavefront at the camera for MORTI for the various objective lenses. The objective is located to the left, one focal length from zero.

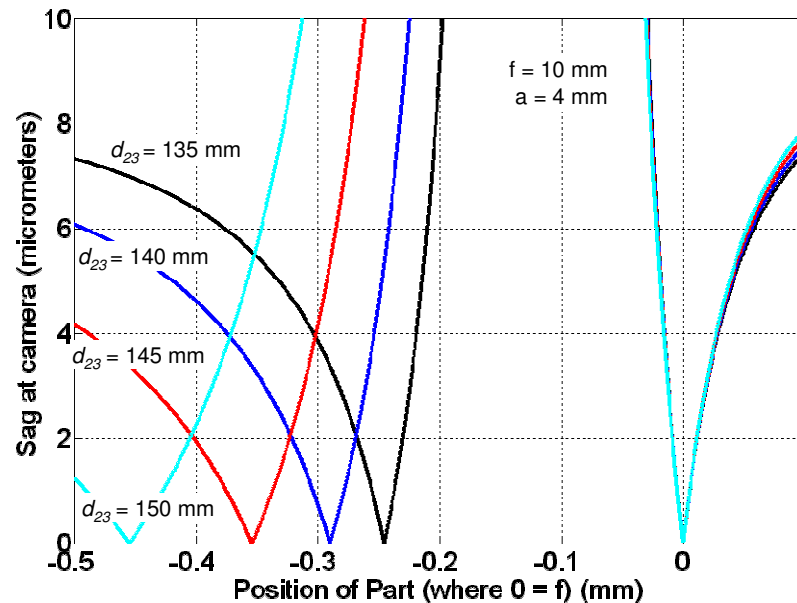


Figure 4-25: The sag at the camera for MORTI when the distance between lens two and three is varied. The objective is located to the left, one focal length from zero.

The nonlinearity effect discussed in Section 4.6.3 is still an effect when the imaging leg is considered. This is obvious in Figure 4-25 below cat's eye where

the curve appears nonlinear below 0.05 mm. This demonstrates that data should not be taken after this point.

4.6.6 Focusing Effect on the Macro-Scale

This focusing effect is not normally seen on macro-scale measurements mainly because the transmission spheres have much longer focal lengths. For example, a measurement on the Veeco RTI interferometer was simulated using the f/1.5 transmission sphere (focal length is 144 mm) with a half aperture of 50 mm. Because the interferometer is enclosed, the distance to the camera is not known and was assumed to be in the range of 400 mm to 1000 mm. The results showing the sag at the camera for varying distances to the camera is shown in Figure 4-26. Point B (the cat's eye position) is located at 144 mm as expected. Point D (the point at which the part is focused on the camera) varies with varying the distance to the camera. But, the distance between points B and D is quite large, around 15 mm in the case of $d_{OC} = 800$ mm. This shows that the part would have to be moved over 1.5 cm for this effect to be seen on the macro-scale. At this long distance, the fringes will be so dense and cannot be measured. For comparison, on the micro-scale the distance between points B and D is less than 0.1 mm.

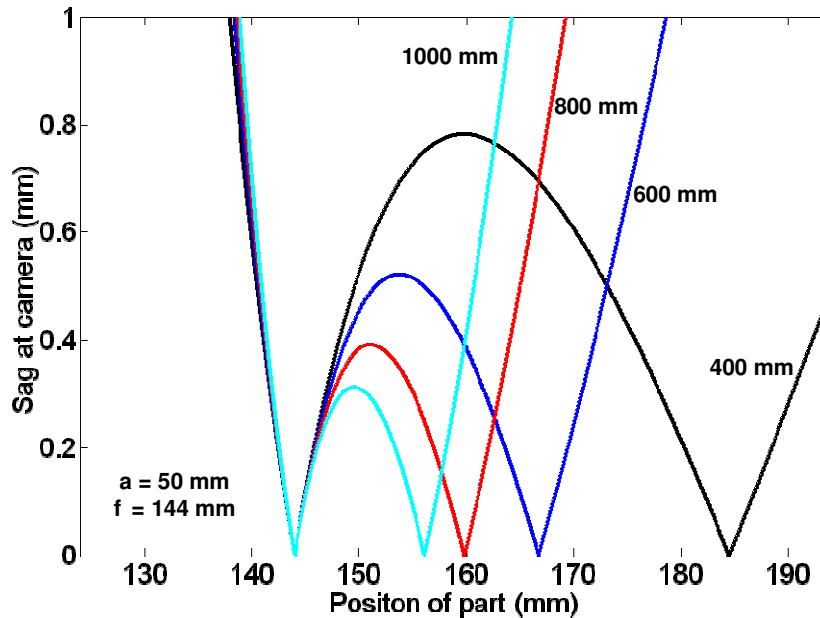


Figure 4-26: Sag at the camera in simplified macro-scale interferometer. Each line is a different d_{OC} value, the focal length of the objective is 144 mm, and the half aperture, a , is 50 mm. The transmission flat is located to the left, at zero on the x-axis.

Of course, the imaging components in the Veeco interferometer will affect the location of Point D. But, in general, it is the long focal lengths in macro-scale interferometers that eliminate this focusing issue.

4.6.7 Comparison to Theoretical, Without Imaging Leg

The following is a comparison between the theories described in Section 4.6.2 and data taken on MORTI without the imaging leg. This data is summarized in Figure 4-27 where the distance between the objective and camera was varied. This data is similar to the data shown in Figure 4-14, with the unexpected positive values for defocus as the optical flat traveled past cat's eye. Figure 4-28 shows the same data as Figure 4-27, but on a smaller scale to show the area around the cat's eye position.

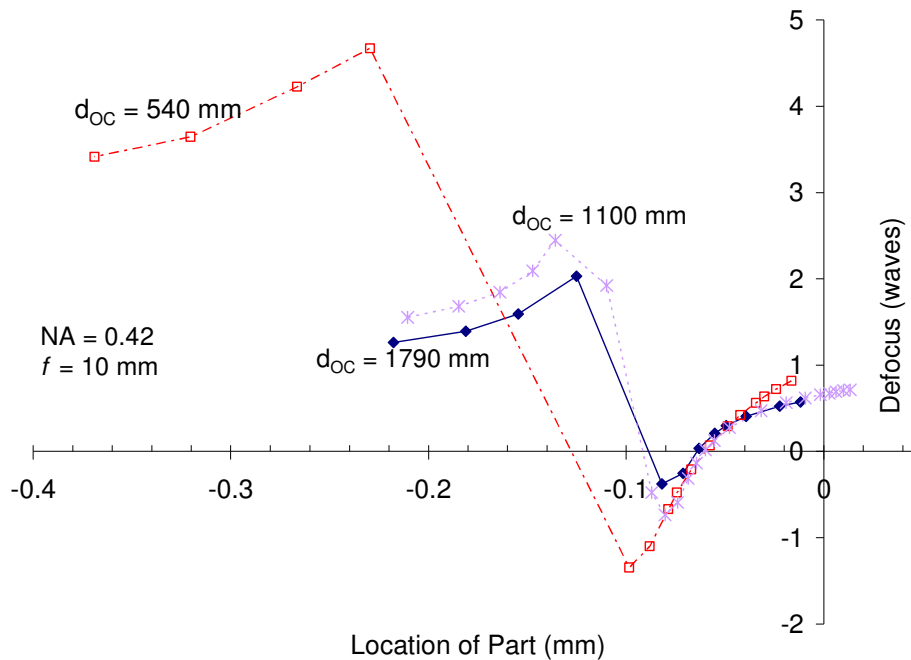


Figure 4-27: Defocus vs. Location of Part on MORTI without an imaging leg, as measured on an optical flat using the 0.42 NA objective, $f = 10$ mm. The objective is located to the right.

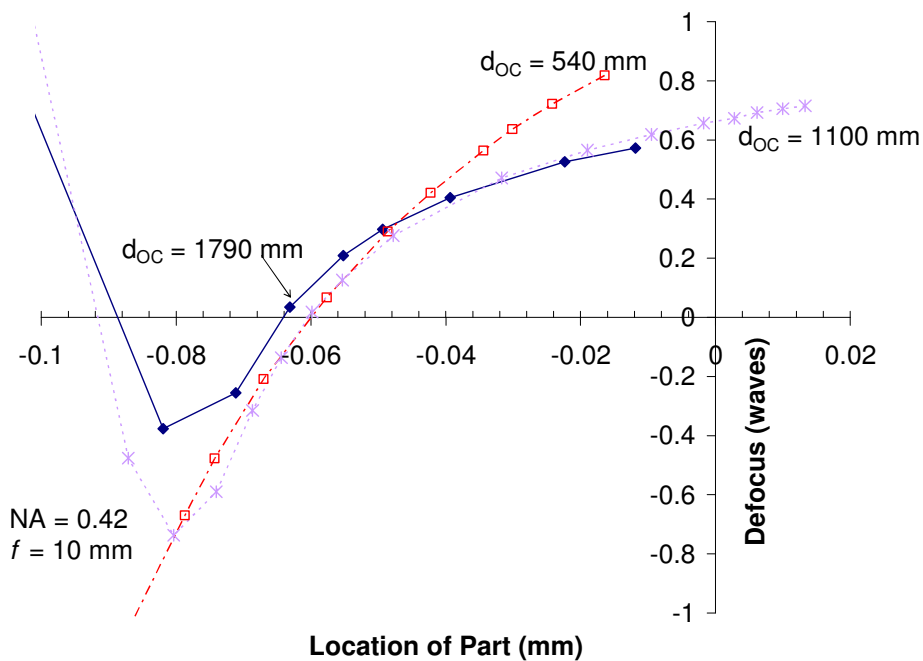


Figure 4-28: Defocus vs. Location of Part on MORTI without an imaging leg, same data as Figure 4-27, different scale. The objective is located to the right.

The distance between points B and D are used to compare between the Matlab simulation (Figure 4-17) and data from MORTI (Figure 4-27) when d_{OC} was varied for the 0.24 NA objective. Table 4-1 shows a summary of this data. The uncertainty values shown for the location indicate the repeatability in determining the location of the cats's eye position (Point B) and the bright spot (Point D). The uncertainty shown in the simulation indicates the uncertainty in knowing d_{OC} to only 5 mm. The values for the distance between points B and D compare well as shown.

Table 4-1: Comparison between the simulation and actual positions of points B (cat's eye) and D (bright spot) without imaging leg for 0.42 NA objective.

		d_{OC} (mm)		
		540	1100	1720
MORTI	Point B (mm) ± 0.001 mm	-0.0575	-0.0585	-0.0633
	Point D (mm) ± 0.008 mm	-0.1486	-0.0994	-0.0995
	abs(Point B - Point D) (μm)	91 ± 8	41 ± 8	36 ± 8
Simulation	Point B (mm) ± 0.000 mm	10.0000	10.0000	10.0000
	Point D (mm) ± 0.004 mm	10.0943	10.0459	10.0292
	abs(Point B - Point D) (μm)	94 ± 4	56 ± 4	29 ± 4

4.6.8 Comparison to Theoretical, With Imaging Leg

The next step was to consider MORTI with the imaging optics in and compare the simulation results to actual data taken on MORTI. The data from the measurements from the optical flat for the 0.42 NA and 0.28 NA objectives are shown in Figure 4-29 and Figure 4-30 where the distance between lens two and three was varied. The comparison between the simulation and this data is

shown in Table 4-2 and Table 4-3. The uncertainty values for the simulation are much higher when the imaging leg is considered than when it is not. This is due to the sensitivity of the location of point D to the distances used in the interferometer.

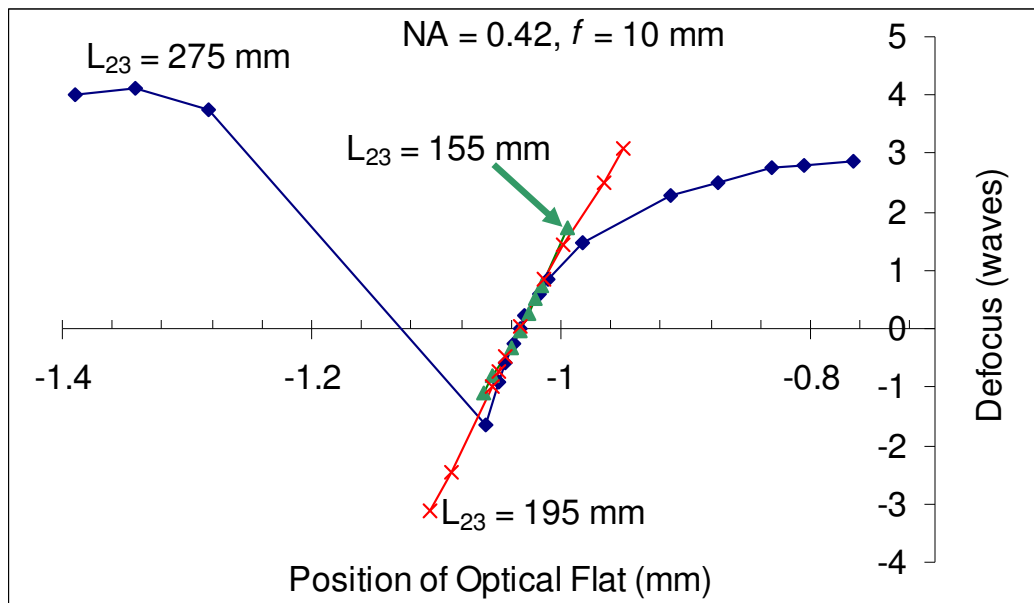


Figure 4-29: Defocus vs. Location of Part on MORTI with the imaging leg, as measured on an optical flat using the 0.42 NA objective, $f = 10 \text{ mm}$. The objective is located to the right.

Table 4-2: Comparison between the simulation and actual positions of points B (cat's eye) and D (bright spot) with imaging leg for the 0.42 NA objective.

NA = 0.42, f = 10 mm		Location of D relative to B	d _{oc} (mm)		
			145	195	275
MORTI	Point B (mm) ±0.001 mm	Above	-1.0354	-1.0305	-1.031
	Point D (mm) ±0.008 mm	Below	-0.74	-1.5256	-1.526
	abs(Point B - Point D) (mm)	Below	0.295 ±0.008	0.495 ±0.008	0.494 ±0.008
Simulation	Point B (mm) ±0.000 mm	Above	0	0	0
	Point D (mm) ±0.2 mm	Below	-0.354	0.2919	0.074
	abs(Point B - Point D) (mm)	Below	0.354 ±0.2	0.292 ±0.2	0.074 ±0.2

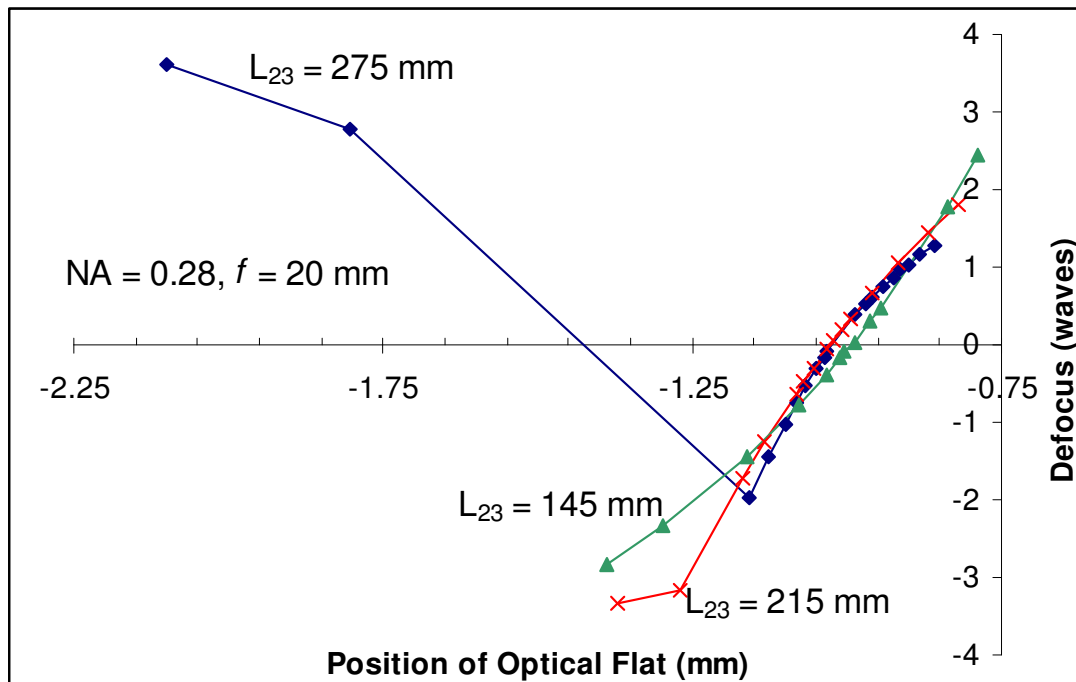


Figure 4-30: Defocus vs. Location of Part on MORTI with the imaging leg, as measured on an optical flat using the 0.28 NA objective, $f = 20$ mm. The objective is located to the right.

Table 4-3: Comparison between the simulation and actual positions of points B (cat's eye) and D (bright spot) with imaging leg for the 0.28 NA objective.

NA = 0.28, $f = 20$ mm		Location of D relative to B	d_{oc} (mm)		
			145	215	275
MORTI	Point B (mm) ± 0.001 mm	Above	-1.001	-1.018	-1.015
	Point D (mm) ± 0.008 mm	Below	0.0638	-2.092	-1.409
	abs(Point B - Point D) (mm)	Below	1.065 ± 0.008	1.074 ± 0.008	0.393 ± 0.008
Simulation	Point B (mm) ± 0.000 mm	Above	0	0	0
	Point D (mm) ± 0.4 mm	Below	-1.322	0.6987	0.3025
	abs(Point B - Point D) (mm)	Below	1.322 ± 0.4	0.699 ± 0.4	0.302 ± 0.4

There are effects that cause differences between the simulation and the experimental data on MORTI. The simulation modeled the microscope objective and the imaging optics as thin lenses. The objective is actually a much more complex set of lenses. The focal length and NA of the objective and the focal lengths of the imaging lenses used in the simulation are as reported by the manufacturer and were not measured. The spherical aberration effect discussed in Section 4.6.4 was not considered. The main cause of uncertainty, though, was that the d_{23} and the other distances in the interferometer can not be measured to high precision. These effects show why there is the discrepancy between the simulation and the measurements on MORTI. There is a correlation though between the simulation and experiment, mainly the location of point D relative to point B (the cat's eye). This value was correct for each distance tested.

4.6.9 Conclusion of the Focusing Effect

The analysis presented here considered an optical flat, not a sphere (required for a radius measurement) and did not consider the confocal position. The analysis for the confocal position would be similar, in examining when the apparent focus point comes from.

The main consideration to take away from this analysis is that the mask size for a radius measurement needs to be picked very carefully and that measurements can only be taken in the linear range. It is likely that a test measurement through confocal and cat's eye is necessary before the true measurement can be taken. The mask must be set when the wavefront at the camera is the smallest, but still large enough to obtain a valid measurement.

This is shown in Figure 4-31 where the radius of the spot at the camera, a_c , is shown for varying objectives. The size of the beam at the camera changes at different rates for the different objectives. This is a consequence of the different numerical apertures. Therefore care must be taken when measuring parts with different objectives. The possible step size and total distance traveled at cat's eye or confocal will not be constant for all the objectives.

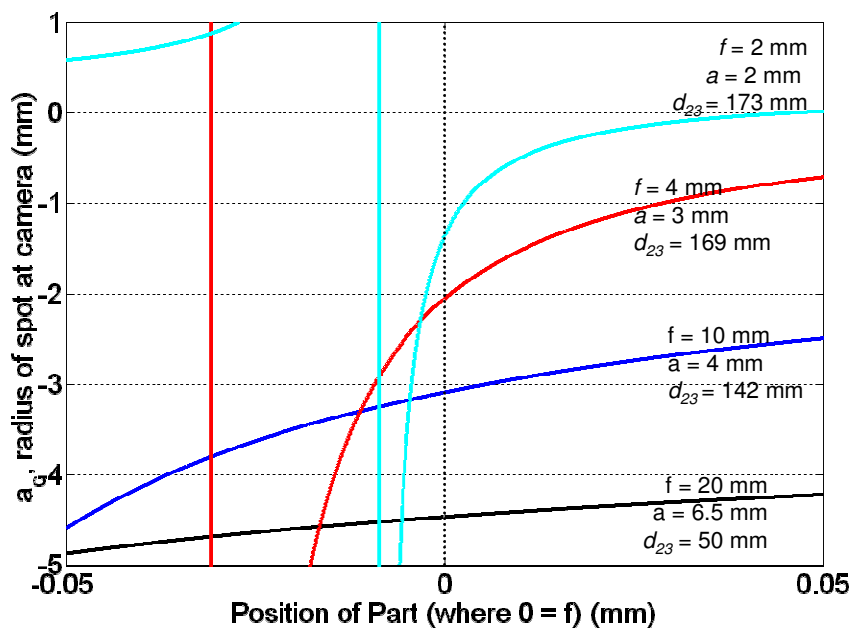


Figure 4-31: The radius of the spot at the camera, a_c , for varying objective lenses near the cat's eye position. The objective is location to the left at one focal length away.

4.7 Operation of MORTI

The software package Intellwave is used to gather the data and analyze the interference pattern. A standard interferometer measurement occurs as follows. The software captures a camera frame and then the software commands the PZT to step a quarter of a wave (90°). Another camera frame is

captured and the pzt steps again. This is repeated until 5 frames have been captured (at 0, $\frac{1}{4}$ wave, $\frac{1}{2}$ wave, $\frac{3}{4}$ wave, and 1 wave distances of the PZT). Note in this setup, a double pass interferometer, the physical step of the PZT is only an $\frac{1}{8}$ of a wave, while the optical step is a $\frac{1}{4}$ of a wave. The PZT actuator is controlled through a digital to analog converter through Intellwave. The PZT is calibrated through the software to produce the required quarter wave (90°) steps for the phase shifting interferometry.

The feed from the Pulnix TM-62EX camera is split by a co-axial splitter between a television screen for viewing and a frame grabber. Intellwave controls the timing of the PZT and frame grabber.

The software then processes these frames through a phase shifting algorithm [39], here a four bucket algorithm, to determine the phase map of the surface. I then masked the data to the area of interest using the mask feature. The unwrapping algorithm minimum discontinuity then converts the wrapped phase map to a height map, known as the optical path difference. The Zernike aberration terms are then calculated in software through a fitting algorithm. The height map and mask data are saved in an .esd file.

4.8 Measurement of Spheres

4.8.1 The Spheres

The results reported here show the nominal radius minus the measured radius. The nominal radius is found from the manufacture of the stainless steel spheres. The spheres used were reported as $\frac{5}{64}$ (0.078) inch, $\frac{3}{64}$ (0.047) inch, and $\frac{1}{32}$ (0.031) inch, all in diameter. This corresponds to nominal values

of 0.992 mm, 0.595 mm, and 0.397 mm in radius. I measured two of the spheres using a pair of calipers. The $\frac{5}{64}$ sphere measured at 0.078 inch (1.98 mm) diameter and the $\frac{3}{64}$ sphere measured at = 0.046 inch (1.17 mm) diameter. The $\frac{1}{32}$ sphere was too small to measure using the calipers.

A picture of the measurement of a sphere is in Figure 4-32. An example measurement of the 0.99 mm radius sphere without aberration is shown in Figure 4-33 and with one glass plate, thickness of 1.39 mm, is shown in Figure 4-34.

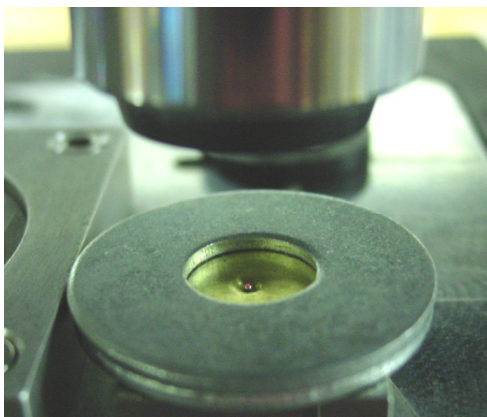


Figure 4-32: Picture of a sphere measurement, the objective is at the top of the picture.

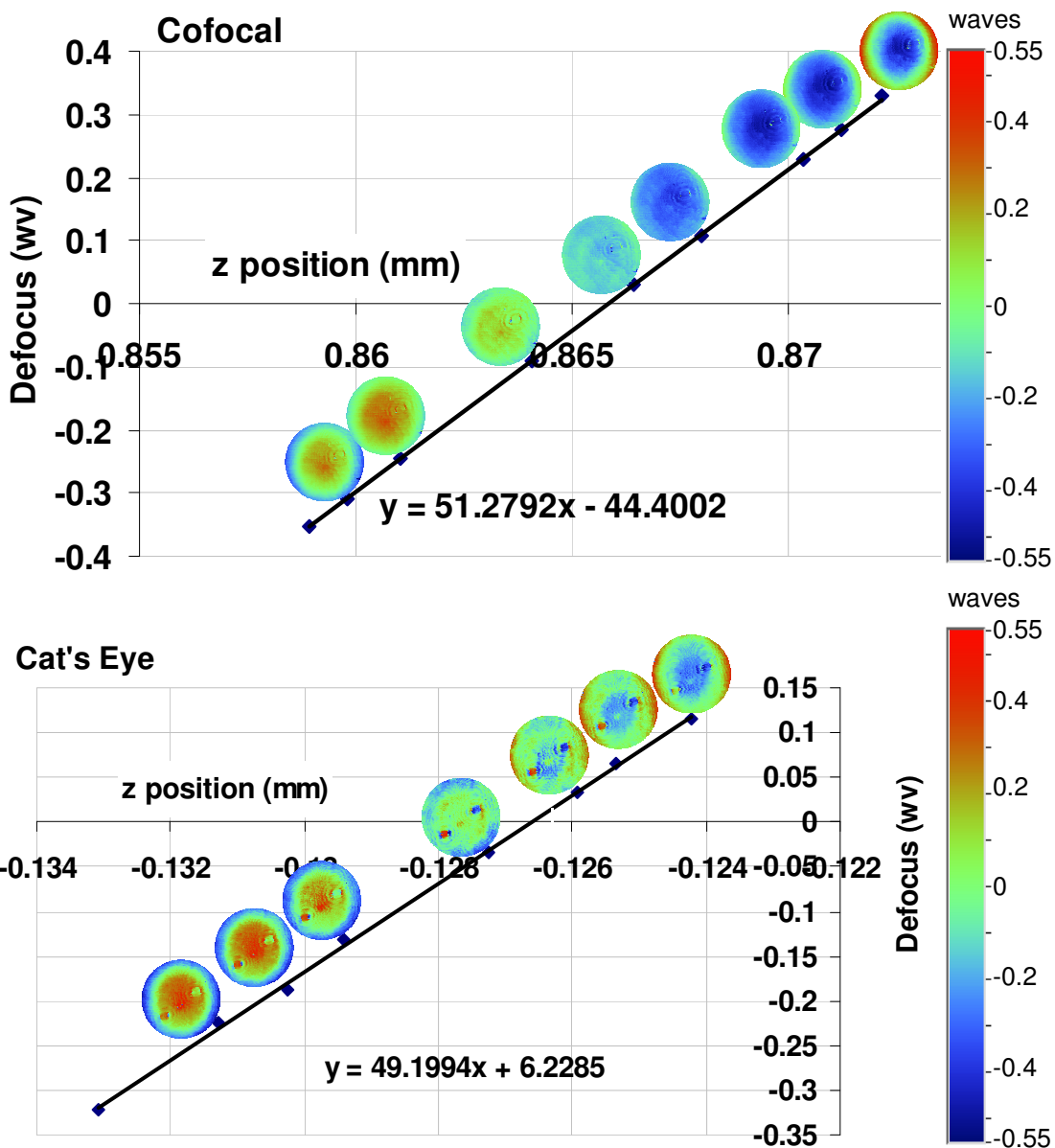


Figure 4-33: A measurement of the 0.99 mm radius sphere. The objective is to the right.

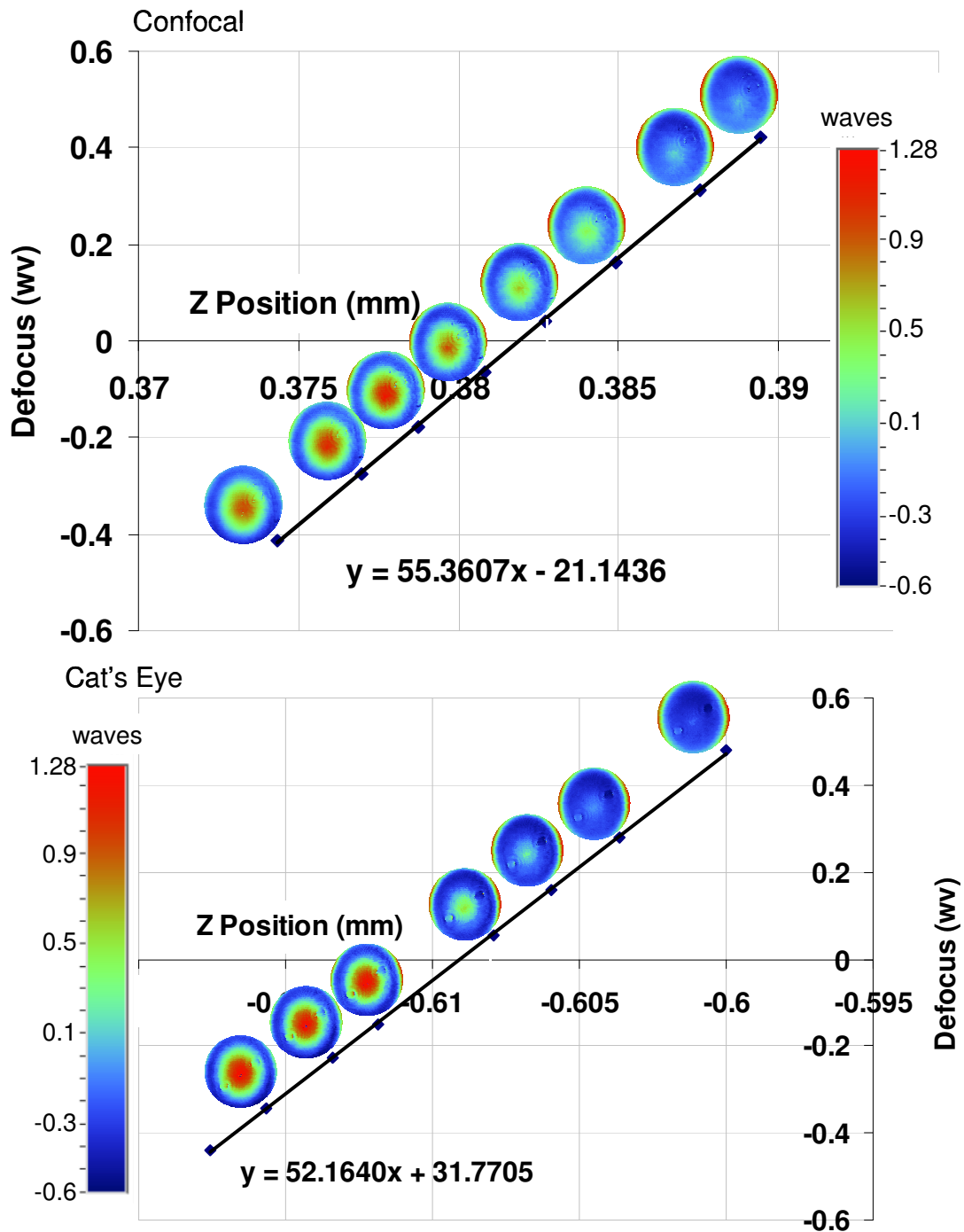


Figure 4-34: A measurement of the 0.99 radius sphere with one glass plate to add spherical aberration. The objective is to the right.

4.8.2 Uncertainty due to Fitting

Errors in the linear fit led to an uncertainty in the radius as introduced in Chapter 1. This uncertainty in radius due to the fit inherently includes uncertainty due to other effects such as masking, spherical and other aberrations, environmental effects such as temperature and vibration, repeatability in phase shifting, unwrapping errors, and figure errors in the part. Examples of the fit uncertainty in radius for different conditions are shown in Table 4-4. The uncertainty in radius due to the fit ranges, but does not seem to correlate to either the objective NA (when the 0.42 and 0.55 NA objective are considered) or the amount of spherical aberration. Previous work [27] shows that the uncertainty in radius due to the fit will dramatically increase with smaller NAs. My initial investigations on MORTI showed this with the 0.28 NA objective. But, the data from the 0.28 NA objective was not used in this research due to imaging problems. Imaging on the surface was not always possible and the wavefront on the camera was too large. In this analysis, the average of $0.4 \mu\text{m}$ will be used as the fit uncertainty.

Table 4-4: The fit uncertainty in radius in the measured data.

Nominal Radius (mm)	Added Aberration?	Objective NA	Fit Uncertainty (nm)
0.99	No	0.42	214
0.99	Yes	0.42	242
0.99	No	0.55	176
0.99	No	0.55	550
0.59	No	0.42	482
0.59	Yes	0.42	447
0.39	No	0.42	482
0.39	No	0.55	447
Average			380 (nm)

4.8.3 Repeatability

I tested the repeatability of the radius measurement by performing one full radius measurement (starting above confocal and moving below cat's eye) and then repeating the measurement as shown in Figure 4-35. The standard deviation of this data is $0.1 \mu\text{m}$.

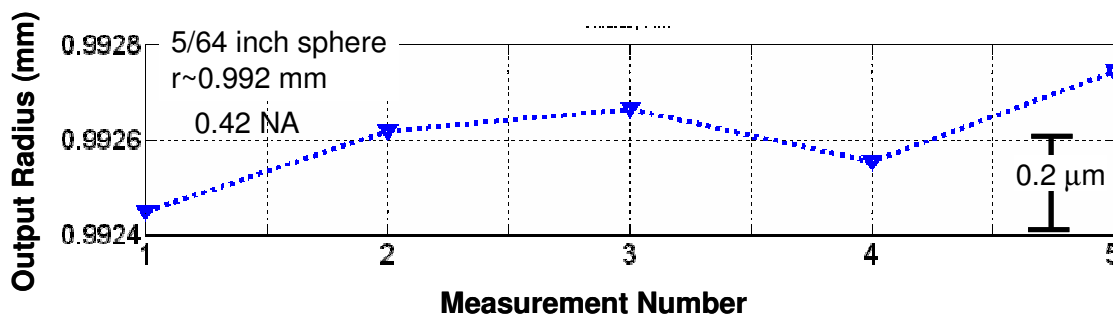


Figure 4-35: Measurements of the 0.99 mm radius sphere to test for repeatability.

4.8.4 Varying L_{23}

I next tested varying the distance between Lens 2 and Lens 3 as shown in Figure 4-36. This distance is used to focus of the part at confocal. The apparent best focus was $L_{23} = 164$ mm, as determined by eye. Figure 4-4 shows that the ray tracing predicated the best focus at 160 mm. Varying the distance over approximately 40 mm did not affect the radius output when compared to the repeatability of $0.1 \mu\text{m}$ as shown in Figure 4-36.

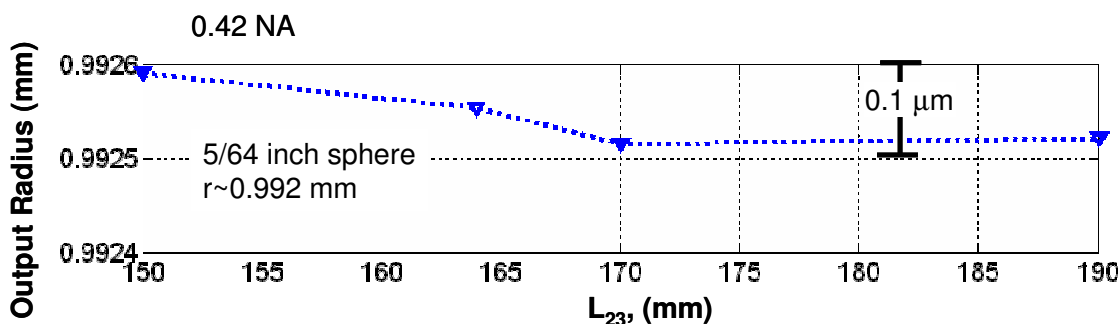


Figure 4-36: Measurements of the 0.99 mm radius sphere while varying the distance between lens 2 and lens 3.

4.8.5 Changing the Mask Size

I next tested reducing the mask size and examining the resultant radius as shown in Figure 4-37, without added spherical aberration and in Figure 4-38, with added spherical aberration. The mask size affects the radius measurement as shown because reducing the mask will change the fit of the Zernike polynomials. What was spherical aberration (with the full mask) is now defocus (with the reduced mask). This causes an offset in the defocus vs. position curve and a bias is the radius (if the spherical aberration is different at confocal and cat's eye,

as it is). The effect of changing the mask size is larger when spherical aberration is added as expected because there is more spherical aberration that will lead to a larger offset in radius. The proper mask size is a trade off. The focusing effect discussed in Section 4.6 will cause bad data on the edges if the mask is set too large. If there is no aberration, the mask size effect will be greatly reduced as shown. Reducing the mask size will reduce the spherical aberration, but may lead to not enough data for a good measurement. Many radius measurements include a figure (also known as form) error measurement at confocal which requires a large mask.

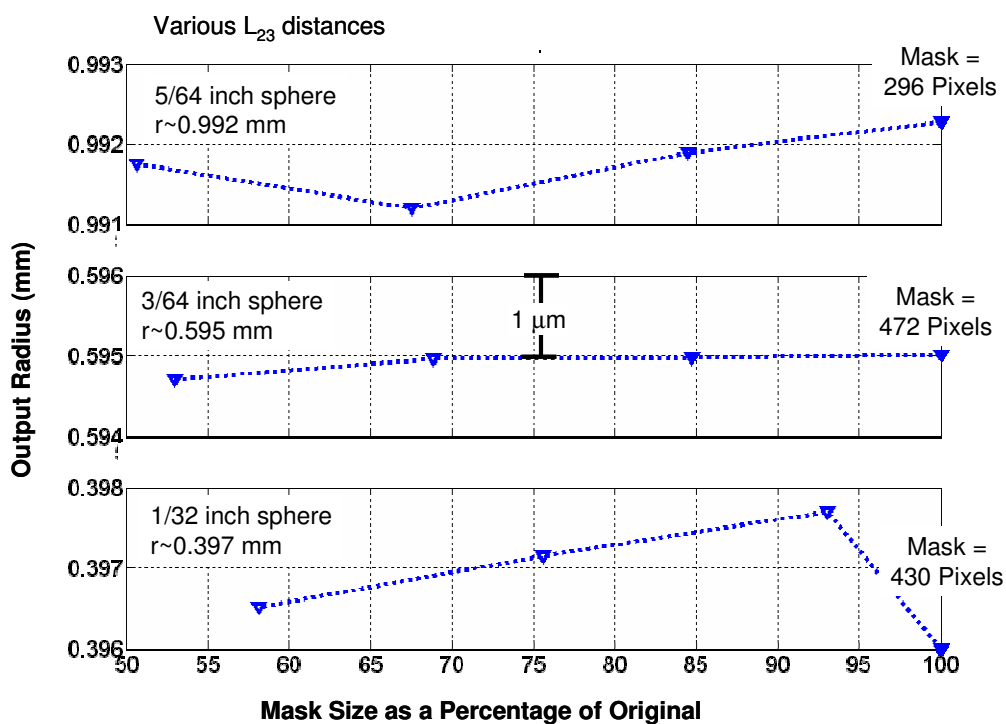


Figure 4-37: The measured radius as the mask size was varied, NA = 0.42 with no added aberration.

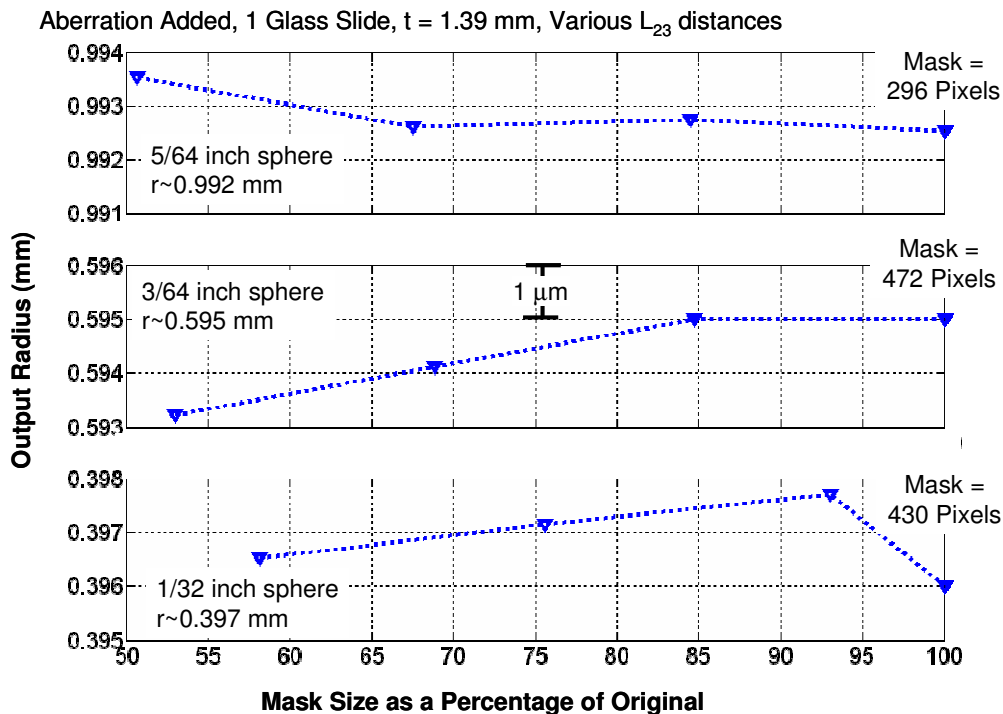


Figure 4-38: The measured radius as the mask size was varied, $NA = 0.42$, added spherical aberration with glass plat 1.39 mm thick.

4.8.6 Vary the Objective Lens NA

Figure 4-39 shows the measured radius as the objective lens is varied. Figure 4-40 and Figure 4-41 show the cat's eye and confocal positions as the objective lens is changed. The objective NA shown is as reported by the company, but is not the full NA from the experiment due to the masking. The masking of the data causes the NA to be reduced to some extent. This does make it difficult to compare between data points and between the different radii. I am unable decisively to say what the trends are when the objective is changed. The 0.397 mm radius sphere indicates that the radius increases with the smaller aperture, but the other size spheres do not follow that trend.

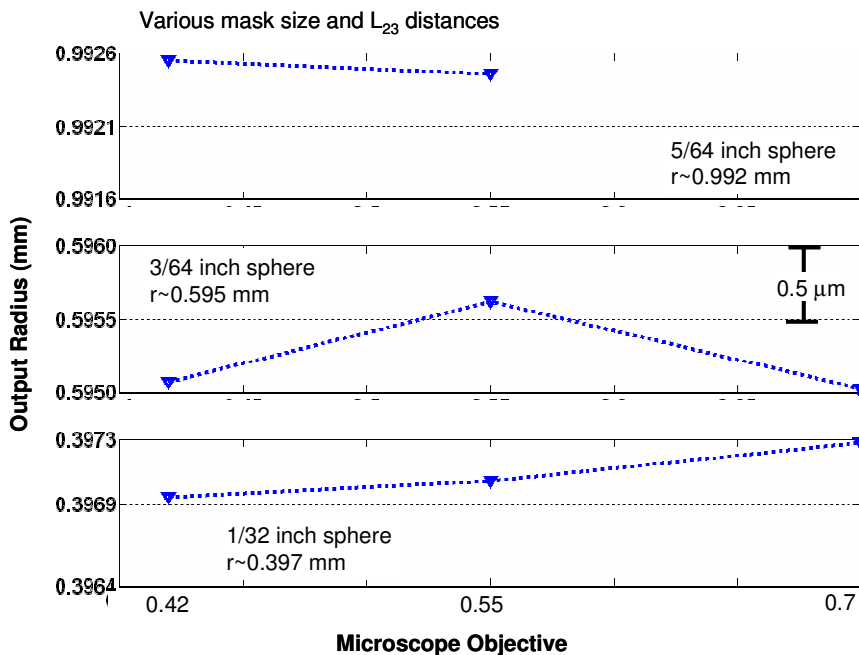


Figure 4-39: The measured radius as the microscope objective is varied.

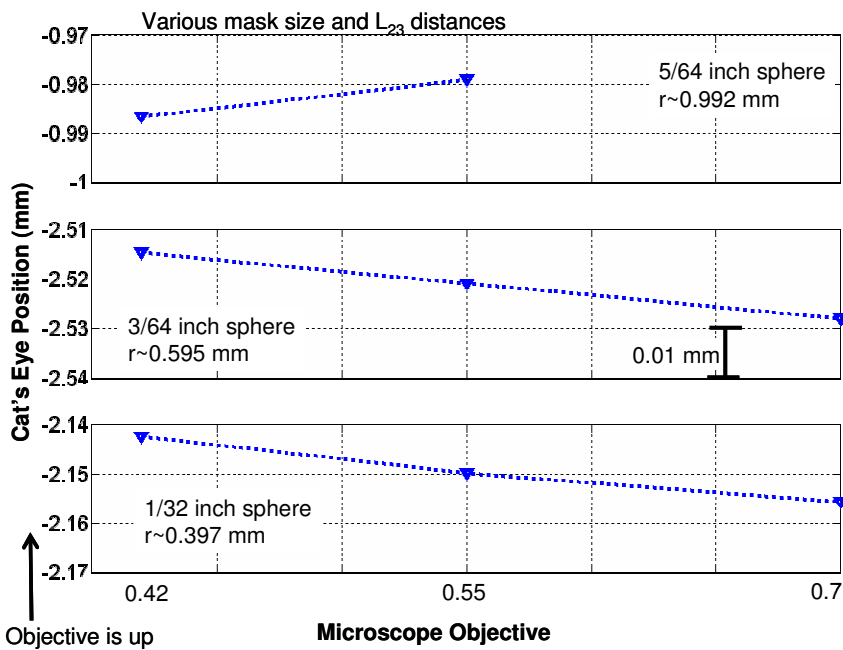


Figure 4-40: The cat's eye position as the microscope objective is varied.

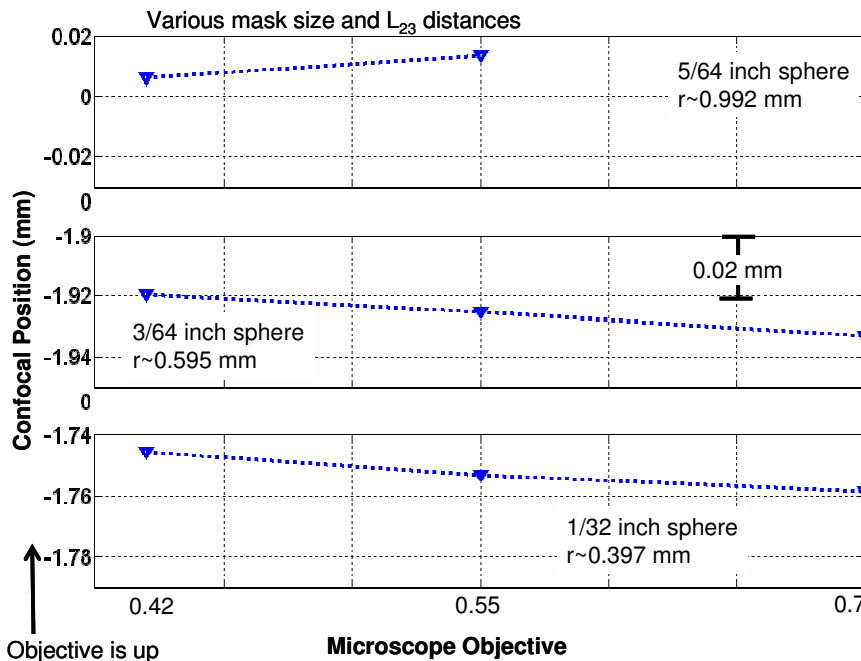


Figure 4-41: The confocal position as the microscope objective is varied.

The variation in the confocal and cat's eye position is not a concern and is not due to an optical effect. I recall a typical microscope when switching to high power objectives. While the mechanical system was designed such the focus of all the objectives would coincide, it never did and I had to refocus for each objective. The variation shown in Figure 4-40 and Figure 4-41 is the same mechanical effect and should not affect the radius measurement except to possibly change the focusing effect to a small amount.

4.8.7 Adding Spherical Aberration

Spherical aberration was added to the measurement by inserting a glass plate between the test optic and the microscope objective. The glass plate is a microscope slide, thickness of approximately 1.4 mm. Two glass slides were also used to add more spherical aberration. Also, I tested using a thin piece of

clear plastic, thickness of approximately 0.25 mm thick. The glass plates have imperfections and are likely not parallel to a high degree of precision, but these errors will have secondary effects. The primary effect is that a converging beam passing through a glass plate will cause the focus to offset and spherical aberration to form in the wavefront.

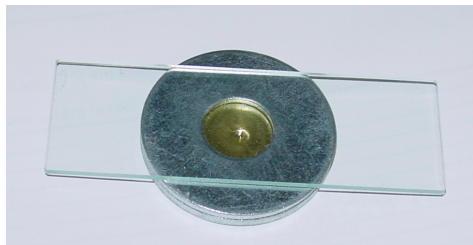


Figure 4-42: The glass plate used to add spherical aberration. The fixture that holds the test sphere (a piece of shim sandwiched between two washers) is unique because the glass plate does not touch the test part.

The measured radius versus the thickness of the glass plate is shown in Figure 4-43. But, we are more interested in the how the radius is affected by the spherical aberration, as shown in Figure 4-44. The spherical aberration shown here is of the wavefront at the camera when the part is located near the cat's eye position. The spherical aberration is not linearly related to the thickness of the glass plate because of the mask size.

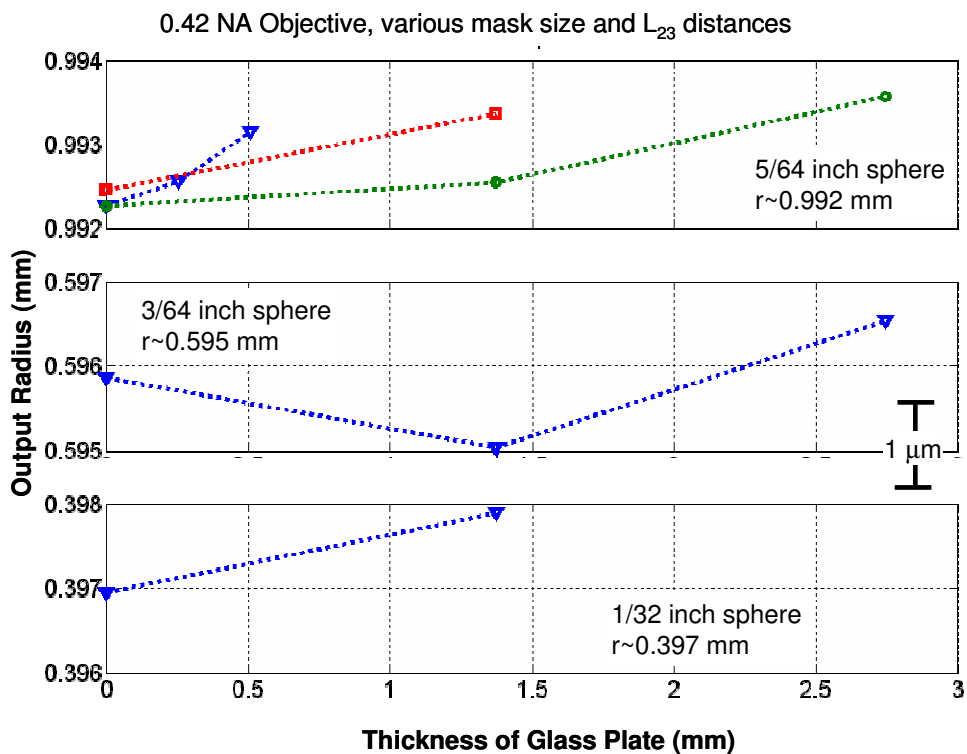


Figure 4-43: The measured radius vs. the thickness of the glass plate as spherical aberration is added. The mask size is constant for each data set.

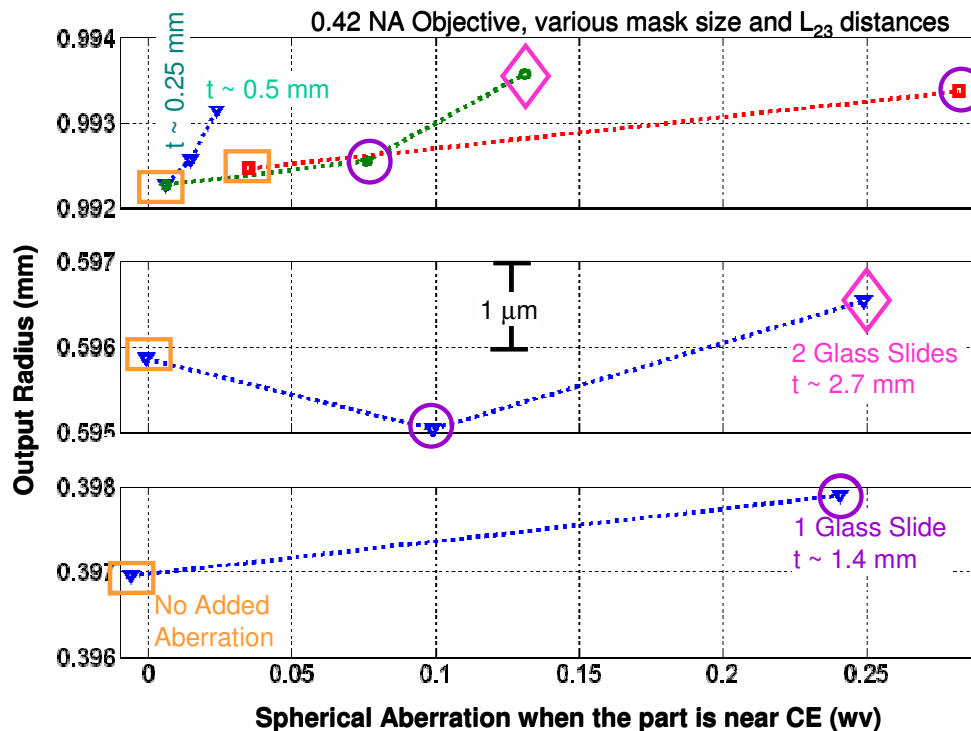


Figure 4-44: The measured radius vs. the spherical aberration as spherical aberration is added.

To compare results, each data set (a dotted line) shown in Figure 4-44 uses the same mask for the measurements. As the spherical aberration increases, the size of the data at the camera reduced, an effect of the focusing effect discussed in Section 4.6. In the green data set in the 0.99 radius sphere, the glass plate with thickness of 2.7 mm required that the mask for all the green data be set small. There is a large difference in the amount of aberration for the for a plate thickness of 1.4 mm in the green data to the red data. This is because the mask is smaller for the green data than the red, and therefore the aberration is smaller in the reduced mask. While the masking does explain the differences between the data sets, it is apparent that increasing the amount of spherical aberration causes the measured radius to increase.

The blue data from the 0.99 mm radius spheres is from using the thin pieces of clear plastic. A large amount of noise was added to the height map when the plastic was used (rather than the glass plate). This shows that even with errors in the glass plate, the primary effect on the radius is to increase the measurement result.

Figure 4-45 and Figure 4-46 show the cat's eye and the confocal positions as aberration was added, note that the scale is now in mm. As is obvious, the dominant effect is that both positions shift down, away from the objective. This effect is so large, it does not matter what the mask size is as shown in the 0.99 mm radius data.

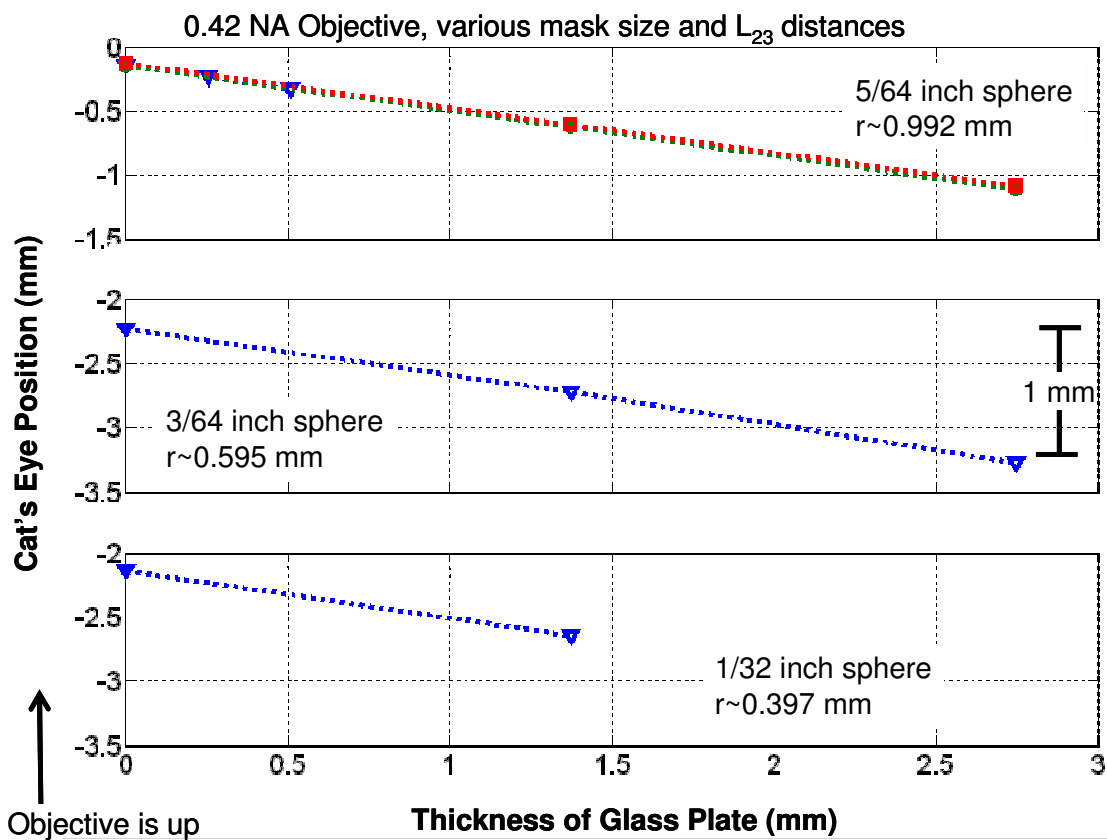


Figure 4-45: The cat's eye position as spherical aberration was added.

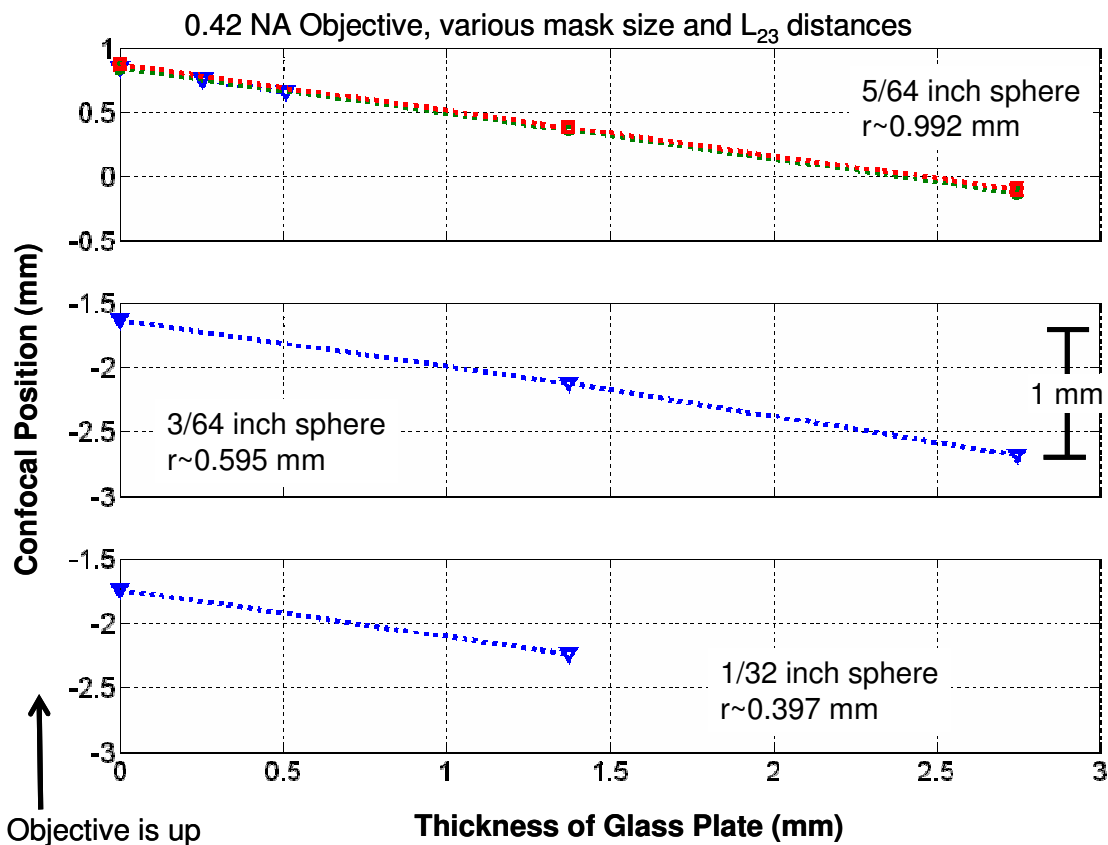


Figure 4-46: The confocal position as spherical aberration was added.

4.9 Measurement of the Microscope Objective

I measured the 0.42 NA microscope objective on the Veeco Interferometer to gain a general knowledge about the aberrations that are in MORTI. I was not able to do a full random ball test to determine the actual errors. The objective was measured in the configured shown in Figure 4-47 which will only measure the Zernike components that are rotationally invariant, like spherical aberration [40]. The measurement of the microscope objective has 0.041 waves of spherical aberration. This measurement is actually the sum of the errors in the microscope objective and the errors in the transmission flat of the Veeco Interferometer. Because only a small part of the transmission flat (8 mm) is used

for this measurement, the error due to the transmission flat is likely small. Therefore the error in the microscope objective is near the 0.041 waves spherical. But, the error in the full interferometric is larger due to the other others in the interferometer and varies with the radius of the sphere tested [41] but is likely on the same order of magnitude as the 0.041 waves. The spherical aberration in Figure 4-44 with additional aberration shows a spherical aberration of near 0.01 waves, which is much lower due to the reduced mask.

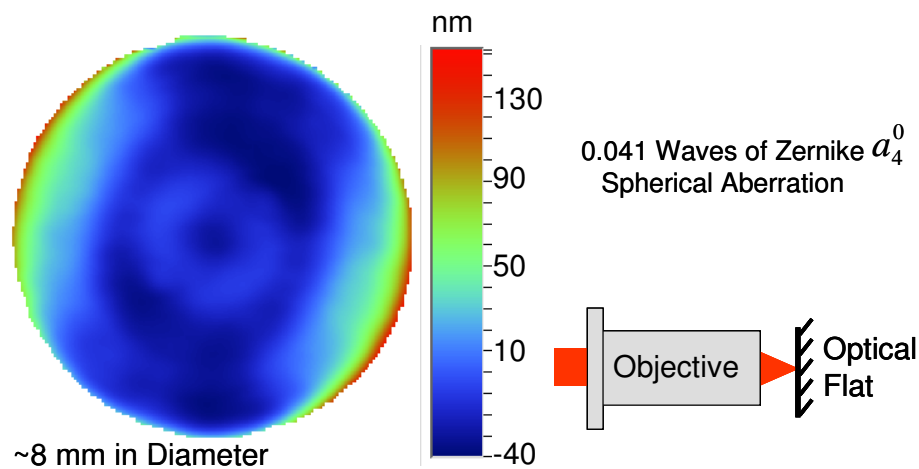


Figure 4-47: The measurement of the 0.42 NA microscope objective on the Veeco interferometer in the configuration shown.

4.10 Uncertainty

A full uncertainty budget for the radius measurement on MORTI is outside the scope of this work. I am more concerned with the trends in the radius measurement as conditions vary, rather than the absolute value of radius. The major source of radius uncertainty is the fitting of the lines to the Zernike defocus vs. position graphs, here calculated at $0.4 \mu\text{m}$. As discussed in Section 4.8.2 this uncertainty includes other effects. The repeatability of the radius measurements

was 0.1 μm . While I did not explicitly study the reproducibility, the zero thickness glass plate data in Figure 4-43 gives an indication of reproducibility, estimated here as 0.2 μm .

There are error motions errors when the part moves between cat's eye and confocal. This error motions cause an error in the absolute radius, but are applicable here when comparing between different part radii. This effect would only be considered if the error motions are different over the different part radii. This is likely not the case here since the size range of parts is so small. Therefore, the uncertainty due to the error motions is not a concern for this analysis.

The current interferometer configuration does not allow for the microscope objectives to be aligned relative to the motion axis. This possible misalignment would cause a bias in the radius measurement, not a concern here. But, I am changing between microscope objectives and comparing the results. If the different microscope objectives have different misalignments (with the motion axis), the biases are different for the various objectives. This may explain why I am unable to draw conclusions about changing the objective. MORTI needs to be modified to check for and correct this misalignment.

The figure error in the sphere can cause a bias in the both the cat's eye and confocal positions. On this scale, the uncertainty due to this is likely small compared to the uncertainty due to fitting.

There are errors in the phase shifting, that is, the PZT may not move in 90° steps as required. This uncertainty may take the form of noise and would

therefore be part of the uncertainty due to fitting. Or this uncertainty may take the form of a bias and therefore would bias all the measurements the same. This is not a concern here because I am looking for trends, not absolute radius.

The absolute radius of the measured part is biased if the temperature is not at 20°C. But, because I am not concerned with absolute radius, it is temperature variations during the course of a measurement that affects the measured radius. Measurement of this effect is outside the scope of this work. I consider the repeatability and reproducibility to account for the temperature variations and other environmental concerns such as vibration.

Combining the three calculated uncertainties in a root sum square method gives an estimated uncertainty for radius of 0.46 μm , equating to 1 part in 10^4 for a 0.4 mm radius test part. This is not the full combined standard uncertainty in the radius measurement, but is valid for comparison. Future research includes investigating methods for reducing uncertainty.

4.11 Conclusions

In this chapter, I described the Micro-Optic Reflection and Transmission Interferometer, MORTI, and the radius measurements experiments. The transmission component of the interferometer is not required for the radius measurement and therefore has not been discussed here. In reflection, the figure measuring interferometer and the laser scale are used for the radius measurement. The imaging leg is designed to relay the image of the part at confocal to the camera. I listed the steps for the alignment of the laser scale, mechanical alignment, calibration of the laser scale, and the optical alignment of

the figure measuring interferometer. The focusing issue described may create problems in the radius measurement, but can be corrected with careful planning. I described and showed the measurements of three different sized stainless spheres with different microscope objectives, varying mask sizes, and with added spherical aberration. A discussion of the uncertainty in the radius measurement followed.

Further discussion of the experimental results and a comparison to the Gaussian and FRED models are in Chapter 6. A discussion of further work, including modifications on MORTI is in Chapter 7.

CHAPTER 5: THE EFFECT OF PHASE CHANGE ON REFLECTION ON THE CAT'S EYE POSITION

5.1 Introduction and Background

Many precision dimensional measurements, including the radius measurement, are based on interferometry which inherently relies on the reflection of light from a target. Upon reflection, light undergoes a phase change. This phase change depends on the material properties and can introduce a bias in the measurement. The phase change on reflection varies with incident angle, material properties, wavelength, and material depth. This variation affects measurements ranging from precision radius of curvature (by changing the cat's eye position), center thickness, gage block calibration, to scanning white light interferometry (SWLI) [42]. The goal of this research is to determine the effect of the phase change on the radius measurement.

The phase change on reflection depends on the material properties on both sides of the interface which are represented by the refractive index. For non-absorbing material, the phase change is identically zero or 180 degrees, depending on the refractive index change across the interface. Values other than zero or 180 degrees only occur when one or both of the materials are absorbing. The absorption of the material is captured by the imaginary component of a complex refractive index. Absorption is strong for metals and the

full complex refractive index must always be considered. In some precision applications the small imaginary component of nominally transparent materials cannot be ignored. Refractive index values are published for many materials [43,44,45], however these values are often contradictory, presumably due to variations in material composition and/or film thickness and measurement uncertainty. Furthermore, the optical properties of many alloys are not well known. Thin films, like those used in MEMS devices (which are commonly measured with SWLI), often do not have the same material properties as the bulk material.

Interferometry is well suited to measure phase changes, but a difference measurement must be made to measure the phase change on reflection. A typical configuration is to deposit a region of material A on a substrate of material B and then measure the apparent step height of material A. A schematic of this is shown in Figure 5-1. However, the physical step height must be known to determine phase change on reflection differences [46].

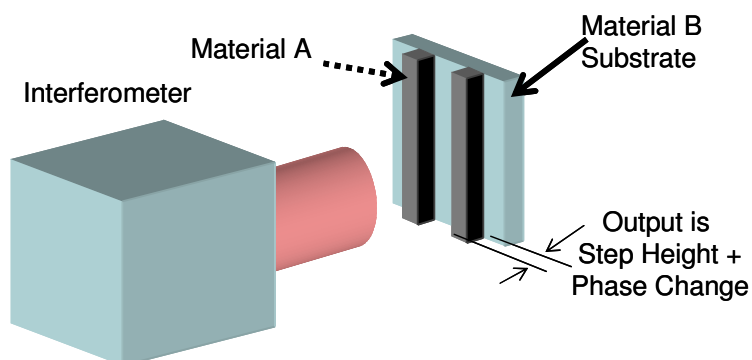


Figure 5-1: Schematic of interferometric phase change measurement where step height is inherently included in the measurement result.

The physical step height contribution can be intrinsically removed by depositing regions of the metal on the back side of a glass substrate and measuring the phase profile of light reflected internally from the back surface as shown in Figure 5-2. Such investigations have been carried out with SWLI [47], but the angle of incidence and wavelength dependence cannot be easily investigated with this method. In an early experiment [48], fringes of equal chromatic order were used to investigate the phase change on reflection over a range of wavelengths. In this experiment, the phase was not directly measured, but calculated through fringe counting.

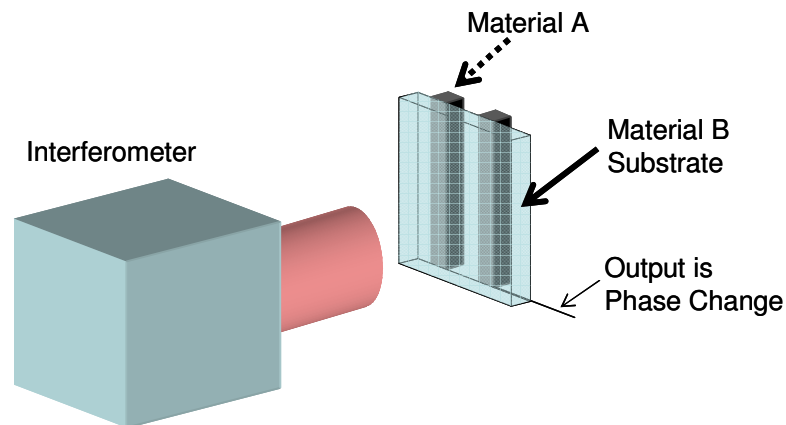


Figure 5-2: Schematic of interferometric phase change measurement where step height is inherently included in the measurement result.

We have investigated the phase change on reflection by using a combination of methods discussed in the literature. We are using phase shifting interferometry (PSI) and a sample geometry where an internal reflection is exploited to intrinsically remove the step height from the measurement. Our initial studies focus on normal incidence reflection for a range of metals with

632.8 nm wavelength light and varying the angle of incidence for a gold sample. Future work will investigate film thickness and wavelength dependence. In this work, we describe the theory behind the measurement, the experimental configuration, present examples of experimental results, and the connection to the cat's eye reflection and radius measurements.

5.1.1 Connection to Radius and Cat's Eye

The radius measurement, discussed in Chapter 1, requires two measurements, at confocal and at cat's eye. The geometrical model with a non-aberrated incoming beam is considered here. In this case, at the confocal position, all the rays hit the surface at normal incidence. Therefore, if there is a phase change, it is constant along the entire aperture. There will be a phase change on reflection at confocal if the test part has a complex component of the index of refraction, but there is no phase change if the complex component is zero. In either case, since the angle of incidence is always zero, the phase change is constant.

But, at cat's eye, in a geometrical model, the angle of incidence is not constant. It varies from 0° to a value dependent on the numerical aperture of the objective. This is the case of interest. Because the phase change is not constant, there may be a bias in the cat's eye position that does not occur in the confocal position. This suggested bias is dependant on polarization state of the incoming beam, the NA of the system, and the material properties of the test optic. If the imaginary component of the complex refractive index of the test optics is zero or can be approximated as zero (most glasses) the phase change

is constant at zero degrees for all incident angles and the bias will not occur. Therefore the suggested phase change bias is only a factor for metals and other materials with a complex component of the index of refraction.

The geometric model used here to predict the error due to the phase change, is of course, not accurate, especially for smaller parts. The focal region has a spread of rays and a much more complicated wavefront. Therefore, the angles that the rays hit the surface does are not the large angles as predicated by the in the geometric model. This leads to a smaller effect of the phase change on the radius measurement. Therefore, the effect calculated here is a worst case error. A method for calculating the phase change in the focal region for a diffracted model is not known.

The purpose of part of this work is to determine if this bias can be calculated and corrected for. Also, I am introducing a method of measuring the phase change using phase shifting interferometry and a new background subtraction method to reduce uncertainty.

5.2 Theoretical Calculations of the Phase Change

The experiments in this work focus on determining the phase change when light reflected from a non-absorbing media (glass) to an absorbing media (metal) interface, as indicated in Figure 5-3. The glass has an index of refraction of n_1 , and the metal has a complex index of refraction, $\hat{n} = n_2(1 - i\kappa_2)$. There is confusion in the literature over the definition of κ_2 . In some cases the complex index is defined as $n + ik$ (the letter k). Here we will use the Born and Wolf [49] convention of $n(1 - i\kappa)$, the Greek letter kappa not the letter k .

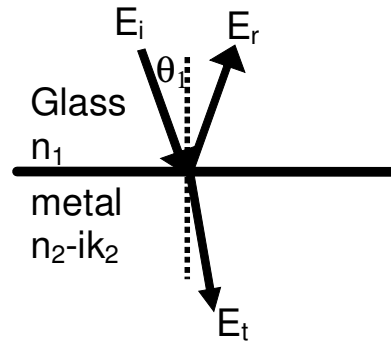


Figure 5-3: An electric field, E_i , from glass is incident from a glass substrate on bulk metal at an angle of θ_1 . The electric field is reflected (E_r) and transmitted in part (E_t).

The phase change, ϕ , of the reflected electric beam (E_r) is desired. We will first derive the case for non-normal angle of incidence, that is, $\theta_1 \neq 0^\circ$. Then the normal case will be derived from the non-normal case.

5.2.1 Non-Normal Angle of Incidence

This derivation comes from Born and Wolf [49]. I first define two new variables, u_2 and v_2 to be

$$u_2 + iv_2 = \hat{n}_2 \cos \theta_2,$$

Equation 5-1

where θ_2 is not physically defined, but is the angle of the transmitted electric field, E_t , to the surface normal in the metal. The law of refraction is used to remove the θ_2 term and to solve for u_2 and v_2 . The law of refraction and its square is

$$\begin{aligned} \hat{n}_2 \sin \theta_2 &= n_1 \sin \theta_1 \\ \sin^2 \theta_2 &= \frac{n_1^2 \sin^2 \theta_1}{\hat{n}_2^2} \end{aligned}$$

Equation 5-2 (a) and (b).

Squaring Equation 5-1 and solving for the cosine term, I find that

$$\cos^2 \theta_2 = \frac{(u_2 + iv_2)^2}{\hat{n}_2^2}$$

Equation 5-3.

By using the trigonometric identity $\sin^2 + \cos^2 = 1$ (Equation 5-2 and Equation 5-3) and setting the real and imaginary components equal, I derive

$$\begin{aligned} (u_2 + iv_2)^2 &= \hat{n}_2^2 - n_1^2 \sin^2 \theta_1 \\ \text{Real: } u_2^2 - v_2^2 &= n_2^2(1 - \kappa_2^2) - n_1^2 \sin^2 \theta_1 \\ \text{Imag: } u_2 v_2 &= n_2^2 \kappa_2 \end{aligned}$$

Equation 5-4.

The variables u_2 and v_2 are found using the quadric equation and substitution and are

$$\begin{aligned} 2u_2^2 &= n_2^2(1 - \kappa_2^2) - n_1^2 \sin^2 \theta_1 + \sqrt{[n_2^2(1 - \kappa_2^2) - n_1^2 \sin^2 \theta_1]^2 + 4n_2^4 \kappa_2^2} \\ 2v_2^2 &= -[n_2^2(1 - \kappa_2^2) - n_1^2 \sin^2 \theta_1] + \sqrt{[n_2^2(1 - \kappa_2^2) - n_1^2 \sin^2 \theta_1]^2 + 4n_2^4 \kappa_2^2} \end{aligned}$$

Equation 5-5.

Now u_2 and v_2 can be found using only physical attributes: the incident angle and the material properties of both materials. The next step is to determine the reflection coefficients at the interface. This is done by starting with the Fresnel formulae for reflection which are defined for both the TE and TM components of the light. TE and TM symbolize the transverse electric and transverse magnetic modes of the light and depend on the polarization state. The TE mode occurs when the polarization state is such that the electric field of the incident light is perpendicular to the plane of incidence and the TM mode occurs when the electric is parallel to the plan of incidence. TE and TM are also called the s- and p- polarization states.

The Fresnel formulae for reflection are

$$r_{TE} = \frac{n_1 \cos \theta_1 - \hat{n}_2 \cos \theta_2}{n_1 \cos \theta_1 + \hat{n}_2 \cos \theta_2} Amp_{TE}$$

$$r_{TM} = \frac{n_2 \cos \theta_1 - \hat{n}_1 \cos \theta_2}{n_2 \cos \theta_1 + \hat{n}_1 \cos \theta_2} Amp_{TM},$$

Equation 5-6 [49]

where Amp is the amplitude of the electric vector of the incident field. By substituting Equation 5-1 into Equation 5-6, the amplitude, p , and phase, ϕ , of the reflected field is calculated. The Fresnel formulae is then represented by

$$r_{TE} = p_{TE} e^{\phi_{TE}} = \frac{n_1 \cos \theta_1 - (u_2 + iv_2)}{n_1 \cos \theta_1 + (u_2 + iv_2)}$$

$$r_{TM} = p_{TM} e^{\phi_{TM}} = \frac{n_2 \cos \theta_1 - (u_2 + iv_2)}{n_2 \cos \theta_1 + (u_2 + iv_2)}.$$

Equation 5-7.

The Amp terms drop out because they are just multipliers. The phase is found from the tangent of the imaginary over real components of Equation 5-7 and is shown by

$$\tan \phi_{TE} = \frac{2v_2 n_1 \cos \theta_1}{u_2^2 + v_2^2 - n_1^2 \cos^2 \theta_1}$$

$$\tan \phi_{TM} = 2n_1 n_2^2 \cos \theta_1 \frac{2\kappa_2 u_2 - (1 - \kappa_2^2)v_2}{n_2^4 (1 - \kappa_2^2)^2 \cos^2 \theta_1 - n_1^2 (u_2^2 + v_2^2)}.$$

Equation 5-8.

To explicitly solve for the phase change values, Equation 5-5 for u_2 and v_2 is substituted into Equation 5-8. This is not shown here for clarity. Also, the amplitude of the reflection term and the amplitude and phase of the transmission term are not defined here. While these are required for a full description of the

light beyond the interface, they are not required here; only the phase change of the reflected light is necessary.

5.2.2 Normal Angle of Incidence

At normal incidence, $\theta_1=0^\circ$ the state of polarization is inconsequential. The phase change for both the TM and TE mode are equal [50]. By substituting $\theta=0^\circ$ in Equation 5-5, $u_2 + v_2$ is equal to $n_2(1 + \kappa_2)$. Therefore, for normal incidence, the Fresnel amplitude reflection coefficient, r , is

$$r = pe^\phi = \frac{n_1 - n_2(1 + i\kappa_2)}{n_1 + n_2(1 + i\kappa_2)}$$

Equation 5-9

And the phase change, ϕ , is calculated using

$$\tan \phi = \frac{2n_2\kappa_2n_1}{n_2^2 + n_2^2\kappa_2^2 - n_1^2}$$

Equation 5-10

5.2.3 Determining the Values of the Index of Refraction

While the phase change on reflection is a function of the thickness of the metal, I first consider the case of a bulk material. The refractive indices of the materials are in published literature. Many of the published values list k for the complex part of the refractive index; k is then divided by n to find κ (kappa) (see Section 5.2). Published values of n and k [43,44,45] vary, even within the same source. Also, in each source, the values are listed in a table form relative to the measured (or calculated) wavelength. I used various methods of interpolation to

find the values required at 632.8 nm: a two point fit around 632.8 nm, a 10 point linear fit, and a 10 point two-degree polynomial fit. Table 5-1 shows an average value for the complex index of refraction for copper and gold. The average is of three sources [43,44,45] and three different interpolation methods for each source. The percent variation is one standard deviation of all the values as a percentage of the average.

Table 5-1: Table of published n , k , and κ values and their percent variation (one standard deviation).

	n , average	k , average	κ , average	n , %variation	k , %variation	κ , %variation
Copper	0.294	3.370	12.426	27.0	1.7	35.0
Gold	0.182	3.188	19.729	41.5	2.0	34.4

5.2.4 Phase Change Values at Normal Incidence

Using the complex index of refraction for copper and gold from Table 5-1 and Equation 5-10 I calculated the phase change on reflection for normal incidence, shown in Table 5-2. The variation in the $\phi,^\circ$ column shows one standard deviation of the phase change due to the variation in the n and κ values. The glass substrate is fused silica with a refractive index of 1.457 [51]. The uncertainty in the index of the glass is very low as compared to the metal and can be neglected. One can see that the phase change on gold has a large variation due to the large variations in n and κ .

Table 5-2: The complex index of refraction and the calculated phase change values at normal incidence, for glass to metal.

	$\phi, ^\circ$	Uncertainty in $\phi, ^\circ$
Copper	43.3	+36.3, -23.1
Gold	44.0	+48.2, -20.0

5.2.5 Phase Change Values at Non-Normal Incidence

The phase change on reflection from a glass to gold interface as the angle of incidence varies for both the TE and TM modes is shown in Figure 5-4. As a check, I calculated the reflection coefficients, Equation 5-7, for a glass/gold interface, shown in Figure 5-5. As expected, the reflection is above 90%. Also, the phase change for an air/gold interface is shown in Figure 5-6. This is required for further models.

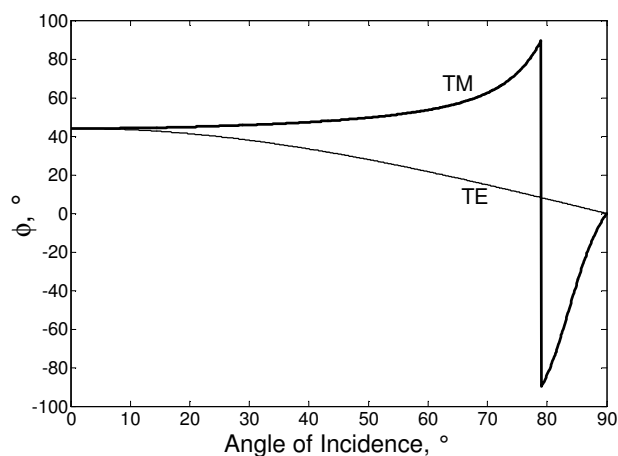


Figure 5-4: Phase change at glass/gold interface for varying angle of incidence. The governing equation is Equation 5-8 and the complex refractive index of refraction in Table 5-1.

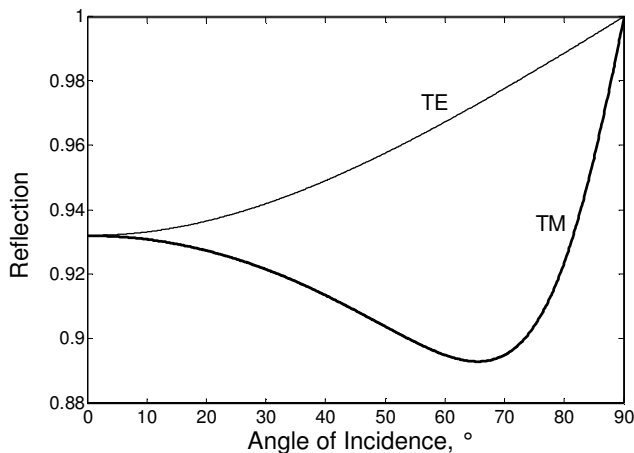


Figure 5-5: The reflection coefficients at glass/gold interface for varying angle of incidence.

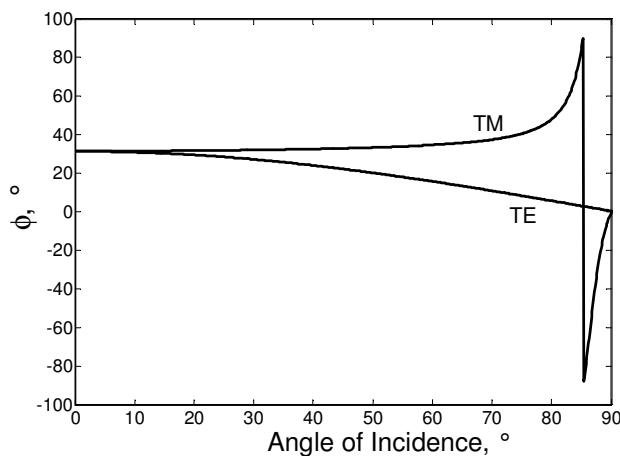


Figure 5-6: Phase change at air/gold interface for varying angle of incidence.

5.3 Impact on the Cat's Eye Position

5.3.1 Added Defocus Due to the Phase Change

As shown in Section 5.2.5, the phase change varies as the angle of incidence varies. This section shows the relationship between this phase variation and the determination of the cat's eye position, assuming a geometric model for the cat's eye reflection. I am initially only investigating the TE mode for

two reasons. The Vereco interferometer used in for the experiments is linearly polarized in the TE mode and the TE mode has a larger variation (than the TM mode) in phase change. Investigating the TE mode demonstrates the worst case bias in the cat's eye position due to the phase change. First, the phase shown in Figure 5-6 is converted to a height using

$$Phase = \frac{4\pi Height}{\lambda}$$

Equation 5-11

where λ is the wavelength of the light, 632.8 nm. The additional factor of 2 in Equation 5-11 corrects the phase change measurement, which is double pass for height measurements but single pass for phase change measurements. This equation is true for the radius measurements. Then, I consider the largest NA of interest (0.7), where the maximum angle of incidence at the cat's eye position is 44.4°. At this aperture, the phase change is well approximated with a quadratic line fit, as shown in Figure 5-7. A quadratic fit is also valid at the smaller NAs.

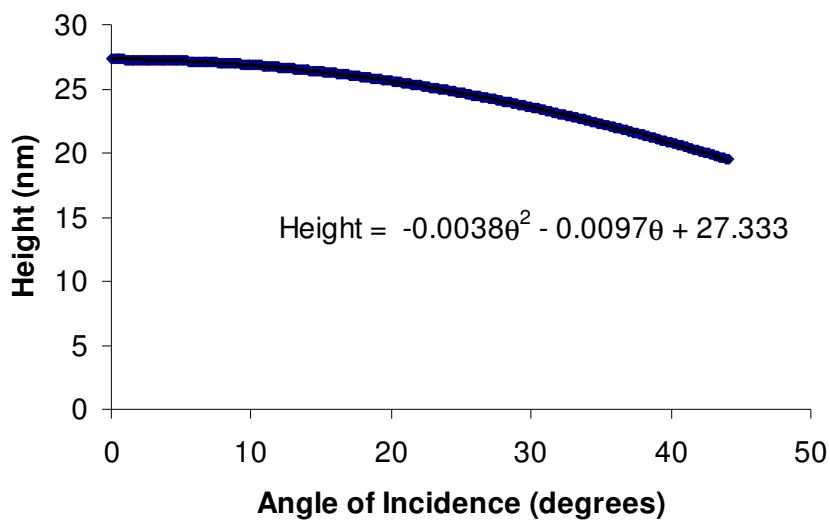


Figure 5-7: Height error due to phase change at air/gold interface for TE mode showing the fit line and parameters for NA = 0.7.

Using this phase change profile, I created a map of apparent height for the full aperture at each NA of interest (0.28, 0.42, 0.55, and 0.7) by rotating the above profile around the height axis. These results are shown in Figure 5-8. The Zernike defocus term was calculated for each map and is also shown.

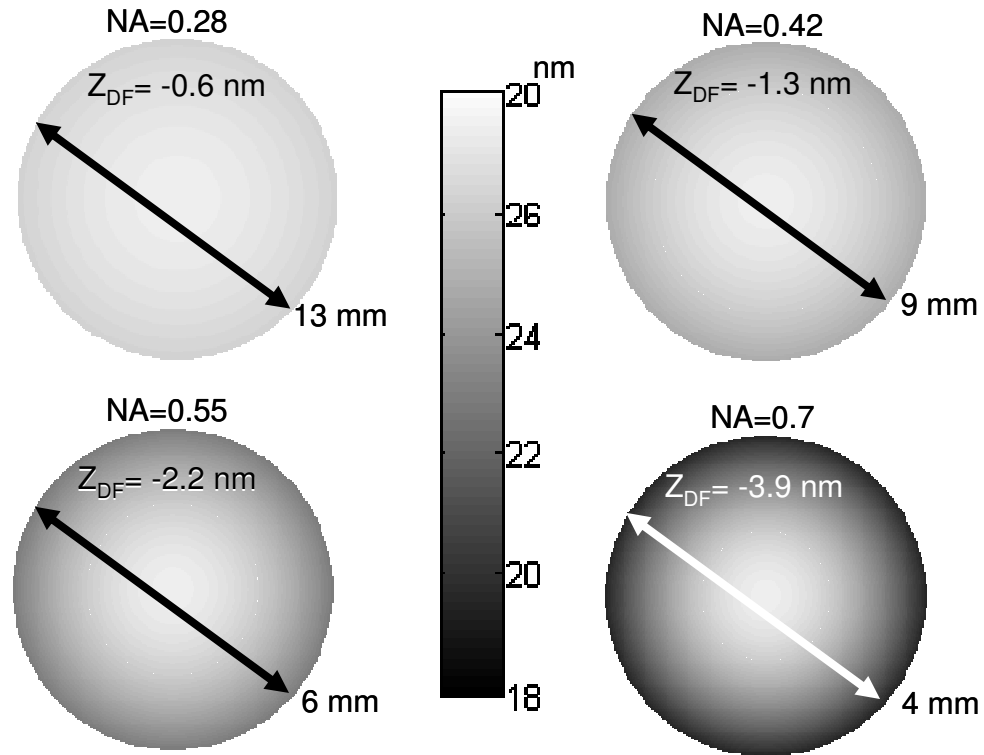


Figure 5-8: Height error maps (8 mm diameter, all) due to phase change at varying NA showing the Zernike defocus term.

5.3.2 The Offset Due to Phase Change

In the radius measurement, a chart of Zernike defocus vs. position (along the optical axis) is required to determine the cat's eye position. The slope of this chart is required to determine the offset in the cat's eye position due to the phase change. Also required is the Zernike defocus value from the height error maps shown in Figure 5-8. The slope is best determined from experimental data, but can be approximated theoretically using [52]

$$\text{Slope} \left[\frac{nm}{nm} \right] = 1 - \sqrt{1 - NA^2} .$$

Equation 5-12

By simple multiplication the worst possible case of offset in the cat's eye position due to the phase change on reflection is determined. The results are summarized in Table 5-3. It is important to note that the aperture of the objective was used for visualization purposes only and does not affect the offset of the cat's eye position if the NA of the objective does not vary.

Table 5-3: The worst case offset values due to phase change.

NA	Theoretical Slope (nm (defocus) per nm (position))	Zernike Defocus Term (nm)	Offset (nm)
0.28	0.04	-0.6	-0.0
0.42	0.09	-1.3	-0.1
0.55	0.16	-2.2	-0.4
0.7	0.28	-3.9	-1.1

The phase change adds a negative Zernike defocus value to all the phase maps at cat's eye. Therefore, the offset due to the phase change is toward the interferometer and the measured radius is smaller than the actual. This can be seen in the following data set in Figure 5-9 (created for example purposes only). One set of data demonstrates the dependence of defocus on position without consideration of phase change on reflection. The phase change on reflection effect is considered in the other data set by adding a (negative) defocus. The true cat's eye reflection at the intercept of the no phase change data, but the interferometer measures the cat's eye position at the intercept of the phase change data.

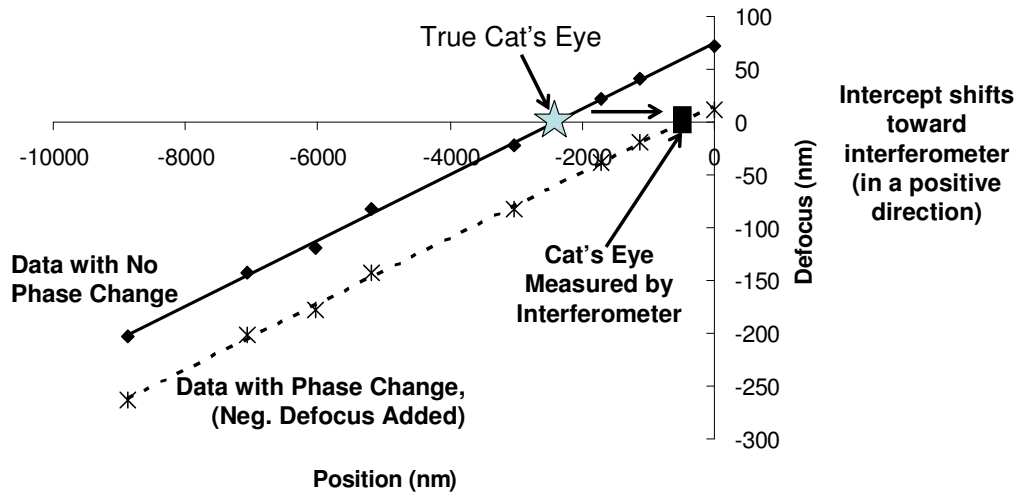


Figure 5-9: Example data set demonstrating the shift toward the interferometer with phase change. The amount of defocus added is exaggerated.

The offset is small, less than one nm in most cases. This demonstrates that this phase change does not have a large effect on the cat's eye position. Next, I will test to determine how much the offset varies with the uncertainty in the refractive index.

5.3.3 Offset as a Function of Uncertainty in the Refractive Index

If the uncertainty in the refractive index demonstrated in Section 5.2.3 is considered, the Zernike defocus values shown in Figure 5-8 vary and consequentially the offset varies, as shown in Table 5-4. One standard deviation on both sides of the average n and κ were considered. As shown, the offset does vary, but the magnitude still remains small, less than 3 nm for the worst case. For the most accurate offset results, the slope from the radius experiment (not the theoretical values) and the actual phase change of the test optic material are required.

Table 5-4: Offset in the cat's eye position when considering the variation in the complex index of refraction.

NA	Offset (nm) Away From Interferometer		
	Original ($n = 0.18, \kappa = 19.73$)	$n+U_n, \kappa+U_\kappa$ ($n = 0.26, \kappa = 26.44$)	$n-U_n, \kappa-U_\kappa$ ($n = 0.11, \kappa = 13.02$)
0.28	-0.0	-0.1	-0.0
0.42	-0.1	-0.3	-0.1
0.55	-0.4	-0.9	-0.2
0.7	-1.1	-2.7	-0.6

5.3.4 Offset due to the TM mode

The above analysis shows the TE mode of polarization as a worst case offset. The actual cat's eye reflection is a combination of the TE and TM modes and is interferometer dependent. Consider the case of the Veeco interferometer where the light is polarized linearly up and down. As the light is focused by a transmission sphere, the polarization does not change. But, because the part is spherical, the plane of incidence changes, therefore both TE and TM modes are reflected from the surface. This is shown in Figure 5-10. Before the reflection, Figure 5-10(a), all light is linearly polarized up and down. The cross sections at 1, 2, and 3 demonstrate how the light is reflected. At 1 (Figure 5-10 (b)), the TM light coming in is reflection as TM light. At 2, Figure 5-10(c), the TE light coming in is reflection as TE light. At 3, Figure 5-10(d), the light is both TE and TM coming in, but because the TE and TM modes have different phase changes, the TM will be delayed. This delay will result in elliptically polarized light.

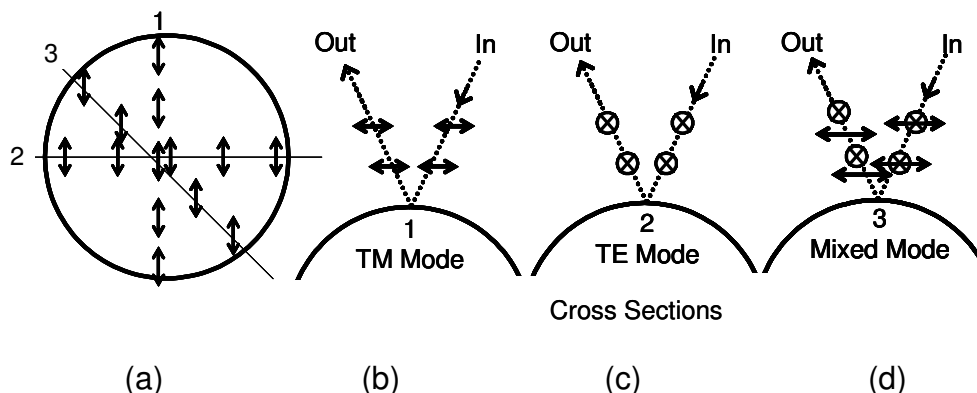


Figure 5-10: A schematic of the polarization state at the CE reflection: (a) before reflection, (b) TM Mode (parallel to plane of incidence), (c) TE mode (perpendicular to plane of incidence), and (d) TE and TM modes.

With an input of linearly polarized light, astigmatism will result because the TE and TM modes have different phase change values, but the defocus value will be dominated by the TE mode phase change value because it is larger than the TM mode. It is important to note that the defocus is depends in a complicated way on the input polarization state.

5.4 Experimental Plan

The above analysis demonstrates the need to accurately know the phase change on reflection value for the test optic. I used the experiment and sample design introduced in Figure 5-2 to measure the phase change as described in the following sections.

5.4.1 Sample Preparation

The samples were 12.7 mm diameter glass substrates with 3.0 mm wide strips of evaporated metal as shown in Figure 5-11(a). The metal was deposited using a Varian 3125 Vacuum Thin Film System. The metal strips have a nominal

height of 500 nm. The height was determined by a quartz crystal thickness monitor in the evaporator and confirmed using a calibrated profilometer. The mask used in the evaporator is shown in Figure 5-11(b).

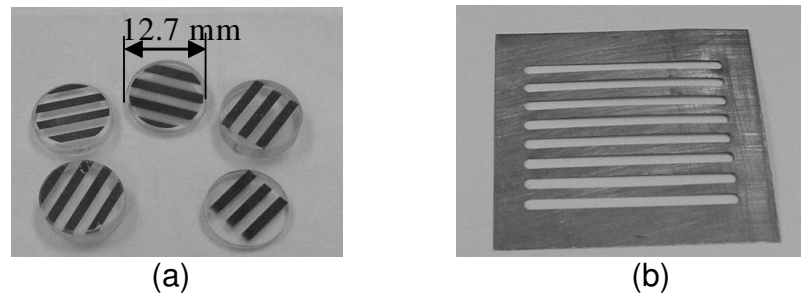


Figure 5-11 (a) The samples with Au, Al, or Cu and (b) The 50 mm square metal mask.

5.4.2 Measurement Plan, Normal Incidence

A Veeco/Wyco PSI was used to measure the phase change. The sample was configured for a back measurement as shown in Figure 5-12. By measuring through the sample, we are directly measuring the phase change difference between the glass/air interface and the glass/metal interface. A front configuration would measure the phase change plus the step height. A Claphamdue flat was used as the transmission flat which provides a reasonable fringe contrast between the glass and metal regions of the sample and greatly improves measurement quality. A picture of the measurement is shown in Figure 5-13.

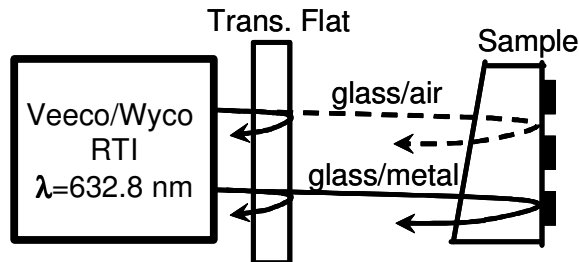


Figure 5-12: The measurement configuration for normal incidence. The substrate is wedged to prevent interference from the front surface.

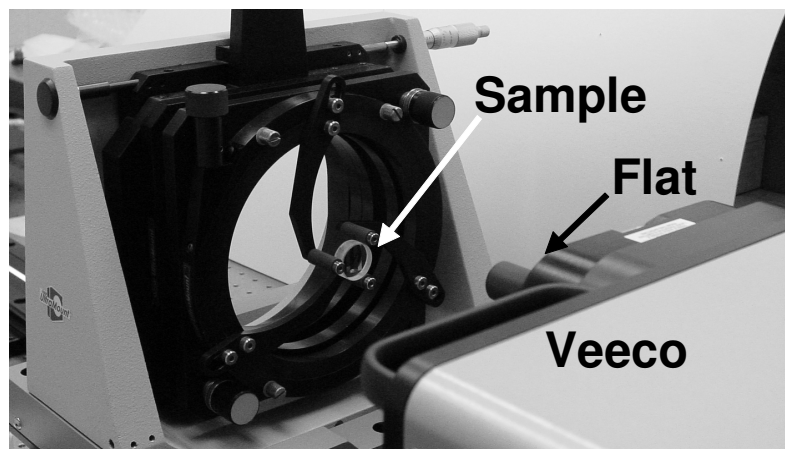


Figure 5-13: The sample as measured in the interferometer for normal incidence.

The apparent step height observed in the data is the phase change at the glass/metal interface relative to a glass/air interface. The absorption of fused silica is very low; consequently, the phase change on reflection for the glass/air interface is approximately zero (an internal reflection). This assumption leads to a negligibly small contribution to the final uncertainty.

5.4.3 Determining the Phase Change at a Air/Metal Interface

In the experiment described above, the phase change occurs at glass/metal interface and Equation 5-10 is used to determine the theoretical phase change. But, many interferometric measurements involve a different interface

combination, namely reflection at an air/metal interface. The air/metal change cannot be directly determined from a single measurement of the glass/metal interface. But, the measurement of the glass/metal interface can be repeated for different glass substrates and the results used to estimate the value of the phase change at an air/metal interface.

The desired quantity is ϕ_{AM} , phase change at the air/metal interface. Using Equation 5-10 and substituting the appropriate material properties, the tangent of ϕ_{AM} is

$$\tan \phi_{AM} = \frac{2n_M \kappa_M n_A}{n_M^2 + n_M^2 \kappa_{M^2}^2 - n_A^2}.$$

Equation 5-13

where A indicates air and M , metal. The phase change for the glass to metal interface, ϕ_{G1M} and ϕ_{G2M} , is measured experimentally for the two samples with different substrate glass (n_{G1} and n_{G2} , known) and the same metal (n_M and κ_M , unknown). The equations for this phase change are

$$\tan \phi_{G1} = \frac{2n_M \kappa_M n_{G1}}{n_M^2 + n_M^2 \kappa_{M^2}^2 - n_{G1}^2} \quad \text{and} \quad \tan \phi_{G2} = \frac{2n_M \kappa_M n_{G2}}{n_M^2 + n_M^2 \kappa_{M^2}^2 - n_{G2}^2}$$

Equation 5-14.

Assuming that the indices of refraction of the glasses are known, the remaining unknowns in the equation, n_M and κ_M , can be solved for. By substituting these values into Equation 5-13 and assuming the index of refraction of air is 1, the phase change at the air/metal interface can be calculated.

This method for determining the phase change at the air/metal interface is outside the scope of this work and is presented here only to demonstrate the method.

5.4.4 Measurement Plan, Non-Normal Incidence

Initial measurements were performed on the Veeco interferometer for non-normal incident angles. In this measurement, the sample is placed in a skip-flat geometry, [53] as shown in Figure 5-14 and Figure 5-15. The sample is on a rotary stage that rotates in the plane of the paper as shown in the figure. First the sample is aligned straight on, as in a normal angle of incidence measurement. Then the rotary stage is turned to the desired incident angle. At each angle, the return flat is aligned such that the light reflected from the back of the sample reflects off the return flat to the back of the sample and then back to the Veeco. Two areas of concern are that the measurement of the phase change occurs twice; therefore the conversion from height to phase is not the same as the normal angle of incidence measurement. In addition, the angle of incidence on the glass/metal interface is not the same angle of the rotary stage due to the wedge geometry of the sample and the refraction of the light. The relationship between the angle of the rotary stage and the angle of incidence can be solved for using simple geometric relationships.

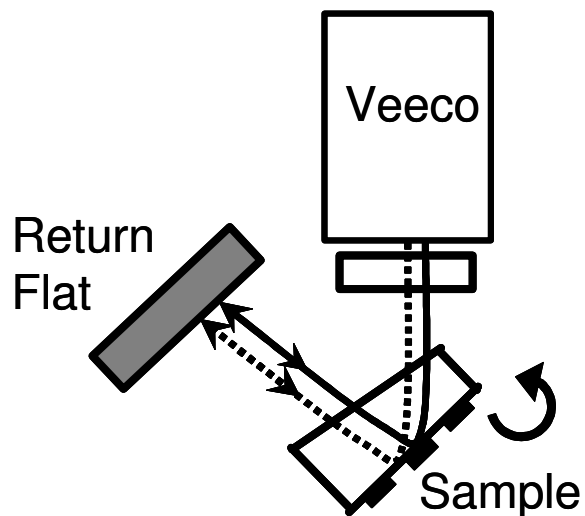


Figure 5-14: The sample for a non-normal incidence measurement.

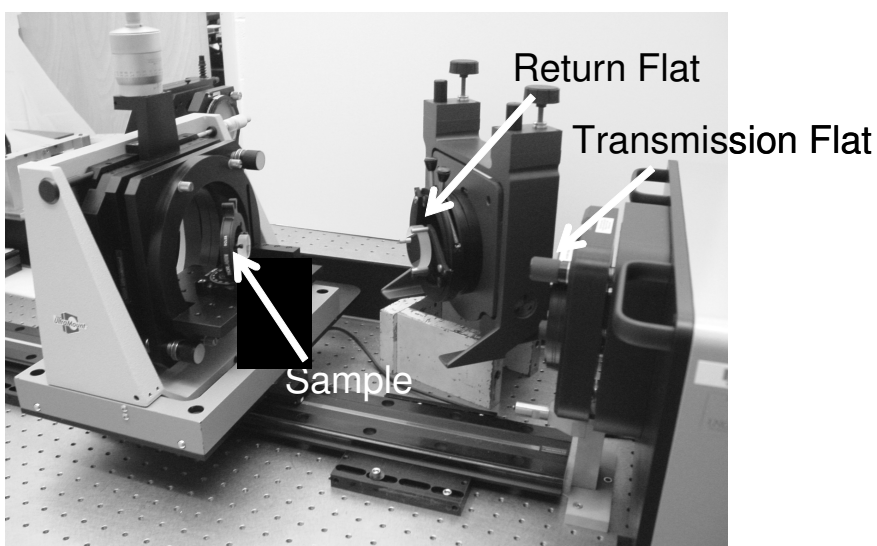


Figure 5-15: The sample in the non-normal incidence configuration.

5.5 Analysis and Results

Because the measurements are conducted through the glass substrate, the inhomogeneities and surface figure error of the glass are included in the phase change measurement. This will limit how well the phase change difference between the two regions can be estimated. To minimize uncertainty due to this,

the back of the substrate is measured in the same configuration and nominally the same position before the metal is deposited. This background measurement is then subtracted from all subsequent measurements. This was done for each substrate and for both the normal and varying angle of incidence measurements. The subtraction process leads to a significant contribution to the uncertainty and is discussed in more detail in Section 5.5.3.

5.5.1 Analysis, Normal Angle of Incidence

An example measurement after background subtraction is shown in Figure 5-16. Note that the apparent height shown in Figure 5-16 is not a physical height, but an artifact of the phase change on reflection. All of the light is reflected from the nominally flat back of the glass substrate. The apparent height, h , is converted to phase, ϕ , using Equation 5-11 because the normal angle of incidence experiment is double pass for height features but single pass for phase change measurements.

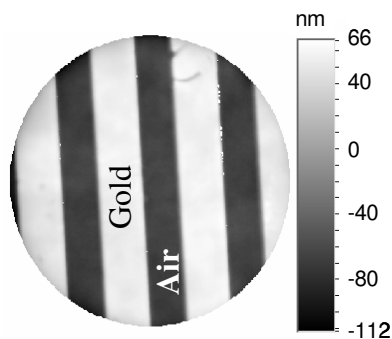


Figure 5-16: A measurement of the normal angle of incidence post background subtraction.

The multiple region analysis tool in the Vision software was used to separate the metal and air regions and to calculate the RMS, the number of points, and the mean value of each region. The difference between the mean value for the air and metal regions is the phase change on reflection for the glass/metal interface. The number of points and RMS are used to calculate the uncertainty in the mean value.

5.5.2 Analysis, Varying Angle of Incidence

Only one sample, gold, was measured for the effect of varying incident angle. The analysis for this measurement is the same as for the normal angle analysis, including the phase to height conversion. The skip flat test is double pass in phase and quadruple in height leading to Equation 5-11. As above, the multiple region analysis tool was used to separate the metal and glass regions. Again, the difference in the mean value of the metal region and the mean value in the height region is the phase change.

5.5.3 Uncertainty

I have investigated the primary sources of uncertainty and estimated their contribution to the measured phase change using a gold measurement as an example for all of the following cases. Variations in the evaporation process create a level of uncertainty not studied here.

The RMS of each area (metal and air), when divided by the square root of the number of points indicates the uncertainty in the mean value (phase). Without subtraction, the uncertainty in the phase of the metal and air regions are

both 0.09° , with subtraction, they are 0.07° and 0.06° , respectively. This reduction demonstrates the importance of the background subtraction.

The background subtraction is a major source of uncertainty. The pre- and post-deposition samples can not be exactly repositioned in the same orientation in the interferometer. Rotation, translation, and zoom differences occur between the two measurements. Also, shadowing effects required that the edge of each strip be trimmed in the measurement; this trimming is subjective and also contributes to uncertainty.

A simplified Monte Carlo simulation was performed to determine the uncertainty associated with repositioning and trimming. In software, I manipulated the data, performed the normal subtraction process, and calculated the resultant phase change. The manipulation was done such that it would represent reasonable uncertainty in repositioning in the lab: translating ± 20 pixels in both x and y , rotating $\pm 10^\circ$, zooming 5%, and trimming 0 to 5 pixels. I then calculated the phase change for each of the above manipulations. The worst case for each situation is shown in Table 5-5. The difference from the non-manipulated case is indicated in the difference column. These differences were then combined in a root sum square method to estimate the uncertainty associated with repositioning and trimming, 3.8° .

Table 5-5: Calculated phase change for the worst case for each case for an example measurement of gold.

Without Subtraction	140.5°	
With Subtraction	132.1°	
With Subtraction and Manipulation		Difference
Trim	133.8°	1.7°
Rotate	132.5°	0.4°
Zoom	135.5°	3.3°
Translate	132.2°	0.1°
Subtraction Uncertainty:		3.8°

Repeatability and reproducibility studies helped determine uncertainty due to environmental effects. Reproducibility was estimated by removing the sample from the interferometer, waiting a day, and repeating the measurement. The repeatability of the measurement is 0.26° and reproducibility 0.50°. The final uncertainty is then estimated by combining all the above uncertainties in a root sum square method. The final combined uncertainty for phase change is on reflection for this experimental method is 3.8°.

5.5.4 Results, Normal Angle of Incidence

I measured the gold sample on three days, twenty times each, for a total of 60 measurements, where each measurement is an average of eight. The calculated average phase change for gold is 131.4° ±3.8, corresponding to a height change of 115 nm ±3.8 nm. This compares well to the values in Table 5-2 from the literature.

The result for the copper sample is only preliminary because measurements of the substrate before the metal was deposited were not

possible. I used the following modified background subtraction, though. In software, I masked the metal region of the measurement and performed a Zernike analysis on the remaining glass region. Using these Zernike coefficients, I generated a simulated substrate, which was used for subtracting the blank substrate.

I measured the copper sample 20 times each, where each measurement is an average of eight. The calculated phase change for copper is $173.73^\circ \pm 3.8^\circ$. This does not agree well with the values from Table 5-2. For comparison, the phase change for gold using the same method is 137° . Repeated experiments would have to be carried out to pinpoint the cause of the discrepancy. Contamination of the copper source in the evaporator, which would significantly change the refractive index, is a likely cause.

5.5.5 Results, Varying Angle of Incidence

Results from the non-normal incidence measurements are not presented here because of the following. The range of allowable incident angles is 17° to 33° due to physical constraints. At an incident angle of 17° , the theoretical phase change for the TE mode is approximately 42° (Figure 5-4) and at 33° it is approximately 36° . Therefore, the measurement requirement is to distinguish between 8° (and smaller for incident angles between 17° and 33°) of phase change.

The uncertainty for the phase change measurement in a normal incidence setup is $\pm 4^\circ$. The uncertainty for the non-normal phase change measurement is not calculated here, but will be larger than $\pm 4^\circ$. It will be larger due to the

roughness of the return flat, traveling through the sample twice, and the incident angle measurement.

The approximately 8° phase change that I am trying to distinguish is not that much larger than the 4° uncertainty. The measurement uncertainty must be reduced to achieve a useful measurement of the angle dependence. This could be done with improved fixturing and is beyond the scope of this project. The method presented is meant to demonstrate the possible effect of phase change on reflection on the radius measurement, and to offer a methodology to estimate and measure the effect.

5.6 Conclusions and Continuing Work

The effect of the phase change on interferometric radius measurements was presented along with some initial measurements of the phase change and normal and non-normal incidence.

The worst-case offset in the cat's eye position for a gold test part is on the order of 3 nm toward the interferometer. Therefore the measured radius of a typical metal sphere is too small by 0 to 3 nm.

Using an internal reflection at a glass/metal interface, interferometric measurement show a phase change for normal incidence glass to gold is $131.4^\circ \pm 3.8^\circ$ and glass to copper of $173.73^\circ \pm 3.8^\circ$. The measured values agree well with theoretical calculations for gold, but not for copper, presumably to copper contamination in the evaporator. Initial measurements of the phase change for glass to gold at varying incident angle were performed, but not presented due to the high uncertainty.

The uncertainty in the phase change measurement is dominated by the background subtraction process. This uncertainty could be reduced with more improved fixturing and careful planning of the blank substrate measurement. The blank substrate and the sample with metal must be measured at the same zoom, x-y position, and rotation. The best way to reduce the position contribution would be to build a kinematic fixture for the sample. The substrate would go into the fixture and be measured on the interferometer with the opposing side of the kinematic fixture constraining it to one position. Then the fixture (with the substrate) would go directly to the evaporator. After evaporation, the fixture with the sample (with metal) would be measured in the same opposing fixture on the interferometer.

CHAPTER 6: DISCUSSION OF RESULTS AND COMPARISON

6.1 Introduction

In this chapter I discuss and compare the results from the Gaussian model (Chapter 2), the FRED Physical Optics model (Chapter 3), and the experimental data from MORTI (Chapter 4). There are limitations on how well the comparison can be performed. There is no “known” radius for experimental data. The uncertainty in radius in the FRED model, like with all physical optics modeling packages, is large. The model depends to a high degree on the actual experimental setup, such as the imaging optics, the spacing of the components, aberrations in the system, the microscope objective (which is proprietary information), and the masking. These parameters can not be modeled exactly. The final limitation on comparison is that the measurement uncertainty is large. Future work includes reducing this uncertainty.

The results from the Gaussian model, the FRED model, and the phase change calculations are summarized in Figure 6-1. This chart is a reprint of Figure 1-5 and shows the error in the simulated radius measurement when a geometric model is used instead of a Gaussian or FRED Model. The spread in the data from the Gaussian and FRED models is due to the different input parameters (NA, input beam type, aberrations, etc.) and the uncertainty in the model.

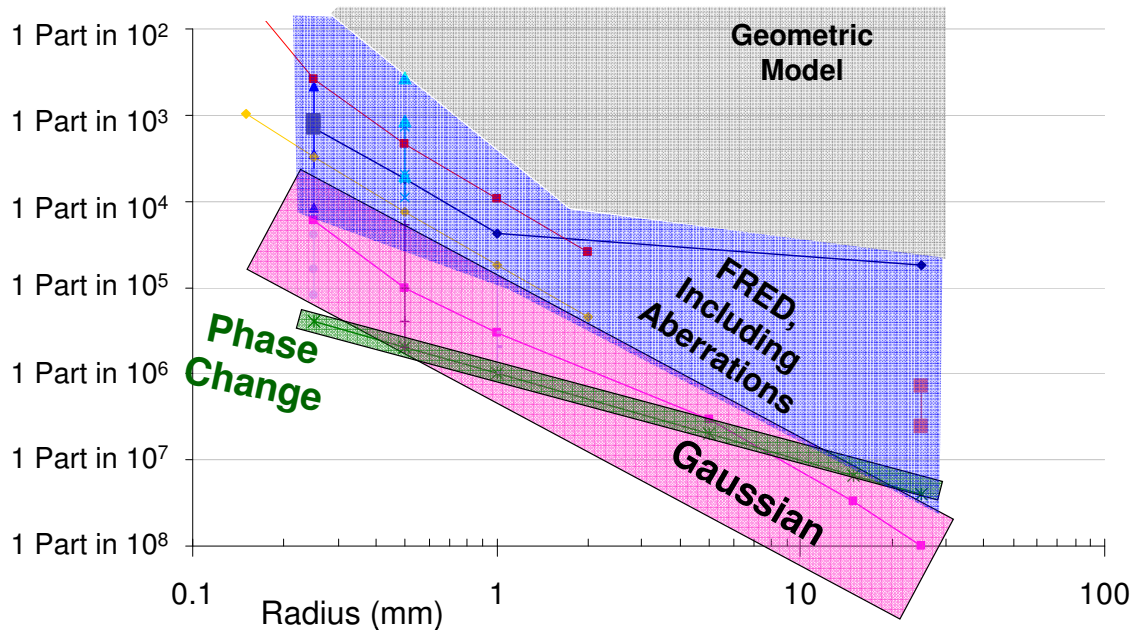


Figure 6-1: The error in the radius measurement when the geometric model is used instead of a more detailed model.

6.2 Numerical Aperture and Part Size

I varied the numerical aperture in experiment by using different microscope objectives but am unable to draw any conclusions about these experiments due to the observed small changes and the high uncertainty. The cat's eye and confocal positions did shift when the objective was changed. This is most likely a mechanical effect, not optical, and should not affect the measured radius.

I varied the numerical aperture in simulation by varying the focal length and input aperture size of the lens (or parabola) in the Gaussian and FRED models. A schematic of these results is shown in Figure 6-2. The numerical results are shown in Section 2.6.2 (Gaussian Model) and Sections 3.8.2 and 3.9.2 (FRED Model). The error is larger for smaller input part size and for smaller NAs (smaller light cone angle). This is expected because the smaller NA leads to a larger

caustic region. The error in the radius is larger in the FRED model than the Gaussian Model, by about an order of magnitude. This is likely because the FRED model takes into account more effects than the Gaussian model.

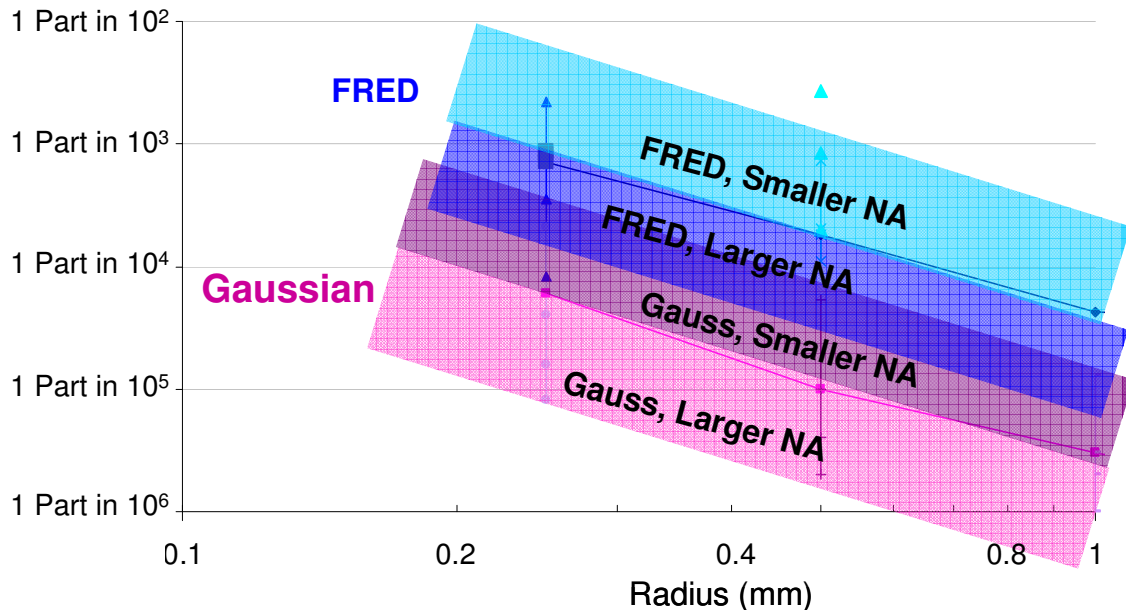


Figure 6-2: Error in the simulated radius measurement from the FRED and Gaussian models with varying the NA.

Results for varying part radii at 0.42 NA for the Gaussian and FRED models are shown in Table 6-1. These results can not be compared to experiment because I do not know the error in the measured radius. The errors in radius increase for the smaller parts for both models. The errors are larger in the FRED model than the Gaussian model for both the Gaussian and the circular aperture input beams. The results from the FRED model Gaussian input and the Matlab Gaussian model do not compare well, even though they were nominally the same setup. They differ by at least an order of magnitude. Some of this

difference is due to the pixilation of the camera in FRED, the lens (Gaussian) parabola (FRED) difference, errors in the Zernike fitting algorithm, and most likely, the clipping of the data in FRED. When the single Gaussian beam (infinite in area) is propagated in FRED, the program must clip the beam when it interacts with the parabola and the camera. In addition, by forcing FRED to propagate a single Gaussian beam, I am asking the program to do something it was not intended to do. Because of this, the results from FRED using the single Gaussian beam are questionable.

Table 6-1: The results when varying the radius.

Radius	Gaussian Model	FRED, Gaussian Input	FRED, Circular Aperture
0.2 or 0.25	5 parts in 10^5	1 part in 10^4	7 parts in 10^4
1	2 parts in 10^6	1 part in 10^5	4 parts in 10^5

6.3 Spherical Aberration

An explanation of retrace errors is required for this discussion. Retrace errors occur in systems with aberrations, that is, for all the experimental measurements and in the FRED simulation with added spherical aberration. All of the experimental measurements have inherent aberrations, even without the added spherical aberration of a glass plate.

6.3.1 Ray Trace Model

I first consider retrace errors in a geometric ray model of the radius measurement. At confocal, in a system with aberrations, the rays are not normal to the sphere surface. Therefore, the rays reflect from the surface at an angle and travel back through the interferometer along a different path than they came in on, causing an interferometer bias in the surface map that is not exactly twice the aberration from a single pass. This interferometer bias will offset the defocus terms that are used to determine the confocal position and therefore will cause an error in the position. The retrace errors at confocal will be larger for smaller radii (larger curvature) parts because the highly curved surfaces will cause the angle of the reflected rays to be even larger meaning the incoming and outgoing beams will be more offset in the interferometer.

This retrace error is normally not a large concern in precision macro-scale radius measurements because the error is considered to be the same at confocal and cat's eye position. In this case, the error will cause an offset in both positions, but the difference between the two positions, and therefore the radius, will remain the same. But, for micro-scale parts, the retrace error is different for confocal and cat's eye positions. Figure 6-3 shows a geometric ray model of cat's eye with no aberration and with a half wave of added spherical aberration from a geometric ray trace Zemax simulation by Davies [41]. Without aberration, there is no retrace error at cat's eye (or confocal). With the aberration, the beam spot size at cat's eye is approximately $4\ \mu\text{m}$. With this relatively large spot size as compared to the radius of the part, the rays are reflecting from the surfaces at

large angles and causing larger retrace errors at cat's eye than at confocal. The analysis of the retrace errors at confocal is not shown here.

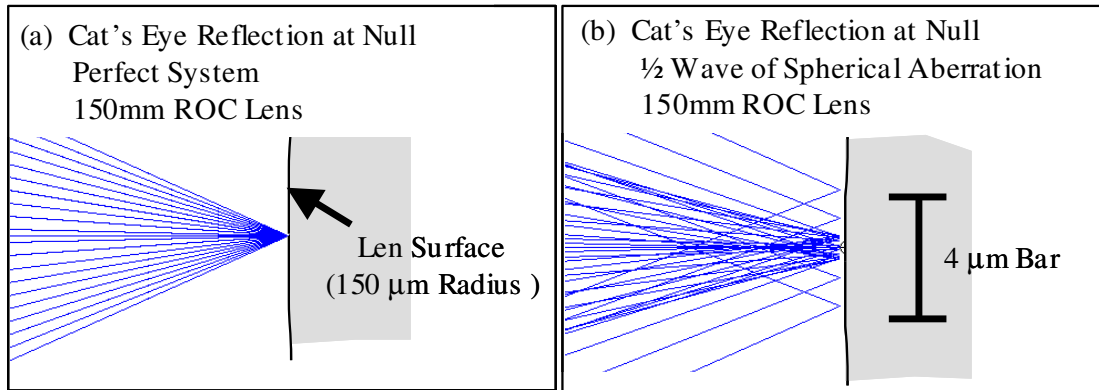


Figure 6-3: Picture of cat's eye reflection from a Zemax model of a radius measurement [54].

These retrace errors are the reason the measured radius changed in experiment and the FRED simulation when the glass plate was introduced into the system. The error in the radius measurement from the geometric Zemax model is shown in Figure 6-4 [54].

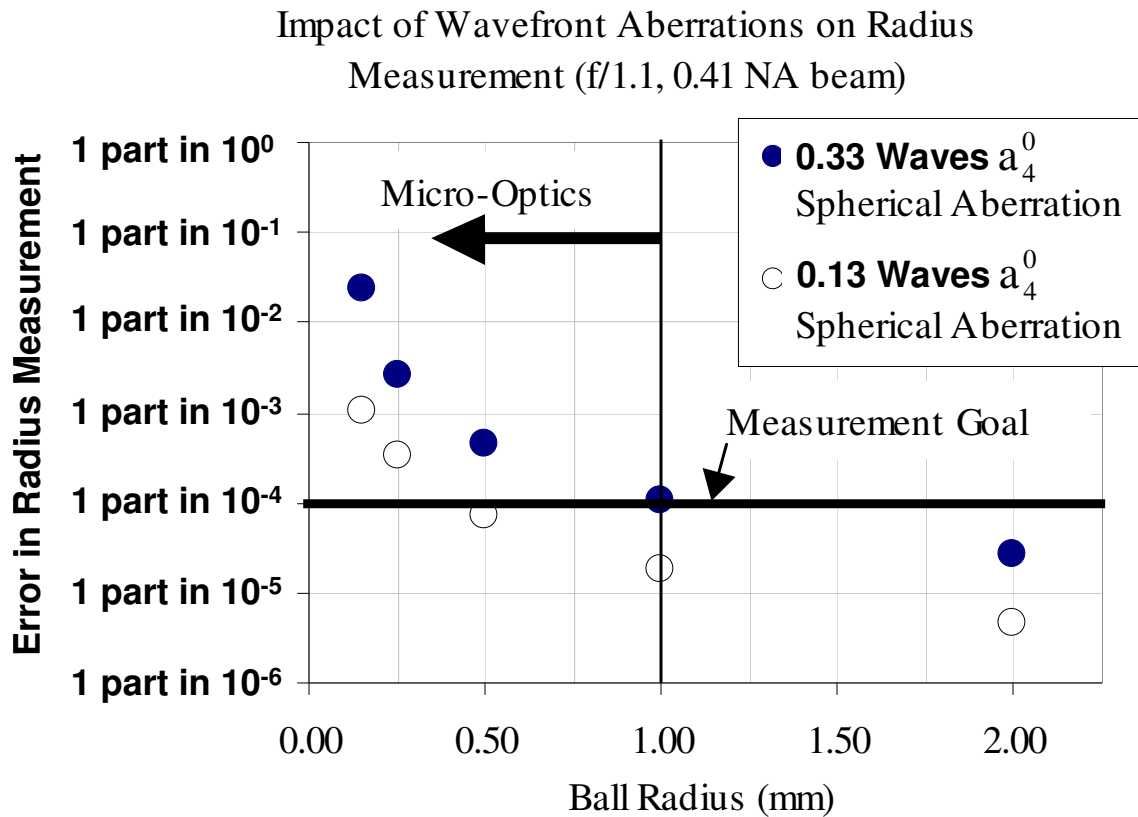


Figure 6-4: Error in radius from a Zemax model of a radius measurement with added spherical aberration.

Schmitz, et. al [27], considered this retrace error in the measurement of a nominally 25 mm radius sphere. Schmitz performed a ray trace simulation of the radius measurement in Zemax. For the transmission sphere in the model, he used the actual errors in an f/1.1 transmission sphere. This simulation led to an 18 nm bias in radius, a bias of 7 parts in 10^7 . This simulation also showed a larger bias in radius with smaller parts, similar to the error shown in Figure 6-4. Schmitz did not describe in detail how much spherical aberration (a_4^0) was present in the transmission sphere, but is likely less than 0.20 waves of a_4^0 .

6.3.2 Retrace in the FRED Model and in Experiment

The FRED model and the results from the experiment both show this retrace error. This is easily shown by comparing the amount of spherical aberration at confocal to the amount of spherical aberration at cat's eye. Of course, in experiment, the spherical aberration of the test part will contribute to the spherical aberration at confocal, and but not at cat's eye. The spherical aberration that was added in the form of the glass plates is so much larger than the spherical aberration contribution from the test part; therefore the test part contribution is negligible.

The difference in the confocal a_4^0 term and the cat's eye a_4^0 in a FRED model with one 1.397 mm thick glass plate are shown in Figure 6-5. The height maps shown are near, but not exactly at confocal and cat's eye, because the exact cat's eye and confocal positions are found through the linear fit.

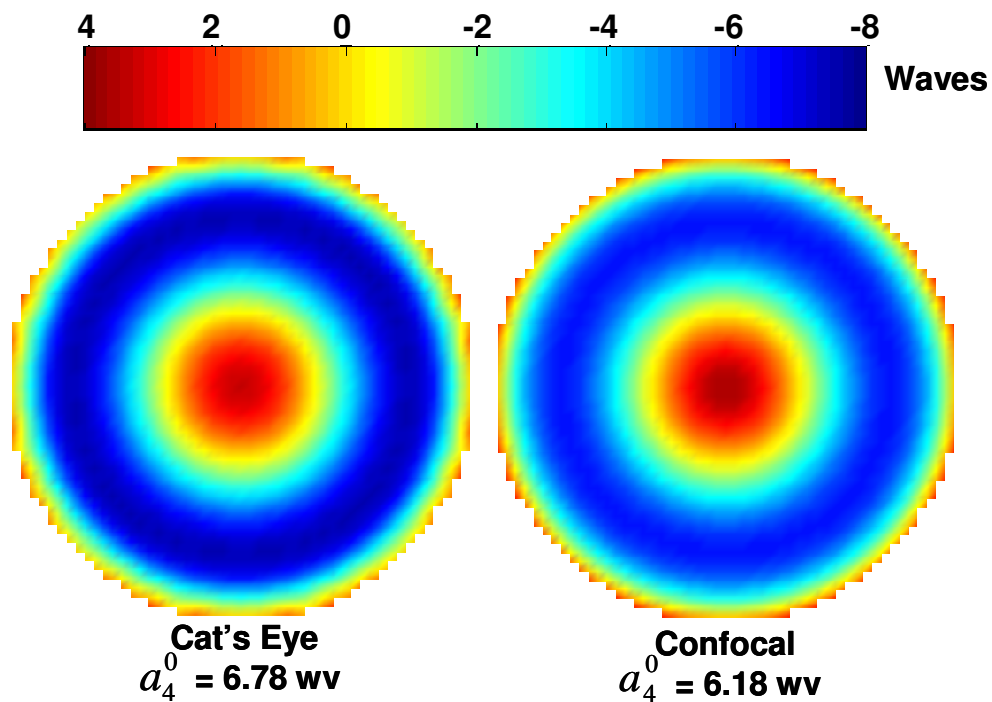


Figure 6-5: Phase Maps from FRED model when part is positioned at cat's eye and confocal for 0.42 NA system with a 1.397 mm thick glass plate for a nominally 0.5 mm radius sphere.

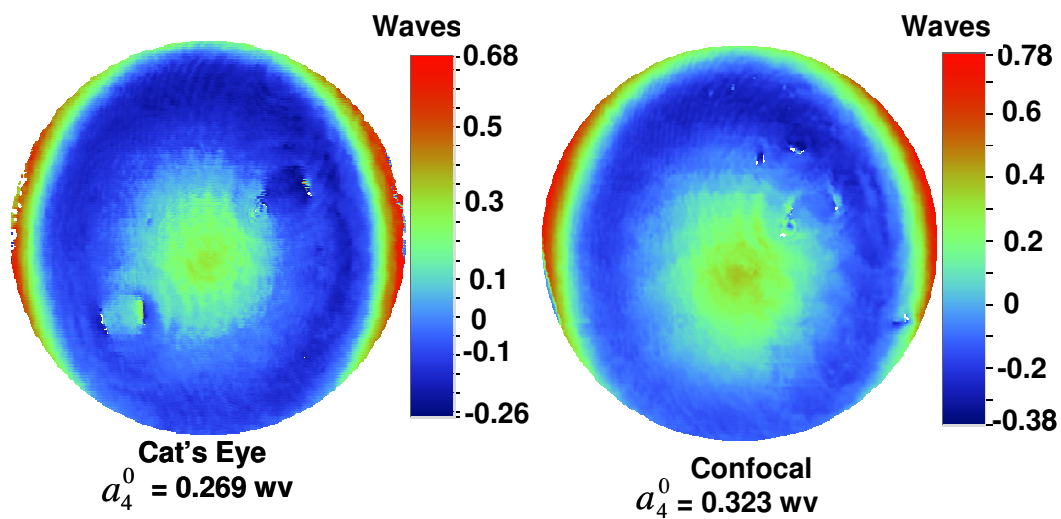


Figure 6-6: Experimental measurements on 0.99 mm radius stainless steel sphere on MORTI using 0.42 NA objective with 1.397 mm glass slide.

6.3.3 Spherical Aberration

There is a large difference between the amounts of a_4^0 as predicated by FRED and the experimental data. This is due in part to using a parabola in FRED instead of a thin lens, but mainly due to masking as described elsewhere. The parabola was used because FRED cannot model the perfect “thin lens” required to obtain a perfect focus point. Figure 6-7 shows the schematics of the focusing of a perfect thin lens and a parabolic reflector used in FRED. The experimental microscope objective is, of course, not a perfect thin lens, but is modeled as such because the design of the components in the objective is proprietary.

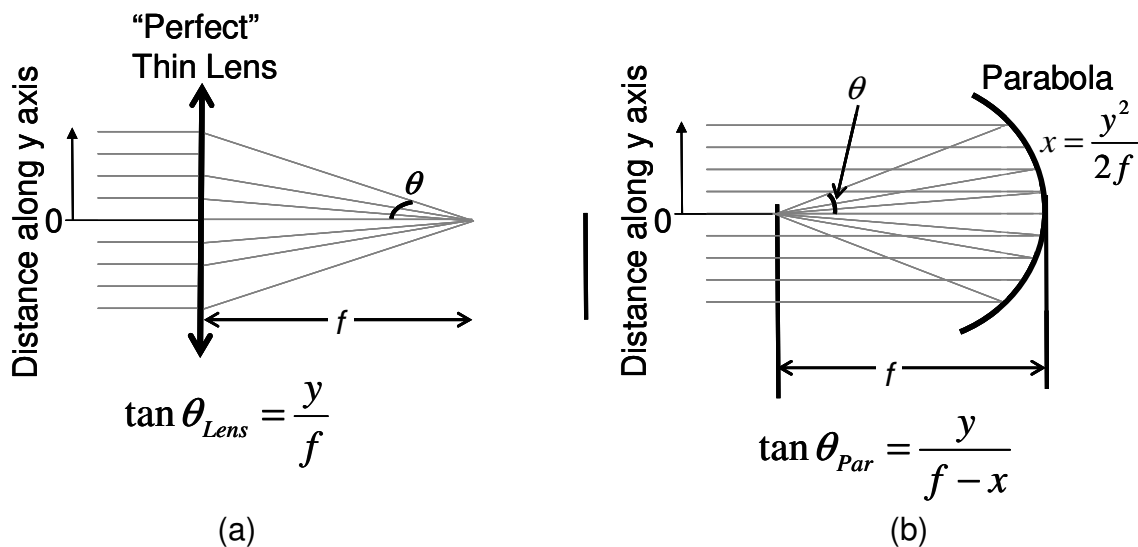


Figure 6-7: Schematic of (a) “perfect” thin lens focusing and (b) a parabola focusing.

The calculation of the angle, θ , that each ray approaches the focal region is shown in Figure 6-7. It is because the angles of corresponding rays of the thin

lens and the parabola are not the same that the spherical aberration is different in the thin lens and the parabola. The calculated results of angle θ are shown in Figure 6-8 for a 0.42 NA objective where the aperture radius (corresponding to the distance along the y-axis) is 4.5 mm. This shows the deviation between the parabola and the thin lens which leads directly to a difference in the amount of spherical aberration when a glass plate is inserted in the converging beam. This is also demonstrated in Figure 6-9, which shows the results from a FRED model simulating the measurement of a 0.25 mm radius sphere. The amount of spherical aberration, a_4^0 , of each height map is shown in the black triangles. This simulation had no additional aberration. Without aberration, the offset of the test part should only result in additional defocus, not spherical aberration as is shown. The amount of spherical aberration is not insignificant either. This shows that the parabola instead of the thin lens does have an effect on the simulated radius measurement.

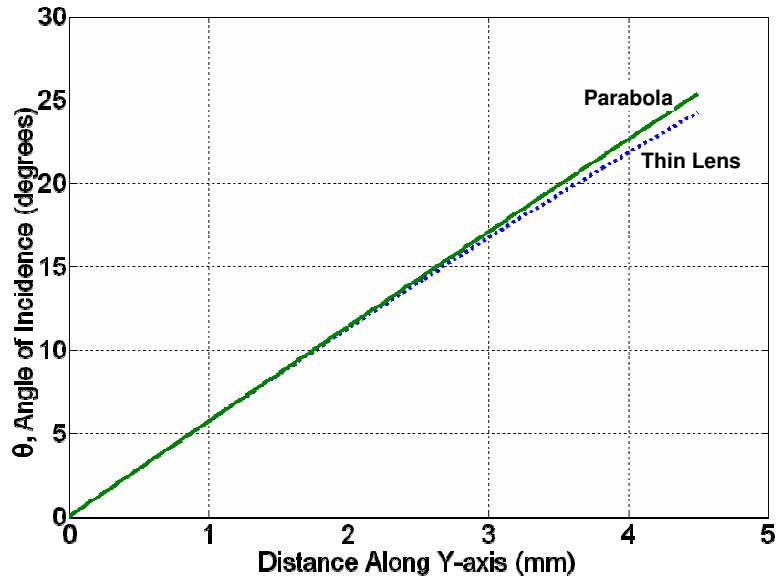


Figure 6-8: Angle that each ray approaches the focus point.

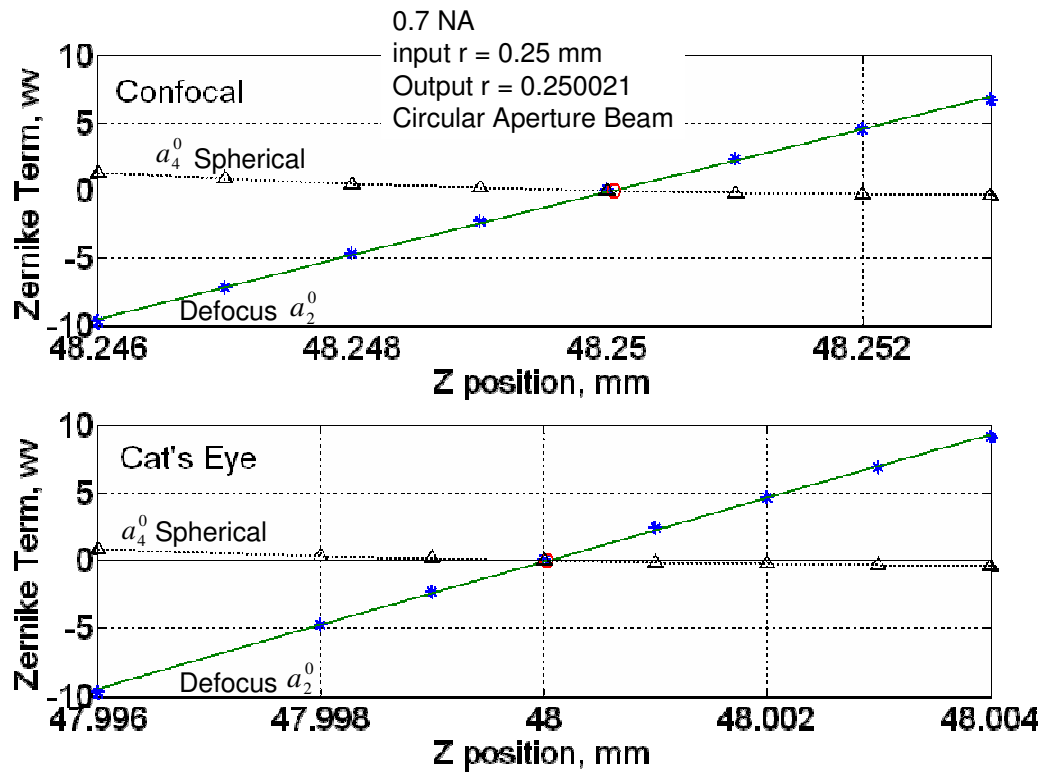


Figure 6-9: Results of parabolic FRED model.

But, the larger effect (that explains the difference in the amount of spherical aberration) is the masking of the data as described in Chapter 4. The quadratic shape of the spherical aberration curve causes a large reduction in the amount of a_4^0 with masking.

6.3.4 The Focal Shift

The major affect of introducing the glass plate in the converging beam is that the focus point shifts away from the objective. This shift is given by

$$Focus\ Shift = thickness \left(1 - \frac{1}{n_g} \right)$$

Equation 6-1

as derived from the paraxial geometric ray model using Snell's Law and geometric principles. The index of refraction, n_g of the glass is near 1.5. A plot of the theoretical focus shift and the results from the experiments and the FRED Model are shown in Figure 6-10. Both the FRED model and the experiment show a shift in the cat's eye position away from the objective, as expected. The magnitude of the shift is comparable between the experiments, FRED, and the theoretical shift. The differences are due to the uncertainty discussed earlier in the FRED chapter and the experimental chapter, the uncertainty in the index of refraction of the glass plate, and that a paraxial geometric ray model is used to derive the theoretical focus shift.

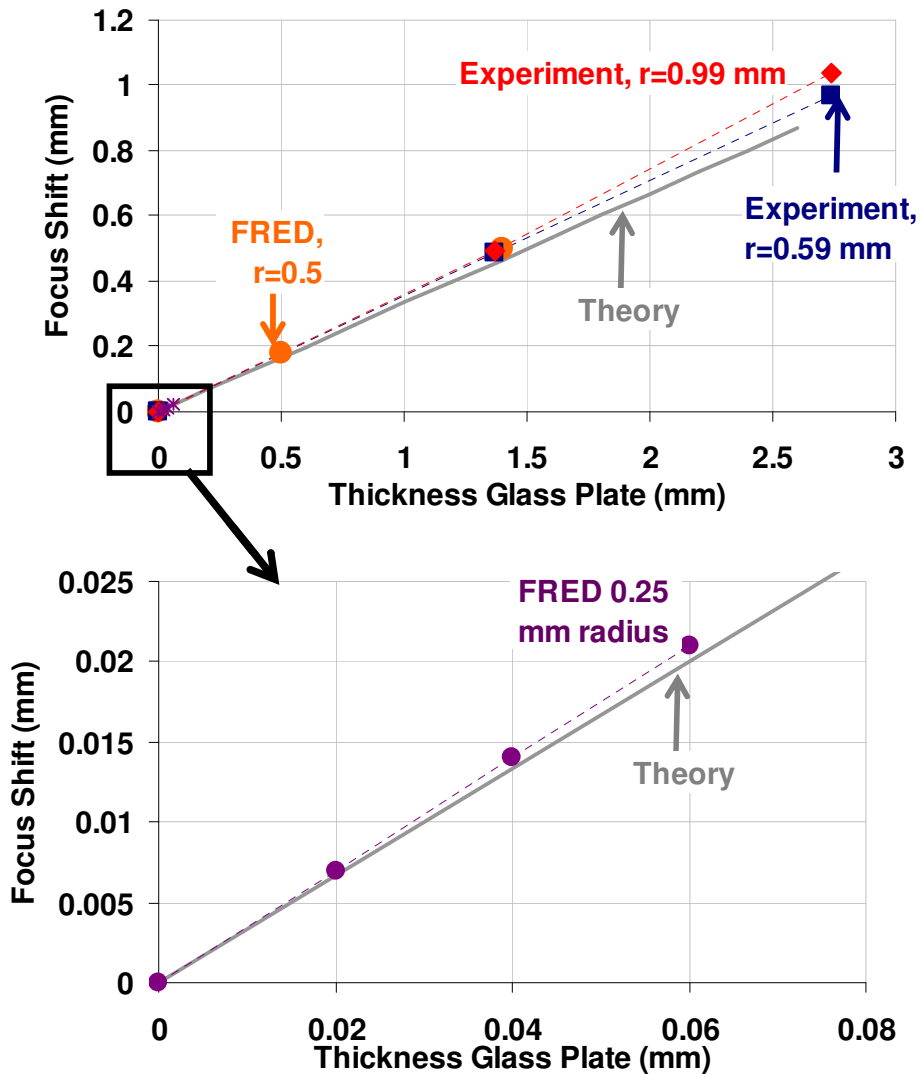


Figure 6-10: The focus shift as calculated using Equation 6-1 compared to the focus shift from the FRED model and the experimental results.

6.3.5 Comparing FRED and Experiment with Spherical Aberration

While the FRED model showed a larger amount of spherical aberration than the experiments, for the same thickness of plate, the data can still be examined for trends. I have shown that the shift in the cat's eye position is similar in FRED and in experiment, both away from the objective (or parabola). The shift in the

confocal position follows a similar pattern and is comparable between FRED and the experiments.

Both FRED and the experiments show an increasing radius with increased aberration as shown by the geometric ray model by Davies [41], Figure 6-4. This comparison is shown schematically in Figure 6-11 and numerically in Table 6-2. In the schematic, the experimental data is shown in the red stars. This data is the maximum change in the radius measurement when spherical aberration is added. In Table 6-2, the left hand column is the amount of spherical aberration in the wavefront at the camera when the part is located near cat's eye. The top rows are the methods of simulation or measurement and the nominal (or input) radius. The error in the radius is shown in the blocks for the different conditions as shown. Because I am unable to plot the absolute radius error of the experiment, I only plot the change from no aberration to aberration. This change is shown with the lines in the experiment columns. There is a break in the rows because the aberration is so much larger than the other cases.

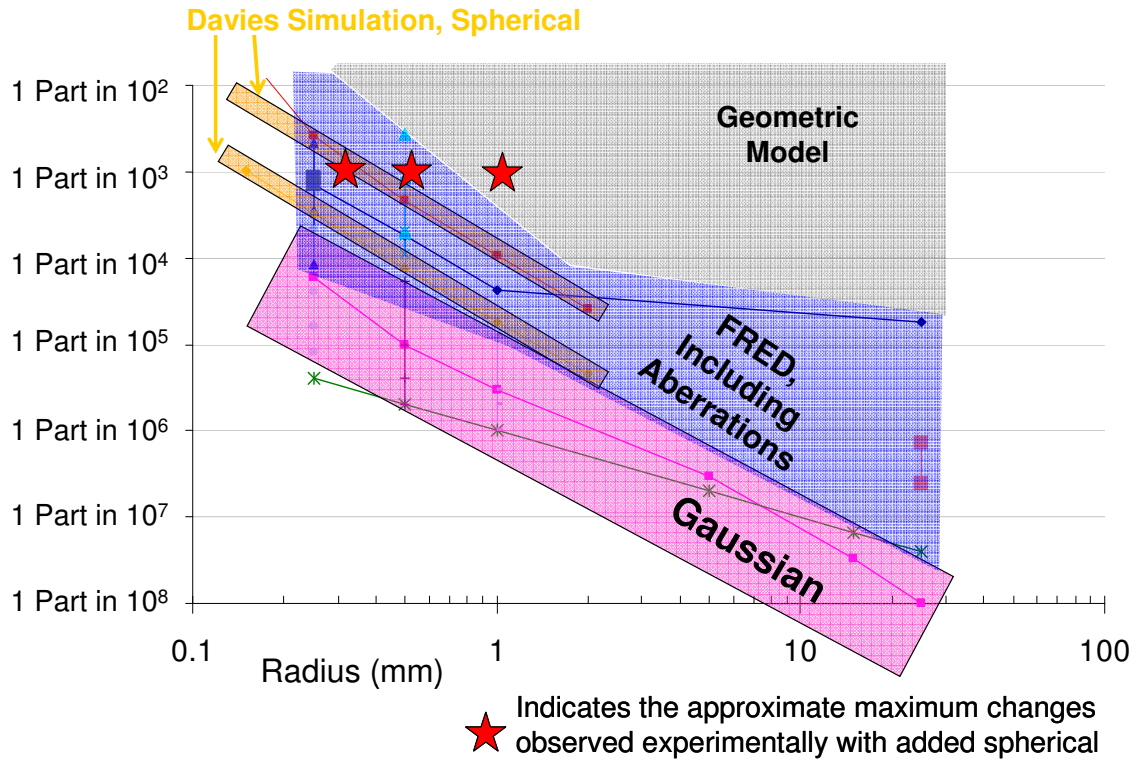


Figure 6-11: The error in the radius measurement showing the experimental data with added spherical aberration (red star). The value of the red star is the amount that the radius changed with added spherical aberration.

Table 6-2: The comparison of the error in the radius measurement with added spherical aberration.

	FRED	Experiment on MORTI	Geo. Ray Model (Davies)	FRED	Experiment on MORTI	Experiment on MORTI
	Nominal Radius (mm)					
Spherical Aberration (wv)	0.25	0.39	0.5	0.5	0.59	0.99
0	7 parts in 10^{-4} , 176 nm	↑		2 parts in 10^{-4} , 100 nm	↑	↑
0.13		Change is 2 parts in 10^{-3} , 1000 nm	1 part in 10^{-4} , 50 nm		Change is 1 part in 10^{-3} , 600 nm	Change is 9 parts in 10^{-4} , 900 nm
0.16	8 parts in 10^{-4} , 205 nm	↓			↓	↓
0.27						
0.33	9 parts in 10^{-4} , 215 nm		5 parts in 10^{-4} , 250 nm			
3.8				9 parts in 10^{-4} , 420 nm		
6.8				3 parts in 10^{-3} , 1350 nm		

I draw the following conclusions based on these results. The change in the measured radius is larger in experiment than predicated by the model. This is due to the uncertainty in the experimental radius measurement and because the experimental aberrations are more than just spherical aberration. The error in FRED is larger than the geometric ray model, but is on the same order of magnitude. The error increases with more aberration. Over this small range of

radii (0.25 mm to 1 mm), the experimental errors do not correlate well to the size of the test part. That is, the error does not seem to grow as the radius decreases. The ray trace simulation predicts this however. It is likely that the experimental uncertainty is too high to see this effect.

6.4 Masking

The masking of the data in the FRED model and in experiments affects the measured radius as shown in schematic in Figure 6-12 and numerically in Table 6-3 in the presence of added spherical aberration. The radius changes when the data is masked because when the spherical aberration is clipped it presents as defocus, as described in Section 3.11. This defocus will cause the defocus vs. position curves to offset and therefore will change the radius. The change in radius is larger in experiment because of the much more complex wavefront in experiment. Masking this data changes how the defocus term fits much more so than in the more “perfect” simulation data. The simulation data has very little, if any, higher order amounts of aberration, whereas the experimental does.

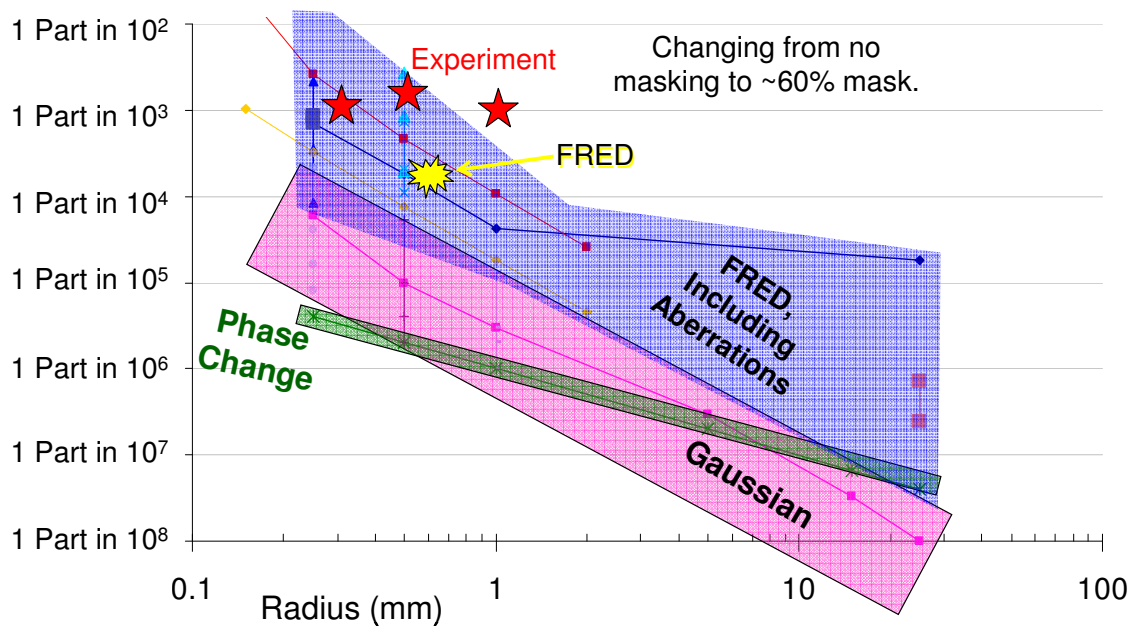


Figure 6-12: The effect of changing the mask size on the radius measurement.

Table 6-3: The change in the radius when the mask is varied.

% of Original	Change in Radius from 100%	
	FRED, Spherical Aberration ~ 1.2 wv, r = 0.5 mm	Experiment, Spherical Aberration ~ 0.2 wv, r = 0.39 mm
50	4 parts in 10^4 (200 nm)	2 parts in 10^3 (780 nm)
75	3 parts in 10^4 (150 nm)	1 part in 10^3 (390 nm)

6.5 Macro-Scale Parts

I tested a 25 mm radius macro-scale part in the Gaussian simulation and in the FRED model. The error in the radius as calculated from the Gaussian model is 4 parts in 10^7 (11 nm). This model compares well to the 6 nm radius error as

calculated by Schmitz, et.al [27] even though Gaussian propagation was treated only approximately in this study. The FRED model with the circular aperture input beam showed a radius error of 2 parts in 10^5 , 461 nm. This error is much larger than the Gaussian model and may explain the discrepancy between the interferometric and mechanical radius measurements found by Schmitz. The simulation of macro-scale measurements needs more work to further investigate this possibility, including adding aberration.

6.6 Uncertainty

I described the estimated uncertainty of the modeling in FRED and in the experiment. These are not combined uncertainty estimates, but rather capture either repeatability or sensitivity to model parameters. The results are shown in Table 6-4. It is difficult to estimate an uncertainty for the Gaussian model. I am able to step in 0.1 nm steps in this model, so a position error in Z is not an effect. One method to estimate an uncertainty contribution is to compare the two different input beam types, the apertured and the un-apertured beam. The difference between these two input beams is shown in Table 6-4. An affect not shown here, is the model break down for the 0.55 0.7 NA objectives. This would affect the uncertainty but and estimate of the amount is difficult.

Table 6-4: The estimated uncertainty in the radius measurement.

Radius (mm)	Gaussian Model	FRED	Experiment
0.2 or 0.25	1 part in 10^5	3 parts in 10^4	2 parts in 10^3
0.5		2 parts in 10^4	9 parts in 10^4
1	1 part in 10^6	8 parts in 10^5	5 parts in 10^4

The uncertainty increases by about an order of magnitude for the Gaussian model, the FRED model, and in experiment. The uncertainty increases for the smaller radii parts.

CHAPTER 7: FUTURE WORK AND CONCLUSIONS

7.1 Future Work

7.1.1 Retrace Errors

The retrace errors that occur when the interferometer has aberration lead to an uncertainty in the radius measurement. This uncertainty could be reduced as follows. Ultimately, the inherent spherical aberration needs to be as low as possible. This is accomplished by using well designed microscope objectives and transmission spheres and by having a well collimated aberration free input wavefront. After the inherent aberration is reduced, the remaining can be measured.

The inherent aberration in an interferometer can be measured by performing a random ball test [41]. This random ball test eliminates the error in the height map that is caused by errors in the test part. The output of the random ball test is a height map that is then subtracted from all subsequent measurements. The data remaining after subtraction is then just the error in the test part (and any alignment errors, such as the z-axis offset leading to defocus). But Gardner [41] has shown that the results from the random ball test will be different for different size test spheres. In addition the result of the random ball test at confocal is not equal to the aberration in the interferometer at cat's eye.

Therefore, the retro-reflection test at cat's eye must be used to determine the rotationally invariant components of the wavefront at cat's eye [40]. Because the part can not be positioned exactly at cat's eye, I must step through cat's eye and determine the cat's eye position at defocus equal to zero. Then, the value of the spherical aberration (and higher order aberrations) is found at the corresponding z-value. This now gives us a value of the spherical aberration at cat's eye, but only for that specific radius part.

In summation, a random ball test (~100 measurements) and then a measurement through cat's eye is required can tell how much spherical aberration is present for the measurement. But this information is still not enough to correct for the error in the radius measurement caused by the interferometer bias.

7.1.2 Phase Change

While the results from the phase change model predict small errors in the radius measurement due to the phase change, other areas of research could be explored. The effect of the polarization state in the converging beam will change the offset due to the polarization which could be examined in theory and through experiments. Some of this current research could be extended in examining the phase change effect in scanning white light interferometers which are used measure surface finish. The current calculation of the phase change considered the geometric model of the focus point. The calculation of the phase change when diffraction is considered is not known, but future work could include examining this effect.

To extend the current measurements, the uncertainty in the background subtraction must be reduced as discussed. Then, the measurements of the phase change with varying incident angle could be performed along with measurements that examine the phase change as a function of material thickness.

7.1.3 MORTI

The interferometer needs to be improved to reduce the uncertainty in the radius measurement. The uncertainties due to the fit and to the repeatability are too high. The uncertainty due to the fit includes many components including repeatability, wavefront aberration and phase shifting errors. This uncertainty can be reduced by taking more data points for the defocus vs. position graph and reducing the aberration in the wavefront. Improving the mechanical stability of the instrument and using a motor to control the z-axis motion could also reduce the uncertainty. The automatic motion control reduces the amount of heat near the instrument and can be controlled with more precision. The part test stage is currently on an x-y stage that is good for course motions but a new fine motion x-y stage for the test part would help in positioning.

The mechanical alignment of the axis of the objective lens to the motion axis is not a current option in MORTI. To fix this, a tip/tilt stage must be added to the microscope objective fixture. Then the base of an indicator is placed on the test part stage (after the mechanical alignment of this stage) and the point of the indicator is on the side the microscope objective. As the stages moves up and down, the indicator point varies. With adjusting the tip/tilt of the objective, I could

align the microscope objective to the mechanical axis. A problem in this method occurs when switching to a different objective. The new objective has a different alignment and therefore would need to be checked for each objective.

The imaging leg on MORTI needs to be able to focus on a range of radii with the whole range of objectives. Currently the wavefront on the camera is too large for the 0.28 NA objective and may be too small for the 0.7 NA objective. The current configuration also does not allow for good focusing when the 0.28 NA objective is used for smaller parts. It may not be possible to arrange the current imaging lenses in such a manner to fix this problem. New lenses may be required, but the best likely solution is that different imaging lenses must be used for the different objectives.

Another improvement related to the experiment is calculating the effect that the focusing effect (changing spot size) has on the radius measurement when spherical aberration is present. This was presented here only to demonstrate that this could be a factor. The calculation of this requires an estimate of the amount of spherical aberration, the definition of the spherical aberration and defocus terms, and the amount that the spot size changes.

7.1.4 Model of Focal Region

It is apparent that the FRED model does not accurately describe the wave field in the focal region. New models still being researched [37] may describe this wave field better. The new model removes the uncertainty due to variations in the source. The application of these models to the cat's eye reflection (and radius measurement) is an area for future research.

7.1.5 FRED

The uncertainty in FRED must be reduced if I want to use FRED to correct for the biases in the radius measurement. Some of the uncertainty in FRED comes from using the parabola instead of a thin lens. A method to correct this may be to create a converging beam that simulates the thin lens. I would direct each ray in this beam to focus on the same spot, with the proper angle of incidence. This is not an easy solution because each ray (the beamlet) would have to be input as a new source leading to near 1000 different sources. I am unsure if FRED could handle this type of ray trace. The Gaussian model may be able to do this by replacing the single large Gaussian beam with smaller beamlets in the same manner as FRED. The combination of the beams at the detector is a problem though, because it is not a simple sum.

If the model of the microscope objective is available, I could use it in the FRED simulation for the comparison to the experimental results. It is unlikely though, that the manufacturer would ever divulge this information. The wavefront of the microscope objective that I measured on the Veeco could be used in FRED to simulate (with an uncertainty) the actual aberrations of the objective.

7.2 Conclusions

Figure 1-5, reprinted here as Figure 7-1, shows the error in radius measurement when the geometric model is used instead of a more detailed model. If the desired measurement uncertainty and the nominal radius of the measured part are known, this graph can be used to determine if the geometric model is valid. For example, if the part radius is 2 mm, the spherical aberration is

0.1 waves, and the desired measurement uncertainty is 1 part in 10^4 , the non-aberrated geometric model will likely give an acceptable result. For low uncertainty measurements, the more complex methods need to be considered. Another example is the effect of phase change on the radius measurement, which does not need consideration until ultra-precision measurements are required.

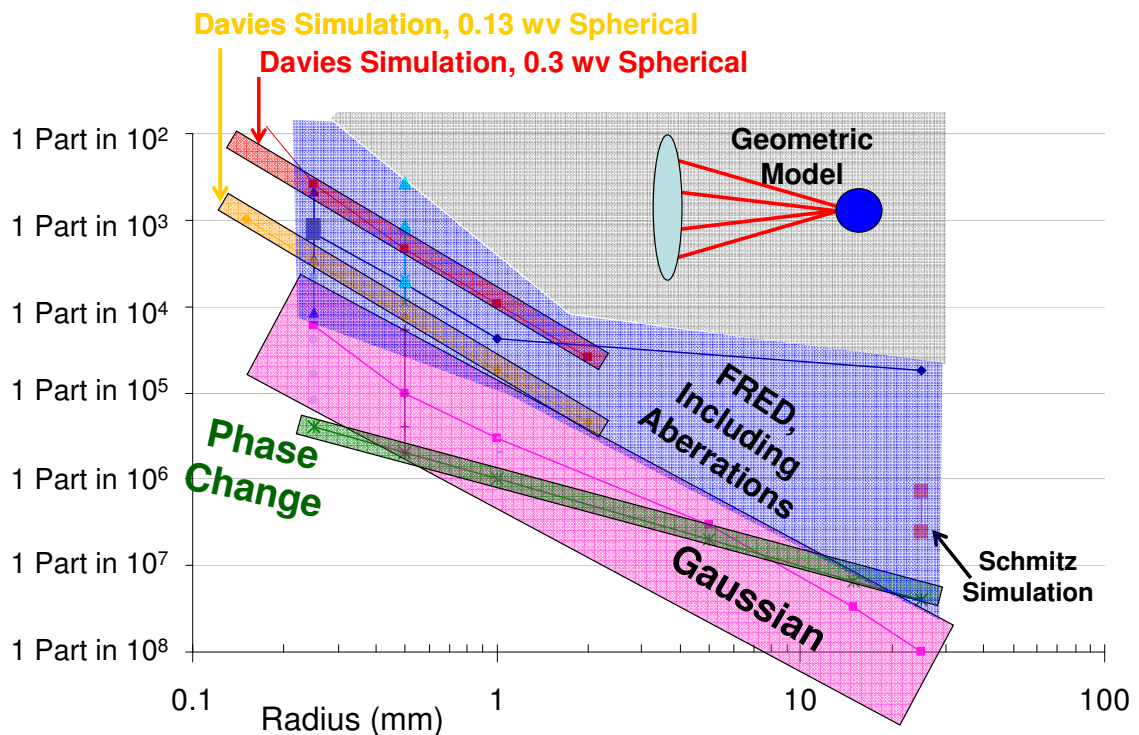


Figure 7-1: The error in the radius measurement when the geometric model is used instead of a more detailed model [41, 54, 27].

Not shown on this graph is the uncertainty in using the model to correct for the bias in the radius measurement. The uncertainty in using the FRED model to correct for the bias in radius is a few parts in 10^4 . This means that if the error is

smaller than a few parts in 10^4 (as is the case for 1 mm radius part with a desired uncertainty of 1 part 10^4), there is no point in using FRED to correct the bias.

I have drawn conclusions throughout this work about when the models are valid and what parameters affect the measured radius. These conclusions are summarized here. The Gaussian and FRED models predict increased errors with smaller radius parts and with smaller NA objectives. Both the confocal and cat's eye positions shift in both models. The simple Gaussian model loses validity with higher numerical apertures. The FRED model shows an increased error in radius with increased spherical aberration. The uncertainty in the FRED model is too high to use the model to correct for biases in many cases. The phase change has a very small effect on the measured radius.

The experiments show an effect on the measured radius with increased aberration and reducing the mask size. The key issue in the experiments is the combination of the focusing effect, spherical aberration, and the mask size. In the presence of spherical aberration, the focusing effect will change the radius of curvature and the mask size will have an effect. This interplay is not completely understood, but the effect should be reduced if the mask size is checked and the measured data stays in the linear range.

REFERENCES

1. T.W. Liepmann, "How Retroreflectors Bring the Light Back," *Laser Focus World*, Vol. 309, No. 10, p. 129-132, 1994.
2. Precy Shaw, "Improvements relating to blocks for road surface marking," Patent number:GB436290, Classification: International: - European: E01F9/07B Application number:GB19340009943 19340403 Priority number(s): GB19340009943 19340403, 10/3/1935
3. A. Lundvall, T. Lindström, F. Nikolajeff, "Novel type of micromachined retroreflector," *Micromachining Technology for Microoptics and Nano-optics*, Proceedings of SPIE, Vol 4984, p. 118-127, 2003.
4. W. Zurcher, R. Loser, S.A. Kyle, "Improved reflector for interferometric tracking in three dimensions," *Optical Engineering* Vol. 34, No. 9, p. 2740-2742, 1995.
5. L. Yongbing, Z. Guoxiong, L. Zhen, "An improved cat's-eye retroreflector used in a laser tracking interferometer system," *Measurement Science and Technology*, Vol 14, p. 36-40, 2003.
6. R.L. Richardson, P.R. Griffiths, "Design and performance considerations of cat's-eye retroreflectors for use in open-path Fourier-transform-infrared spectrometry," *Applied Optics*, Vol. 41, NO. 30, p. 6332-6340, 2002.
7. Z. Xu, S. Zhang, Y. Li, W. Du, "Adjustment-free cat's eye cavity He-Ne laser and its outstanding stability," *Optics Express*, Vol. 13, No. 14, p. 5565-5573, 2005.
8. R. Beer and D. Marjaniemi, "Wavefronts and Construction Tolerances for a Cat's-Eye Retroreflector," *Applied Optics*, Vol. 5No. 7, p. 1191-1197, 1966.
9. M.L. Biermann, W.S. Ravinovich, R. Mahon, G.C. Gilbreth, "Design and analysis of a diffraction-limited cat's-eye retroreflector," *Optical Engineering*, Vol. 41, No. 7, p. 1655-1660, 2002.
10. J.J. Snyder, "Paraxial ray analysis of a cat's-eye retroreflector," *Applied Optics*, Vol. 14, No. 8, p. 1825- 1828, 1975.
11. J.J. Stamnes, Waves in Focal Regions, Taylor & Francis, Abingdon, UK, 1986.
12. Y. Li and E. Wolf, "Three-dimensional intensity distribution near the focus in systems of different Fresnel numbers," *Journal of the Optical Society of America A*, Vol. 1, No. 8, p. 801-808, 1984.

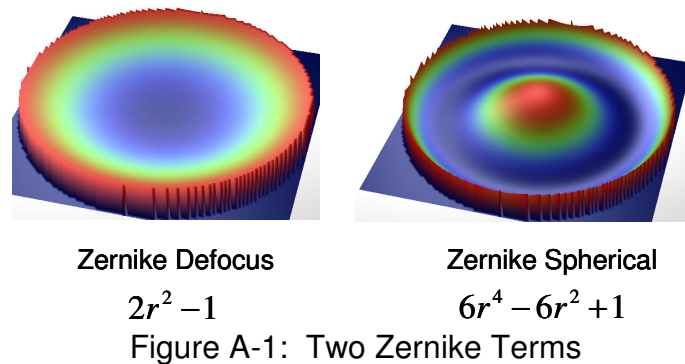
13. J.H. Bruning, D.R. Herriott, J.E. Gallagher, D.P. Rosenfeld, A.D. White, and D.J. Brangaccio, "Digital Wavefront Measuring Interferometer for Testing Optical Surfaces and Lenses," *Applied Optics*, Vol. 13, No. 11, p. 2693-2703, 1974.
14. J.Z. Malacara, "Angle, Distance, Curvature, and Focal Length Measurements," in *Optical Shop Testing*, Ed. D. Malacara, John Wiley and Sons, Inc., New York, 1992.
15. S.C. Irick and A.D. Franck, "Radius of curvature limitation and accuracy of a surface profile measurement", Lawrence Berkley National Laboratory Note 604, July, 2001.
16. A.W. McFarland and J.S. Colton, "Production and Analysis of Injection Molded Micro-Optic Components," *Polymer Engineering and Science*, Vol. 44, No. 3, p. 564-580, 2004.
17. U. Griesmann, J. Soons, Q. Wang, "measuring Form and Radius of Spheres with Interferometry," *Annals of the CIRP*, Vol 53, No. 1, p. 451-454, 5004.
18. A. Davies and T. Schmitz, "Correcting for stage error motions in radius measurements," *Applied Optics*, Vol. 44, No. 28, p. 5884-5893, 2005.
19. M. Testorf and S. Sinzinger, "Evaluation of microlens properties in the presence of high spherical aberration," *Applied Optics*, Vol. 34. No. 28, p. 6431-6437, 1995.
20. J. Schwider and H. Sickinger, "Arraytest for microlenses," *Optik*, Vol. 107, No. 1, p. 26-34, 1997.
21. J. Schwider and O. Falkenstörfer, "Twyman-Green interferometer for testing microspheres," *Optical Engineering*, Vol. 34, No. 10, p. 2972-2975, 1995
22. K. Mersereau, R.J. Crisci, C.R. Nijander, W.P. Townsend, D. Daly, and M.C. Hutley, "Testing and measurement of microlenses," *Miniature and Micro-Optics and Micromechanics*, Proceedings of SPIE, Vol. 1992, p. 210-215, 1992.
23. Zygo Corporation 2001 Annual Report, Laurel Brook Road Middlefield, CT, 06455, 860-347-8506
http://zygo.com/library/annrep/ar2001/zygo_ar2001_comp.pdf
24. Zygo Corporation, Laurel Brook Road Middlefield, CT, 06455, 860-347-8506
<http://zygo.com/?/products/pti250/>
25. L. Selberg, "Radius measurement by interferometry," *Optical Engineering*, Vol. 31, No. 9, p. 1961-1966, 1992.

26. J.E. Greivenkamp and J.H. Bruning, "Phase Shifting Interferometry," in *Optical Shop Testing*, Ed. D. Malacara, John Wiley and Sons, Inc., New York, 1992.
27. T.L. Schmitz, A.D. Davies, and C.J. Evans, "Uncertainties in interferometric measurements of radius of curvature," in *Optical Manufacturing and Testing IV*, Ed. H.P. Stahl, *Proceedings of SPIE Vol. 4451*, p. 432-447, 2001.
28. K.M. Medicus, J. Snyder, A.D. Davies, "Gaussian beam modeling of the radius of curvature," *Proceedings of the SPIE, Recent Developments in Traceable Dimensional Measurements III*, Vol. 5879, p. 97-105, 2005.
29. F.L Perrotti, and L.S. Perotti, *Introduction to Optics*, 4th Edition, Prentice Hall, NJ, 1993.
30. Yariv, Amnon, *Optical Electronics*, 4th Edition, Oxford University Press, New York, 1991.
31. H. Kogelnik, "On the propagation of Gaussian Beams of Light Through Lenslike Media Including those with a Loss or Gain Variation," *Applied Optics*, Vol. 4, No. 12, December 1965.
32. "M Plan Apo," Mitutoyo Optics, Intefrated Imaging Systems, Somerstown Center, P.O. Gox 536, Sommers, NY, 10589. 914-277-8826.
33. FRED 4.70.0, Photon Engineering Headquarters, 440 South Williams Blvd., Suite # 106, Tucson, Arizona 85711, +1- 520-733-9557, info@photonengr.com, <http://www.photonengr.com>., January 2006.
34. Jacques Arnaud, "Representation of Gaussian beams by complex rays," *Applied Optics*, Vol. 24, No. 4, p. 538-543, February 1985.
35. R. Herloski, S. Marshall, and R Antos, "Guassian beam ray-equivalent modeling and optical design," *Applied Optics*, Vol. 22, No. 8, p. 1168-3151, April 1983.
36. Personal Communication, Fall 2001.
37. G.W. Forbes and M.A. Alonso, "Using rays better. I. Theory for smoothly varying media," *Journal of the Optical Society of America*, Vol. 18, No 5, p. 1132-1145, May 2001.
38. G.W. Forbes and M.A. Alonso, "Using rays better. III. Theory for smoothly varying media," *Journal of the Optical Society of America*, Vol. 18, No 6, p. 1357-1370, June 2001.

39. J.E. Breivenkamp and J.H. Bruning, "Phase Shifting Interferometry," *Optical Shop Testing*, Ed. D. Malacara, John Wiley & Sons, Inc. New York, 1992.
40. D. Malacara, "Twyman_Green Interferometer," *Optical Shop Testing*, Ed. D. Malacara, John Wiley & Sons, Inc. New York, 1992.
41. N. Gardner, *Self-Calibration for Micro-Refractive Lens Measurements*, UNC Charlotte, Thesis, 2003.
42. M. Park and S Kim, "Compensation of phase change on reflection in white-light interferometry for step height measurement," *Optics Letters*, 26, 7, 2001.
43. E. Palik, *Handbook of Optical Constants of Solids*, Academic, San Deigo, CA, 1985.
44. D.E. Gray, Ed, *American Institute of Physics Handbook*. McGraw-Hill, New York, 3rd Edition, 1982.
45. D.R. Lide, Ed., *CRC Handbook of Chemistry and Physics*. CRC Press, Boca Raton, 84th Edition, 2003.
46. T. McWaid, T. Vorburger, J.F. Song, D. Chandler-Horowitz, "The effects of thin films on interferometric step height measurements," *SPIE Interferometry: Surface Characterization and Testing*, 1776, 2-13, 1992.
47. T. Doi, K. Toyoda, and Y. Tanimura, "Effects of phase changes on reflection and their wavelength dependence in optical profilometry," *Applied Optics*, 36, 28, 7157-7161, 1997.
48. J. M. Bennett, "Precise Method for Measuring the Absolute Phase Change on Reflection," *JOSA*, 54, 5, 1964.
49. M. Born and E. Wolf, *Principles of Optics*, "Optics of Metals," Seventh Edition Cambridge University Press, 1999.
50. L. Ward, *The Optical Constants of Bulk Materials and Films*, Adam Hilger, Bristol, 1988.
51. Melles Griot, www.mellesgriot.com/
52. L.A. Selberg, "Radius measurement by interferometry," *Optical Engineering*, Vol. 31, No. 9, p. 1961-1966, 1992.
53. C.J.Evans and R.N Kestner, "Test optics error removal," *Applied Optics*, 35, p. 1015- 1021, 1996.
54. Personal Communication with A. Davies, September 2003.

APPENDIX A: ZERNIKES

The set of Zernike polynomials were developed to represent wavefront aberration over a circular aperture. The center of the circular aperture defines the center x,y of the Zernike set and the r, θ coordinates are set as usual. The Zernikes are orthogonal and separate the rotationally invariant and rotationally variant. Rotationally invariant indicates that the surface height (or phase) at any r value is the same or all theta values. The two terms of interest for the radius measurement are the spherical aberration and the defocus and are shown in a Figure A-1. Other Zernike terms, such as x-coma, astigmatism, and others, are relevant in other applications.



Commonly, the first 36 Zernike terms are used to describe a wavefront. But, different systems use different numbering orders, which is why I specially say defocus and spherical. Defocus is the a_2^0 term because it is the zero-order term in theta and the second-order term in radius. Spherical is the a_4^0 term because it is the zero-order term in theta and the fourth-order term in radius.

APPENDIX B: MATLAB PROGRAMS

Program 1: gaussian.m

```

close all;
clear all;

%inputs

r=0.5;
NA = 0.42; %the na
f = 10; %the focal length, mm
ha = 4.5; %the half aperature, mm

dt = 50; %mm distance to focusing lens from bs
dr = 150; %mm distance to reference mirror from bs
da = 50; %mm distance from aperature to bs

n = 1; %index of air
lam = 632.8e-6; %wavelength mm

%finding the input q, different cases

qin_1 = -sqrt(-1)*pi*ha^2*n/lam; %case1
qin_2 = da - i*pi*ha^2*n/lam; %case2
qin_3 = (dt-f - sqrt(-1)*f.^2.*NA.^2*pi/lam)'; %case3
%picking which case to use
qin = qin_3

%this section is just to find where in z to look for the solutions.
%this is just for the general case - both ce and cf
%soultions will be near f and f-r. so we look from f -2r to f+r
maxs = f+r;
mins = f-2*r;

%the position of the test part for the general case
s = mins:1e-3:maxs;

%the reference arm:
%
%propagation matrix for the reference arm (travels 2*dr)
ref_matrix = [1 2*dr; 0 1];

```

```

%calculating the output complex curv and curv of the reference arm
qref_out =
(qin*ref_matrix(1,1)+ref_matrix(1,2))/(qin*ref_matrix(2,1)+ref_matrix(2,2));
curv_ref_out = real(1./qref_out);

%the test arm matrices
%
%matirx for mirror (test part)
mirror = [1 0 ; 2/r 1];
%matrix for lens
lens = [ 1 0 ; -1/f 1];
%matrix for propagation of test arm from bs to lens
dt_prop = [1 dt; 0 1];

%initializing variables to make it run faster
qtest_out = zeros(size(s));
curv_test_out = zeros(size(s));
qreal_test_out = zeros(size(s));

%this is for the general case, both ce and cf, in large steps.
for i = 1:length(s)
    %prop matix for distance from lens to part
    s_prop = [1 s(i); 0 1];
    %full matrix for test arm
    test_matrix = dt_prop*lens*s_prop*mirror*s_prop*lens*dt_prop;
    %output complex curv for test arm

    qtest_out(i) = (test_matrix(1,1)*qin + test_matrix(1,2))/(test_matrix(2,1)*qin +
test_matrix(2,2));
end % i loop

%real curv of test arm
curv_test_out = real(1./qtest_out);
qreal_test_out = real(qtest_out);
%ploting the general case
%
% figure
% plot(s,curv_test_out-curv_ref_out)
% title('Curv test general')
%

%this section will find a point inbetween ce and cf, split the s vector in
%two at this point, find the max and min values of the curv in the 2
%sections, and then build new s vectors that have small steps inbetween the
%max and min values

```

```

%split point inbetween ce and cf
split_point = single(f-r/2) ;
%index of spilt point
index_split = find(single(s) == split_point);

%the cf curv - long
qreal_cf_long = qreal_test_out(1:index_split);
%the ce curv - long
qreal_ce_long = qreal_test_out(index_split+1:length(s));

%finding the max and min values in ce curv long and the index of them
max_ce_qreal = max(qreal_ce_long);
index_max_ce = find(qreal_test_out == max_ce_qreal);
min_ce_qreal = min(qreal_ce_long);
index_min_ce = find(qreal_test_out == min_ce_qreal);

%bulding the new ce s vector from s at the max value to s at the min value
s_ce = s(index_max_ce):1e-7:s(index_min_ce);

%finding the max and min values in cf curv long and the index of them
max_cf_qreal = max(qreal_cf_long);
index_max_cf = find(qreal_test_out == max_cf_qreal);
min_cf_qreal = min(qreal_cf_long);
index_min_cf = find(qreal_test_out == min_cf_qreal);

%bulding the new cf s vector from s at the max value to s at the min value
s_cf = s(index_max_cf):1e-7:s(index_min_cf);

%ce
%initalizing variables to make it run faster
qtest_out_ce = zeros(size(s_ce));
curv_test_out_ce = zeros(size(s_ce));
%this is for the ce, in small steps.
for i = 1:length(s_ce)
    %prop matix for distance from lens to part
    s_prop = [1 s_ce(i); 0 1];
    %full matrix for test arm
    test_matrix = dt_prop*lens*s_prop*mirror*s_prop*lens*dt_prop;
    %output complex curv for test arm
    qtest_out_ce(i) = ( test_matrix(1,1)*qin+ test_matrix(1,2))/(
test_matrix(2,1)*qin+ test_matrix(2,2));

end %i loop

```

```

%real curv of test arm for ce
curv_test_out_ce = real(1./qtest_out_ce);

%ploting ce
% figure
% plot(s_ce,curv_test_out_ce, '*')
% title('CE curv')
%

%cf
%initializing variables to make it run faster
qtest_out_cf = zeros(size(s_cf));
curv_test_out_cf = zeros(size(s_cf));

%this is for the cf, in small steps.
for i = 1:length(s_cf)
    %prop matrix for distance from lens to part
    s_prop = [1 s_cf(i); 0 1];
    %full matrix for test arm
    test_matrix = dt_prop*lens*s_prop*mirror*s_prop*lens*dt_prop;
    %output complex curv for test arm
    qtest_out_cf(i) = (test_matrix(1,1)*qin +
test_matrix(1,2))/(test_matrix(2,1)*qin + test_matrix(2,2));
end

%real curv of test arm for cf
curv_test_out_cf = real(1./qtest_out_cf);
rad_test_out_cf = 1./curv_test_out_cf;

%ploting cf
% figure
% plot(s_cf,curv_test_out_cf, '*')
% title('CF curv')

    %finding where the curvature matches, cf
    %offset the test curv, so the it easiest, i can just find the find, instead
%of searching for a number match ce
curv_inter_cf = curv_test_out_cf - curv_ref_out;
abs_curv_inter_cf = abs(curv_inter_cf);
cf_min = min(abs_curv_inter_cf);
cf_index = find( abs_curv_inter_cf == cf_min);
cf_position = s_cf(cf_index);

%finding where the curvature matches, ce
    %offset the test curv, so the it easiest, i can just find the find, instead

```

```

%of searching for a number match ce
curv_inter_ce = curv_test_out_ce - curv_ref_out;
abs_curv_inter_ce = abs(curv_inter_ce);
ce_min = min(abs_curv_inter_ce);
ce_index = find( abs_curv_inter_ce == ce_min);
ce_position = s_ce(ce_index);

%the radius of the part is the difference in position.
output_radius = ce_position-cf_position;

radius_error = output_radius - r ;

ce_offset= ce_position-f;
cf_offset = cf_position-(f-r);

%outputs
cf_position=cf_position'
ce_position=ce_position'
ce_offset=ce_offset'*1e6
cf_offset=cf_offset'*1e6
output_radius=output_radius'
r
radius_error = radius_error'*1e6

```

Program 2: der_test.m

```

close all;
clear all;

R1 = 1e4; %input radius
w1 = 25; % mm, input waist
n=1; %index of air
lam = 632.8e-6; % mm, wavelength

f=100; %focal length
k = 2*pi/lam; %k number, wave number

A = 1/((1/R1)-(i*lam/(pi*w1^2))-(1/f));%from equation

%counting distance past lens
dist = 50:1e-2:110;
for v = 1:length(dist)

```

```

d = dist(v);
q3(v) = A + d; %new q
R3 = 1./real(1./q3); %new radius
w3(v) = sqrt(-lam./(pi*imag(1./q3(v)))); %new waist

r = w3(v); %position too lok at derivative (g in equation)
B = k*r.^2/2;
phi(v) = exp(-i*B./(A+d)); %phi
phi1(v) = exp(-i*B./(A+d)).*(i*B./(A+d).^2); %frist derivative of phi
phi2(v) = exp(-i*B./(A+d)).*(-i*B./(A+d).^2).^2 + exp(-i*B./(A+d)).*((-
2*i*B)/(A+d).^3); %second derivative of phi
end

%the amplitude of each of the phis and derivatives
amp_phi = sqrt(real(phi).^2+imag(phi).^2);
amp_phi1 = sqrt(real(phi1).^2+imag(phi1).^2);
amp_phi2 = sqrt(real(phi2).^2+imag(phi2).^2);

%plotting, phi, and the ders
plot(dist,(k^2*amp_phi),dist,(k*amp_phi1),dist,(amp_phi2))
ylabel('Amplitude Electric Field per mm^2')
xlabel('Distance from Objective (mm)')
grid

%plotting R and w
figure
subplot(2,1,2)
plot(dist,w3)
ylabel('w_3 (mm)')
xlabel('Distance from Objective (mm)')
grid

subplot(2,1,1)
plot(dist,R3)
ylabel('R_3 (mm)')
xlabel('Distance from Objective (mm)')
grid

%the values of the amplitude to compare
[(k^2*amp_phi(1:15))' (k*amp_phi1(1:15))' (amp_phi2(1:15))]'
k^2*amp_phi(1)
k*amp_phi1(1)
amp_phi2(1)

```

Program 3: get_20_40_from_fred.m

```

function [z_a20, z_a40] =
get_20_40_from_fred(file_name,matrix_size,want_plot,i)
%
%inputs: file_name (with .dat), matrix_size (pixels)
%want plot( 'y' if want to plot the data), i, a number for the title of the plot
%outputs: z_a20 (defocus),z_a40 (spherical)

num_zerns = 36;
%the zern parameters we want 1 to 36
viz = 1:1:num_zerns;

%getting the data from the fred file in phase
[x_vect,y_vect,z_rad] = read_fred(file_name);

%center and radius of data
pos = [round(matrix_size/2) round(matrix_size/2)];
r = round(matrix_size/2);

%masking the data to a circle
[z_rad] = mask_circle(z_rad,pos,r);

%unwrapping
z_rad = unwrap(z_rad);
z_rad = unwrap(z_rad,[],2);

z = z_rad./4*pi; %phase map is now in waves (2 pi rads = 1 wave)

%plotting the data
if want_plot == 'y'

    figure
    pcolor(x_vect,y_vect,z)
    shading interp
    % colormap gray

    axis equal
    colorbar
    axis off
    tit_str = ['the ' num2str(i) 'th dataset'];
    title(tit_str)
end

%size of map
vsize= size(z);

```



```

    %getting mr and ma from the function
    [mr,ma] = zern_radius_angle(vsize,pos,r);

    %getting the zens
    [zern,rmse,spar,tpar,ppar] = zern_estim(z,mr,ma,viz);

    %outputing the defocus and spherical
    z_a20 = zern(5,:);
    z_a40 = zern(13,:);

```

Program 4: read_fred.m

```

function [x_vect,y_vect,z]=read_fred(fname_str)
%read_fred.m
%
%a subfunction program to read in the .dat files exported by fred's intensity map
function
%
%input
% fname_str  string of the file name (including the .dat)
%
%output
% x_vect,y_vect  x and y coords in units from fred (likely mm?)
% z             Height map of data in units from fred (likely mm?)

%open the file up
fid = fopen(fname_str);

%we can discard the first 5 lines
for i = 1:5
    tline1 = fgetl(fid);
end

%getting the infor about the size of the data
matrix_size_info = fgetl(fid);
ignore = fgetl(fid);
step_size_x_y = fgetl(fid);
min_x_y = fgetl(fid);

%getting this info in the correct form
[min_x min_y] = strread(min_x_y,'%n%n');
[step_size_x step_size_y] = strread(step_size_x_y,'%n%n');

```

```

[ignore lengthx lengthy] = streadd(matrix_size_info,'%s%n%n');

%forming the vectors for x and y
max_x = lengthx*(step_size_x) + min_x-step_size_x;
max_y = lengthy*(step_size_y) + min_y-step_size_y;

x_vect = min_x:step_size_x:max_x;
y_vect = min_y:step_size_y:max_y;

for i = 1:lengthy
    line = fgetl(fid);
    z(:,i) = str2num(line)';
end

fclose(fid);

```

Program 5: mask_circle.m

```

function [map] = mask_circle(map,pos,r,binner,mval)
% function [map] = mask_circle(map,pos,r,binner,mval)
%
% mask_circle: apply one or more circular masks to an image or
%             generate circular masks.
%
% map   : image array
% pos   : each row contains the center of a circle (in pixels)
% r     : circle radii in pixels (can be a vector)
% binner: OPTIONAL, for each circle, a value of 1 indicates that
%         the inner part of the circle will be removed from the
%         image. Default is 0 i.e. mask the outside.
% mval  : OPTIONAL, value to which the masked areas will be set.
%         Default is NaN.
%
% EXAMPLES:
%
% img = mask_circle(img,[550,500],350);
%
%     Masks an image 'img' with a circular mask. The outside of
%     the circle is masked with NaN values.
%
% mask = mask_circle(ones(size(img)),[550,500],350,0,0);
%
%     Generates a mask with the dimensions of 'img' with the area
%     inside the circle set to one and the area outside the

```

```

%   circle set to 0. The mask can then be applied (with .*) to
%   several images.
%

% This software was developed at the National Institute of Standards and
% Technology
% by employees of the Federal Government in the course of their official duties.
% Pursuant to title 17 Section 105 of the United States Code this software is not
% subject to copyright protection and is in the public domain. This software is an
% experimental system. NIST assumes no responsibility whatsoever for its use
% by other
% parties, and makes no guarantees, expressed or implied, about its quality,
% reliability,
% or any other characteristic. We would appreciate acknowledgement if the
% software is used.
%
% This software can be redistributed and/or modified freely provided that any
% derivative
% works bear some notice that they are derived from it, and any modified
% versions bear
% some notice that they have been modified.
%
% Revision history:
% Hans Soons, NIST, November 2001   initial version
% Ulf Griesmann, 11 Jan 2002,   allow masking with something
%                               other than NaN.
% -----

% check parameters
if nargin <= 4, mval = NaN; end;
if nargin <= 3, binner = zeros(1,size(pos,1)); end;

[n1,n2] = size(map);

vx = (1:1:n2)';
vy = (1:1:n1)';

[mx,my] = meshgrid(vx,vy);

% transform y offset to proper coordinate frame
pos(:,2) = (n1-pos(:,2)+1);
for i = 1:length(pos(:,1)),
    if binner(i) == 1,
        map((((mx-pos(i,1)).^2+(my-pos(i,2)).^2) <= r(i)^2)) = mval;
    else
        map((((mx-pos(i,1)).^2+(my-pos(i,2)).^2) > r(i)^2)) = mval;
    end
end

```

```

end;
end;

```

Program 6: zern_radius_angle.m

```

function [mr,ma] = zern_radius_angle(vsize,vpos,radius)
% function [mr,ma] = zern_radius_angle(vsize,vpos,radius)
%
% zern_radius_angle: calculate normalized radii and angles for
%                   each point of a map
%
% mr   : array with normalized radii at each point of the map
% ma   : array with angles at each point of the map
%       (defined relative to y, x corresponds to pi/2)
% vsize : vertical and horizontal dimension of the map
%       (i.e. result of size(map))
% vpos  : center position circle within which to estimate
% radius : radius circle

% This software was developed at the National Institute of Standards and
% Technology
% by employees of the Federal Government in the course of their official duties.
% Pursuant to title 17 Section 105 of the United States Code this software is not
% subject to copyright protection and is in the public domain. This software is an
% experimental system. NIST assumes no responsibility whatsoever for its use
% by other
% parties, and makes no guarantees, expressed or implied, about its quality,
% reliability,
% or any other characteristic. We would appreciate acknowledgement if the
% software is used.
%
% This software can be redistributed and/or modified freely provided that any
% derivative
% works bear some notice that they are derived from it, and any modified
% versions bear
% some notice that they have been modified.
%
% Version 1.0
% Hans Soons, NIST, November 2001
% -----

% generate maps with x and y coordinates

```

```

[mx,my] = meshgrid(1:1:vsize(2),1:1:vsize(1));

% put y coordinate in proper coordinate frame

my = vsize(1)-my+1;

% generate angle and radius maps

mr = sqrt((mx-vpos(1)).^2+(my-vpos(2)).^2);
ma = atan2((mx-vpos(1)),(my-vpos(2)));

% normalize

mr = mr/radius;

```

Program 7: zern_estim.m

```

function [vpar,rmse,spar,tpar,ppar] =
zern_estim(map,mr,ma,viz,weights,salgor,snoise)
% function [vpar,rmse,spar,tpar,ppar] =
zern_estim(map,mr,ma,viz,weights,salgor,snoise)
%
% zern_estimate: estimates Zernike coefficients
%
% Zernike terms are numbered as follows:
% (D. Malacara, Optical Shop Testing, 2nd edition, p.465 John Wiley 1992)
%
% term   n   m   l
%
% 1     0   0   0
% 2     1   0   1
% 3     1   1  -1
% 4     2   0   2
% 5     2   1   0
% 6     2   2  -2
% :     :   :   :
%
% Where n equals the degree of the radial polynomial and l the angular
% dependence (exponential) parameter (l=n-2m)
%
% map      : matrix or vector with heights
% mr       : matrix or vector with normalized radii at each point of the map
% ma       : matrix or vector with angles at each point of the map
%          (defined relative to y, x corresponds to pi/2)

```

```

% viz    : vector with the numbers of the zernike terms to be estimated
% vpar   : estimated parameters (padded with zeros)
% weights : optional, array having the same size as the phase map used to
weigh
%         each observation (e.g., the intensity map). The weights are assumed to
%         equal the inverse of the noise variance at each point.
% salgor  : optional, algorithm used to solve the least squares problem
%         'qr' : Solution by QR decomposition of the design matrix using
%         Householder transformations. This is a numerically accurate
method but very
%         memory intensive. Use for many Zernike terms may yield memory
problems.
%         'normal': DEFAULT. This algorithm explicitly calculates the normal
equations  $(X'X) b = X'y$ 
%         before solving them. The algorithm does not assume
orthogonality but
%         is numerically inferior to the QR procedure. This option is fast and
%         not memory intensive, allowing for many Zernike terms to be
estimated.
%         'orthogonal' : This algorithm assumes orthogonality of the Zernike terms.
In practice
%         this is only an approximation due to the discretization of the map.
%         The algorithm explicitly calculates the relevant elements of the
normal
%         equations. This option is fast and not memory intensive, allowing
for many
%         Zernike terms to be estimated.
% snoise  : optional, estimate of the standard deviation of uncorrelated
measurement noise.
%         If present, this standard deviation is used to estimate the statistical
properties of
%         each estimated parameter. If snoise is not defined, the root mean
squared residual
%         error is used instead, which is not an accurate measure if the model is
incomplete.
% rmse   : root mean squared residual error
% spar   : estimated standard deviation for each estimated parameter
% tpar   : t-statistic for each estimated parameter (ratio of parameter value to its
standard deviation)
%         As the model is close to being orthogonal, this parameter can be used
to evaluate the
%         significance of individual parameters and subsets of parameters.
% ppar   : probability that an estimated parameter is significant (has a value
unequal to zero),
%         assuming Gaussian uncorrelated noise.
%

```

```

% The weights are implemented to yield the following problem:
%
% Minimize the sum of weights .* (map - fitted_map).^2

% This software was developed at the National Institute of Standards and
% Technology
% by employees of the Federal Government in the course of their official duties.
% Pursuant to title 17 Section 105 of the United States Code this software is not
% subject to copyright protection and is in the public domain. This software is an
% experimental system. NIST assumes no responsibility whatsoever for its use
% by other
% parties, and makes no guarantees, expressed or implied, about its quality,
% reliability,
% or any other characteristic. We would appreciate acknowledgement if the
% software is used.
%
% This software can be redistributed and/or modified freely provided that any
% derivative
% works bear some notice that they are derived from it, and any modified
% versions bear
% some notice that they have been modified.
%
%
% NOTE: STATISTICS NEED TO BE MODIFIED FOR WEIGHTS
%
% Version 0.2
% Hans Soons, NIST, 11/2001, 12/2001, 01/2002
% -----

% set default values

if (nargin <= 6), snoise = []; end;
if (nargin <= 5), salgor = []; end;
if (nargin <= 4), weights = []; end;

if isempty(weights), weights = ones(size(map)); end;
if isempty(salgor), salgor = 'normal'; end;
%
% limit evaluation to non NaN values
%
vi = find((~isnan(map)) & ((mr <= 1) & ~isnan(mr)));
mr = mr(vi);
ma = ma(vi);
map = map(vi);
weights = weights(vi);
%

```

```

% center data
%
rmean = mean(map);
map = map-rmean;
%
% solve according to desired routine
%
switch lower(salgor)
case 'qr'
[vpar,mcov,mse] = zern_estim_qr(map,mr,ma,viz,weights);
case 'normal'
[vpar,mcov,mse] = zern_estim_normal(map,mr,ma,viz,weights);
case 'orthogonal'
[vpar,mcov,mse] = zern_estim_ortho(map,mr,ma,viz,weights);
otherwise
error(['salgor,' is not a valid algorithm option']);
end;
%
% add mean
%
vi = find(viz == 1);
if ~isempty(vi),
vpar(viz(vi(1))) = vpar(viz(vi(1)))+rmean;
end;
%
% calculate statistical properties
%
rmse = sqrt(mse);

if isempty(snoise),
snoise = rmse;
end;

no = length(map);
np = length(viz);
nz = max(viz);

spar = zeros(nz,1);
tpar = zeros(nz,1);

spar(viz) = snoise*(diag(mcov)).^(1/2);
tpar(viz) = abs(vpar(viz)./spar(viz));

ppar = zeros(nz,1);
for i = 1:length(viz),
ppar(viz(i)) = tcdf(tpar(viz(i)),no-np);
end;

```



```

end;

% -----
% Subfunction zern_estim_qr
% -----

function [vpar,mcov,mse] = zern_estim_qr(map,mr,ma,viz,weights)
%
% zern_estim_qr: estimates Zernike coefficients

% -----

%
% initialize design matrix
%
    no = length(map);
    np = length(viz);
    nz = max(viz);
%
    mX = zeros(no,np);
%
% calculate design matrix
%
    disp(' ');
    disp(' Estimating Zernike Polynomial ...');
    disp(' ');
%
    for i = 1:np,
%
% get Zernike term
%
        vp = zeros(nz,1);
        vp(viz(i)) = 1;

        mX(:,i) = zern_eval(mr,ma,vp);

    end;
%
% Estimate parameters

    vpar = zeros(nz,1);
%
% Apply weights
%
    weights = weights.^(1/2);

```

```

map = map.*weights;
for i = 1:np,
    mX(:,i) = mX(:,i).*weights;
end;
%
% solve system
%
vpar(viz,1) = mX\map;
%
% return statistics
%
mcov = inv(mX'*mX);
sse = map'*map-vpar(viz)*mX'*map;
mse = sse/(no-np);

% -----
% Subfunction zern_estim_ortho
% -----

function [vpar,mcov,mse] = zern_estim_ortho(map,mr,ma,viz,weights)
%
% zern_estim_ortho: estimates Zernike coefficients assuming orthogonality of the
%                   Zernike terms.

% -----

% note: don't worry about scaling and centering the design matrix
%       columns as the Zernike terms are already scaled
%
% initialize
%
np = length(viz);
nz = max(viz);
no = length(map);

vX = zeros(np,1);
vY = zeros(np,1);
%
disp(' ');
disp(' Estimating Zernike Polynomial ...');
disp(' ');

for ip = 1:length(viz),
%

```

```

% get Zernike term
%
    vp = zeros(nz,1);
    vp(viz(ip)) = 1;
    [vdes] = zern_eval(mr,ma,vp);
%
% calculate contribution to system
%
    vX(ip,1) = vX(ip,1)+vdes*(vdes.*weights);
    vY(ip,1) = vY(ip,1)+vdes*(map.*weights);

end;

% solve weighted least squares problem

    vpar = zeros(nz,1);
    vpar(viz,1) = vY./vX;
%
% return statistics
%
    mcov = diag(vX.^(-1));

% As orthogonality is only an approximation, the sse estimate will not
% be correct. Re-evaluation of the full model however takes time
% that may not be warranted for this option.

    sse = map*(map.*weights)-2*vpar(viz)*vY+vpar(viz)*diag(vX)*vpar(viz);
    mse = sse/(no-np);

% -----
% Subfunction zern_estim_normal
% -----

function [vpar,mcov,mse] = zern_estim_normal(map,mr,ma,viz,weights)
%
% zern_estim_normal: Estimates Zernike coefficients by explicit calculation
%                   of the normal equations before solving them. This procedure
%                   is numerically inferior to say the QR decomposition of the
%                   design matrix.

% Version 1.0
% -----

% note: don't worry about scaling and centering the design matrix
%       columns as the Zernike terms are already scaled

```

```

%
% set maximum number of elements in the design matrix to avoid memory
problems

nmax = 1E7;

% initialize

np = length(viz);
nz = max(viz);
no = length(map);

mX = zeros(np,np);
vY = zeros(np,1);
%
weights = weights.^(1/2);
%
% estimate number of sub problems
%
ns = ceil((no*np)/nmax);

disp(' ');
disp(' Estimating Zernike Polynomial ...');
disp(' ');

ic = 0;

for is = 1:ns,
%
% set observations in this patch
%
vi = (is:ns:no)';
%
mdes = zeros(length(vi),np);
%
for ip = 1:np,
%
% get Zernike term
%
vp = zeros(nz,1);
vp(viz(ip)) = 1;
mdes(:,ip) = zern_eval(mr(vi),ma(vi),vp).*weights(vi);
%
ic = ic+1;

end;

```

```

%
% calculate contribution to system
%
    mX = mX+mdes'*mdes;

    vY = vY+mdes*(map(vi).*weights(vi));
end;
%
% solve normal equations
%
    vpar = zeros(nz,1);
    vpar(viz,1) = mX\vY;

% return statistics
%
    mcov = inv(mX);
    sse = map*(map.*weights)-2*vpar(viz)*vY+vpar(viz)*mX*vpar(viz);
    mse = sse/(no-np);

```

Program 8: foc_effect_no_image.m

```

close all;
clear all;

f = 2; %mm, focal length
A = 4.5; % mm, half aperature

d = 1000; %distance objective to camera in mm

f=10;
partd = f-.1:0.00001:f+.25;
s=2*(partd-f)+f;

s_prime = (s*f)./(s-f);
R = -s_prime + d;

a_prime = A*(R)./s_prime;
h =abs(R)- sqrt(R.^2-a_prime.^2);

figure
plot(partd-f,h*1000,'k')
xlabel('Position of Part (where 0 = f) (mm)')
ylabel('Sag at camera (micrometers)')

```

```

title_str = ['focal length is ' num2str(f) ' mm, d is ' num2str(d) ' mm, a is '
num2str(A) ' mm' ];
%title(title_str)
grid
axis([min(partd-f) max(partd-f) 0 3])
hold on

```

Program 9: foc_effect_w_image.m

```

close all;
clear all;

f1 = 250;    %FL of lens1
f2 = 100;    %FL of lens2
f3 = 75.6;   %FL of lens3
f4 = 130;    %FL of lens4

lo1 = 310;   %dist obj to L1
l12 = f1+f2; %dist to L1 to L2 do not change

%using my lookup cahrt for a 0.5 mm part
%dist to L2 to L3

l34 = f3+f4; %dist to L3 to L4 do not change
l4c = 130;   %dist to L4 to Lcam

na = 0.42;

radius_part = 0.5 %mm

l23 = 145;%%using my lookup cahrt for a 0.5 mm part
%dist to L2 to L3

fo = 10%mm fL of objective lens
A = 4.5% 1/2 width of aperature, mm

partd = fo-2:0.00001:fo+2;
so=2*(partd-fo)+fo;

%so = 9.2:0.0001:10.2;
so_p = (so*fo)./(so-fo);
s1 = lo1-so_p;
s1_p = (s1*f1)./(s1-f1);

```

```

s2= l12-s1_p;
s2_p = (s2*f2)./(s2-f2);

%l23 = 142;    %dist to L2 to L3
s3= l23-s2_p;
s3_p = (s3*f3)./(s3-f3);
s4= l34-s3_p;
s4_p = (s4*f4)./(s4-f4);
R = -s4_p + l4c;
Ml = (f2/f1)*(f4/f3);
Ac = Ml.*A.*R./s4_p;
%
sag = abs(R)- sqrt(R.^2-Ac.^2);

%figure
plot(partd-fo,sag*1000)
xlabel('Position of Part (where 0 = f) (mm)')
ylabel('Sag at camera (micrometers)')
title_str = ['morti(with image) f=' num2str(fo) ', Lo1= ' num2str(lo1) ', L23= '
num2str(l23) ', L4c= ' num2str(l4c) '];
%title(title_str)
axis([-0.5 0.1 0 10])%0 10]
grid

```

APPENDIX C: CALIBRATION DATA

The laser scale was calibrated using the displacement measuring interferometer as follows. The final calibration is 0.862153 mm per edisplay unit.

SET 1

Moving Stage Up
Steps of ~0.1 mm

Edisplay	DMI
0	0
-0.153	0.132
-0.322	0.2781
-0.373	0.3218
-0.4786	0.4129
-0.5808	0.501
-0.7072	0.6101
-0.8269	0.7126
-0.937	0.8082
-1.065	0.9186
-1.1795	1.0173
-1.2988	1.1202
-1.4055	1.2121
-1.504	1.2971
-1.6239	1.4005
-1.7395	1.5002
-1.8633	1.6067

SET 2

Moving Stage Up
Steps of ~0.25 mm

Edisplay	DMI
0	0
-0.2893	0.2496
-0.5715	0.4928
-0.8714	0.7515
-1.156	0.9968
-1.458	1.2572
-1.7336	1.4949
-2.0419	1.7607
-2.3304	2.0094
-2.6128	2.253
-2.9188	2.5167
-3.1917	2.752
-3.4769	2.998
-3.7833	3.2626
-4.0619	3.5025
-4.3603	3.76
-4.6316	3.9938
-4.9307	4.2516
-5.2259	4.5062
-5.5192	4.759
-5.8042	5.0046
-6.0898	5.2251
-6.3862	5.5066
-6.6704	5.7517
-6.9628	6.0039
-7.2517	6.253
-7.5383	6.5
-7.8439	6.7636

SET 3

Moving Stage Up
Steps of ~0.5 mm

Edisplay	DMI
0	0
-0.5794	0.4998
-1.1625	1.0025
-1.7457	1.5052
-2.321	2.0021
-2.9165	2.5147
-3.494	3.0128
-4.0904	3.5269
-4.636	3.9972
-5.2376	4.516
-5.8114	5.0107
-6.3869	5.507

SET 4

Moving Stage Down
Steps of ~0.25 mm

Edisplay	DMI
0	0
0.3045	-0.2623
0.5981	-0.5151
0.8724	-0.7519
1.1743	-1.0121
1.4535	-1.2526
1.8073	-1.5574
2.0355	-1.7543
2.3218	-2.0012
2.6108	-2.2503
2.8968	-2.4969
3.2072	-2.7642
3.4769	-2.9968
3.7676	-3.2475
4.0545	-3.4948
4.4029	-3.7951
4.6985	-4.05
4.9449	-4.2622
5.216	-4.496
5.521	-4.7588
5.7991	-4.9984
6.086	-5.2459
6.3767	-5.4964
6.696	-5.7718
6.9836	-6.0194

	Slope mm/Scale Unit
SET 1	0.862244
SET 2	0.862004
SET 3	0.862422
SET 4	0.861944
Average	0.8621535
Std Dev	0.000221

